

Thesis presented to the Instituto Tecnológico de Aeronáutica, in partial fulfillment of the requirements for the degree of Doctor of Science in the Graduate Program of Physics, Field of Atomic and Molecular Physics.

Gusthavo Miranda Simões Brizolla

TIGHT-BINDING MODELING OF VAN DER WAALS QUBITS

Thesis approved in its final version by signatories below:



Prof. Dr. Ivan Guilhon Mitozo Rocha

Advisor



Prof. Dr. João Milton Pereira Junior

Co-advisor

Cataloging-in Publication Data
Documentation and Information Division

Brizolla, Gusthavo Miranda Simões

Tight-Binding modeling of van der Waals qubits / Gusthavo Miranda Simões Brizolla.
São José dos Campos, 2024.
165f.

Thesis of Doctor of Science – Course of Physics. Area of Atomic and Molecular Physics –
Instituto Tecnológico de Aeronáutica, 2024. Advisor: Prof. Dr. Ivan Guilhon Mitozo Rocha.
Co-advisor: Prof. Dr. João Milton Pereira Junior.

1. Materiais 2D 2. qubits 3. Teoria do Funcional da Densidade 4. Aproximação Tight-Binding
I. Instituto Tecnológico de Aeronáutica. II. Title.

BIBLIOGRAPHIC REFERENCE

BRIZOLLA, Gusthavo Miranda Simões. **Tight-Binding modeling of van der Waals qubits**. 2024. 165f. Thesis of Doctor of Science – Instituto Tecnológico de Aeronáutica, São José dos Campos.

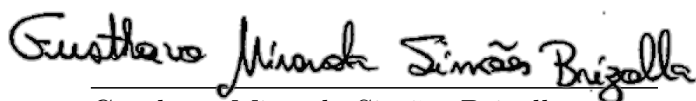
CESSION OF RIGHTS

AUTHOR'S NAME: Gusthavo Miranda Simões Brizolla

PUBLICATION TITLE: Tight-Binding modeling of van der Waals qubits.

PUBLICATION KIND/YEAR: Thesis / 2024

It is granted to Instituto Tecnológico de Aeronáutica permission to reproduce copies of this thesis and to only loan or to sell copies for academic and scientific purposes. The author reserves other publication rights and no part of this thesis can be reproduced without the authorization of the author.



Gusthavo Miranda Simões Brizolla
Rua Conselheiro Rodrigues Alves, 571
12209-540 – São José dos Campos-SP

TIGHT-BINDING MODELING OF VAN DER WAALS QUBITS

Gusthavo Miranda Simões Brizolla

Thesis Committee Composition:

Prof. Dr. Marcelo Marques	President	-	ITA
Prof. Dr. Ivan Guilhon Mitozo Rocha	Advisor	-	ITA
Prof. Dr. João Milton Pereira Junior	Co-advisor	-	UFC
Prof. Dr. Filipe Matusalém	Internal member	-	ITA
Prof. Dr. Diego Rabelo da Costa	External member	-	UFC
Prof. Dr. Caio Henrique Lewenkopf	External member	-	UFF

I dedicate this to my family for all the
love

Acknowledgments

First, I want to thank all the teachers who contributed to my education. With their guidance, effort, and support, I came this far. Mainly, I would like to thank my advisor, Prof. Dr. Ivan Guilhon, for all the precious support, patience, friendship, and conversations (about physics or not). To Prof. Dr. João Milton, for all the discussions and contributions to my work and the enthusiasm.

True friends have also supported my journey. I thank Luckeciano Melo for more than 10 years of true friendship and enthusiasm. You always believed in me more than I did. To my colleagues at ITA, Luiz Gustavo, and Victor Morele, for the collaboration and the pleasant moments spent together.

I am also highly thankful for those who believed in and welcomed me to be part of the Group of Semiconductor Materials and Nanotechnology. CAPES has provided financial support, and computational resources have been provided by the National Laboratory of Scientific Computing (LNCC/MCTI, Brazil) via the Sdumont supercomputer, making possible the development of this Ph.D. thesis, to whom I am deeply grateful.

Finally, I have a special thanks to my family. I want to thank my mother, Francely, for all her care, love, and support throughout my life. My aunts, Fracylene and Yara, my grandmother, Isabel, to Reginaldo, Paulo de Tarso, and Francisco Pires (*in memorium*), for all the love and encouragement. I want to thank my wife, Victória, for always being a place of comfort, peace, and love, making the most challenging days of this journey lighter. In particular, I want to thank my father (*in memorium*); wherever you are, you always live in my heart.

*“Der Mensch kann nur Mensch werden durch Erziehung.
Er ist nichts, als was die Erziehung aus ihm macht.”*

— IMMANUEL KANT

Resumo

A computação quântica tem potencial para revolucionar campos como desenvolvimento de medicamentos, previsão de doenças, design de materiais, aprendizado de máquina, big data e segurança cibernética. O componente fundamental dos processos de informação quântica é o qubit, que aproveita a superposição quântica para representar 0 e 1 simultaneamente, ao contrário dos bits clássicos que só podem representar um valor de cada vez. Várias abordagens para implementação de qubits foram propostas, incluindo supercondutores, spins nucleares e eletrônicos, íons aprisionados e qubits fotônicos.

Recentemente, foi proposta uma nova maneira de implementar o qubit para computação quântica através de uma aplicação inovadora de heteroestruturas de van der Waals (vdW) como qubits de carga, aqui denominadas qubits vdW. Ele explora a superposição espacial de elétrons das camadas individuais, estudando a composição orbital das bandas em função do campo aplicado. Dada a extensa lista de combinações possíveis de materiais bidimensionais (2D), a proposta oferece uma nova perspectiva na área.

Neste trabalho, investigamos as propriedades estruturais e eletrônicas de vinte dichalcogenetos de metais de transição (TMDs) usando a Teoria do Funcional da Densidade (DFT). Selecionamos camadas com níveis de energia bem alinhados que resultaram em estados hibridizados para formar qubits vdW. Para estudar esses qubits com menor esforço computacional do que DFT, empregamos a abordagem Tight-Binding (TB), usando Funções de Wannier Maximamente Localizadas (MLWF) derivadas de cálculos DFT. Nosso modelo simplificado é consistente com os resultados DFT, validado e generalizado para outros sistemas com estados hibridizados semelhantes. Identificamos novas combinações de materiais 2D como candidatos promissores para a implementação de qubits vdW.

Para explorar as propriedades de transporte de regiões de dispersão influenciadas por estados hibridizados em materiais 2D, focamos em nanofitas (NRs) para nossos cálculos de transporte quântico. Esses cálculos nos permitem analisar como as ondas planas se dividem devido aos estados hibridizados, facilitando a transmissão de corrente entre as camadas dentro da heteroestrutura. As NRs simuladas foram baseados em modelos TB anteriores para os materiais 2D com confinamento adicional, garantindo o caráter *ab*

initio do nosso modelo, mantendo baixo custo computacional. Inicialmente, exploramos o impacto do confinamento nas NRs formadas a partir de monocamadas TMD, avaliando como a terminação química e a configuração das bordas influenciam o surgimento dos estados de bordas e das propriedades de transporte. Com uma compreensão clara dos efeitos do confinamento, procedemos à investigação do transporte em estruturas altamente hibridizadas para observar a divisão de pacotes de onda. Essas descobertas abrem caminho para a implementação de qubits de carga.

Abstract

Quantum computing has the potential to revolutionize fields like drug development, disease prediction, materials design, machine learning, big data, and cybersecurity. The fundamental component of quantum information processes is the qubit, which leverages quantum superposition to represent both 0 and 1 simultaneously, unlike classical bits that can only represent one value at a time. Various approaches to qubit implementation have been proposed, including superconductors, nuclear and electronic spins, trapped ions, and photonic qubits.

Recently, a new way of implementing the qubit for quantum computation through an innovative application of gated van der Waals (vdW) heterostructures as charge qubits has been proposed, here named vdW qubits. It explores the spatial superposition of electrons from the individual layers by studying the orbital composition of the bands as a function of the gate field. Given the extensive list of possible combinations of two-dimensional (2D) materials, the proposal provides a new perspective in the area.

In this work, we investigate the structural and electronic properties of twenty 2D transition metal dichalcogenides (TMDs) using Density Functional Theory (DFT). We selected layers with well-aligned energy levels that resulted in hybridized states to form vdW qubits. To study these qubits with lower computational effort than DFT, we employed the Tight-Binding (TB) approach, using Maximally Localized Wannier Functions (MLWF) derived from DFT calculations. Our simplified model is consistent with DFT results, validated, and generalized to other systems with similar hybridized states. We identified new combinations of layered materials as promising candidates for implementing vdW qubits.

To explore the transport properties of scattering regions influenced by hybridized states in 2D materials, we focused on nanoribbons (NRs) for our quantum transport calculations. These calculations allow us to analyze how plane waves split due to hybridized states, facilitating current transmission between layers within the heterostructure. The NRs simulated were based on previous TB models for the 2D materials with additional confinement, ensuring the *ab initio* character of our model while maintaining low computational cost. Initially, we explored the impact of confinement on NRs formed from

TMD monolayers, assessing how chemical termination and edge configuration influence the appearance of edge states and transport properties. With a clear understanding of confinement effects, we proceeded to investigate transport in highly hybridized structures to observe wave packet splitting. These findings pave the way for implementing charge qubits.

List of Figures

FIGURE 1.1 – Performance comparison of a classical vs. quantum computer with system’s complexity.	28
FIGURE 1.2 – (a) a graphical representation of a qubit on a Bloch sphere. (b) Landau–Zener evolution of a two-level system represented on the Bloch sphere. Figures generated using QuTip package (JOHANSSON <i>et al.</i> , 2012; JOHANSSON <i>et al.</i> , 2013).	29
FIGURE 1.3 – Sythesis of MoS ₂ /graphene heterostructure by chemical vapor decomposition. The top left is a high-resolution STEM imaging of the resulting materials. The bottom left shows FFT patterns. Source: (SHI <i>et al.</i> , 2012).	32
FIGURE 1.4 – (a) Schematic of the hBN-encapsulated superconductor–graphene–superconductor junctions embedded in a circuit quantum electrodynamics system. (b) Assembly of vdW heterostructures using a dry polymer-based pick-up and transfer technique. (c) Optical micrograph of the graphene transmon qubit. SC, superconducting. Inset, atomic force microscopy image of the encapsulated graphene before making electrical contact to the superconducting electrodes. (d) Qubit chip made of high-quality aluminium. Adapted from: (WANG <i>et al.</i> , 2019).	34
FIGURE 2.1 – Flow chart of SCF cycle.	48
FIGURE 2.2 – Quantum point contact conductance as a function of a gate voltage. The conductance plateaus can be seen, indicating its quantization. Figure adapted from (WEES <i>et al.</i> , 1988).	64
FIGURE 2.3 – Color map of a nanostructure subjected to a gaussian potential on its central region configuring a QPC. Due to the potential, depending of the energy of the modes leaving the contacts, one may obtain an open or a closed channel.	67

FIGURE 2.4 – Schematic representation of a one dimensional device (lead + scattering region) and how the sites are numbered on Kwant.	73
FIGURE 3.1 – Top and side view of MoS ₂ allotrope H.	79
FIGURE 3.2 – Top and side view of HfS ₂ allotrope T.	79
FIGURE 3.3 – Energy levels and band gaps of monolayers considering quasi-particle effects. The bar edges represent the valence band maximum and the conduction band minimum for each material. All energies are in eV and with the vacuum as reference.	83
FIGURE 3.4 – Types of band alignment. Type I (electrons and holes are on the same layer), the VBM and CBM are on the same material. Type II (electrons and holes in different layers), where the VBM and CMB are on different materials, or type III, which is a broken gap situation (ÖZÇELİK <i>et al.</i> , 2016).	84
FIGURE 4.1 – Side view (a) and top view (b) of the heterostructure. Light green is the Thin atoms, dark green Selenium, and grey Zirconium atoms.	88
FIGURE 4.2 – ZrSe ₂ /SnSe ₂ DFT band structure without electric field applied. A strong hybridization at the M point is present.	89
FIGURE 4.3 – The correspondence of the two lowest conduction bands as a two-level system for a charge qubit.	90
FIGURE 4.4 – ZrSe ₂ /SnSe ₂ band structure subjected to different electric fields.	91
FIGURE 4.5 – Orbital change for the state $ 0\rangle$ obtained from a DFT calculation.	92
FIGURE 4.6 – Orbital resolved band structure of ZrSe ₂ /SnSe ₂ used to provide an initial guess to obtain the MLWFs. (a) Projected band structure showing the orbital contribution of the $d_{xy}+d_{z^2}+d_{x^2-y^2}$ orbitals of Zirconium. (b) Projected band structure showing the orbital contribution of the p orbital of Selenium.	92
FIGURE 4.7 – TB band structures for the ZrSe ₂ /SnSe ₂ heterobilayer when an electric field of (a) -0.05 V/\AA (b) 0.0 V/\AA and (c) $+0.1 \text{ V/\AA}$ is applied in the z direction. Palette color indicates the percentage of bands formed by orbitals from the SnSe ₂ and ZrSe ₂ layers. The top of the valence band is taken as reference.	93
FIGURE 4.8 – Change of the orbital contribution to the state $ 0\rangle$ from the TB model as a function of the electric field applied.	93

- FIGURE 4.9 – ZrSe₂/SnSe₂ TB band structure in red and DFT band structure in black with the change of d_{hop} 95
- FIGURE 4.10 – TB band structures considering quasi particle effects for the ZrSe₂/SnSe₂ heterobilayer when an electric field of (a) -0.05 V/Å (b) 0.0 V/Å and (c) +0.1 V/Å is applied in the z direction. Palette color indicates the percentage of bands formed by orbitals from the SnSe₂ and ZrSe₂ layers. The top of the valence band is taken as reference. 96
- FIGURE 4.11 – Change of the orbital contribution in the function of the electric field applied. The solid lines represent the change on $|0\rangle$, and the dotted lines represent the change on $|1\rangle$. The colors are used to identify the layers: orange is for ZrSe₂ and blue for SnSe₂. 96
- FIGURE 4.12 – The *ab initio* TBH results for the orbital contribution as a function of the electric field applied considering the effect of polarizability. The solid lines represent the change on $|0\rangle$, and the dotted lines represent the change on $|1\rangle$. Blue is for ZrSe₂ and orange for SnSe₂. 97
- FIGURE 4.13 – Band structures for the ZrSe₂/SnSe₂ heterobilayer when an electric field of (a) -0.3 V/Å (b) 0.0 V/Å and (c) +0.3 V/Å is applied in the z direction. Palette color indicates the percentage of bands formed by orbitals from the SnSe₂ and ZrSe₂ layers. The top of the valence band is taken as reference. 98
- FIGURE 4.14 – (a) Side view of the heterostructure. (b) Top view of the heterostructure. Light green atoms represent Thin, blue Hafnium and yellow Sulfur. 99
- FIGURE 4.15 – HfS₂/SnS₂ TB band structure in red and DFT band structure in black for the values $d_{hop} \leq 7\text{Å}$ and $|hop| \geq 0.02\text{ eV}$ 100
- FIGURE 4.16 – Band structures for the HfS₂/SnS₂ heterobilayer when an electric field of (a) -0.27 V/Å (b) 0.0 V/Å and (c) +0.27 V/Å is applied in the z direction. Palette color indicates the percentage of bands formed by orbitals from the HfS₂ and SnS₂ layers. The top of the valence band is taken as reference. 100
- FIGURE 4.17 – The *ab initio* TBH results for the orbital contribution as a function of the electric field applied considering the effect of polarizability. The solid lines represent the change on $|0\rangle$, and the dotted lines represent the change on $|1\rangle$. Green is for HfS₂ and red for SnS₂. 101

FIGURE 4.18 –(a) Side view of the heterostructure. (b) Top view of the heterostructure. Light green atoms represent Selenium, grey Zirconium, and yellow Sulfur.	102
FIGURE 4.19 –ZrS ₂ /SnS ₂ TB band structure in red and DFT band structure in black for the values $d_{hop} \leq 8.5\text{\AA}$ and $ hop \geq 0.004\text{ eV}$	103
FIGURE 4.20 –Band structures for the ZrS ₂ /SnS ₂ heterobilayer when an electric field of (a) -0.24 V/\AA (b) 0.0 V/\AA and (c) $+0.24\text{ V/\AA}$ is applied in the z direction. Palette color indicates the percentage of bands formed by orbitals from the ZrS ₂ and SnS ₂ layers. The top of the valence band is taken as reference.	103
FIGURE 4.21 –The <i>ab initio</i> TBH results for the orbital contribution as a function of the electric field applied considering the effect of polarizability. The solid lines represent the change on $ 0\rangle$, and the dotted lines represent the change on $ 1\rangle$. Light-blue is for ZrS ₂ and purple for SnS ₂	104
FIGURE 4.22 –(a) Side view of the heterostructure. (b) Top view of the heterostructure. Blue atoms represent Hafnium, grey Zirconium, and yellow Sulfur.	105
FIGURE 4.23 –Band structures for the ZrS ₂ /HfS ₂ heterobilayer when an electric field of (a) 0.0 V/\AA (b) -0.05 V/\AA and (c) $+0.05\text{ V/\AA}$ is applied in the z direction showing the change of hybridization at the Γ point. Palette color indicates the percentage of bands formed by orbitals from the ZrS ₂ and HfS ₂ layers. The top of the valence band is taken as reference.	106
FIGURE 4.24 –Band structures for the ZrS ₂ /HfS ₂ heterobilayer when an electric field of (a) 0.0 V/\AA (b) -0.16 V/\AA and (c) -0.23 V/\AA is applied in the z direction showing the change of hybridization now at the conduction bands at the M point. Palette color indicates the percentage of bands formed by orbitals from the ZrS ₂ and HfS ₂ layers. The top of the valence band is taken as reference.	106
FIGURE 4.25 –The same of Fig. 4.17, but now for ZrS ₂ /HfS ₂	107

- FIGURE 5.1 – Top view of NRs based on the allotropes 2H and 1T. (a) and (c) Top view of NRs based on the 2H allotrope, showcasing ZZ and AR edge configurations. (b) ZZ edge termination of NRs based on the 1T allotrope. Orange, red, and light-blue rectangles denote different chemical terminations: MC, MM, and CC, respectively. (d) AR-NR of the 1T allotrope. Blue atoms represent the metal, and dark and light green are the chalcogens. 111
- FIGURE 5.2 – (a) Band dispersion for the 2H-MoS₂-AR-NR in solid blue lines with the translational symmetry along the vector $\vec{a}_1 + 2\vec{a}_2$. In dotted red lines is the band structure for the 2D-MoS₂ 11 band TB model plotted along the path M'- Γ -M. (b) The plot of the wavefunctions of the edges states for each state is labeled on the dispersions in (a). 112
- FIGURE 5.3 – Band dispersion for the 2H-MoS₂-ZZ-NR with edges ended with metal and chalcogen, for a width of 50 nm in solid blue lines with the translational symmetry along the vector \vec{a}_1 . In dotted red lines is the band structure for the 2D-MoS₂ 11 band TB model plotted along the path K'- Γ -K. 113
- FIGURE 5.4 – Band dispersion for the 2H-MoS₂-ZZ-NR with edge terminations of (a) MC in solid blue lines subjected to an electric field of 0.01 V/Å. In dotted red lines is the band structure for the 2D-MoS₂ 11 band TB model plotted along the path K'- Γ -K. (b) The plot of the wavefunctions of the edges states for each state labeled on the dispersions in (a). 114
- FIGURE 5.5 – Dispersions of AR (a) MoSe₂, (b) WS₂, and (c) WSe₂ NRs in solid blue lines. In dotted red lines is the band structure of the 2D material correspondent for each nanoribbon along the path M'- Γ -M. . . . 115
- FIGURE 5.6 – Band dispersion for the 1T-ZrSe₂-NR with ZZ with edge terminations of (a) MC (b) MM and (c) CC in solid blue lines. In dotted red lines is the band structure for the 2D-ZrSe₂ 11 band TB model plotted along the path K'- Γ -K. At the bottom of each dispersion is shown the lead and in pink circles where the wave function is localized. The numbers label the subbands and are associated with the wave functions. 117
- FIGURE 5.7 – Band dispersion for the 1T-ZrSe₂-NR with AR edges in solid blue lines. In dotted red lines is the band structure for the 2D-ZrSe₂ 11 band TB model plotted along the path M'- Γ -K. The plot of the wavefunctions of the states circled is shown at the bottom of the panel. 118

- FIGURE 5.8 – Band dispersion for the ZrS_2 NR with edge terminations of (a) MC (b) MM (c) CC in solid blue lines. In dotted red lines is the band structure for the 2D- ZrS_2 11 band TB model plotted along the path $K'-\Gamma-K$ 118
- FIGURE 5.9 – Band dispersion for the 1T- SnSe_2 -NR with edge terminations of (a) MC (b) MM and (c) CC in solid blue lines. In dotted red lines is the band structure for the 2D- SnSe_2 11 band TB model plotted along the path $K'-\Gamma-K$. At the bottom of each dispersion, the plot of the wavefunctions of the edges states for each state labeled. 119
- FIGURE 5.10 – Band dispersion for the 1T- SnSe_2 -NR with AR edge in solid blue lines. In dotted red lines is the band structure for the 2D- SnSe_2 11 band TB model plotted along the path $K'-\Gamma-K$. At the bottom of each dispersion, the plot of the wavefunctions of the edges states for each state is labeled. 120
- FIGURE 5.11 – Band dispersion for the 1T- SnS_2 -NR with edge terminations of (a) MC (b) MM and (c) CC in solid blue lines. In dotted red lines is the band structure for the 2D- SnS_2 11 band TB model plotted along the path $K'-\Gamma-K$. At the bottom of each dispersion, the plot of the wavefunctions of the edge states for each state is labeled. 121
- FIGURE 5.12 – Band dispersion for the 1T- SnS_2 -NR with AR edge in solid blue lines. In dotted red lines is the band structure for the 2D- SnS_2 11 band TB model plotted along the path $K'-\Gamma-K$. At the bottom of each dispersion, the plot of the wavefunctions of the edge states for each state is labeled. 122
- FIGURE 6.1 – vdWNR composed by a central scattering region with leads attached on the bottom layer (A and B) and the top layer (C). 127
- FIGURE 6.2 – Conductance on leads B (G_B) and C (G_C) for a vdWNR with a length of 115 nm. 128
- FIGURE 6.3 – Mean value of the conductance on lead C for a vdWNR with different lengths. 128
- FIGURE 6.4 – Mean value of the conductance on lead C for a vdWNR with 230 nm subjected to different gate fields in the stacking direction. 129
- FIGURE 6.5 – Band dispersion for the lead C subjected to a field of (a) -0.5 V/\AA (b) 0 V/\AA (c) 0.5 V/\AA in solid blue lines. 130

FIGURE A.1 – Graphite convergence: (a) Cutoff energy ($ecutwfc$) for the plane wave expansion; (b) k-points sampling on an $N \times N \times 8$ grid. . . .	157
FIGURE A.2 – Results of several functionals for the structural parameters in-plane and out-of-plane compared with experimental results. Dark green represents the in-plane and light green out-of-plane graphite parameters.	157
FIGURE A.3 – Band structure of graphite.	158
FIGURE A.4 – Graphene band structure: (a) Band structure of graphene AA stacking; (b) Band structure of graphene AB stacking.	158
FIGURE B.1 – Fat bands of $ZrSe_2/SnSe_2$ used to provide an initial guess to obtain the MLWFs. (a) Projected band structure showing the orbital contribution of the $d_{xy}+d_{z^2}+d_{x^2-y^2}$ orbitals of Zirconium. (b) Projected band structure showing the orbital contribution of the p orbital of Selenium.	159
FIGURE B.2 – Workflow of typical Wannierization procedure.	160
FIGURE B.3 – Final spreads of the WFs and information about each term that composes the spread functional.	160

List of Tables

TABLE 2.1 – Cutoff energy for the plane wave expansion (E_{cut}) and the mesh of kpoints (k-mesh) that assures well converged DFT results.	76
TABLE 3.1 – Structural properties of TMDs. Cell parameter a and distance metal chalcogen d_{MX} were calculated using vdW-DF-obk8 functional. The experimental values were taken from [1],[2] and are in good agreement with <i>ab initio</i> calculations (SAHA <i>et al.</i> , 2020). The distance M-X is in excellent agreement with [3] and [4], in which the values are given between parentheses. The allotrope marked with * is to identify the most stable phase.	80
TABLE 3.2 – Electronic properties of monolayers TMDs. The band gap (E_g), VBM, and CBM with respect to the vacuum level obtained with hybrid exchange-correlation functional HSE06.	82
TABLE 4.1 – Summary of the energy levels (DFT) of freestanding monolayers and the heterojunction. All values are in eV.	88
TABLE 4.2 – Ω^2 of the WFs after the minimization procedure. The first line on the information about the spreads of p orbitals is for those connected with Zr, and the line below is for those bonded with Sn.	91
TABLE 4.3 – Change on the orbital contribution and band gap with parameter d_{hop} . CBM1 (ZrSe ₂ /SnSe ₂) is the orbital contribution of the respective layer to the first lowest conduction band.	94
TABLE 4.4 – Change on the orbital contribution and band gap with parameter $ hop $. CBM 1(ZrSe ₂ /SnSe ₂) is the orbital contribution of the respective layer to the first lowest conduction band.	94
TABLE 4.5 – Summary of the energy levels (DFT) of freestanding monolayers and the heterojunction. All values are in eV.	99

TABLE 4.6 – Ω^2 of the WFs after the minimization procedure. The first line on the information about the spreads of p orbitals is for those connected with Hf, and the line below is for those bonded with Sn.	99
TABLE 4.7 – Summary of the energy levels (DFT) of freestanding monolayers and the heterojunction.	102
TABLE 4.8 – Ω^2 of the WFs after the minimization procedure. The first line on the information about the spreads of p orbitals is for those connected with Zr, and the line below is for those bonded with Sn.	103
TABLE 4.9 – Summary of the energy levels (DFT) of freestanding monolayers and of the heterojunction.	105
TABLE 4.10 – Ω^2 of the WFs after the minimization procedure. The first line on the information about the spreads of p orbitals is for those connected with Zr and Hf, and the line below is for those bonded with Se. . . .	105
TABLE 4.11 – Summary of electric field required to concentrate 80% and 20% of the orbital contribution in the two lowest conduction bands.	107
TABLE A.1 – Parameters in-plane (a) and out-of-plane (c) compared with the experimental value.	157
TABLE C.1 – Energy difference between conduction and valence edges. For those pairs of materials that presented offsets falling below 0.6 eV were marked in green, as promising candidates for hosting vdW qubits. . .	163

List of Abbreviations and Acronyms

BZ	First Brillouin Zone
2D	Two dimensional
ATM	Atomic Force Microscopy
CBM	Conduction band minimum
CC	Classical computer
CVD	Chemical Vapor Decomposition
DFT	Density Functional Theory
FET	Field effect transistor
GGA	Generalized-Gradient Approximation
HF	Hartree-Fock
LCAO	Localized combination of atomic orbitals
LDA	Local Density Approximation
LSDA	Local Spin Density Approximation
MLWF	Maximally Localized Wannier Functions
QC	Quantum computer
QE	Quantum ESPRESSO
QM	Quantum mechanics
RPA	Random phase approximation
RS	Raman Spectroscopy
STM	Scanning Tunneling Microscopy
TB	Tight-Binding
TEM	Transmission Electron Microscopy
TFET	Tunneling field effect transistor
TMD	Transition Metal Dichalcogenide
VBM	Valence band maximum
vdW	van der Waals
WFs	Wannier functions
XC	Exchange-correlation

List of Symbols

\mathbf{a}_i	Direct Bravais vector
\mathbf{b}_i	Reciprocal lattice vector
e	Electron charge
e_c	Density of correlation energy
e_x	Density of exchange energy
e_{xc}	Density of exchange and correlation energy
E	Energy
E_c	Correlation energy
E_F	Fermi energy
E_{II}	Nucleus-nucleus classical interaction
erf	Error function
$erfc$	Complementary error function
E_x	Exchange energy
E_{xc}	Exchange and correlation energy
E_0	Ground state energy
$f(\mathbf{r})$	scalar function
\mathbf{G}	Vector of the reciprocal lattice
\hat{H}	Hamiltonian operator
\hbar	Reduced Planck constant
\hat{I}	Identity operator
k_F	Fermi wave vector
m_e	Electron mass
m_i	Integer number ($i \in \mathbb{Z}$)
M_I	Mass of nucleus I
n	Electronic density
\tilde{n}	Pseudo-electronic density
n^1	Electronic density of the real function at the atomic site
\tilde{n}^1	Electronic density of the real function at the atomic site
\mathbf{r}	Position of an arbitrary point in space
r_c	Radius of a sphere centered at an atomic site

\mathbf{r}_i	Position of the electron i
\mathbf{R}	Vector of the direct lattice
\mathbf{R}_I	Position of the nucleus from atom I
\hat{T}	Kinetic energy operator
T_0	Kinetic energy operator of non-interacting electrons
$T_{\mathbf{R}_n}$	Translation operator
$\hat{\tau}$	Transformation from wavefunctions to pseudo-wavefunctions
U_{mn}	Matrix representation of a unitary transformation
U_0	Potential energy for non-interacting electrons
\hat{V}	Potential energy operator
\hat{V}_{eff}	Effective potential energy operator
V_{ee}	Electron-electron interaction potential
\hat{V}_{ext}	External potential acting on the electrons
V_H	Hartree potential
V_{KS}	Kohn-Sham potential
V_{xc}	Exchange and correlation potential
$\hat{V}_{eff}^{i,\sigma}$	Effective potential of a single particle orbital i with spin σ
$\hat{V}_x^{i,\sigma}(\mathbf{r})$	Exchange potential of $\hat{V}_{eff}^{i,\sigma}$
w_n	Wannier function of the n -th band
Z_I	Atomic number of nucleus I
α, β	Complex numbers
ε_i	Independent-particle eigenvalue
θ	Azimuthal angle on spherical coordinates
σ	Spin
ϕ	Polar angle on spherical coordinates
Ω	Spread functional
Ω_I	Invariant part of the spread functional
$\phi(r, \sigma)$	Wavefunction; Kohn-Sham orbitals; Hartree-Fock orbitals
ψ	Spatial part of a wavefunction
ψ_i	Wavefunction i from a basis of orbitals
Ψ	Many electron wavefunction
Ψ^*	Complex-Conjugated of the Ψ wavefunction
$\tilde{\Psi}$	Pseudo-wavefunction
Ψ^1	Real wavefunction at the atomic site
$\tilde{\Psi}^1$	Pseudo-wavefunction at the atomic site
$ \Psi\rangle$	Wavefunction in Dirac's notation
$\langle\Psi $	Dual wavefunction in Dirac's notation
$\{ 0\rangle, 1\rangle\}$	qubit canonical basis
∇_k	Gradient operator in k coordinates

∇^2 Laplacian operator

Contents

1	INTRODUCTION	27
1.1	Motivation	27
1.2	General Objectives	35
1.3	Organization	36
2	THEORETICAL BACKGROUND	39
2.1	Electronic structure calculation	39
2.1.1	Hartree-Fock approximation	40
2.1.2	The Bloch's Theorem	42
2.2	Density Functional Theory (DFT)	44
2.2.1	The Hohenberg-Kohn theorems	45
2.2.2	The Kohn-Sham Auxiliary System	46
2.2.3	Local Density Approximation (LDA)	49
2.2.4	Generalized Gradient Approximation (GGA)	50
2.2.5	Hybrid Functionals	50
2.2.6	Van der Waals Functionals	52
2.2.7	Hellman-Feynman Theorem	53
2.2.8	Norm Conserving Pseudopotentials	54
2.3	Maximally Localized Wannier Functions (MLWF)	55
2.3.1	Overview of the formalism	55
2.3.2	Spread functional: Localization of the WFs	57
2.4	Tight-Binding formalism	61
2.5	Transport Formalism	63

2.5.1	Energy, length and time scales	63
2.5.2	Current and conductance	66
2.5.3	Multiterminal systems	68
2.5.4	Scattering matrix	70
2.5.5	Numerical transport calculations - Kwant Software	72
2.6	Computational Details	76
3	STRUCTURAL AND ELECTRONIC PROPERTIES OF TMDs	78
3.1	Motivation	78
3.2	Structural properties	78
3.3	Electronic properties	81
3.4	Criteria on forming vdW heterostructures	84
4	VDW HETEROSTRUCTURES OF TMDs	86
4.1	Motivation	86
4.2	ZrSe₂/SnSe₂ heterostructure	87
4.3	HfS₂/SnS₂ heterostructure	98
4.4	ZrS₂/SnS₂ heterostructure	101
4.5	ZrS₂/HfS₂ heterostructure	104
5	TRANSITION METAL DICHALCOGENIDES NANORIBBONS	108
5.1	Motivation	108
5.2	NR Terminations	110
5.3	Lead's band structure	112
5.3.1	NRs on the 2H phase	112
5.3.2	NRs on the 1T phase	115
6	VAN DER WAALS HETEROSTRUCTURES NANORIBBONS	125
6.1	Introduction	125
6.2	ZrSe₂/SnSe₂ heterostructure nanoribbon	126
6.3	Transport properties	127
7	CONCLUSIONS	131

BIBLIOGRAPHY	133
APPENDIX A – TESTING FUNCTIONALS FOR ACCURATE VAN DER WAALS INTERACTIONS	156
APPENDIX B – WORKFLOW OF WANNIERIZATION PROCEDURE . .	159
APPENDIX C – ELECTRONIC BAND OFFSETS BETWEEN MONO- LAYER MATERIALS	162
ANNEX A – PUBLISHED WORKS	164
ANNEX B – PARTICIPATION IN SCIENTIFIC CONGRESSES AND CON- FERENCES	165

1 Introduction

1.1 Motivation

The creation of the transistor in Bell Labs in 1947 impacted several branches of the technology industry, but that impact was mighty in computer design. Integrated circuits, often containing billions of microscopic transistors, are the building blocks of current electronic devices. The trend of increasing ever smaller transistors being included in each processor chip was expressed as an empirical law, known as Moore's law (MOORE, 1998). While still relevant, the pace of this exponential growth has slowed slightly, as noted by Intel's CEO. Instead of the doubling every two years, the contemporary trajectory now extends to a three-year cycle for doubling the transistor count on chips.

The large number of miniaturized transistors included in a single chip helps to increase the performance and portability of the processors, making it possible to deal with complex numerical problems that require substantial computational power. However, some difficulties arise, such as shape engineering and gate design, due to the large-scale integration causing the dimensions of the elements to approach the atomic level. In that length scale, the laws of Quantum Mechanics (QM) dictate the operations: tunneling, entanglement, and superposition of states are intrinsic properties that one needs to deal with. By learning how to create and manipulate operational devices that exploit quantum effects can help guide us toward the next leap on the development of second-generation quantum technologies (GEORGESCU; NORI, 2012).

Presently, one can tackle a large class of complex problems computationally. However, many other problems are still out of reach since they demand a large amount of computing time to be answered, even with the most powerful processors available. From a fundamental point of view, even if one has complete knowledge of the physical laws relevant to the problem, numerical solutions are still a non-trivial task. For instance, in quantum many-body problems, a standard computer cannot deal with the wave function of a many-body system with $\approx 3 \times 10^{23}$ coordinates. Problems in weather forecasting, gene mapping, drug development, molecular simulations, cellular reactions, cryptography, and the emergent evolution of machine learning and artificial intelligence need a device capa-

ble of performing complex tasks reasonably fast. This machine is the quantum computer (QC), and its building blocks are known as quantum bits or qubits.

In Fig.(1.1), one may note the difference concerning performance between a classical computer (CC) and a QC. Since the qubits are described by a superposition of any two quantum states, the amount of information carried by n qubits would require 2^n classical bits. Once the system's complexity and the amount of data increase, the QC is superior to its classical counterpart since it can handle several entries of information simultaneously, reflecting the time required to execute a certain task.

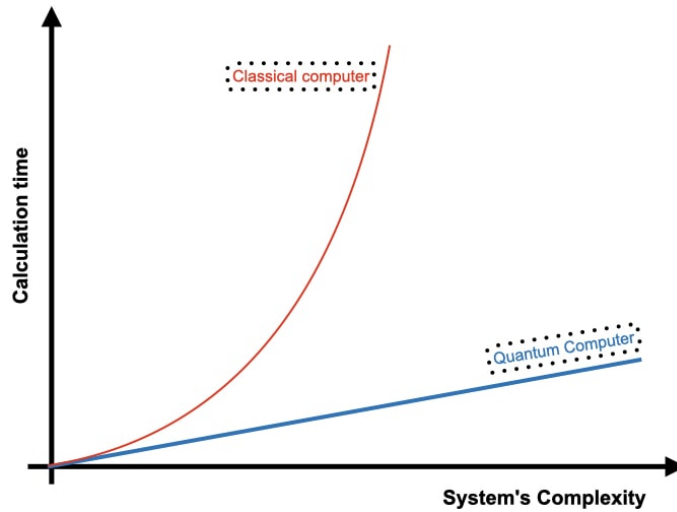


FIGURE 1.1 – Performance comparison of a classical vs. quantum computer with system's complexity.

Since the qubits on a QC are a superposition of two quantum states, the probability of either outcome depends on the qubit's quantum state immediately before measurement (interaction with the observer). Mathematically, it can be described as a superposition of $|\psi_0\rangle$ with energy ε_0 and $|\psi_1\rangle$ with energy ε_1

$$|\psi\rangle = \alpha |\psi_0\rangle + \beta |\psi_1\rangle, \quad (1.1)$$

where α and β are complex numbers and $|\psi\rangle$ is constrained to the orthonormalization condition,

$$|\alpha|^2 + |\beta|^2 = 1. \quad (1.2)$$

This two-level system can be represented graphically on a Bloch sphere, Fig.(1.2), in the basis $\{|0\rangle, |1\rangle\}$

$$|\psi\rangle = \cos\left(\frac{\theta}{2}\right) |0\rangle + e^{i\phi} \sin\left(\frac{\theta}{2}\right) |1\rangle, \quad (1.3)$$

where θ and ϕ are the azimuthal and polar angles on spherical coordinates, respectively. This representation gives a useful visualization once logical operations are performed on the qubit.



FIGURE 1.2 – (a) a graphical representation of a qubit on a Bloch sphere. (b) Landau–Zener evolution of a two-level system represented on the Bloch sphere. Figures generated using QuTip package (JOHANSSON *et al.*, 2012; JOHANSSON *et al.*, 2013).

Nevertheless, this desire for a universal QC that can perform any task, not just specific ones, is not new (DEUTSCH, 1985). In a lecture by Richard Feynman in the 60s, he argues that nothing in the physical laws prohibits this continuous miniaturization of electronic components and explores quantum phenomena that emerge on this length scale to solve complex problems. He stated: “nature is not classical... if you want to make a simulation of nature, you had better make it quantum mechanically” (FEYNMAN, 1959), and today a QC can be used not just to tackle complex problems but also test the foundations of QM itself (SADANA *et al.*, 2022). Since it can be difficult to predict certain properties of quantum materials and due to the expenses in doing it in several experiments, the use of simulations is often used in a predictive way of obtaining excellent approximation about several properties (HEAD-MARSDEN *et al.*, 2021).

To guide theoretical research and industry investments in the creation of a QC, David DiVincenzo proposed five requirements for a physical implementation (DIVINCENZO, 1996; DIVINCENZO; IBM, 2000):

- A Hilbert space well delineated and a scalable physical system with well-characterized qubits (two-level system: spin, ground and excited state, photons polarization);
- Initialization of the qubits (knowledge of the initial state before the start of the computation, for instance, be cool down to the ground state of its Hamiltonian);
- The quantum system must be isolated from its environment for its state not to be mixed, resulting in decoherence. This requirement is directly related to error

correction and quantum computation fault tolerance. We must have coherent times longer than the gate operation time (it is essential to look at the coherence time because any quantum system is characterized by this time when in contact with the external environment - the shorter this time, the faster the system becomes classical);

- Universal quantum gates. This requirement is the basis for all quantum computation. One must be able to perform a sequence of unitary operations that act on specified pairs of qubits and generates entangled states;
- One must be able to perform a “strong” measurement on the system to extract information after it (a strong coupling with the quantum system must be made).

Since then, a considerable amount of research has been done to obtain a functional and universal QC due to the massive investment of industries such as Microsoft, IBM, Google, Amazon, Intel, and D-Wave that are investing millions (or even billions) on the development of technologies and encouraging theoretical studies to put in practice a QC. To cite some movements already made by the industry and academia, Google, with universities, simulated a hydrogen molecule computing the energy surface using an array of qubits in 2016. After, they performed a Hartree-Fock calculation using the Google Sycamore quantum processor where the simulations used 12 qubits (NULL *et al.*, 2020) and recently, in 2019, Google claim reached quantum supremacy (ARUTE *et al.*, 2019). In the same year, IBM revealed a QC with 53 qubits, and in 2021 they claimed that they built a quantum processor with 127 qubits, the “IBM Eagle”. Right after, a Chinese group claimed that they had achieved quantum supremacy, performing better than previously claimed by Google (PAN *et al.*, 2022).

A significant challenge in creating a functional QC resumes creating an environment where the qubits live (host material and design), controlling them (modulation of properties), and analyzing their dynamics (transport properties), which is the basis for performing logical operations without losing coherence. Based on these four points, investigating thin layered materials is appealing due to their broad electronic properties and manufacturing flexibility, reduced dimensionality, and symmetry, and how they lead to phenomena absent in their bulk counterparts, giving rise to properties that could be valuable for technological applications, such as the implementation of solid-state qubits which is a direct use of collective phenomena of quantum states which favors scalability and the possibility to assemble devices on a nanometre scale.

Moreover, one could be discouraged from exploring low-dimensional materials due to arguments by Landau and Peierls that 2D materials, if they existed, would be thermodynamically unstable (PEIERLS, 1935; LANDAU, 1937). Nonetheless, the class of 2D materials

has already impacted the design of the current electronic devices, and a significant interest in them started with the isolation of graphene by Novoselov and his co-workers in 2004 (NOVOSELOV *et al.*, 2004), resulting in a profound curiosity and investment in the field. Since then, a search for other 2D materials began due to the exceptional properties that graphene presents, such as outstanding electronic transport properties, high thermal conductivity, stiffness, half-integer quantum hall effect, and the existence of a non-zero Berry's phase due to the topology of its band structure (YU *et al.*, 2000-01; HIRATA *et al.*, 2004; NOVOSELOV *et al.*, 2005; ZHANG *et al.*, 2005a; ZHANG *et al.*, 2005b). The transition from bulk to a layer thickness, as occurs with graphite, was figured for other 2D materials, resulting in one of the most explored families of 2D materials, the layers of transition metal chalcogenides (TMDs), and they are interesting because they can overcome some of graphene's limitations due to its absence of a band gap. The TMDs are described by the chemical formula MX_2 with M a metal and X a chalcogen; they have hexagonal structures presented in two main ways: the trigonal prismatic phase (allotrope H) and an octahedral phase (allotrope T). The H phase is more stable thermodynamically and presents a semiconducting behavior, and the phase T is metastable exhibits a metallic behavior, and is interesting for their topological properties (FEI *et al.*, 2017).

There are several specialized demands for the intrinsic properties of layered materials and their combination, which form the so-called van der Waals (vdW) heterostructures where numerous stacking combinations are possible due to the weak covalent bonds formed in the interlayer environment that maintain the hole structure stable (GEIM; GRIGORIEVA, 2013). The individual electronic properties can be preserved in constructing heterojunctions, or hybrid ones can emerge (LINDER; SUDBØ, 2007) resulting in the freedom to modulate the properties as desired via external perturbations such as electric fields, strain (WU *et al.*, 2017), doping (ZHAO *et al.*, 2017), substrate effects (LI *et al.*, 2018; FEIJÓ *et al.*, 2021), and many others, getting promising features for high-performance integrated circuits. Numerous layers of vdW heterostructures are assembled experimentally, and machine learning models make uncountable combinations of materials predicting their structural and electronic properties (WILLHELM *et al.*, 2022; HU *et al.*, 2022). Moreover, the quality of solid-state qubits is correlated with the quality of the host material (SCAPPUCCI *et al.*, 2021). To this end, it is crucial to produce high-quality materials to improve current technological components and enable their applications.

The assembling of thick layered materials dates back to the 60's (FRINDT, 1966) where crystals of MoS_2 were mechanically exfoliated, and even today, a significant fraction of layered materials is isolated in this way, particularly vdW materials, due to the weak bonds that facilitate the exfoliation. Besides this procedure, a large class of other techniques was developed. For instance, the direct growth of MoS_2 in a solid electrolyte substrate by chemical vapor decomposition (CVD) resulted in high mobility FETs (ALAM *et al.*,

2021). Still in the CVD technique, graphene can be used as a substrate to grow other layered materials epitaxially forming vdW heterostructures (SHI *et al.*, 2012), as illustrated in Fig.(1.3). This procedure results in high-quality products because even if there is a lattice mismatch between the materials, this technique avoids some interfacial effects that can change the electronic properties (NOVOSELOV *et al.*, 2005).

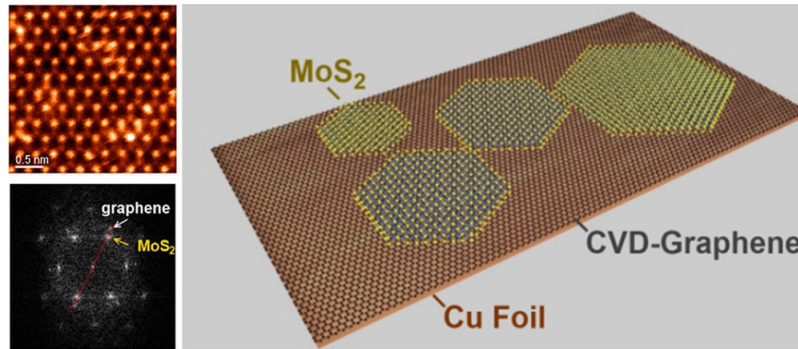


FIGURE 1.3 – Sythesis of MoS_2 /graphene heterostructure by chemical vapor decomposition. The top left is a high-resolution STEM imaging of the resulting materials. The bottom left shows FFT patterns. Source: (SHI *et al.*, 2012).

Once the material is assembled, verifying if the final product has the desired properties is the next step. In order to determine the layer thickness of the resulting product, the technique of Atomic Force Microscopy (ATM) is broadly used (DRESSELHAUS *et al.*, 2010). Raman Spectroscopy (RS) helps fingerprint a material by identifying layer-dependent changes of the vibrational structure (BUTLER *et al.*, 2013), detecting oscillating modes, and it has the advantage of not interfering with the sample. Transmission Electron Microscopy (TEM) provides information on the layer's size, stacking, and composition details (SCHLIEHE *et al.*, 2010). Scanning Tunneling Microscopy (STM) helps analyze the topography and electronic structure (AUWÄRTER *et al.*, 1999; HELVEG *et al.*, 2000) of a single-atom-thick material and can also manipulate single atoms (BUTLER *et al.*, 2013). X-ray diffraction supplies information about the unit cell structure, constituents, structure factors, and orientation concerning the substrate (BUTLER *et al.*, 2013). These experimental techniques display such high accuracy and result in a large amount of data that enables one to simulate materials, build theoretical models, and investigate properties in several scenarios where emergent functionalities can be theoretically anticipated guiding further advances in experimental techniques.

Once high-quality materials on a nanometer scale are obtained with well-known properties, exploring their intrinsic collective behavior can find a reason for using them as electronic components for hosting qubits, opening an exciting route to obtain many of them due to the scalability of nanomaterials. The merging of the fields of materials science with quantum information already showed the capability of revolutionizing the electronic components industry, first with the creation of transistors and now on obtaining qubits.

An exciting use of 2D materials to this end occurred just a few years after graphene's isolation, in which spin qubits on ribbons of graphene quantum dots were obtained, showing long coherence times (TRAUZETTEL *et al.*, 2007). Moreover, the exploration of solid-state qubits started before the isolation of graphene where superconducting qubits had been investigated (BOUCHIAT *et al.*, 1998; NAKAMURA *et al.*, 1997; NAKAMURA *et al.*, 1999), consisting in an artificial two-level system of charge states coupled by Cooper pairs (NAKAMURA *et al.*, 1999) in which coherent oscillations were verified, encouraging, even more, the combination of materials science and quantum information fields. Nowadays, superconducting qubits represent one of the most promising for being implemented on quantum hardware (WENDIN, 2017; KRANTZ *et al.*, 2019) and these qubits show coherence times around 50-100 μs , reaching at most 8 ms (EARNEST *et al.*, 2018) and gate speeds on the order of tens of ns . Motivated by promising results of superconducting qubits and the proposal of quantum dots as universal gates for quantum computation (LOSS; DIVINCENZO, 1998), other physical implementations began to be explored: usage of the electronic and nuclear spin degree of freedom (KANE, 1998; GAO *et al.*, 2022), exploration of entanglement among electrons and nuclear spins (SIMMONS *et al.*, 2011), qubit logic mediated by holes in germanium (HENDRICKX *et al.*, 2020), trapped ions (RIEBE *et al.*, 2004; HÄFFNER *et al.*, 2005) which have coherence times longer than 10 min observed (WANG *et al.*, 2017), the entanglement of photons (O'BRIEN *et al.*, ; SHADBOLT *et al.*, 2012; FLAMINI *et al.*, 2018), charge states of nitrogen-vacancy centers in diamond (GROTZ *et al.*, 2012), and more recent proposals such as molecular spins (CHIESA *et al.*, 2023), are just a few examples of developments on the field and the use of semiconducting platforms demonstrated the functionality of two-qubit quantum logic (NOWACK *et al.*, 2011; VELDHORST *et al.*, 2015; HENDRICKX *et al.*, 2020).

The superabundance of properties of vdW materials also makes them promising to be part of components on quantum computing platforms. For instance, the coherent temporal control of charge carriers in vdW materials was verified (WANG *et al.*, 2019) in a superconducting circuit. Fig.(1.4) shows using a vdW heterostructure as part of a quantum circuit.

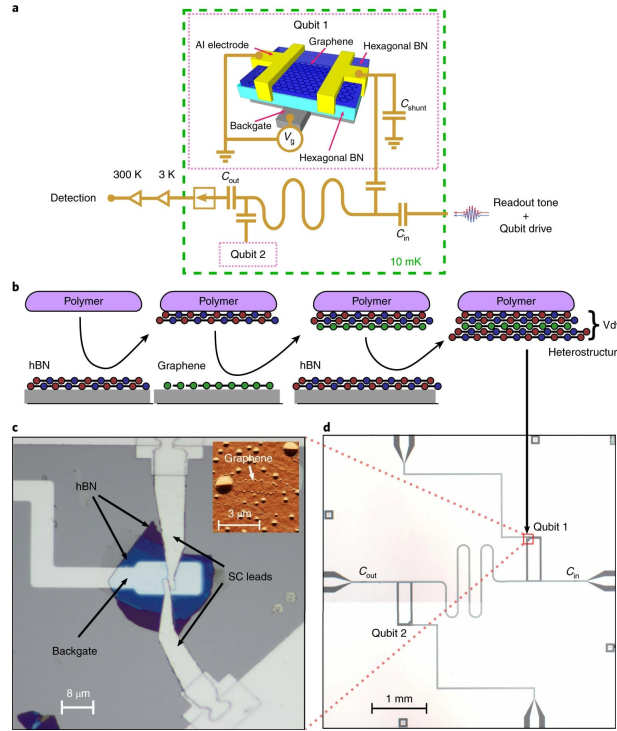


FIGURE 1.4 – (a) Schematic of the hBN-encapsulated superconductor–graphene–superconductor junctions embedded in a circuit quantum electrodynamics system. (b) Assembly of vdW heterostructures using a dry polymer-based pick-up and transfer technique. (c) Optical micrograph of the graphene transmon qubit. SC, superconducting. Inset, atomic force microscopy image of the encapsulated graphene before making electrical contact to the superconducting electrodes. (d) Qubit chip made of high-quality aluminium. Adapted from: (WANG *et al.*, 2019).

Besides previously discussed implementations for obtaining qubits, recently, a new proposal through an innovative application of gated vdW heterostructures as charge qubits has been suggested (LUCATTO *et al.*, 2019), here named vdW qubits. This proposal explores the spatial superposition of electrons from the individual layers by studying the orbital composition of the bands as a function of the gate field. Such control of the orbital composition of the bands were already observed experimentally (KIEMLE *et al.*, 2020). Given the extensive list of possible combinations of 2D materials, the proposal provided a new perspective in the area. To obtain this spatial superposition of electrons, we are particularly interested in the alignment of the individual layers' energy levels before being combined to form heterostructures. The interest in investigating this feature is due to the possibility of hybridized states appearing, caused by the superposition of quantum states coming from different materials.

Expanding on the concept of the vdW qubit in terms of operability, one can confine the heterostructure with highly hybridized states in a quantum dot. This would yield well-defined single-electron states characterizing the states $|0\rangle$ and $|1\rangle$. These well-characterized states, isolated from environmental disturbances within a quantum dot, can be manipulated using an electric field to prepare the state by concentrating the wave function in a particular layer. The readout can then be measured via a single-electron

transistor, as discussed in Refs. (TSUKANOV, 2019; CAO *et al.*, 2022). Scalability of such qubits can be achieved by exploiting equivalent high-symmetry points in the BZ, where entanglement can be described using a $k \cdot p$ approach.

Not only looking at the energy matching but also computing the band offsets is important, which determines the type of band alignment. This quantity is a critical parameter to obtain good heterojunctions because it determines properties such as quantum confinement and chemical activity (PIERUCCI *et al.*, 2016), essential for electronic and photonic devices and depending on the offset's value, the resulting band structure can exhibit a strong signature of one of the different materials or hybridize due to the strong coupling (ZRIBI *et al.*, 2019).

In this work, we search for heterostructures that display this hybridization on the band structure based on energy alignment and interpret this superposition or charge separation between the layers as a two-level system suited for implementing a vdW qubit. Taking advantage of the freedom of manipulating electronic properties, an electric field is applied in the stacking direction, changing the alignment of the energy levels and, consequently, the charge contribution of the layers for the qubit. Manipulating quantum states via external perturbations is viable. For instance, spin qubits in silicon were coherently coupled to an electric field and mechanical oscillations (LAUCHT *et al.*, 2017). On what concerns high scalability, it is crucial to have short field pulses. Several ways of controlling qubits were already proposed, most requiring a complex experimental apparatus and the simulations requiring substantial computational power.

Here, to give courses on maintaining and analyzing the dynamics of a vdW qubit in a low computational cost, we use a Tight-Binding (TB) model obtained from an *ab initio* calculation mapping the Bloch wave functions into Wannier Functions (WFs) and get several host platforms where this vdW qubit can be implemented and controlled. Then we compare our results from the TB model with those from the DFT, ponderating accuracy and computational cost. Combining the electronic properties of vdW materials with the ease of manipulating them, a device to explore the dynamics of the charge qubit is proposed based on vdW heterostructures.

1.2 General Objectives

The present work aims to identify a family of vdW heterostructures suitable for hosting charge qubits, develop a methodology with low computational costs based on *ab initio* results, and investigate the transport properties of nanoribbons derived from these heterostructures as the investigation of the dynamics of such qubit. We aim to establish a modeling approach that balances accuracy and computational efficiency to facilitate

the exploration of transport phenomena in these systems. Here the vdW qubit is based on the band alignment of different materials, which implies a quantum superposition of the energy levels. The electron affinities and ionization energies computed for layered materials are used to derive chemical trends. Once the solid-state qubits are well established, this two-level system is subjected to an external electric field to investigate how the host materials' properties are modified, aiming to control the quantum state localization and dynamics. This proposed qubit is shown to be compatible with the current developments in the technology of two-dimensional material technology and operable at high temperatures when compared with other semiconductor-based qubits.

To achieve this goal of providing an accurate description on the localization and dynamics of a charge qubit at a low computational cost, some sub-objectives were proposed:

1. Use the formalism of DFT to obtain the desired quantities (band gaps and energy levels with respect with to the vacuum level) with high accuracy;
2. Combine the individual layers based on their energy alignment and verify if this requirement gives the superposition of levels to implement a charge qubit;
3. Create a Tight-Binding model from the Bloch wavefunctions to verify if the results obtained on the full *ab initio* level are captured on the simplified model;
4. Investigate the dynamics and transport of a wave packet in a van der Waals heterostructures nanoribbons.

We combined the formalism of Density Functional Theory (DFT) developed by Pierre Hohenberg, Walter Kohn, and Lu Sham (HOHENBERG; KOHN, 1964; KOHN; SHAM, 1965) with Maximally Localized Wannier Functions (MLWFs) (MARZARI; VANDERBILT, 1997; SOUZA *et al.*, 2001) to construct a Tight-Binding (TB) model from first-principles calculations. The Bloch wavefunctions were mapped into Wannier functions using the Wannier90 package (MOSTOFI *et al.*, 2008; MOSTOFI *et al.*, 2014). Once the TB parameters were obtained, we used the Kwant software (GROTH *et al.*, 2014) to perform numerical simulations of quantum transport.

1.3 Organization

In Chapter 1, we provide a contextualization of the current study by establishing a connection between the field of materials science and quantum computing. Subsequently, a link is made between these fields, elucidating the reasons layered materials emerge as an enticing platform for hosting qubits. Additionally, we articulate the primary objectives of this work.

In Chapter 2, the theoretical background is presented. Starting from the first attempts to solve the electronic Hamiltonian of many electrons, the first approximations considered by D. R. Hartree and V. A. Fock are discussed. Then the most used approach to study electronic properties is introduced: the Density Functional Theory approximation. Next is the formalism to obtain the Maximally Localized Wannier Functions that will serve as basis functions for constructing the Tight-Binding Hamiltonian, followed by a short description of the Tight-Binding formalism. The chapter concludes with a discussion on the formalism of coherent quantum transport, followed by its numerical implementation within the simulation package employed for modeling such transport phenomena.

In Chapter 3, an *ab initio* investigation of the structural and electronic properties of monolayers of TMDs is performed. We aim to identify those candidates exhibiting highly hybridized states within the band structure, thereby qualifying them as potential host materials for a vdW qubit, contingent upon the alignment of energy levels. The prediction of candidates for hosting materials is also discussed.

In Chapter 4 presented the vdW heterostructures formed, based on the alignment of the energy level of its components, to explore the electronic properties and the modulation of its properties via an electric field, showing the viability of such heterostructures being host materials for a vdW qubit. It also discusses how the TB model is obtained, its accuracy, and its limitations compared with the DFT results.

In Chapter 5, we utilize *ab initio* Tight-Binding Hamiltonians to explore the confinement effects on nanoribbons derived from transition metal dichalcogenides. This study is essential before exploring nanoribbons of van der Waals heterostructures, which exhibit highly hybridized states in their band structures. The investigation of nanoribbons is driven by our interest in examining the transport properties of these systems using the plane wave formulation of the scattering problem, as implemented in the KWANT software. We examine nanoribbons of monolayer TMDs, considering various edge configurations and chemical terminations to fully understand their electronic properties and the emergence of edge states.

In Chapter 6, the transport property of a nanoribbon derived from 2D van der Waals heterostructure discussed in Chapter 4 that exhibits highly hybridized states in their band structure was investigated. Our investigation focuses on how the conductance of this nanoribbon is influenced by its length and the application of an external electric field along the stacking direction. By varying the length of the nanoribbon, we analyze the oscillatory behavior of conductance and identify the stabilization point. Additionally, we explore the impact of external electric fields on the conductance, observing how they can modulate the electronic and transport properties by altering the distribution of the wave functions across different layers. These studies provide valuable insights into the potential for tuning the transport characteristics of nanoribbons for various applications

in nanoelectronics and quantum computing.

In Chapter 7, we highlight the most significant contributions of this work to the scientific literature. Additionally, a comprehensive summary of the results discussed throughout the thesis is provided, offering a clear and concise overview of the key findings and their implications.

In the end, we present some appendices and annexes. Appendix A discusses the tests performed with the van der Waals functionals implemented in the *ab initio* package used in this thesis. Appendix B provides a brief description of the wannierization procedure and presents the typical final spread of the Wannier functions for one system investigated. Appendix C lists the 222 potential heterostructure candidates for hosting charge qubits, based on the small mismatch of energy levels in the conduction or valence bands. Finally, Annexes A and B contain a list of published works in peer-reviewed journals and participation in scientific events, where partial results of this thesis were presented to the scientific community.

2 Theoretical Background

2.1 Electronic structure calculation

Theories to understand electronic behavior in the matter began at the end of the XIX century. The pioneers in considering quantum mechanics to understand this problem were Niels Bohr and Ernest Rutherford (PHIL, 1913), yielding the first spark to a deep understanding of electronic dynamics. Later, Plank, Einstein, de Broglie, Schrödinger, Heisenberg, Pauli, Dirac, and many others helped the development of a rigorous mathematical description of quantum mechanics to obtain not only the descriptions of phenomena already seen experimentally but also to make predictions. Around 1930, the basis for the modern theories of the electronic structure of matter was already well established (MARTIN, 2020).

The central problem is to deal with the full Hamiltonian of a system of electrons and nuclei given by

$$\hat{H} = -\frac{\hbar}{2m_e} \sum_i \nabla_i^2 - \sum_{i,I} \frac{Z_I e^2}{|\mathbf{r}_i - \mathbf{R}_I|} + \frac{1}{2} \sum_{i \neq j} \frac{e^2}{|\mathbf{r}_i - \mathbf{r}_j|} - \sum_I \frac{\hbar^2}{2M_I} \nabla_I^2 + \frac{1}{2} \sum_{I \neq J} \frac{Z_I Z_J e^2}{|\mathbf{R}_I - \mathbf{R}_J|}, \quad (2.1)$$

in which m_e is the electron mass, M_I , Z_I , and $Z_I e$ are the mass, atomic number and the charge of the nuclei, respectively, \mathbf{r}_i is the vector position of electrons and \mathbf{R}_I is the vector position of the nuclei, e is the charge of the electron, and \hbar is the reduced Plank's constant. To obtain the solution to this Hamiltonian is necessary to solve the Schrödinger equation for many electrons, and unraveling this computationally is intractable - some approximations must be considered. The great challenge is solving this equation that deals with the electron-electron interaction with great accuracy.

Since early calculations, scientists realized how is difficult to treat the problem of many interacting particles. Two independent-particle approaches were developed to tackle the problem: the mean-field and the Hartree-Fock (HF) theories, where the electrons are uncorrelated but obey the exclusion principle. The mean-field approach describes the system as an effective one-particle Hamiltonian with an effective potential acting on the

electrons. One of the first models that used the idea of the non-interacting electron was performed by Pauli and Sommerfeld (PAULI, 1927; SOMMERFELD, 1928). However, despite some advances, a few problems remained, such as the inadequacies of the free electron transport calculation and static thermodynamic predictions, what determined the number of conduction electrons, and what differs a metal from an insulator, for instance, (ASHCROFT; MERMIN, 1976).

2.1.1 Hartree-Fock approximation

Advances in treating electronic calculations numerically were strikingly performed first by Hartree (HARTREE, 1928), who was the pioneer of the self-consistent method, and then by Fock (FOCK, 1930) using a more rigorous quantum mechanical approach taking into account the anti-symmetrization of the wave function: Hartree-Fock (HF) method. All these significant advances in electronic structure calculation were mainly due to the more rigorous band structure theory and the Schrödinger equation. Even though this non-interacting picture gives good results, a complete description that concerns the electronic behavior of electrons, the interactions must be taken into account.

Since the Hamiltonian Eq.(2.1) cannot be solved easily, some approximations are considered. First, the term

$$-\sum_I \frac{\hbar^2}{2M_I} \nabla_I^2 \quad (2.2)$$

can be ignored since it describes the kinetic energy of the nuclei that, in comparison with the energy of electrons, is much smaller; such approximation is called the Born-Oppenheimer or adiabatic approximation (BORN; OPPENHEIMER, 1927), where the electrons can be seen as instantaneously following the motion of the nuclei, while always remaining in the same stationary state of the electronic hamiltonian (KOHANOFF, 2006). With this simplification, our Hamiltonian becomes

$$\hat{H} = \hat{T} + \hat{V}_{ext} + \hat{V}_{int} + E_{II}, \quad (2.3)$$

where \hat{T} is the kinetic energy operator of the electrons, \hat{V}_{ext} is the interaction acting on the electrons due to the nuclei, \hat{V}_{int} takes account of the electron-electron interaction and the term E_{II} is the classical interaction of the nuclei with one another, which can be seen just as a constant when one aims to describe only the electronic motion. Then, the Hamiltonian Eq.(2.3) is the one to be solved. In principle, if we want to obtain the ground state energy of the previous Hamiltonian, all we have to do it to take its expectation value with respect to the many-body wave function

$$E_0 = \frac{\langle \Psi | \hat{H} | \Psi \rangle}{\langle \Psi | \Psi \rangle} = \langle \Psi | \hat{T} | \Psi \rangle + \langle \Psi | \hat{V}_{int} | \Psi \rangle + \int d^3r V_{ext}(\mathbf{r})n(\mathbf{r}) + E_{II}, \quad (2.4)$$

and minimize it with respect to Ψ , with the constraint that the trial wave function obeys the particle symmetry and conservation laws. One of the first approaches to minimize this functional is to propose a wave function that is the product of the individual orbitals $\phi(\mathbf{r}_j)$, first performed by Hartree, in which

$$\Psi(\mathbf{r}_1, \mathbf{r}_2, \dots, \mathbf{r}_N) = \phi(\mathbf{r}_1)\dots\phi(\mathbf{r}_N). \quad (2.5)$$

A more rigorous approach is to write the trial wave function as a determinant of the single particle orbitals, the HF method, where one transforms the N-body wave function into N wave functions of a single particle that is coupled with all the others and takes into account the antisymmetry of the fermionic wave function, in which one minimizes the total energy of the full interacting Hamiltonian

$$\Psi = \frac{1}{(N!)^{1/2}} \begin{vmatrix} \phi_1(\mathbf{r}_1, \sigma_1) & \phi_1(\mathbf{r}_2, \sigma_2) & \dots & \phi_1(\mathbf{r}_N, \sigma_N) \\ \phi_2(\mathbf{r}_1, \sigma_1) & \phi_2(\mathbf{r}_2, \sigma_2) & \dots & \phi_2(\mathbf{r}_N, \sigma_N) \\ \cdot & \cdot & \cdot & \dots \\ \cdot & \cdot & \cdot & \dots \\ \phi_N(\mathbf{r}_1, \sigma_1) & \phi_N(\mathbf{r}_2, \sigma_2) & \dots & \phi_N(\mathbf{r}_N, \sigma_N) \end{vmatrix}, \quad (2.6)$$

where the single-particle orbitals $\phi_j(\mathbf{r}_i, \sigma_i)$ can be written as a product of a function that depends only on the coordinate ψ_i and a function that depends only on the spin α_i , once spin-orbit effects are neglected. Then, the expectation value of \hat{H} becomes

$$\begin{aligned} \langle \Psi | \hat{H} | \Psi \rangle &= \sum_{i,\sigma} \int d\mathbf{r} \psi_{i,\sigma}^*(\mathbf{r}) \left(-\frac{1}{2} \nabla^2 \right) \psi_{i,\sigma}(\mathbf{r}) + \sum_{i,\sigma} \int d\mathbf{r} \psi_{i,\sigma}^*(\mathbf{r}) V_{ext}(\mathbf{r}) \psi_{i,\sigma}(\mathbf{r}) + E_{II} \\ &+ \frac{1}{2} \sum_{i,j,\sigma_i,\sigma_j} \int d\mathbf{r} d\mathbf{r}' \psi_{i,\sigma_i}^*(\mathbf{r}) \psi_{j,\sigma_j}^*(\mathbf{r}') \frac{1}{|\mathbf{r} - \mathbf{r}'|} \psi_{i,\sigma_i}(\mathbf{r}) \psi_{j,\sigma_j}(\mathbf{r}') \\ &- \frac{1}{2} \sum_{i,j,\sigma} \int d\mathbf{r} d\mathbf{r}' \psi_{i,\sigma}^*(\mathbf{r}) \psi_{j,\sigma}^*(\mathbf{r}') \frac{1}{|\mathbf{r} - \mathbf{r}'|} \psi_{j,\sigma}(\mathbf{r}) \psi_{i,\sigma}(\mathbf{r}') \end{aligned} \quad (2.7)$$

where the first, second, and third terms are calculated in terms of single particle orbitals, and the fourth and fifth are the direct and exchange terms that emerges due to the antisymmetry of the wave function. Now, taking the functional derivative with respect to $\psi_{i,\sigma}^*(\mathbf{r})$, we arrive at a Schrödinger-like equation given by

$$\left[-\frac{1}{2} \nabla^2 + \hat{V}_{eff}^{i,\sigma}(\mathbf{r}) \right] \psi_{i,\sigma}(\mathbf{r}) = \varepsilon_{i,\sigma} \psi_{i,\sigma}(\mathbf{r}), \quad (2.8)$$

where the effective potential is composed of the external contribution, V_{ext} , the Hartree contribution $V_H(\mathbf{r})$ and the exchange part, $\hat{V}_x^{i,\sigma}(\mathbf{r})$, given by

$$\hat{V}_x^{i,\sigma}(\mathbf{r}) = - \sum_j \int d\mathbf{r}' \psi_{j,\sigma}^*(\mathbf{r}') \psi_{i,\sigma}(\mathbf{r}') \frac{1}{|\mathbf{r} - \mathbf{r}'|} \frac{\psi_{j,\sigma}(\mathbf{r})}{\psi_{i,\sigma}(\mathbf{r})}. \quad (2.9)$$

For each orbital, there is an equation to solve and an exchange that depends on all the others, so this method is generally expensive computationally. In the HF approximation, the electrons are treated independently since the Slater determinant gives our wave function, which is the product of single-particle orbitals. However, the Pauli's principle is considered, and this deliberation gives rise to the exchange term, resulting in a reasonable estimation of the ground state energy. However, it is possible to obtain better results, including more degrees of freedom in the wave function that will give rise to a term that will decrease the total energy, the correlation energy E_c (MACDONALD, 1933). This correlation energy can also be defined as the difference between the total energy on the exact ground state, E_0 , and the HF energy

$$E_c = E_0 - E_{HF}, \quad (2.10)$$

where E_0 given by Eq.(2.4) with respect to the full many body wave function Ψ and E_{HF} is computed with respect to the wave function given by Eq.(2.6).

2.1.2 The Bloch's Theorem

Independent of the approximation taken to treat the behavior of electrons, we are mainly interested in solving Schrödinger's equation for those electrons on condensed matter subjected to a periodic potential and periodic boundary conditions. The Bravais lattice describes the periodicity

$$\mathbf{R} = m_1 \mathbf{a}_1 + m_2 \mathbf{a}_2 + m_3 \mathbf{a}_3, \quad (2.11)$$

where the \mathbf{a}_i are vectors that describe the system and m_i integer numbers, containing all the information of the periodic crystal, and describe the unit cell of the crystal, which is the smallest part of space that reproduces all the crystal when translated by lattice vectors.

Since the Hamiltonian for independent particles is invariant to lattice translations, it commutes with the translation operator defined in Eq.(2.12)

$$T_{\mathbf{R}_n} f(\mathbf{r}) = f(\mathbf{r} + \mathbf{R}_n), \quad (2.12)$$

and the electrons subjected to a periodic potential $V(\mathbf{r}) = V(\mathbf{r}+\mathbf{R})$ gives origin to wave functions stated by the Bloch theorem (ASHCROFT; MERMIN, 1976)

$$\psi_{n\mathbf{k}}(\mathbf{r}) = e^{i\mathbf{k}\cdot\mathbf{r}}u_{n\mathbf{k}}(\mathbf{r}), \quad (2.13)$$

where \mathbf{k} is the wave vector and n is the band index, and $u_{n\mathbf{k}}(\mathbf{r})$ is a periodic function that has the same period of the Bravais lattice, that is

$$u_{n\mathbf{k}}(\mathbf{r}) = u_{n\mathbf{k}}(\mathbf{r} + \mathbf{R}). \quad (2.14)$$

As a consequence, the wave function has the property

$$\psi_{n\mathbf{k}}(\mathbf{r} + \mathbf{R}) = e^{i\mathbf{k}\cdot\mathbf{R}}\psi_{n\mathbf{k}}(\mathbf{r}), \quad (2.15)$$

so the Bloch wavefunction can be seen as a product of a periodic function with the periodicity of the Bravais lattice modulated by a plane wave. We must perform integrals over the k space to obtain properties of interest. The crucial point is to choose periodic boundary conditions, in our case, Born-von Karman periodic conditions so that we can solve the Schrödinger equation in k space. Making this transition, we work now on the reciprocal space, using the reciprocal lattice vectors, \mathbf{G} , that exhibit the same periodicity as the original cell. The first Brillouin zone (BZ) is the smallest cell in this k space centered in origin.

Once the transition to k space is well established and the periodicity employed by the boundary condition, it is well suited to use the Fourier transform of the quantities of interest since some functions will have translational invariance symmetry. Then, the Fourier transform of $f(\mathbf{r})$ is given by

$$f(\mathbf{G}) = \frac{1}{V_{cell}} \int d\mathbf{r} f(\mathbf{r}) e^{i\mathbf{G}\cdot\mathbf{r}}, \quad (2.16)$$

where \mathbf{G} are points of the reciprocal lattice. Taking the periodic boundary condition to our wave function given by Eq.(2.13), we can express it as an expansion of the form

$$\psi_{n\mathbf{k}}(\mathbf{r}) = e^{i\mathbf{k}\cdot\mathbf{r}} \sum_{\mathbf{G}} c_{\mathbf{G}} e^{i\mathbf{G}\cdot\mathbf{r}} \quad (2.17)$$

and the same way for the periodic potential

$$V(\mathbf{r}) = \sum_{\mathbf{G}} V_{\mathbf{G}} e^{i\mathbf{G}\cdot\mathbf{r}}, \quad (2.18)$$

and then we put these terms on the single particle Schrödinger equation, arriving at

$$\left[\frac{\hbar^2}{2m} (\mathbf{k} - \mathbf{G}')^2 - \varepsilon \right] c_{\mathbf{k}-\mathbf{G}'} + \sum_{\mathbf{G}} V_{\mathbf{G}-\mathbf{G}'} c_{\mathbf{k}-\mathbf{G}} = 0. \quad (2.19)$$

Now, the goal is to obtain the coefficients $c_{\mathbf{k}-\mathbf{G}'}$. For this, we have to truncate our Fourier expansion into some cutoff wave vector obtained via convergence tests, putting in this way an upper limit for the kinetic energy of the plane waves considered. A convergence test must also be performed to obtain our k-mesh, where the widely used was proposed by Monkhorst and Pack (MONKHORST; PACK, 1976).

2.2 Density Functional Theory (DFT)

A good result for the ground state can be achieved with the Hartree-Fock approximation, but computing the exchange term is quite expensive computationally since this term is different for each orbital considered, and the problem is then solved in a self-consistent cycle until some convergence criterium predefined. However, as mentioned before, this approach is a good starting point once the correlation effects are entirely ignored. The most significant leap in the electronic structure was in the '60s with the seminal papers from Pierre Hohenberg and Walter Kohn (HOHENBERG; KOHN, 1964) and Kohn and Lu Sham (KOHN; SHAM, 1965): the theory of Density Functional Theory (DFT) was born. DFT is a theory of an interacting, correlated many-body system of electrons by choosing only the ground state density and total energy.

Since the properties of electrons in solids fall into two categories, ground and excited states, they showed that instead of being concerned with the full many-body wave function, one could look at the electronic density of the ground state as an essential property of the system in which one can extract all the properties - all belongings of the system can be considered to be unique functionals of the ground state density. DFT is attractive because one equation for the electronic density substitutes the whole many-body Schrödinger equation of N electrons with $3N$ coordinates, providing a much more practical way to study systems with a large number of electrons and an arbitrary level of complexity. With DFT becomes possible to compare theoretical predictions with experimental results, providing, in this way, a good view of how good the approximation is in treating the electrons as non-interacting particles.

Nevertheless, this revolutionary approach of dealing with a many body system raises some questions: how does one conclude that the electronic density can describe the whole system? How can a function of N variables play the same role as the full many-body wave function of $3N$ coordinates? Two theorems from Hohenberg and Kohn provide the

answers.

2.2.1 The Hohenberg-Kohn theorems

DFT relies on two theorems, and their proofs are straightforward (MARTIN, 2020), but its consequences are profound.

Theorem 1. *For any system of interacting particles in an external potential $V_{ext}(\mathbf{r})$, $V_{ext}(\mathbf{r})$ is determined uniquely, except for a constant, by the ground state particle density $n_0(\mathbf{r})$.*

Proof. The proof is performed by *reductio ad absurdum*. First we suppose that two different external potentials $V_{ext}^{(1)}(\mathbf{r})$ and $V_{ext}^{(2)}(\mathbf{r})$ that lead to the same ground state electronic density $n(\mathbf{r})$. The two external potentials result in two different hamiltonians \hat{H}_1 and \hat{H}_2 each having different ground state wavefunctions Ψ_1 and Ψ_2 that we suppose that lead to the same ground state electronic density $n_0(\mathbf{r})$. Since Ψ_2 is not ground state of \hat{H}_1 , it follows that

$$\begin{aligned} E_1 &= \langle \Psi_1 | \hat{H}_1 | \Psi_1 \rangle < \langle \Psi_2 | \hat{H}_1 | \Psi_2 \rangle \\ E_1 &< \langle \Psi_2 | \hat{H}_1 - \hat{H}_2 + \hat{H}_2 | \Psi_2 \rangle \\ E_1 &< \langle \Psi_2 | \hat{H}_2 | \Psi_2 \rangle + \langle \Psi_2 | [\hat{H}_1 - \hat{H}_2] | \Psi_2 \rangle \\ E_1 &< E_2 + \int d^3r [V_{ext}^{(1)}(\mathbf{r}) - V_{ext}^{(2)}(\mathbf{r})] n_0(\mathbf{r}) \end{aligned} \quad (2.20)$$

We could perform the same procedure starting from the expected value concerning the Hamiltonian \hat{H}_2 and arrive at the result

$$E_2 < E_1 + \int d^3r [V_{ext}^{(2)}(\mathbf{r}) - V_{ext}^{(1)}(\mathbf{r})] n_0(\mathbf{r}) \quad (2.21)$$

now, if we sum the previous two inequalities

$$E_1 + E_2 < E_2 + E_1, \quad (2.22)$$

which is a contradiction. Two different external potentials cannot result in the same nondegenerate ground state. There is a unique correspondence between external potentials and wave functions. Since any observable is computed as an expectation value of the wave function, every observable is also a unique functional of the external potential. \square

Here we highlight the following: until now, a prescription has yet to be given to solve the problem. We still have the problem of solving the many-body wave function in the

presence of an external potential. In summary, we can write Theorem 1 as follows,

$$\boxed{n_0(\mathbf{r})} \rightarrow \boxed{V_{ext}(\mathbf{r})} \rightarrow \boxed{\Psi(\mathbf{r})} \rightarrow \boxed{O = \langle \Psi | \hat{O} | \Psi \rangle}, \quad (2.23)$$

where it says that the electronic density determines all the observables of a system.

The second theorem certifies that the ground state density minimizes the energy, as proved below.

Theorem 2. *A universal functional for the energy $E[n]$ in terms of the density $n(\mathbf{r})$ can be defined, for any valid external potential $V_{ext}(\mathbf{r})$. For any particular $V_{ext}(\mathbf{r})$, the exact ground-state of the system is the global minimum value of this functional, and the density that minimizes this functional is the ground state density $n_0(\mathbf{r})$.*

Proof. Being restricted to densities that are ground state densities of the electronic hamiltonian with some external potentials (these densities are called “V-representable”), and since all properties are uniquely defined if $n(\mathbf{r})$ is specified, then each such property can be view as a functional of $n(\mathbf{r})$, including the total energy functional.

$$\begin{aligned} E_{HK}[n] &= T[n] + E_{int}[n] + \int V_{ext}(\mathbf{r})n(\mathbf{r}) + E_{II} \\ &= F_{HK}[n] + \int V_{ext}(\mathbf{r})n(\mathbf{r}) + E_{II} \end{aligned}$$

where $F_{HK}[n]$ is a universal quantity independent of the external potential. Now consider a system with the ground state density $n_0(\mathbf{r})$, then we have

$$E[n_0] = F_{HK}[n_0] + \langle \Psi_0 | V_{ext} | \Psi_0 \rangle \quad (2.24)$$

From the variational principle, any density that is not the density of the ground state will result in higher energy. Obviously, only the ground state density minimizes $E_{HK}[n]$. \square

2.2.2 The Kohn-Sham Auxiliary System

An attempt to solve this many-body problem is based on the theorem of Hohenberg and Kohn and was proposed by Kohn and Lu Sham (KOHNS; SHAM, 1965). Here the fully interacting system is mapped onto a non-interacting system that possesses the exact ground state electronic density of the original system. As a consequence of the first theorem of Hohenberg-Kohn, these systems will also have the same energy. In this non-interacting picture, all the many body properties are encoded on the exchange-correlation energy, $E_{XC}[n]$, that is given by

$$E_{XC}[n] = (T[n] - T_0[n]) + (V[n] - V_0[n]), \quad (2.25)$$

where the first (second) term is the kinetic (electrostatic) energy difference between the interacting and the non-interacting systems. Now, since we are treating a system of non-interacting particles, our energy functional is given by

$$E_{KS}[n] = T_0[n] + E_{ext}[n] + E_{hartree}[n] + E_{II}[n] + E_{xc}[n], \quad (2.26)$$

with the subscript “0” standing for single particle, and

$$\begin{aligned} T_0[n] &= -\frac{1}{2} \sum_i \langle \psi_i | \nabla^2 | \psi_i \rangle, \\ E_{hartree}[n] &= \frac{1}{2} \int d\mathbf{r} d\mathbf{r}' \frac{n(\mathbf{r})n(\mathbf{r}')}{|\mathbf{r} - \mathbf{r}'|}, \end{aligned} \quad (2.27)$$

and the density is given by

$$n(\mathbf{r}) = \sum_{\sigma} \sum_{i=1}^N |\psi_i^{\sigma}(\mathbf{r})|^2, \quad (2.28)$$

subjected to the constraint

$$\begin{aligned} \int d\mathbf{r} n(\mathbf{r}) &= N \\ \langle \psi_i^{\sigma} | \psi_j^{\sigma'} \rangle &= \delta_{ij} \delta_{\sigma\sigma'}. \end{aligned} \quad (2.29)$$

Now one minimizes the energy functional $E_{KS}[n]$ following a similar procedure done in the Hartree-Fock method, using Lagrange multipliers to deal with the constraints, arriving at

$$\left[-\frac{1}{2} \nabla^2 + V_{ext}(\mathbf{r}) + V_{hartree}(\mathbf{r}) + V_{xc}(\mathbf{r}) \right] \psi_i^{\sigma}(\mathbf{r}) = \epsilon_i \psi_i^{\sigma}(\mathbf{r}), \quad (2.30)$$

where we define the Kohn-Sham potential as

$$V_{KS}^{\sigma}(\mathbf{r}) = V_{ext}(\mathbf{r}) + V_{hartree}(\mathbf{r}) + V_{xc}(\mathbf{r}). \quad (2.31)$$

The exchange and correlation potential $V_{xc}(\mathbf{r})$ and the Hartree potential $V_{hartree}(\mathbf{r})$ are obtained by functional derivatives with respect to density

$$V_{xc}(\mathbf{r}) = \frac{\delta E_{XC}}{\delta n(\mathbf{r}, \sigma)}, \quad (2.32)$$

and

$$V_{hartree}(\mathbf{r}) = \frac{\delta E_{hartree}}{\delta n(\mathbf{r}, \sigma)}. \quad (2.33)$$

The Kohn-Sham equation is a set single-particle equation that can be solved selfconsistently, giving the energy of the full-interacting system. Once the KS potential depends on the ground state wave function, we must solve the KS equation selfconsistently.

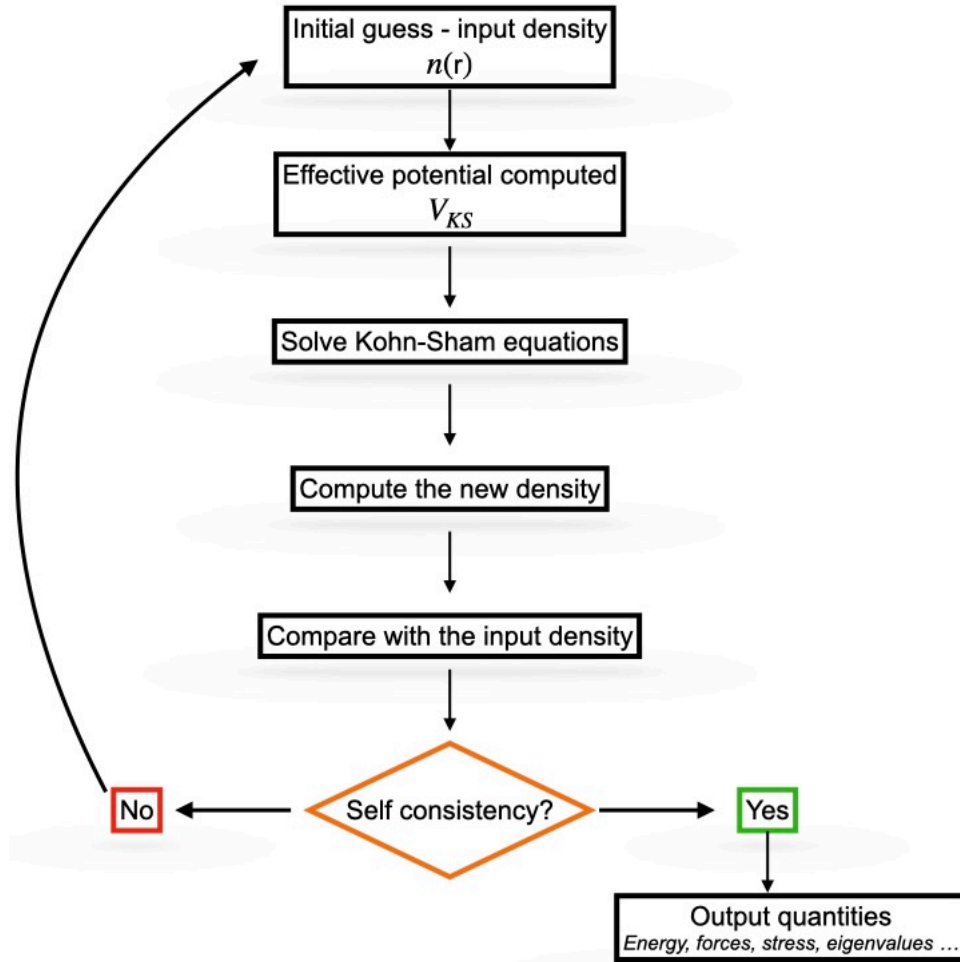


FIGURE 2.1 – Flow chart of SCF cycle.

An initial guess for the electronic density is given, and the Kohn-Sham potential is computed. Then, a usual diagonalization procedure is performed to obtain the KS equation's eigenvalues, enabling one to compute the new electronic density. If the new electronic density computed is equal or very close to the input density (a pre-defined convergence threshold gives the comparison), the quantities of interest are obtained. If not, the SCF cycle is restarted until convergence. A schematic is shown in Fig.2.1.

Until now, there is no approximation: all the expressions found are exact, so DFT is an exact theory. However, once one wants to describe real systems, some approximations are considered, especially for the $E_{XC}[n]$ term where all the many-body interactions are included. Then, here we have the first approximation of the DFT theory. In advance, the $E_{XC}[n]$ term can be broken into a sum of $E_X[n]$ and $E_C[n]$. The first term is relatively easy to estimate, and it has an analytic form for the case of the homogeneous electron gas, such as the LDA approximation in the next section; however, the correlation term is much

more difficult to compute due to many-body effects. A first quantitative approximation for this term was proposed by Wigner (WIGNER, 1934; WIGNER, 1938). Moreover, proper correlation treatment is connected with advances in many-body theory, where a series of Feynman diagrams were summed to eliminate the divergencies (MARTIN, 2020; CARR; MARADUDIN, 1964). The most precise results are obtained via quantum Monte Carlo calculation (CEPERLEY; ALDER, 1980; ORTIZ; BALLONE, 1994). The correlation part is, for typical solids, much smaller than the exact exchange energy, but at very low densities, the correlation becomes a relevant part of the energy (MARTIN, 2020).

We stress that the single-particle states obtained in the Kohn-Sham approach are not necessarily associated with electrons, but a better interpretation is treating them as *quasiparticles*.

2.2.3 Local Density Approximation (LDA)

Together with the idea of the auxiliary system, Kohn and Sham, in the same paper (KOHNS; SHAM, 1965), proposed the first approximation to solids to deal with the exchange-correlation term. They considered that a solid could be treated as a homogeneous gas of electrons such that the effects of exchange and correlation are local: Local Density Approximation (LDA).

$$E_{xc}^{LDA}[n] = \int \varepsilon_{xc}(n)n(\mathbf{r}')d^3r', \quad (2.34)$$

where $\varepsilon_{xc}(n)$ is the exchange-correlation energy per particle of a uniform electron gas. Since we are treating the approximation of a uniform electron gas, the eigenfunctions will be plane waves, and the exchange part will be given by the Hartree-Fock term $\hat{V}_x^{i,\sigma}(\mathbf{r})$ in which we can obtain an exact expression for $\varepsilon_x(n)$ given by (KOHNS; SHAM, 1965)

$$\varepsilon_x = -\frac{3}{4} \left(\frac{3}{\pi} n \right)^{1/3}, \quad (2.35)$$

and the correlation part does not have an analytical expression but has been obtained with high accuracy with Monte Carlo methods (CEPERLEY; ALDER, 1980; ORTIZ; BALLONE, 1994; MAGGIO; KRESSE, 2016).

LDA performs badly whenever there is an odd number of electrons since it needs to distinguish between spin densities, but it is well suited to systems with slow-varying densities. To overcome this limitation, it is possible to use LSDA, where spin effects are considered.

2.2.4 Generalized Gradient Approximation (GGA)

Even with the LDA successfully describing many physical quantities, one needs to go beyond to treat the system under study, not just as a homogeneous electron gas, to obtain more reliable results. The first step beyond local approximation is to consider variations in the density. Since it is a scalar quantity, it is natural to take its gradient yielding on the gradient expansion approximation (GEA) suggested by Kohn and Sham. However, this approach led to inconsistent results and violated conditions such as sum rules (HERMAN *et al.*, 1969). The improvement over GEA is considering variations in the density, taking its gradient but in a different form to preserve essential properties. The exchange-correlation energy on the Generalized Gradient Approximation (GGA) can be written as (PERDEW; BURKE, 1996)

$$\begin{aligned} E_{XC}^{\text{GGA}}[n^\uparrow, n^\downarrow] &= \int d^3r n(\mathbf{r}) \epsilon_{xc}(n^\uparrow, n^\downarrow, |\nabla n^\uparrow|, |\nabla n^\downarrow|, \dots) \\ &= \int d^3r n(\mathbf{r}) \epsilon_x^{\text{homo}}(n) F_{xc}(n^\uparrow, n^\downarrow, |\nabla n^\uparrow|, |\nabla n^\downarrow|, \dots), \end{aligned} \quad (2.36)$$

where F_{xc} is the enhancement factor that is dimensionless and $\epsilon_x^{\text{homo}}(n)$ is the exchange energy of the unpolarized homogeneous gas. The argument of F_{xc} is assigned to be a certain quantity s that depends on the gradient of the density and is given by, for its first order

$$s = \frac{|\nabla n|}{2k_F n}, \quad (2.37)$$

where k_F is the Fermi wave vector. The most widely used GGA approximation is the implementation given by Perdew-Burker-Ernzerhof (PBE) (PERDEW *et al.*, 1996; PERDEW *et al.*, 1997). Improving binding energies is one of the most significant achievements of GGA approximation (KOCH; HOLTHAUSEN, 2001). However, despite the improvement in the properties prediction, the GGA gives larger bond lengths and does not give the correct band gap. To obtain high-accuracy results, we must go a step further.

2.2.5 Hybrid Functionals

As discussed earlier, the Hartree-Fock approximation results in band gaps that are too large, while the Kohn-Sham eigenvalues tend to underestimate the gap. A natural search for better accuracy is to mix the best of these two worlds, resulting in hybrid functionals that improve band gaps and excitation energies. This combination of Hartree-Fock and Kohn-Sham contributions for the hybrid functional is given by a particular parameter α

$$E_{XC}^{hybrid} = \alpha E_{XC}^{HF} + (1 - \alpha) E_{XC}^{KS}. \quad (2.38)$$

Becke, based on arguments of the coupling constant for the exchange-correlation energy, proposed a hybrid functional of the form

$$E_{XC}^{hybrid} = \frac{1}{2}(E_{XC}^{HF} + E_{XC}^{LSDA}). \quad (2.39)$$

A more accurate treatment of the coupling constant resulted in a widely used hybrid functional, the PBE0 proposed by Perdew, Ernzerhof, and Burke (PERDEW *et al.*, 1996; PERDEW *et al.*, 1996) given by

$$E_{XC}^{PBE0} = E_{XC}^{PBE} + \frac{1}{4}(E_X^{HF} - E_X^{PBE}). \quad (2.40)$$

Other widely used XC term is the B3LYP, which uses the Becke B88 exchange functional (BECKE, 1988) and the LYP correlation (LEE *et al.*, 1988)

$$E_{XC}^{B3LYP} = E_{XC}^{LDA} + a_0(E_X^{HF} - E_X^{LDA}) + a_x(E_X^{B88} - E_X^{LDA}) + a_c(E_c^{LYP} - E_c^{LDA}), \quad (2.41)$$

with the coefficients parametrized by atomic and molecular data. However, there are diverse reasons to construct hybrid functionals that are just a fraction of the Hartree-Fock exchange. For instance, any functional with non-zero α cannot be used for metals since the long-range part coming from the Coulomb potential must be eliminated since it gives rise to unphysical results at the Fermi surface (MARTIN, 2020). This range separation is to “break” the Coulomb interaction into two parts, a short-range (SR) and a long-range (LR)

$$\frac{1}{r} = \underbrace{\frac{\text{erfc}(\omega r)}{r}}_{SR} + \underbrace{\frac{\text{erf}(\omega r)}{r}}_{LR}, \quad (2.42)$$

where erf is the error function, ω is the range parameter and $\text{erfc}(\omega r) = 1 - \text{erf}(\omega r)$.

For solids, the most widely used hybrid functional with this kind of treatment is the HSE (HEYD *et al.*, 2003; HEYD *et al.*, 2006; KRUKAU *et al.*, 2006), in which the long-range Hartree-Fock is eliminated, resulting in a functional the form

$$E_X^{HSE} = \frac{1}{4}E_X^{HF} + \frac{3}{4}E_X^{PBE,SR} + E_X^{PBE,LR}, \quad (2.43)$$

where in the HSE06 functional, the range parameter is chosen to be $0.11/a_0$, and the superscript SR stands for short range. The correlation part is given by being the same as

PBE

$$E_c^{HSE} = E_c^{PBE}. \quad (2.44)$$

However, the price paid on using HSE06 for obtaining more accurate results on band gaps is on computational cost, which can be 2-4 times more expensive than pure DFT calculation (HEYD; SCUSERIA, 2004).

2.2.6 Van der Waals Functionals

The local approximations' success is remarkable, and the implementation of hybrid functionals improved the excitations energies and gave a better result for the band gap. However, the local approximation cannot describe the van der Waals interactions on the 2D materials and heterostructures. The longest-range interaction is a correlation effect due to quantum fluctuations that induce dipoles. This attraction is called the London interaction, which is a long-range interaction (proportional to $1/r^6$). For this reason, the approximations such as LDA and GGA does not give good result for such interaction. These long-range interactions can be considered via a completely nonlocal exchange-correlation functional or modeled by effective interactions parametrized empirically or by first-principles calculations.

There are two main approaches to obtaining a nonlocal functional that describes with sufficient accuracy the effects from long to short-range correlations (MARTIN, 2020). The first approach is a long-range pair-wise interaction in which a damping function $f(R)$ is introduced to eliminate short-range divergences in the sum over pairs of the interactions

$$E_{dispersion} = -\frac{1}{2} \sum_{AB} \frac{C_{6AB}}{(R_{AB})^6} f(R_{AB}), \quad (2.45)$$

where

$$C_{6AB} = \frac{3}{\pi} \int_0^\infty du \alpha_A(iu) \alpha_B(iu), \quad (2.46)$$

with α being the polarizability. A convenient form for the damping function and result for the integral Eq.(2.46) has been proposed and developed (TKATCHENKO; SCHEFFLER, 2009; DION *et al.*, 2004) and showed good performance for molecules and solids (MARTIN, 2020).

The other approach is based on fundamentals of many-body theory, such as random phase approximation (RPA), where the XC term is given in function of the electronic density, and the correlation part is treated as a sum of a local correlation part, and a genuinely nonlocal correlation part (DION *et al.*, 2004; DION *et al.*, 2005)

$$E_c[n] = E_{xc}^{LDA}[n] + E_c^{nl}[n], \quad (2.47)$$

in which the nonlocal part is responsible for the van der Waals forces. The nonlocal part is given by

$$E_c^{nl}[n] = \frac{1}{2} \int d\mathbf{r}d\mathbf{r}' n(\mathbf{r})\Phi(\mathbf{r}, \mathbf{r}')n(\mathbf{r}'), \quad (2.48)$$

where $\Phi(\mathbf{r}, \mathbf{r}')$ is some given general function.

In 2D systems, it is essential to consider this kind of interaction since it gives the correction of weak but relevant non-local terms resulting in more accurate results for binding distances and stability. For this reason, vdW functionals implemented on the *ab initio* package used in this work were tested, and the results will be compared with those in the literature as discussed in Appendix A.

2.2.7 Hellman-Feynman Theorem

The Born-Oppenheimer approximation is valuable once we have an atomic configuration free of internal stress. The force on the nuclei is given in terms of the charge density independent of the electron kinetic energy and the effects of exchange and correlation. This is the force theorem derived by Feynman (FEYNMAN, 1939). The force on a system with respect to the nuclei position \mathbf{R}_I can be given by

$$\mathbf{F}_I = -\frac{\partial E}{\partial \mathbf{R}_I}. \quad (2.49)$$

From the expression of total energy, given by the expectation value of the Hamiltonian concerning some normalized wave function 2.4

$$\mathbf{F}_I = -\langle \Psi | \frac{\partial \hat{H}}{\partial \mathbf{R}_I} | \Psi \rangle - \langle \frac{\partial \Psi}{\partial \mathbf{R}_I} | \hat{H} | \Psi \rangle - \langle \Psi | \hat{H} | \frac{\partial \Psi}{\partial \mathbf{R}_I} \rangle - \frac{\partial E_{II}}{\partial \mathbf{R}_I}, \quad (2.50)$$

and since any variation of the ground state wave function is zero,

$$\mathbf{F}_I = -\int d^3\mathbf{r} n(\mathbf{r}) \frac{\partial V_{ext}(\mathbf{r})}{\partial \mathbf{R}_I} - \frac{\partial E_{II}}{\partial \mathbf{R}_I} \quad (2.51)$$

so the force has an explicit dependence on the electronic density. The procedure to obtain the optimal structure is relatively standard: the initial atomic coordinates are given, and the electronic density is computed, followed by forces and stress. Then, to reduce stress and optimize the atomic positions minimizing the energy, the atomic arrangement is changed, and the electronic density of the first calculation is used to start a new relaxation procedure. This is repeated until a predefined convergence criterion is achieved.

2.2.8 Norm Conserving Pseudopotentials

Besides all the approximations already considered, there are some problems related to technical issues when solving the KS equations: the divergence of the Coulomb potential. As one approaches the cores, it is required a significant number of plane waves, which has, as a consequence, the increasing on the cutoff energy on the expansion Eq.(2.17); heavy atoms would be much more challenging to simulate due to the large number of electrons involved. It is intuitive to think that the core electrons can be treated separately from the valence ones because the latter are responsible for the atom's chemical activity since they are more weakly bound to the nucleus. The detachment of the electronic behavior of these two "kinds" of electrons gave rise to the idea of the pseudopotential (PHILLIPS; KLEINMAN, 1959) in which the core electrons are ignored, but not completely: it is considered smooth potential acting on the valence electrons.

The emergence of *ab initio* norm-conserving and ultrasoft pseudopotentials has paved the way for precise calculations, serving as the cornerstone for much of the ongoing research and development in electronic structure methods. The notion of "norm-conservation" holds particular significance in the evolution of *ab initio* pseudopotentials, since they are derived from calculations without any fitting to properties of a molecule or a solid, facilitating their application and enhancing their accuracy and transferability. Norm-conserving pseudo-functions $\psi^{PS}(\mathbf{r})$ are normalized solutions of a model potential meticulously selected to replicate the valence properties observed in an all-electron calculation (MARTIN, 2020).

Once the pseudopotential is applied to different systems, the valence pseudo functions must satisfy the usual orthonormality conditions

$$\langle \psi_i^{\sigma,PS} | \psi_j^{\sigma',PS} \rangle = \delta_{i,j} \delta_{\sigma,\sigma'}, \quad (2.52)$$

so that the KS equations have the same form as derived in subsection 2.2.2.

The starting point for defining norm-conserving potentials is the list of requirements for a good *ab initio* pseudopotential given by Hamman, Schluter, and Chiang (HAMANN *et al.*, 1979):

- All-electron and pseudovalence eigenvalues agree for the chosen atomic reference configuration.
- All-electron and pseudovalence wavefunctions agree beyond a chosen core radius R_c .
- The logarithmic derivatives of the all-electron and pseudo-wavefunctions agree at R_c .
- The integrated charge inside R_c for each wavefunction agrees (norm conservation).

- The first energy derivative of the logarithmic derivatives of the all-electron and pseudowavefunctions agrees at R_c , and therefore for all $r \geq R_c$.

From points 1 and 2, it logically follows that the Norm Conserving Pseudopotentials coincide with the atomic potential beyond the core region. Point 3 is a direct consequence of the continuity of the wavefunction and its radial derivative at R_c for any smooth potential. While inside the core region, both the pseudopotential and radial pseudo-orbital diverge from their all-electron counterparts, point 4 ensures that the integrated charges remain the same as for the all-electron radial orbital for a valence state. This charge conservation principle guarantees the accuracy of the total charge within the core region, while the normalized pseudo-orbital, particularly for local functionals, is equal to the true orbital beyond R_c . Point 5 is crucial for a high-quality pseudopotential: it should be producible within a straightforward framework yet adaptable to complex environments. Within a molecule or solid, the wavefunctions and eigenvalues undergo alterations, and a pseudopotential meeting the criteria of point 5 will accurately replicate these changes in eigenvalues to a linear extent relative to the modifications in the self-consistent potential (CHRISTIANSEN *et al.*, 1979; KRAUSS; STEVENS, 1984; MARTIN, 2020).

In our study, we employed Optimized Norm-Conserving Vanderbilt (ONCV) pseudopotentials sourced from the PseudoDojo library (SETTEN *et al.*, 2018). These ONCV pseudopotentials are characterized by multiple projectors, with their pseudofunctions normalized. The term “optimized” denotes the meticulous attention paid to ensuring the softness of the potentials, achieved by minimizing residual kinetic energy. Optimization of the projector set for each angular momentum l was undertaken, leading to the development of a novel approach centered on auxiliary functions to fulfill various continuity constraints (SETTEN *et al.*, 2018). Extensive testing of these pseudopotentials (HAMANN, 2013; HAMANN, 2017) has demonstrated their remarkable agreement with results from all-electron calculations.

2.3 Maximally Localized Wannier Functions (MLWF)

2.3.1 Overview of the formalism

First-principles codes typically solve the electronic structure of periodic materials in terms of Bloch states $\psi_{n\mathbf{k}}(\mathbf{r})$, where n is the band index and \mathbf{k} is the quasi-momentum crystal number. An alternative representation can be given in terms of localized orbitals, first proposed by Felix Bloch (BLOCH, 1929), which is a procedure called Linear Combination of Atomic Orbitals (LCAO) that consists in making linear combinations of atomic orbitals and after this method was proposed by Slater and Koster (SLATER; KOSTER, 1954)

as good interpolation procedure to fit band structures from *ab-initio* calculations. Here we follow a recipe to obtain our localized atomic orbitals from a first principle calculation, so-called Wannier functions (WFs) first introduced by Gregory Wannier (WANNIER, 1937). The WFs centered on a lattice site \mathbf{R} and associated with a band index n , $|\mathbf{R}n\rangle$, is written in terms of the set of Bloch states, $|\psi_{n\mathbf{k}}\rangle$, as

$$|\mathbf{R}n\rangle = \frac{V}{(2\pi)^3} \int_{BZ} d\mathbf{k} e^{-i\mathbf{k}\cdot\mathbf{R}} |\psi_{n\mathbf{k}}\rangle, \quad (2.53)$$

where V is the volume of the unit cell and the integral is over the BZ. It's noteworthy that the Wannier WFs are orthonormal, and that two WFs represented as $|\mathbf{R}n\rangle$ and $|\mathbf{R}'n\rangle$ transform into one another through a translation by $\mathbf{R} - \mathbf{R}'$ (BLOUNT, 1962). This property of WFs serves as a bridge, facilitating the reconciliation between the real-space localization and the reciprocal-space delocalization frameworks. Moreover, WFs cannot be attributed to a well-defined energy eigenvalue since they do not directly correspond to eigenstates of the single-particle Hamiltonian.

A primary challenge with WFs lies in their lack of uniqueness. This issue arises because any Bloch wavefunction can be multiplied by a phase factor (gauge transformation), which essentially represents the same physical state. This inherent ambiguity can lead to difficulties in achieving precise localization in real space, particularly when bands exhibit degeneracies at specific points within the BZ, making the Bloch states indistinguishable at \mathbf{k} that this occurs. For more than one band, instead of a phase factor, the gauge freedom is identified as a unitary matrix $U_{nj}^{(\mathbf{k})}$ that transforms occupied Bloch orbitals into the Wannier representation at every wave vector. In Hilbert space, a unitary transformation is the generalization of an orthogonal one, so in a band structure, one has the freedom that a given \mathbf{k} -point to apply a unitary transformation in those multidimensional functions and obtain the same physics. This unitary matrix is chosen to make the WFs as meaningful as possible while mapping the Bloch states into the Wannier representation.

In a general scenario involving a set of J bands, which may not be isolated within their set, the associated Wannier functions (WFs) are defined as follows:

$$|\mathbf{R}j\rangle = \frac{V}{(2\pi)^3} \int_{BZ} d\mathbf{k} e^{-i\mathbf{k}\cdot\mathbf{R}} \sum_{n=1}^J |\psi_{n\mathbf{k}}\rangle U_{nj}^{(\mathbf{k})}, \quad (2.54)$$

where $U_{nj}^{(\mathbf{k})}$ represents a $J \times J$ unitary transformation acting within the chosen subspace and periodically dependent on \mathbf{k} . This phenomenon is termed gauge freedom. Utilizing this freedom, a new representation of electronic states is developed, wherein instead of existing in a Bloch state with band index n and quasi-momentum quantum number \mathbf{k} , they reside in a Wannier representation with an equivalent band index. In this context, the representation is more closely associated with the labeling of atomic orbital states

and a lattice vector quantum number, indicating the unit cell inhabited by that state. However, this unitary transformation must be well-defined to ensure its effectiveness.

A careless application of Eq.(2.54) would give poorly localized WFs, since we do not know how to choose the unitary rotations. In addition, since this matrix mixes the Bloch states at the k-points, different choices lead to WFs with different localizations. Also, it does not preserve the individual Wannier centers. For this new representation to make sense, it needs to be localized and associated with a specific unit cell. Then, it is necessary to explore the space of unitary transformations that bring from a Bloch representation to a Wannier representation, demanding four key factors:

- $|w_n(\mathbf{r})\rangle$ span the same space as $\{|\psi_{n\mathbf{k}}\rangle\}$;
- States that have the same label n but correspond to a different unit cell are periodic images of one another, $w_n(\mathbf{r}) = w_n(\mathbf{r} - \mathbf{R})$;
- $\langle w_n(\mathbf{R})|w_m(\mathbf{R}')\rangle = \delta_{n,m}\delta_{\mathbf{R},\mathbf{R}'}$: orthogonality of WFs;
- It is required that they be as localized as possible in real space to have only one.

Even with the previous requirements, one still has an infinite set of solutions. A simple route to obtain the unitary transformation through a projection onto a predefined set of localized orbitals (CLOIZEAUX, 1964)

$$|\phi_{n\mathbf{k}}\rangle = \sum_{m=1}^J |\psi_{m\mathbf{k}}\rangle \langle \psi_{m\mathbf{k}}|g_n\rangle, \quad (2.55)$$

where $|g_n\rangle$ is a initial guess. The functions $|\phi_{n\mathbf{k}}\rangle$ passes through a symmetric orthonormalization, and they are converted into the periodic part of the Bloch functions. A more rigorous approach to deal with the gauge freedom is to choose a particular set of $U_{nj}^{(\mathbf{k})}$ which the sum of the wavefunction spreads Ω of the corresponding WFs be minimized (MARZARI; VANDERBILT, 1997), as discussed in the next subsection.

2.3.2 Spread functional: Localization of the WFs

As a measure of the total delocalization or spread of the WFs, one introduces the spread functional

$$\Omega = \sum_{n=1}^J [\langle r^2 \rangle_n - \bar{\mathbf{r}}_n^2], \quad (2.56)$$

which measures the sum of the quadratic spreads of the WFs and it has to be minimized with respect to the unitary transformations $U_{nj}^{(\mathbf{k})}$. One can decompose the functional Ω in

three terms: invariant, diagonal, and off-diagonal. First, the functional can be splitted as

$$\Omega = \Omega_I + \tilde{\Omega}, \quad (2.57)$$

where

$$\Omega_I = \sum_n \left[\langle r^2 \rangle_n - \sum_{\mathbf{R}m} |\langle \mathbf{R}m | \mathbf{r} | \mathbf{0}n \rangle|^2 \right], \quad (2.58)$$

$$\tilde{\Omega} = \sum_n \sum_{\mathbf{R}m \neq \mathbf{0}n} |\langle \mathbf{R}m | \mathbf{r} | \mathbf{0}n \rangle|^2. \quad (2.59)$$

Both terms are positive definite, and Ω_I is gauge invariant (MARZARI; VANDERBILT, 1997). The first measures the k-space dispersion of the band projection operator, while the second reflects the extent to which the WFs fail to be eigenfunctions of the band-projection position operators. The criterion to find a set of Maximally Localized Wannier Functions (MLWFs) is reducing, as far as possible, the mean-square average of all off-diagonal matrix elements of x , y , z between WFs, which is encoded into $\tilde{\Omega}$. The vital point is that all these quantities defined here in real space are transformed into k-space where the matrix elements of position operators are well-defined (BLOUNT, 1962) and are given by:

$$\langle \mathbf{R}n | \mathbf{r} | \mathbf{0}m \rangle = i \frac{V}{(2\pi)^3} \int d\mathbf{k} e^{i\mathbf{k}\cdot\mathbf{R}} \langle u_{n\mathbf{k}} | \nabla_{\mathbf{k}} | u_{m\mathbf{k}} \rangle, \quad (2.60)$$

$$\langle \mathbf{R}n | \mathbf{r}^2 | \mathbf{0}m \rangle = -\frac{V}{(2\pi)^3} \int d\mathbf{k} e^{i\mathbf{k}\cdot\mathbf{R}} \langle u_{n\mathbf{k}} | \nabla_{\mathbf{k}}^2 | u_{m\mathbf{k}} \rangle, \quad (2.61)$$

and now one is able to define the quantities $\bar{\mathbf{r}}_n = \langle \mathbf{0}n | \mathbf{r} | \mathbf{0}n \rangle$ and $\langle r^2 \rangle_n = \langle \mathbf{0}n | \mathbf{r}^2 | \mathbf{0}n \rangle$ at the origin, and then

$$\bar{\mathbf{r}}_n = i \frac{V}{(2\pi)^3} \int d\mathbf{k} \langle u_{n\mathbf{k}} | \nabla_{\mathbf{k}} | u_{n\mathbf{k}} \rangle, \quad (2.62)$$

and

$$\langle r^2 \rangle_n = \frac{V}{(2\pi)^3} \int d\mathbf{k} |\nabla_{\mathbf{k}} u_{n\mathbf{k}}|^2. \quad (2.63)$$

In the k-space representation, performing derivatives on regular meshes will be necessary, so one has to express the positions of the WFs and their spread as a function of the phase relation between the Bloch orbitals. To this end, it is used finite-difference expressions for $\nabla_{\mathbf{k}}$ and $\nabla_{\mathbf{k}}^2$ and requires that these quantities are invariant with lattice translations. Then, Eqs. (2.62) and (2.63) are rewritten, becoming

$$\bar{\mathbf{r}}_n = -\frac{1}{N} \sum_{\mathbf{k}, \mathbf{b}} w_b \mathbf{b} \text{Im} M_{nn}^{(\mathbf{k}, \mathbf{b})}, \quad (2.64)$$

$$\langle r^2 \rangle_n = \frac{1}{N} \sum_{\mathbf{k}, \mathbf{b}} w_b \{ [1 - |M_{nn}^{(\mathbf{k}, \mathbf{b})}|^2] + [\text{Im} \ln M_{nn}^{(\mathbf{k}, \mathbf{b})}]^2 \}, \quad (2.65)$$

where

$$M_{m,n}^{(\mathbf{k}, \mathbf{b})} = \langle u_{m\mathbf{k}} | u_{n, \mathbf{k}+\mathbf{b}} \rangle, \quad (2.66)$$

and \mathbf{b} are the vectors connecting each \mathbf{k} -point to its neighbors, and w_b are the associated weights, and the expression Eq.(2.66) represents the overlap matrix among the Bloch orbitals at neighboring \mathbf{k} points. It should be noted that the only ingredient required to compute the spread functional is the overlap term of the Bloch orbitals. Then, the corresponding expression for Ω_I becomes:

$$\Omega_I = \frac{1}{N_{kp}} \sum_{\mathbf{k}, \mathbf{b}} w_b \sum_{m=1}^N \left[1 - \sum_{n=1}^N |M_{mn}^{(\mathbf{k}, \mathbf{b})}|^2 \right]. \quad (2.67)$$

For $\tilde{\Omega}$ we can decompose into band-off-diagonal and band-diagonal pieces, $\tilde{\Omega} = \Omega_{OD} + \Omega_D$, where

$$\Omega_{OD} = \sum_{m \neq n} \sum_{\mathbf{R}} = |\langle \mathbf{R}m | \mathbf{r} | \mathbf{0}n \rangle|^2 = \frac{1}{N} \sum_{\mathbf{k}, \mathbf{b}} w_b \sum_{m \neq n} |M_{m,n}^{(\mathbf{k}, \mathbf{b})}|^2, \quad (2.68)$$

and

$$\Omega_D = \sum_n \sum_{\mathbf{R} \neq \mathbf{0}} = |\langle \mathbf{R}n | \mathbf{r} | \mathbf{0}n \rangle|^2 = \frac{1}{N_{kp}} \sum_{\mathbf{k}, \mathbf{b}} w_b \sum_n (-\text{Im} \ln M_{nn}^{(\mathbf{k}, \mathbf{b})} - \mathbf{b} \cdot \bar{\mathbf{r}}_n)^2, \quad (2.69)$$

in which N_{kp} is the number of \mathbf{k} -points on the Monkhorst-Pack grid and $\bar{\mathbf{r}}_n$ is the center of the n th WF.

The minimization procedure with a predefined sample of \mathbf{k} -points begins with the minimization of Ω_I , which is gauge invariant. Then the other quantities, Ω_D and Ω_{OD} are minimized. The minimization only involves the updating of the unitary matrices obtained first as the overlap of the Bloch orbitals

$$M_{mn}^{(0)(\mathbf{k}, \mathbf{b})} = \langle u_{m\mathbf{k}}^{(0)} | u_{n\mathbf{k}+\mathbf{b}}^{(0)} \rangle, \quad (2.70)$$

and then, at every update of the unitary matrices towards the minimum, the overlap matrices are updated with inexpensive matrix algebra (MARZARI *et al.*, 2012)

$$M^{(\mathbf{k}, \mathbf{b})} = U^{(\mathbf{k})\dagger} M^{(0)\mathbf{k}+\mathbf{b}} U^{(\mathbf{k}+\mathbf{b})}. \quad (2.71)$$

It's crucial to highlight that, at the global minimum, WFs are real. To avoid potential local minima, initiating the localization procedure with a smoothly varying gauge choice

is essential (MARZARI *et al.*, 2012). For this purpose, it is important to offer a set of initial guess orbitals derived from prior analyses of the orbital characteristics within the *ab-initio* band structure.

While the preceding discussion adequately outlines the process for obtaining MLWFs for an isolated set of bands, our primary focus often centers on entangled bands, such as those encompassing the Fermi energy in a semiconductor (including both valence and conduction bands). The challenge in deriving WFs for such scenarios arises from the uncertainty on the selection of states to form J WFs. To address this, the projection onto trial orbitals offers a simple and effective method for extracting a smooth Bloch subspace from a set of entangled bands. By localizing these trial functionals, smoothness in k -space can be achieved, facilitating the generation of MLWFs.

The smoothness of a Bloch state in k -space is quantified by Ω_I , which encapsulates the intrinsic smoothness inherent in the underlying Hilbert space. Its expression in k -space formulation reveals that Ω_I provides a BZ average of the local subspace mismatch. The optimized subspace selection process can be formulated as follows (SOUZA *et al.*, 2001): Initially, a set of $\mathfrak{J}_{\mathbf{k}} > J$ Bloch states is identified at each point on a uniform BZ grid, typically using a range of energies or bands. Subsequently, an iterative procedure is employed to extract, self-consistently at each k -point, the J -dimensional subspace that yields the smallest possible value of Ω_I when integrated across the BZ. When viewed as a function of k , the Bloch subspace obtained at the end of this iterative minimization is deemed “optimally smooth,” as it exhibits minimal variation with respect to k . Furthermore, the algorithm can be easily adapted to retain a selected subset of Bloch eigenstates within a specified disentanglement window, such as those spanning a narrower range of energies or bands, which we refer to as a frozen window (MARZARI *et al.*, 2012).

As in the case of the one-shot projection, the outcome of this iterative procedure is a set of J Bloch-like states at each \mathbf{k} which are linear combinations of the initial $\mathfrak{J}_{\mathbf{k}}$ eigenstates

$$|\phi_{n\mathbf{k}}\rangle = \sum_{m=1}^{N_{window}} |\psi_{m\mathbf{k}}\rangle \langle \psi_{m\mathbf{k}} | g_n \rangle. \quad (2.72)$$

Once a suitable J -dimensional Bloch manifold is identified, the same methodology outlined earlier for isolated bands can be applied to generate localized WFs. Then we orthonormalize the resulting J orbitals to produce a set of J smoothly varying Bloch-like states across the BZ,

$$|\tilde{\psi}_{m\mathbf{k}}\rangle = \sum_{n=1}^{N_{bands}} (S_{\mathbf{k}}^{-1/2})_{mn} |\phi_{n\mathbf{k}}\rangle, \quad (2.73)$$

where $(S_{\mathbf{k}})_{mn} = \langle \phi_{m\mathbf{k}} | \phi_{n\mathbf{k}} \rangle$. This orbital projection will introduce a gauge fixing that can be redefined by minimizing Ω over the subspace. The other part of the spread functional

$\tilde{\Omega}$, is minimized following the previous approach of Marzari and Vanderbilt (MARZARI; VANDERBILT, 1997).

2.4 Tight-Binding formalism

DFT is a well-established way to obtain materials' electronic and structural properties of different systems. Approaches based only on the symmetry of the system and the use of valence states to describe the physics, without any parameter given a priori, are called first principles or *ab initio* methods. However, in general, methodologies based purely on DFT tend to be quite expensive computationally, which motivates the search for other methods to describe the electronic behavior of a system with many electrons.

Methods characterized by their low computational cost are often favored for approximating low-energy bands, particularly those surrounding the Fermi energy. The bands in this range frequently suffice in describing pertinent properties, as the electrons within this energy window are typically treated as non-interacting with others at similar energy levels, yet are strongly bound to their respective atoms. Following a single-particle framework, electrons in this scenario can be modeled as independent particles navigating within a periodic potential generated by the atomic structure's ions. One well-known approach that operates within this framework is the Tight-Binding (TB) approximation. Essentially, the TB method utilizes a collection of localized orbitals with onsite energy, while considering only specific hopping terms, typically adequate for describing low-energy bands. In general, to construct a localized basis, one may consider a set of atomic orbitals given by

$$\phi_l(\mathbf{r} - \mathbf{R}_i), \quad (2.74)$$

where \mathbf{R}_i is the position of atomic i in the unit cell and $\phi_l(\mathbf{r})$ are the atomic states associated with an atom and $l = s, p, d, f$. Now, one writes a basis using these localized states, satisfying the Bloch theorem. A direct basis is given by:

$$\chi_{\mathbf{k},l,i}(\mathbf{r}) = \frac{1}{\sqrt{N}} \sum_{\mathbf{R}'} e^{i\mathbf{r}\cdot\mathbf{R}'} \phi_l(\mathbf{r} - \mathbf{R}_i - \mathbf{R}'), \quad (2.75)$$

with \mathbf{R}' covering all the crystal cells and i denoting the atomic position of the atom at \mathbf{R}_i and l representing the orbital part. The single-particle eigenstates can be expanded as a linear combination on this basis

$$\psi_{\mathbf{k}}^{(n)}(\mathbf{r}) = \sum_{l,i} c_{\mathbf{k},l,i}^{(n)} \chi_{\mathbf{k},l,i}(\mathbf{r}), \quad (2.76)$$

remaining to determine the coefficients $c_{\mathbf{k},l,i}^{(n)}$. This can be achieved requiring $\psi_{\mathbf{k}}^{(n)}(\mathbf{r})$ being eigenstate of the single-particle (SP) hamiltonian

$$H^{sp}\psi_{\mathbf{k}}^{(n)}(\mathbf{r}) = \varepsilon_{\mathbf{k}}^{(n)}\psi_{\mathbf{k}}^{(n)}(\mathbf{r}). \quad (2.77)$$

Projecting this eigenvalue equation on the basis $\chi_{\mathbf{k},l,i}(\mathbf{r})$, one obtain the secular equation

$$\sum_{l,i} \left[\underbrace{\langle \chi_{\mathbf{k},m,j} | H^{sp} | \chi_{\mathbf{k},l,i} \rangle}_{(II)} - \varepsilon_{\mathbf{k}}^{(n)} \underbrace{\langle \chi_{\mathbf{k},m,j} | \chi_{\mathbf{k},l,i} \rangle}_{(I)} \right] c_{\mathbf{k},l,i}^{(n)} = 0, \quad (2.78)$$

where the term (I) can be rewritten as

$$\begin{aligned} (I) &= \frac{1}{N} \sum_{\mathbf{R}''} \sum_{\mathbf{R}'} e^{i\mathbf{k}(\mathbf{R}'-\mathbf{R}'')} \langle \phi_m(\mathbf{r} - \mathbf{R}_j - \mathbf{R}'') | \phi_l(\mathbf{r} - \mathbf{R}_i - \mathbf{R}') \rangle \\ &= \sum_{\mathbf{R}} e^{i\mathbf{k}\cdot\mathbf{R}} \underbrace{\langle \phi_m(\mathbf{r} - \mathbf{R}_j) | \phi_l(\mathbf{r} - \mathbf{R}_i - \mathbf{R}) \rangle}_{\delta_{m,l}\delta_{i,j}\delta(\mathbf{R}) \rightarrow \text{overlap terms}}, \end{aligned} \quad (2.79)$$

once is being considered an orthonormal and localized basis, and

$$\begin{aligned} (II) &= \langle \chi_{\mathbf{k},m,j} | H^{sp} | \chi_{\mathbf{k},l,i} \rangle \\ &= \sum_{\mathbf{R}} e^{i\mathbf{k}\cdot\mathbf{R}} \langle \phi_m(\mathbf{r} - \mathbf{R}_j) | H^{sp} | \phi_l(\mathbf{r} - \mathbf{R}_i - \mathbf{R}) \rangle \\ &= \underbrace{\delta_{m,l}\delta_{i,j}\delta(\mathbf{R})\varepsilon_l}_{\text{on site term } (j=i, \mathbf{R}=0)} + \underbrace{e^{i\mathbf{k}\cdot\mathbf{R}}\delta[(\mathbf{R}_j - \mathbf{R}_i - \mathbf{R}) - \mathbf{d}_{nn}]V_{lm,ij}}_{\text{hopping term}} \end{aligned} \quad (2.80)$$

where the first term gives the onsite energy elements and the second the hopping ($V_{lm,ij}$) term between nearest neighbors separated by a distance \mathbf{d}_{nn} .

Owing to their localized nature, WFs serve as an ideal orbital basis for TB models, facilitating the derivation of various quantities of interest alongside first-principle calculations, a procedure called Wannier interpolation. This technique proves invaluable not only for obtaining band structures but also for computing physical quantities that require a fine sampling of the BZ. The Wannier interpolation process typically begins with a first-principles calculation conducted on a coarse, uniform reciprocal-space mesh. Subsequently, the states within the bands of interest are transformed into WFs, allowing the desired quantity to be expressed in the Wannier representation. Leveraging the maximum localization property of WFs, this quantity exhibits exponential decay with distance, enabling the original properties to be efficiently interpolated on a much denser k-mesh.

In this thesis, we extensively use Wannier interpolation to generate band structure

plots, particularly due to the use of hybrid functionals in our DFT calculations, which significantly increases computational costs. From the WFs that expand a group of J bands, a set of Bloch-like states can be constructed as follows:

$$|\psi_{n,\mathbf{k}}\rangle = \sum_{\mathbf{R}} e^{i\mathbf{k}\cdot\mathbf{R}} |\mathbf{R}n\rangle. \quad (2.81)$$

Notice that Eq.(2.81) closely resembles the sum of orbitals in Eq.(2.76) from the TB theory, with the WFs taking the place of atomic orbitals. Consequently, computing the matrix elements of the Hamiltonian with respect to the WFs enables the calculation of the band structure through Fourier transformations. This approach essentially constitutes a Slater-Koster interpolation method, albeit with TB parameters derived from first principles (MARZARI *et al.*, 2012). The procedure to obtain these WFs was discussed in Sec.2.3 and implemented on the Wannier90 package (MOSTOFI *et al.*, 2008; MOSTOFI *et al.*, 2014). More details on how the TB model is obtained is discussed in Appendix B.

2.5 Transport Formalism

2.5.1 Energy, length and time scales

Transport deals with the investigation of charged particle movement, such as electrons or holes, within conductors. Quantum transport is intricately linked to mesoscopic physics, a discipline that gained prominence in the early 1980s. Coined to underscore the significance of intermediate spatial scales (meso) between the micro and macro scales, mesoscopic physics explores a regime where particles exhibit behaviors that transcend the confines of strict quantum or classical physics. Instead, they showcase an interplay between these domains.

The constant miniaturization of electronic components, coupled with advancements in technology, has underscored the critical significance of understanding particle dynamics. In dealing with nanometer-scale device components and entities in motion, it is necessary a careful consideration of length scales, since the particles in motion may be treated as waves. This approach gives prominence to quantum effects, leading to extraordinary phenomena such as the quantization of conductance, the quantum Hall, the Aharonov-Bohm, and Coulomb-blockade effects (IHN, 2009). Moreover, quantum transport is essentially defined by two primary scales: length and energy. The observable domain is intricately influenced by the interaction between these scales and the internal energy parameters of the nanostructure. In 1988, the first experimental observations of the quantization of conductance were verified in point contacts at zero magnetic fields (WEES *et al.*, 1988;

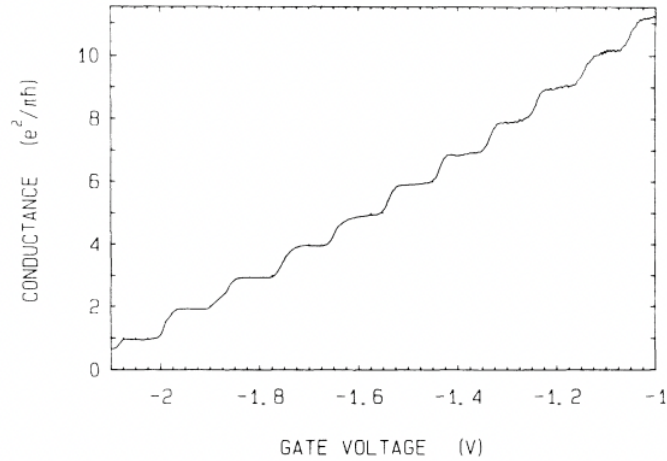


FIGURE 2.2 – Quantum point contact conductance as a function of a gate voltage. The conductance plateaus can be seen, indicating its quantization. Figure adapted from (WEES *et al.*, 1988).

WHARAM *et al.*, 1988). The conductance exhibited distinct plateaus, indicating its quantized nature, as can be seen from Fig.2.2 and showed to have the form

$$G = \frac{2e^2}{h}N, \quad (2.82)$$

where N is an integer number. This implies that the conductance is quantized in unit of twice the conductance quantum

$$G_0 = \frac{e^2}{h} = 3.8740459 \times 10^{-5} \Omega^{-1}. \quad (2.83)$$

As one may remember from basic electromagnetism, the conductance of a certain material is directly proportional to its width and inversely proportional to its length

$$G = \sigma \frac{W}{L}, \quad (2.84)$$

which is valid on the ballistic regime. From this equation, a seemingly intuitive conclusion might suggest that as the sample size diminishes, its conductance approaches infinity. However, this assumption contradicts experimental evidence. It becomes evident that at extremely small sample sizes, quantum mechanical effects significantly contribute to the observed phenomenon of conductance quantization.

To this quantization be observed, certain criteria should be attended: the width of the channel must be comparable to the Fermi wavelength λ_F of the electrons and the temperature must be low compared to the transverse modes in the channel. These criteria give rise to certain regimes of interest:

- If $G \gg G_0$, the electron conductance is easy: many electrons transverse a nanostructure simultaneously and they can do this in many ways, known as transport

channels. In this regime, the scattering approach to electron transport becomes impractical owing to a large number of transport channels resulting in a bigger scattering matrix.

- For $G \ll G_0$, the transport takes place in rare discrete events: electrons tunnel one by one.
- The regions $G \approx G_0$ attract the most experimental interest and are usually difficult to comprehend theoretically.

Here, we encounter our initial examples of energy and length scales that deserve careful consideration in the transport of nanostructures. Other crucial energy scales include thermal energy ($k_B T$), the energy that an electron acquires when traversing a potential difference, the chemical potential (μ), the Fermi energy (E_f), and the Thouless energy, which is a measure of the sensitivity of energy levels to a change in the boundary conditions of the system, (E_T), for instance.

Additional time scales delineating distances where properties, such as electron momentum and the phase of the wave function are subject to randomization through scattering processes are worth noting. One pertinent time scale is the relaxation time (τ), representing the average duration over which the initial momentum of electrons is reversed due to scattering. This time scale is useful in defining the mean free path (ℓ), signifying the average distance electrons traverse before experiencing backscattering. Additionally, the phase relaxation length (ℓ_φ) denotes the average distance electrons diffuse in the material before their phase is disrupted through scattering, incorporating interference effects. Clear observation of interference effects necessitates that this length be comparable to device sizes, often requiring experiments to be conducted at low temperatures (NAZAROV; BLANTER, 2009). The ℓ_φ and ℓ are important scales of the device, where the former sets a limit in which a sample exhibit quantum behavior while the latter defines a ballistic conductor.

Based on the constraints and relations between the length, time, and energy scales, the electronic transport can be investigated in three different regimes:

- Diffusive: the mean free path is much smaller than the sample dimensions and disorder scattering dominates;
- Quasi-ballistic: the mean free path and device size are comparable;
- Ballistic: the conductor contains no impurities and the dominant source of electron scattering is at the device boundaries.

In this thesis, we assume systems that are fully coherent meaning that the phase coherent length is much bigger than other scales and the leads attached to the system, assumed

to be infinite in one direction, are considered ballistic where they are simply regarded as means to inject current into the scattering region.

2.5.2 Current and conductance

When trying to model nanostructures, the task becomes formidable as it involves describing all the subtleties of the sample and accounting for the intrinsic imperfections present in the real-world samples. However, treating a nanostructure as an infinitely long waveguide proves to be a remarkably effective approximation that sidesteps some of the intrinsic complexities. To elaborate on this concept, we initially consider the quantum point contact, a system devoid of potential barriers, and demonstrate its equivalence to a waveguide with a potential barrier (NAZAROV; BLANTER, 2009). Such an example allows us to introduce the concept of modes and momenta.

Considering a waveguide characterized by translational symmetry along the x axis and confinement represented by the potential function

$$V(y, z) = \begin{cases} 0, & |y|, |z| < a/2 \\ \infty, & \text{elsewhere.} \end{cases} \quad (2.85)$$

In this context, the solutions to the Schrödinger equation take the form

$$\psi(x, y, z) = e^{ik_x x} \sum C_{yz} e^{ik_y y} e^{ik_z z}, \quad (2.86)$$

where the wave vectors k_y and k_z are quantized, determining the available transport channels. While the preceding discussion describes the propagation of electrons in a vacuum, electrons within a nanostructure experience the influence of a periodic potential. Despite this, the fundamental description undergoes minimal alteration. The solutions to the Schrödinger equation for such a periodic potential deviate from plane waves and take the form of Bloch waves, as previously explored in subsection 2.1.2.

Moreover, it is important to acknowledge that real-world structures, such as the nanoribbons (NRs) examined in our study, significantly deviate from the idealization of an infinitely long waveguide. Despite this disparity, the simplified model remains invaluable, offering insights that extend to a wide array of nanostructures. Building upon this model, the introduction of a potential along the x axis, typically in the form of a potential barrier, gives rise to transmitted and reflected waves. These confined energy states are commonly known as subbands or transport channels. The incorporation of a potential barrier enhances the basic model, resulting in a configuration frequently encountered in transport measurements—a quantum point contact (QPC). By employing an adiabatic approximation for the system, we can achieve a comprehensive understanding of wave

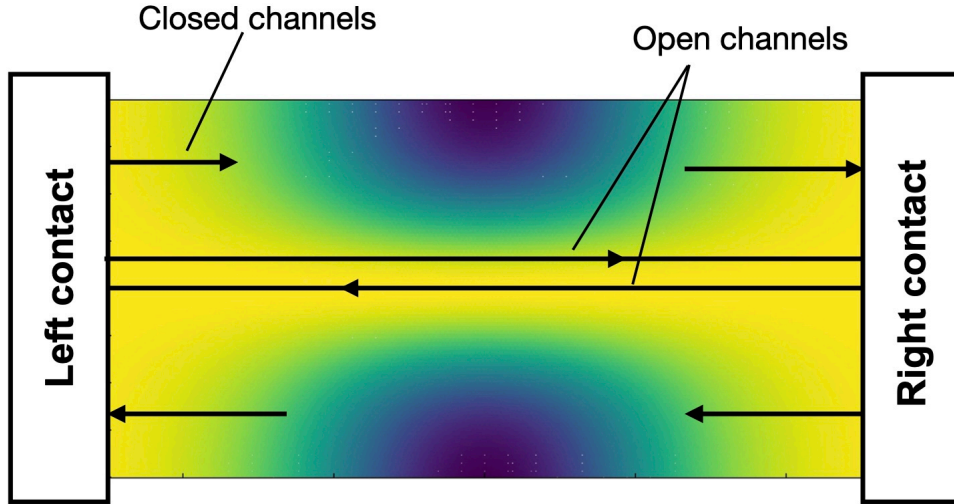


FIGURE 2.3 – Color map of a nanostructure subjected to a gaussian potential on its central region configuring a QPC. Due to the potential, depending of the energy of the modes leaving the contacts, one may obtain an open or a closed channel.

dynamics within such a waveguide (GLAZMAN; JONSON, 1990).

Considering a waveguide extending along the x axis with impenetrable walls in the y and z directions, featuring a variable shape as illustrated in Fig.(2.3). In this scenario, each transport channel is associated with a potential barrier, and depending on the energy of the incoming electron, it can either traverse the barrier or be reflected. Additionally, a finite number of channels are open, while the rest remain closed. For each channel, transmission and reflection amplitudes are defined, ultimately yielding the channel-dependent transmission coefficient $T_n(E)$. This concept forms the essence of quantum transport.

In such a situation, the electric current can be written as

$$I = 2e \sum_n \int \frac{dk_x}{2\pi} v_x(k_x) f_n(k_x), \quad (2.87)$$

where close channels, $f_n(k_x) = f_n(-k_x)$ since the electrons are reflected and there is no net current for these channels. Here n represents the channel index. For open channels, the filling factors are not the same since electrons coming from the left and right reservoirs have different chemical potentials. According to Fig.(2.3), electrons coming from the left have the filling factor given by $f_L(E)$ ($k_x > 0$) and the electrons coming from the right have $f_R(E)$ ($k_x < 0$). Now, since the filling factors depend only on the energy, we may replace the expressions with k for those with E . The velocity can be written as

$$v_n(k_x) = \frac{\hbar k_x}{m} = \frac{1}{\hbar} \frac{\partial E_n(k_x)}{\partial k_x}, \quad (2.88)$$

and we can change the variable of integration writing it in terms of energy, $dk_x = dE \partial k_x / \partial E_n(k_x)$, we obtain

$$\begin{aligned}
I &= \frac{2e}{h} \sum_{n:\text{open}} \int dE [f_L(E) - f_R(E)] \\
&= \frac{2e}{h} N_{\text{open}} (\mu_L - \mu_R),
\end{aligned} \tag{2.89}$$

with μ_L and μ_R being the chemical potential of the left and right contact, respectively. The voltage difference applied, denoted as $eV = \mu_L - \mu_R$, is much less than $k_B T$ (in the linear regime), and it is responsible for the current. Consequently,

$$I = \frac{2e^2}{h} V N_{\text{open}}, \tag{2.90}$$

where the proportionality coefficient is referred to as the conductance quantum. The system's conductance, expressed as the ratio of current (I) to voltage (V), appears quantized in units of $G_0 = \frac{2e^2}{h}$, remarkably different from Ohm's law. This quantity is composed of fundamental constants and remains independent of material properties, nanostructure size, and geometry.

The representation of conductance can be refined as follows:

$$G = \frac{2e^2}{h} M T, \tag{2.91}$$

with M representing the number of available modes, and T being the transmission probability that an electron injected on the left will transmit to the right. This formulation aligns with the Landauer approach (LANDAUER, 1988), wherein the current through a conductor is given in terms of the probability that an electron transmits through it. The Landauer formula captures distinctive characteristics that emerge as device dimensions shrink: the emergence of an interface resistance between the reservoirs and the scattering region, and the departure from the linear decrease in conductance with sample width, as dictated by Ohm's law. Instead, conductance depends on the number of transverse modes in the conductor and changes in discrete steps (DATTA, 1995).

2.5.3 Multiterminal systems

In a more general scenario, a nanostructure is connected to multiple electrodes, some of them being gates and others being terminals. In this context, the linear expansion of the current concerning the applied voltages to the reservoir results in the matrix equation:

$$\begin{pmatrix} I_1 \\ I_2 \\ I_3 \\ \vdots \\ I_n \end{pmatrix} = \begin{pmatrix} G_{11} & G_{12} & G_{13} & \dots & G_{1n} \\ G_{21} & G_{22} & G_{23} & \dots & G_{2n} \\ \vdots & \vdots & \vdots & \ddots & \vdots \\ G_{n1} & G_{n2} & G_{n3} & \dots & G_{nn} \end{pmatrix} \begin{pmatrix} V_1 \\ V_2 \\ V_3 \\ \vdots \\ V_n \end{pmatrix}.$$

Here, the conductance coefficients G_{ij} generalize the conductance G from the two-terminal system. This generalization imposes two crucial constraints:

- Conservation of charge: In a time-independent scenario, the divergence of the current must be zero, implying that the total current entering and leaving the nanostructure must sum up to zero. Consequently, the conductance coefficients in each column of the matrix satisfy the sum rule $\sum_{i=1}^n G_{ij} = 0$.
- Absence of transport currents without voltage differences between contacts: This leads to the second sum rule $\sum_{j=1}^n G_{ij} = 0$ for the rows of the conductance matrix.

From these two sum rules, it can be demonstrated that the stationary current in any nanostructure depends solely on the voltage differences between the contacts.

The extension of conductance to describe nanostructures connected to multiple voltage probes and particle reservoirs was developed by Büttiker (BÜTTIKER, 1988). This framework enables the direct description of multi-terminal phase-coherent conductors in terms of measured currents and voltages, bypassing the need to consider the internal state of the conductor. He extended the two-terminal linear response formula Eq.(2.90) by summing over all terminals, indexed by p and q . The arrows $q \leftarrow p$ simply signify that electron transfer occurs from p to q . Here, \bar{T} represents the product of the number of modes, denoted as M , and the transmission probability per mode, denoted as T , at the Fermi energy

$$\begin{aligned} I_p &= \frac{2e}{h} \sum_q [\bar{T}_{q \leftarrow p} \mu_p - \bar{T}_{p \leftarrow q} \mu_q] \\ &= \sum_q [G_{qp} V_p - G_{pq} V_q], \end{aligned} \tag{2.92}$$

where

$$G_{pq} = \frac{2e^2}{h} \bar{T}_{p \leftarrow q}, \tag{2.93}$$

with the conductance term satisfying the sum rules previously discussed. While this expression can be extended for non-zero temperature situations by linearly expanding the

Fermi distribution, we refrain from exploring this here and reserve it for the subsequent section on the scattering matrix.

It's important to note that this formulation does not hold for non-coherent transport, where the exclusion principle affects the transmission function, rendering this approach invalid. In essence, if the transmission functions exhibit significant variations over the energy range of transport, the applicability of this formalism may be questioned (DATTA, 1995).

2.5.4 Scattering matrix

When the dimensions of the conductor are notably smaller than the phase-relaxation length, the transport is coherent. This coherence allows for the computation of the transmission function through the Schrödinger equation and in this regime, a significant relationship emerges between the transmission function and the scattering matrix (S-matrix) (DATTA, 1995). The S-matrix encapsulates details about electron wave functions far from the structure and the scattering process. It serves as a comprehensive mean of information regarding the transport characteristics, elucidated through a series of transmission eigenvalues derived from itself.

As the flow of particles in nanostructure devices is inherently a quantum mechanical process, it finds a well-suited description within scattering theory. This theory, which specifies an initial state, a scattering region, and a final state, incorporates the entirety of this process through the S-matrix. In this framework, the total conductivity of a system is articulated in terms of the conductor's quantum mechanical transmission, typically represented by the S-matrix, along with the occupation numbers of the exact electronic scattering states (LESOVIK; SADOVSKYY, 2011). Notably, the use of the scattering matrix formalism predates its application in mesoscopic physics; Born, Wheeler, and Heisenberg initially introduced it to elucidate the scattering of particles by atoms (BORN, 1926; WHEELER, 1937; HEISENBERG, 1943), proving to be a valuable tool in various domains.

The pioneering application of scattering formalism in quantum transport is credited to Landauer (LANDAUER, 1988), a framework now commonly referred to as the Landauer-Büttiker formalism. In the context of a two-terminal system, we distinguish between the left and right waveguides using indices L and R , respectively. The coefficient of the plane wave propagating on the ideal wave guide are given by a_{Ln} , a_{Rm} which are the amplitudes of the waves coming from the reservoirs, and b_{Ln} , b_{Rm} are the amplitudes of the waves transmitted through or reflected back from the scattering region for the modes n and m . These coefficients are therefore not independent: the amplitude of the wave reflected from the obstacle linearly depends on the amplitudes of the incoming waves in all the channels

$$\{b\} = [S]\{a\}, \quad (2.94)$$

where the S-matrix has dimensions $(N_L + N_R) \times (N_L + N_R)$, where N_L and N_R are the number of open channels on the right and left leads respectively and $\{a\}$ and $\{b\}$ are column vectors representing the incoming and outgoing wave amplitudes in the different modes in the leads. The S-matrix has the following block structure, in the case of a two-terminal system

$$S = \begin{pmatrix} s_{LL} & s_{RL} \\ s_{RL} & s_{RR} \end{pmatrix} = \begin{pmatrix} r & t' \\ t & r' \end{pmatrix},$$

where r is the reflection matrix for waves coming from the left and r' for the particles coming from the right. The transmission matrix t is responsible for the transmission through the scattering region. The probability of the process of an electron coming in channel n and being reflected in the same lead in channel m is given by the coefficient $|r_{mn}|^2$. The same for the coefficients t_{mn} , which now gives the probability amplitude of being transmitted from channel n to channel m . The scattering matrix has to obey some constraints such as being symmetric concerning time reversal and unitary, to ensure current conservation. This results in $S = S^T$, $t = t^T$, and $S^\dagger S = 1$, which is true for an arbitrary number of leads.

Using the formalism of this section, we can write the current of a two terminal as

$$I = \frac{2e}{h} \int dE \sum_{mn} |t_{mn}(E)|^2 [f_L(E) - f_R(E)] = \frac{2e}{\pi} \int_0^\infty Tr(t^\dagger t) [f_L(E) - f_R(E)], \quad (2.95)$$

where Tr represents the trace of the matrix $t^\dagger t$. For multi-terminal channels, we obtain

$$I_\alpha = -\frac{2G_0}{e} \int_0^\infty dE Tr\{\delta_{\alpha,\beta} - s_{\alpha,\beta}^\dagger s_{\alpha,\beta}\} f_\beta(E) \quad (2.96)$$

where the trace is take over the transport channels and $s_{\alpha,\beta}$ is a block of the S-matrix, which describes the transmission of electrons from terminal β to terminal α or their reflection back to α (NAZAROV; BLANTER, 2009). From this expression, we can extract the matrix elements for the conductance matrix, adopting the linear regime

$$G_{\alpha,\gamma} = 2G_0 Tr\{\delta_{\alpha,\beta} - s_{\alpha,\beta}^\dagger s_{\alpha,\beta}\}, \quad (2.97)$$

which is the generalization of the Landauer formula for the multiterminal case. If we consider a situation of zero temperature and assume that the transmission coefficients $|t_{mn}(E)|$ does not vary for small variations around the Fermi energy, then the current can be expressed as

$$I = \frac{2e^2}{h} V_b \sum_{m,n} |t_{mn}|^2, \quad (2.98)$$

and the conductance

$$G = \frac{2e^2}{h} \text{Tr}(t^\dagger t), \quad (2.99)$$

which was what we obtained previously. This formula gives a relation between a macroscopic quantity (the conductance) and the transmission matrices that are decided from the microscopic model.

2.5.5 Numerical transport calculations - Kwant Software

Solving a scattering problem is present in several branches of physics. Due to the complexity of describing a system with a close geometry such as a ribbon, a quantum dot, or any other shape, one considers the scattering of particles in a finite system couple to infinite leads or contacts. Solving such a problem is much easier and general allowing to obtain the conductance and various other transport properties (GROTH *et al.*, 2014).

The numerical calculations on mesoscopic systems started on early 1980's (LEE; FISHER, 1981; THOULESS; KIRKPATRICK, 1981; MACKINNON, 1985), where the first algorithms were developed, with the most famous ones based on recursive Green's function algorithm however being restricted mainly to one-dimensional geometries or a particular Hamiltonian. In our work, we use the Kwant software which is a Python package for numerical quantum transport calculations. According to the authors, Kwant significantly outperforms the most commonly used recursive Green's function method and avoids usual instabilities occurring in many algorithms. Here we are interested on infinite systems consisting of a finite scattering region where semi-infinite electrodes (leads) are attached. Within the Landauer-Büttiker formalism, these leads acts are waveguides leading to plane waves in and out of the scattering region.

Kwant is based on the wave function formulation of the scattering problem. Without loss of generality, we can consider the case of a scattering region attached to one lead. The ordering of the sites is reversed with the distance to the scattering region, as shown in Fig.(2.4). The Hamiltonian of such a system has a tridiagonal block, as we will discuss now.

In the case of a one dimensional system, a typical real space Hamiltonian is given by

$$H_{1D} = \left(-\frac{\hbar^2}{2m} \nabla^2 + U(x) \right). \quad (2.100)$$

which can be further discretized, using finite difference methods and be written as a

$$\psi_k(x) = \phi_k(x)e^{ikx}, \quad (2.101)$$

and applying this theorem to an eigenvector $\hat{\psi}$ of the discretized infinite lead hamiltonian

$$H_{lead}\hat{\psi} = E\hat{\psi}, \quad (2.102)$$

where

$$\hat{\psi} = \begin{pmatrix} \vdots \\ \psi_{-1} \\ \psi_0 \\ \psi_1 \\ \vdots \end{pmatrix},$$

with ψ_i corresponds to the solution of the i -th unit cell of the lead. Then we have the following matrix equation

$$\begin{bmatrix} \ddots & \ddots & \ddots & & & & \\ & V & H & V^\dagger & & & \\ & & V & H & V^\dagger & & \\ & & & V & H & V^\dagger & \\ & & & \ddots & \ddots & \ddots & \\ & & & & & & \end{bmatrix} \begin{pmatrix} \vdots \\ \psi_{-1} \\ \psi_0 \\ \psi_1 \\ \vdots \end{pmatrix} = E \begin{pmatrix} \vdots \\ \psi_{-1} \\ \psi_0 \\ \psi_1 \\ \vdots \end{pmatrix}.$$

For a arbitrary unit cell of the lead

$$(H - E)\psi_x + V\psi_{x-1} + V^\dagger\psi_{x+1} = 0, \quad (2.103)$$

and since our solutions are of the form Eq.(2.101), where now we consider $\lambda = e^{ik}$, we have

$$(H - E)\phi + V\phi\lambda^{-1} + V^\dagger\phi\lambda = 0, \quad (2.104)$$

which is a quadratic eigenvalue problem. Performing a change of variables, $\xi = \lambda\phi$, we can recast the previous equation into a generalized eigenvalue problem

$$\begin{bmatrix} -V & 0 \\ 0 & 1 \end{bmatrix} \begin{pmatrix} \phi \\ \xi \end{pmatrix} = \lambda \begin{bmatrix} H - E & V^\dagger \\ 1 & 0 \end{bmatrix} \begin{pmatrix} \phi \\ \xi \end{pmatrix}$$

where its solutions can be classified according to the value of $|\lambda|$:

1. Propagating modes: these are solutions such that $|\lambda| = 1$, which consists of outgoing

with positive energy and incoming with negative energy.

2. Evanescent modes: these are solutions with $0 < |\lambda| < 1$ and $|\lambda| > 1$.

The modes are further sorted into incoming ones ϕ_n^{in} , outgoing one ϕ_n^{out} and evanescent ones ϕ_n^{ev} . Now, having a scattering region connected to one or more leads, the total hamiltonian of the nanostructure can be written as

$$H_{tot} = H_{sr} + H_{lead} + V + V^\dagger, \quad (2.105)$$

where H_{sr} is the Hamiltonian of the scattering region, H_{lead} the Hamiltonian of the lead and the connection between the scattering region and the leads is given by V . Then, on matrix form

$$H_{tot} = \begin{bmatrix} H_{sr} & P_{sr}^T V^\dagger & & & \\ V P_{sr} & H & V^\dagger & & \\ & V & H & & \\ & & & \ddots & \ddots & \ddots \end{bmatrix},$$

where P_{sr} is a matrix where its entries satisfy

$$[P_{sr}]_{i,j} = 1 \quad (2.106)$$

if the site i from the lead is connected to the site j of the scattering region and 0 otherwise. Thus, solving the generalized eigenvalue problem for the total Hamiltonian, the eigenstates corresponding to the transverse mode n of a unit cell of the lead has the for,

$$\psi_n(i) = \phi_n^{in} + \sum_m S_{mn} \phi_m^{out}(i) + \sum_p \tilde{S}_{pn} \phi_p^{ev}(i), \quad (2.107)$$

and the scattering wave function inside the system

$$\psi_n(0) = \phi_n^S. \quad (2.108)$$

S_{mn} is the scattering matrix and gives the transmission probability from transverse mode m to transverse mode n as $t_{mn} = |S_{mn}|^2$. From the scattering matrix, the conductance is obtained through the Landauer formula.

2.6 Computational Details

The first principle simulations were done with the Quantum ESPRESSO (QE) package (GIANNOZZI *et al.*, 2009; GIANNOZZI *et al.*, 2017; GIANNOZZI *et al.*, 2020). For the monolayers of TMDs, cutoff energy ranging from 120-160 Ry was used due to the structural and electronic properties of the allotropes considered, and the integrations over the BZ have used a Monkhorst-Pack mesh for k-point sampling (MONKHORST; PACK, 1976). The value used for each material is given on Table (2.1).

TABLE 2.1 – Cutoff energy for the plane wave expansion (Ecut) and the mesh of kpoints (k-mesh) that assures well converged DFT results.

	Ecut (Ry)	k-mesh
HfS ₂ (T)	160	10 × 10 × 1
HfS ₂ (H)	120	10 × 10 × 1
HfSe ₂ (T)	180	12 × 12 × 1
HfSe ₂ (H)	120	10 × 10 × 1
MoS ₂ (T)	160	10 × 10 × 1
MoS ₂ (H)	160	10 × 10 × 1
MoSe ₂ (T)	160	14 × 14 × 1
MoSe ₂ (H)	160	10 × 10 × 1
SnS ₂ (T)	120	10 × 10 × 1
SnS ₂ (H)	120	10 × 10 × 1
SnSe ₂ (T)	140	12 × 12 × 1
SnSe ₂ (H)	120	12 × 12 × 1
WS ₂ (T)	140	10 × 10 × 1
WS ₂ (H)	160	10 × 10 × 1
WSe ₂ (T)	160	14 × 14 × 1
WSe ₂ (H)	120	10 × 10 × 1
ZrS ₂ (T)	120	10 × 10 × 1
ZrS ₂ (H)	120	10 × 10 × 1
ZrSe ₂ (T)	140	12 × 12 × 1
ZrSe ₂ (H)	120	10 × 10 × 1

The atomic positions were relaxed until a convergence threshold of 10^{-5} Ry/Bohr on the forces and 10^{-5} Ry on the energy. The SCF cycle's convergence threshold was 10^{-8} Ry. A vacuum of 30 Å was used to avoid spurious interactions of the periodic images for the monolayers with truncation of the Coulomb interaction perpendicular to the slab (SOHIER *et al.*, 2017).

The wave functions and pseudopotentials are generated within the scalar-relativistic Optimized Norm-Conserving Vanderbilt Pseudopotential (ONCVPSP) code (HAMANN *et al.*, 1979; HAMANN, 2013; HAMANN, 2017) taken from The PseudoDojo project (SETTEN *et al.*, 2018). Exchange and correlation (XC) are described using the Perdew-Burke-Ernzerhof (PBE) (PERDEW *et al.*, 1996; PERDEW *et al.*, 1997).

To describe excited states more accurately, the hybrid functional HSE06 (HEYD *et al.*, 2003; HEYD *et al.*, 2006; KRUKAU *et al.*, 2006) was used. The vdW interaction, where the vdW-DF family was implemented by the Thonhauser group (THONHAUSER *et al.*, 2015; THONHAUSER *et al.*, 2007; LANGRETH *et al.*, 2009), used was vdW-DF-obk8 (KLIMEŠ *et al.*, 2009) because, compared with other interactions implemented on the *ab initio* code, it gave the best results for the structural properties.

The performance of several vdW functionals implemented on QE package is shown in Appendix A. The TB parameters are obtained from the first principles calculations as implemented on the Wannier90 package (MOSTOFI *et al.*, 2008; MOSTOFI *et al.*, 2014). The truncation of the sparse hamiltonian to select the maximum value of the hoppings and how many neighbors will be used on the TB model, the PythTB (<http://www.physics.rutgers.edu/pythtb/index.html>) package was used. The numerical calculations for quantum transport were performed using KWANT software (GROTH *et al.*, 2014).

3 Structural and electronic properties of TMDs

3.1 Motivation

In order to obtain vdW qubits, we initially investigate the properties of the individual layers that comprise the heterostructures. To this end, *ab initio* calculations were performed to obtain the lattice parameters following a precise methodology, considering a well-converged k-point sampling and cutoff energy with the same treatment for the XC functional. These systematic calculations are important since the electronic properties of the crystals are influenced by strain, which may cause a transition from direct (indirect) to indirect (direct) band gaps and even yield a transition to a metallic behavior (YUN *et al.*, 2012; WU *et al.*, 2017), among other effects. After obtaining structural parameters, the electronic properties were investigated using the HSE06 XC functional to correct the band gaps and, consequently, the energy levels, which are of fundamental importance in obtaining the vdW qubits.

3.2 Structural properties

Here, the focus is obtaining the lattice parameter of TMDs, which will be further combined, forming the vdW heterostructures.

TMDs are compounds with the form X-M-X, where X is a chalcogen and M is a metal connected by covalent bonds and displaying hexagonal symmetry. Two typical structural phases are the 2H (trigonal prismatic) and 1T (octahedral) phases, belonging to the D_{3h} and D_{3d} point groups, respectively. The 2H phase has chalcogen atoms located on top of each other in the perpendicular direction of the layer, while the 1T phase has the chalcogen atoms rotated by an angle of 180 degrees to the metal.

Although TMDs are typically semiconducting, some phases are inherently metastable and can exhibit metallic behavior. This work explores both stable and metastable phases

concerning phase stability discussed in the work of Zhuang *et al.* (ZHUANG; HENNIG, 2013). Phase engineering is performed experimentally to assemble metastable phases, as discussed in (KAN *et al.*, 2014; GAN *et al.*, 2018; QIAN *et al.*, 2020). In addition, the stability and degradation of TMDs in various conditions have been investigated, and methods have been proposed to preserve their structural and electronic properties. These methods include stabilization via more precise experimental methods, using dopants or solvents combined with exfoliation assembly, as discussed in (ZHUANG; HENNIG, 2013; ZHANG *et al.*, 2019; SAHA; MAHAPATRA, 2016; GAO *et al.*, 2015; GAO *et al.*, 2016; MIRABELLI *et al.*, 2016; BOIX-CONSTANT *et al.*, 2021; ZHAO *et al.*, 2014; HEISING; KANATZIDIS, 1999). It is important to note that some TMDs, such as MoS₂ and WS₂, are less reactive with oxygen, while others require the control of surrounding gases (LONGO *et al.*, 2017).

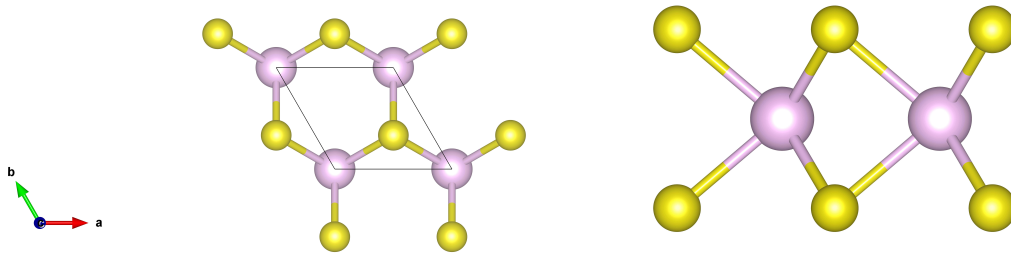


FIGURE 3.1 – Top and side view of MoS₂ allotrope H.

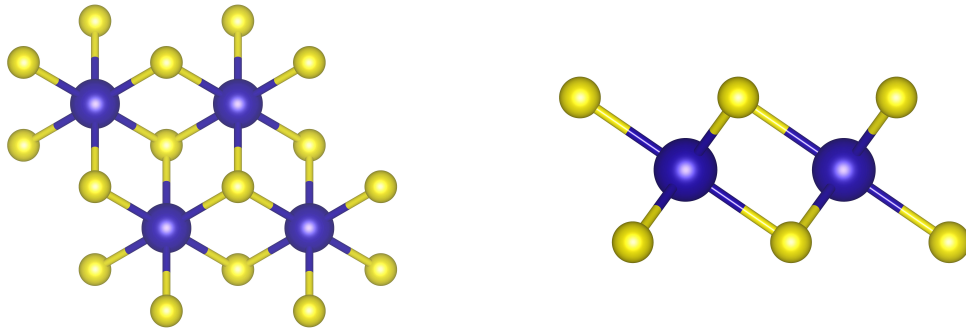


FIGURE 3.2 – Top and side view of HfS₂ allotrope T.

In this study, the structural and electronic properties of 20 phases of 10 TMDs were investigated to obtain the necessary data for forming heterostructures and analyzing their energy alignments. To ensure accurate results, all unit cells were relaxed using a convergence criteria of 10^{-5} Ry/Bohr for forces and 10^{-5} Ry for energy. To avoid spurious interactions with periodic images, a vacuum of 15 Å in the out-of-plane direction was used. The vdW correction vdW-DF-obk8 was chosen for its precision in obtaining structural parameters, following a benchmark with several functionals implemented in the QE package (see Appendix A for details). The lattice parameters (a) and the bond length

between metal (M) and chalcogen (X) (d_{MX}) for each of the 2D materials are presented in Table 3.1.

TABLE 3.1 – Structural properties of TMDs. Cell parameter a and distance metal chalcogen d_{MX} were calculated using vdW-DF-obk8 functional. The experimental values were taken from [1],[2] and are in good agreement with *ab initio* calculations (SAHA *et al.*, 2020). The distance M-X is in excellent agreement with [3] and [4], in which the values are given between parentheses. The allotrope marked with * is to identify the most stable phase.

	a (Å)	a_{exp} (Å)	d_{MX} (Å)
HfS ₂ * (T)	3.649	3.635 ^[1]	2.56 (2.55 ^[4])
HfS ₂ (H)	3.540	3.37 ^[2]	2.58
HfSe ₂ * (T)	3.774	3.748 ^[1]	2.69 (2.67 ^[4])
HfSe ₂ (H)	3.68	3.44 ^[2]	2.71
MoS ₂ (T)	3.19	3.15 ^{[6]†}	2.43
MoS ₂ * (H)	3.185	3.162 ^[1]	2.41 (2.41 ^[3])
MoSe ₂ (T)	3.29	-	2.56
MoSe ₂ * (H)	3.322	3.289 ^[1]	2.54 (2.54 ^[3])
SnS ₂ * (T)	3.705	3.648 ^[2]	2.60 (2.59 ^[4])
SnS ₂ (H)	3.62	3.647 ^[5]	2.64
SnSe ₂ * (T)	3.872	3.811 ^[2]	2.75 (2.73 ^[4])
SnSe ₂ (H)	3.80	3.811 ^[5]	2.79
WS ₂ (T)	3.21	-	2.43
WS ₂ * (H)	3.187	3.153 ^[1]	2.42 (2.42 ^[3])
WSe ₂ (T)	3.29	-	2.57
WSe ₂ * (H)	3.321	3.282 ^[1]	2.55 (2.55 ^[3])
ZrS ₂ * (T)	3.685	3.662 ^[1]	2.57 (2.57 ^[3])
ZrS ₂ (H)	3.57	-	2.59
ZrSe ₂ * (T)	3.800	3.700 ^[1]	2.70 (2.71 ^[3])
ZrSe ₂ (H)	3.71	-	2.73

References: [1](BJÖRKMAN, 2014), [2](BASTOS *et al.*, 2019), [3](ZHUANG; HENNIG, 2013), [4](KODA *et al.*, 2016), [5](OSZ; SALJE, 1989),[6] (GAO *et al.*, 2022), [7](QU *et al.*, 2016). † Since it is an unstable phase of MoS₂, the distance between the two neighbors Mo atoms was slightly different, so to compare with the *ab initio* result, it was taken the mean value of those distances.

The experimental data were not found for the missing values on the table.

Experimental assembly of layered materials, including the more stable phases of TMDs, has been accomplished through various techniques. For instance, ZrS₂ and ZrSe₂, which have an octahedral (1T) symmetry (CdI₂-like) structure, can be obtained through halogen vapor transport techniques, whereas HfS₂ and HfSe₂ can be acquired through iodine vapor transport (RIMMINGTON; BALCHIN, 1974; WHITEHOUSE *et al.*, 1973). SnS₂ crystals were grown by a stoichiometric composition technique at a constant temperature, and their

structural properties were confirmed through X-ray analysis (TRIFONOVA *et al.*, 1996). SnSe₂ crystals can be obtained by unidirectional solidification in an Sn-saturated environment with a temperature gradient (ALBERS; VERBERKT, 1970). For crystals with trigonal prismatic symmetry (2H) as the most stable phase, chemical vapor transport is used to obtain MoS₂, MoSe₂, WS₂, and WSe₂, and their structural arrangement is characterized through X-ray diffraction analysis (LUCOVSKY *et al.*, 1973).

Phase engineering methods have enabled the experimental growth of TMDs that do not occur through conventional procedures. For example, MoS₂ can be obtained in its 1T phase using ion intercalation techniques, where the phase transition to octahedral occurs due to significant charge transfer from the ion (PY; HAERING, 1983). Additionally, substitutional doping of rhenium in WS₂ nanotubes can form the 1T phase, with the Re impurity atoms serving as electron donors (ENYASHIN *et al.*, 2011). Similarly, lithium insertion has been shown to induce the formation of 1T MoS₂ and WS₂ (KAN *et al.*, 2014). Combining ball milling and chemical lithium intercalation can also result in the formation of high percentages of 1T WS₂ and MoSe₂ from their 2H phase, resulting in single-layer TMD nanodots (TAN *et al.*, 2018). Likewise, different growing conditions have been shown to lead to the formation of 2H phases of SnS₂ and SnSe₂ (OSZ; SALJE, 1989).

First principles calculations also allow the simulation of phase transitions between allotropic forms under various conditions, guiding experimentalists on paths to obtain such materials under favorable conditions. For example, hydrogenation can induce a phase transition (H to T and vice versa) for HfS₂, HfSe₂, WSe₂, ZrS₂, and ZrSe₂, resulting in the interplay between metallic and semiconductor behavior depending on the layer's side exposed to the process (QU *et al.*, 2016). Layered 1H SnS₂ can be obtained by *in situ* heating and electron beam radiation, with the growth of each phase being controllable by tuning experimental parameters (XIE *et al.*, 2020). Similarly, 2H SnSe₂ can be assembled using the Bridgman-grown method (BERTRAND *et al.*, 1984).

3.3 Electronic properties

Going beyond the structural properties, the electronic properties are investigated, such as band structures, band gaps, and energy levels with respect to the vacuum level of the previous monolayers. These energies, and consequently the band gap, are obtained, including quasi-particle correction of HSE06 that, even sub-estimating those obtained from GW calculations (RASMUSSEN; THYGESEN, 2015; GRUMET *et al.*, 2018), still gives a good approximation with a much lower computational cost. As implemented on the QE package, the energies are obtained with respect to the vacuum level using the truncation of the long-range Coulomb potential (SOHIER *et al.*, 2017). The valence band maximum

(VBM), conduction band minimum (CBM), and band gaps (E_g) are given in Table 3.2. They have been performed for the primitive unit cell of the materials presented. Fig.(3.3) displays a more didactic view of the energy levels. No spin-orbit is considered here.

The values of VBM and CBM will be fundamental when combining individual layers because the degree of alignment of these energies will dictate the combination to be performed. The ionization energy (I) is related to VBM by $VBM = -I$ and the electron affinity (A) is related to CBM by $CBM = -A$. The quasi-particle band gap is related to these quantities by

$$E_g = I - A. \quad (3.1)$$

TABLE 3.2 – Electronic properties of monolayers TMDs. The band gap (E_g), VBM, and CBM with respect to the vacuum level obtained with hybrid exchange-correlation functional HSE06.

	E_g (eV)	VBM (eV)	CBM (eV)
HfS ₂ * (T)	2.19	-7.08	-4.89
HfS ₂ (H)	1.97	-7.67	-5.70
HfSe ₂ * (T)	1.53	-6.37	-4.84
HfSe ₂ (H)	1.74	-7.19	-5.45
MoS ₂ (T)	metal	metal	metal
MoS ₂ * (H)	2.35	-6.45	-4.10
MoSe ₂ (T)	metal	metal	metal
MoSe ₂ * (H)	1.89	-5.89	-4.00
SnS ₂ * (T)	2.24	-7.40	-5.15
SnS ₂ (H)	1.38	-6.96	-5.57
SnSe ₂ * (T)	1.40	-6.72	-5.31
SnSe ₂ (H)	0.58	-6.28	-5.70
WS ₂ (T)	metal	metal	metal
WS ₂ * (H)	2.49	-6.20	-3.71
WSe ₂ (T)	metal	metal	metal
WSe ₂ * (H)	2.01	-5.63	-3.60
ZrS ₂ * (T)	2.07	-7.11	-5.04
ZrS ₂ (H)	1.81	-7.58	-5.77
ZrSe ₂ * (T)	1.30	-6.39	-5.09
ZrSe ₂ (H)	1.60	-7.13	-5.52

Another critical quantity defined here is the natural band offset between the layers. This quantity is obtained as the difference between the values of I and A in the following way

$$\begin{aligned} \Delta E_v &= I(1) - I(2), \\ \Delta E_c &= A(2) - A(1). \end{aligned} \quad (3.2)$$

where ΔE_v (ΔE_c) is the offset on the valence (conduction), and the indices 1 (2) represent the layers that will compose the heterojunction. Fig.(3.3) presents the energy levels with respect to the vacuum level of the monolayers, and the offsets will be computed from Eq.(3.2) using these values.

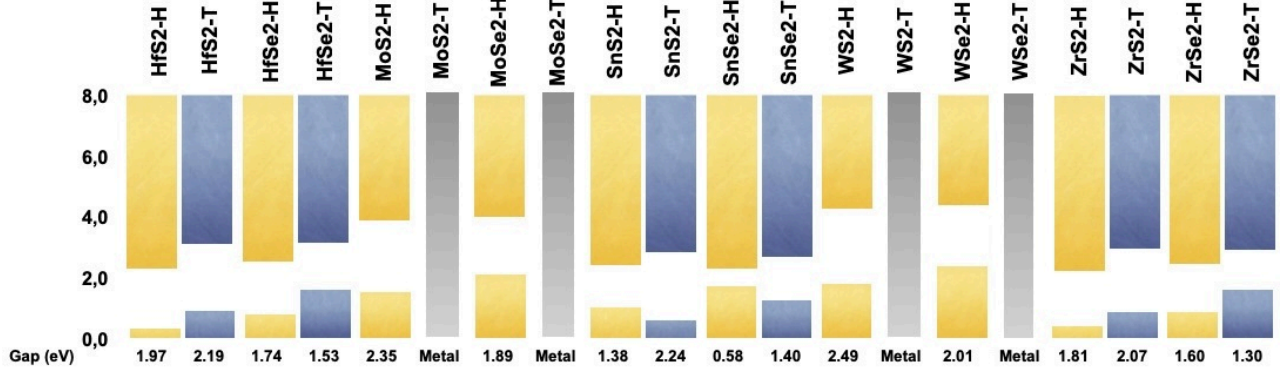


FIGURE 3.3 – Energy levels and band gaps of monolayers considering quasi-particle effects. The bar edges represent the valence band maximum and the conduction band minimum for each material. All energies are in eV and with the vacuum as reference.

A trend can be observed concerning band gaps when considering materials in the same phase, either 2H or 1T, and changing the chalcogen from S to Se. In general, the band gap becomes smaller, except for the case of 1T MoS₂ - MoSe₂, where the compound remains metallic.

Once the band offsets are determined, they fall into three categories: type I, II, and III (broken gap). Each type is well suited for specific technological applications. Heterostructures of type I possess electrons and holes on the same layer, making them excellent candidates for use in optical devices. In type II, electrons and holes are located in different layers, resulting in carrier confinement, which is useful for high-mobility electron mobility transistors. Type III is a broken gap situation, in which materials falling into this category are well suited for Tunneling Field Effect Transistors (TFETs) applications (ÖZÇELİK *et al.*, 2016). A schematic view of these types of band alignments is shown in Fig.(3.4).

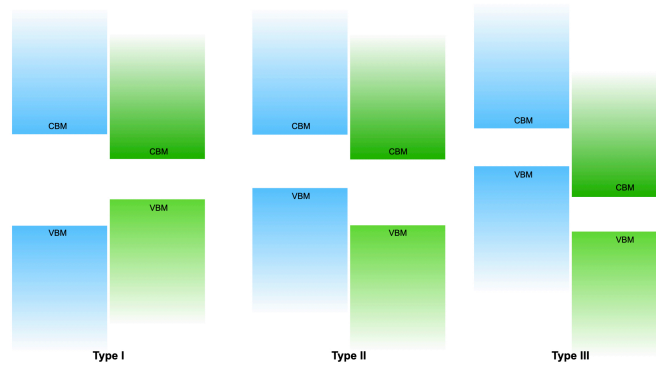


FIGURE 3.4 – Types of band alignment. Type I (electrons and holes are on the same layer), the VBM and CBM are on the same material. Type II (electrons and holes in different layers), where the VBM and CMB are on different materials, or type III, which is a broken gap situation (ÖZÇELİK *et al.*, 2016).

It is important to emphasize the significance of quasi-particle corrections on the band structure of materials. Since DFT tends to underestimate the band gap, it directly impacts energy levels. Therefore, materials that display energy level alignment when quasi-particle effects are considered may not exhibit this characteristic if only a pure DFT calculation is performed.

It's worth noting that all current calculations are based on the unit cell of layered TMDS, which comprises of three atoms: a metal and two chalcogens.

3.4 Criteria on forming vdW heterostructures

TMDS' multitude of properties renders them increasingly prevalent in contemporary components. For instance, SnS₂ exhibits favorable electronic properties, making it a promising candidate for high-performance photodetectors. Additionally, its abundance simplifies experimental synthesis. Furthermore, this material demonstrates n-type transistor behavior, as reported in (HUANG *et al.*, 2014). The deposition of HfO₂ onto MoS₂ results in a transistor with high current on/off at room temperature, low power dissipation, and significant carrier mobility, making it an attractive material for constructing Field Effect Transistors (FETs) and other electronic components (RADISAVLJEVIC *et al.*, 2011). Recent studies have shown that FETs using solid electrolytes as substrates can achieve high current densities (ALAM *et al.*, 2021). In addition, MoS₂ exhibits piezoelectric properties, allowing electricity conversion into mechanical force and vice versa, making it useful for logic components. The angular dependence of this property can also be advantageous for valleytronic devices (ZHU *et al.*, 2015; WU *et al.*, 2014). Furthermore, TMDS such as MoS₂ have been employed in energy storage for coin-cell devices (BISSETT *et al.*, 2016).

With all the data obtained and the relevant quantities defined, presented in Tables 3.1

and 3.2, one can combine the thin layered materials forming heterostructures to obtain the desired property of hybridized states on the band structure. The alignment of the energy levels is the first property explored to combine pairs of materials to this end.

The band offsets will help predict the type of band alignment of the heterostructure, categorizing the material in a specific class well suited for some technological application. This quantity is also essential in estimating the strength of the electric field to control the level of hybridization of states on the heterostructure. Since a certain distance d separates the layers, the electric field given by $E = V/d$, with V being the gate potential, the offset's values will indicate the field's strength to change the alignment. This electric control of hybridized states would be used in controlling the charge contribution of each layer for the qubit, as will be discussed in the next chapter.

A class of host material was already proposed (LUCATTO *et al.*, 2019). Here, this class is enlarged, giving more experimental routes for obtaining host platforms for the vdW qubits, which can be helpful for industry purposes in assembling such materials, choosing those that are economically viable, easier to obtain, and environmentally friendly. The newfound combinations are presented in Appendix.C. Here we are going to explore just a small set of them.

4 vdW Heterostructures of TMDs

4.1 Motivation

After obtaining structural parameters and energy levels listed in Tables 3.1 and 3.2, it is crucial to calculate the band offsets, which play a crucial role in determining quantum confinement, dopability, and chemical activity. By analyzing the energy levels, it is possible to identify combinations of monolayers with good band alignment that can achieve the desired hybridization of the heterojunction band structure. This process is essential for designing efficient and effective heterojunction devices.

Experimental techniques have enabled the production of high-quality vdW materials, creating heterostructures with an atomic thickness suitable for electronic components (SONG *et al.*, 2022). These vdW materials have demonstrated their effectiveness as p-n junctions, resulting in high-performance electronic components (LEE *et al.*, 2014) such as transistors (ZHANG, 2019), digital logic devices (YIN *et al.*, 2021), and in-memory computing systems (LI *et al.*, 2022). For instance, MoSe₂/WSe₂ and WSe₂/SnSe₂ (YANG *et al.*, 2017) have shown to be effective p-n junctions, enabling their integration into FETs with low current leakage. Furthermore, SnSe₂/WSe₂, grown using molecular beam epitaxy, can function as a tunneling field-effect device (TFET) (ARETOULI *et al.*, 2016). Meanwhile, MoSe₂/ZrSe₂ can also be used as a TFET with its band alignments modulated by gate bias.

vdW heterostructures exhibit rich physics, and their properties can be modulated by external means. *Ab initio* simulations have shown that the band gap of these materials can be reduced by vertical compressive strain, resulting in a semiconductor-metal transition and offering the possibility of using them in technological applications (BHATTACHARYYA; SINGH, 2012). In addition, perpendicular electric fields can tune the electronic band structure, with large electric fields achievable through ionic gated transistors, allowing electric fields on the order of 3-4 V/Å (DOMARETSKIY *et al.*, 2022; WEINTRUB *et al.*, 2022), where it was demonstrated that the band gap of WSe₂ can be reversibly closed by applying an electric field perpendicularly to the layer (DOMARETSKIY *et al.*, 2022). While there are several other ways of changing the electronic properties of vdW heterostructures,

this work focuses on applying an electric field perpendicularly to the heterostructure.

The structural parameters previously determined were utilized to construct unit cells. In certain instances, these unit cells were nearly commensurate, facilitating the creation of a unified unit cell through minor stress applied to both layers, simplifying stacking and the heterojunction formation. Subsequently, the relaxed heterostructures were evaluated to ascertain the minimum interlayer distance and total energy. The convergence criteria for the heterostructures are similar those applied to the monolayers, with the exception of incorporating a 30 Å vacuum in the stacking direction during the *ab initio* calculations to prevent interactions between periodic images.

Moreover, to control the properties of hybridized states via an electric field and consequently control the vdW qubit, with DFT calculations using hybrid XC functional, such as HSE06, makes the computational cost of the simulations huge, even with relatively simple systems. This is where the TB approach becomes advantageous. Our simplified model is free of empirical parameters, fitting, or Machine Learning techniques. Instead, it is constructed from Bloch wave functions derived from *ab initio* calculations and transformed into MLWFs. The resulting sparse Hamiltonian is truncated, considering only specific hoppings, typically up to first and second neighbor interactions without losing the accuracy when compared against *ab initio* results.

4.2 ZrSe₂/SnSe₂ heterostructure

To evaluate the methodology proposed in this study, we compared our results with those from a previous investigation on the ZrSe₂/SnSe₂ heterojunction (LUCATTO *et al.*, 2019). In that study, DFT calculations were performed using the VASP (KRESSE; FURTHMÜLLER, 1996) software, with the wave functions and pseudopotentials generated using the PAW method (KRESSE; JOUBERT, 1999). The van der Waals interactions were described using the optB86b (KLIMEŠ *et al.*, 2011) functional, with a mesh of 11 × 11 × 1 Γ-centered. Excitation energies were also corrected using the same hybrid functional used in this study.

Our investigation aimed to determine whether perturbing the onsite energies in the TB model with an electric field could achieve the same degree of hybridization control as in DFT calculations. The heterostructure, which includes stacking different layers of TMDs on top of each other, is depicted in Fig.(4.1). Additionally, we provide the interlayer distance for reference.

Table 3.2 presents the electronic properties of ZrSe₂ (BL) and SnSe₂ (TL). By examining the energy levels depicted in Fig.(3.3), we observe that these two materials exhibit a type II band alignment. BL and TL denote the bottom and top layers, respectively. The

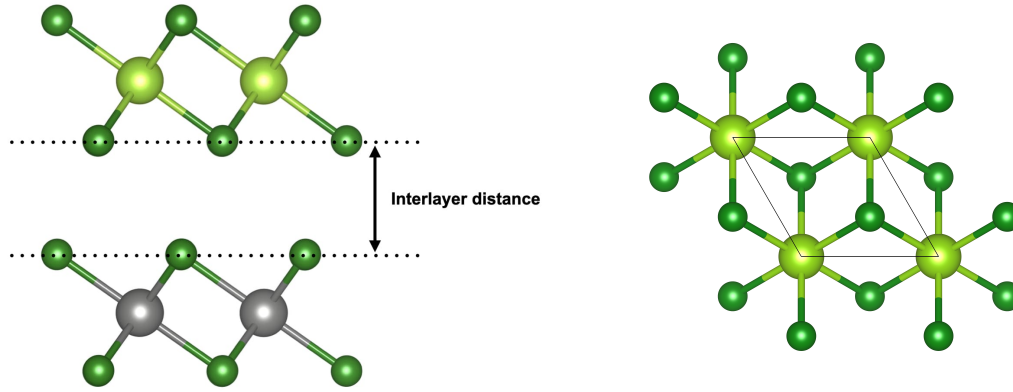


FIGURE 4.1 – Side view (a) and top view (b) of the heterostructure. Light green is the Thin atoms, dark green Selenium, and grey Zirconium atoms.

band offsets can be obtained using Eq.(3.2),

$$\begin{aligned}\Delta E_v &= -0.328 \text{ eV} \\ \Delta E_c &= 0.227 \text{ eV.}\end{aligned}\tag{4.1}$$

The slight offsets of the layers hint at a possible hybridization presented in the band structure of the heterojunction. The energy levels involved in this system are summarized in Table 4.1.

TABLE 4.1 – Summary of the energy levels (DFT) of freestanding monolayers and the heterojunction. All values are in eV.

ZrSe ₂		SnSe ₂		ZrSe ₂ /SnSe ₂	
I	A	I	A	VBM	CBM
7.110	5.043	6.719	5.317	-6.521	-5.283

Concerning the structural properties, the isolated layers present a good lattice match with ZrSe₂ having a lattice parameter of 3.80 Å and SnSe₂ 3.87 Å. Combining these materials in a heterostructure, minor stress is applied on the monolayers, tensile on ZrSe₂ and compressive on SnSe₂, resulting in a heterostructure with a lattice constant of 3.83 Å which corresponds to a relative stress of 0.9% on each layer. After the relaxation procedure, the interlayer distance is 3.04 Å. Looking at the DFT band structure in Fig.(4.2), without HSE06 correction, it is possible to verify a strong hybridization on the two lowest conduction bands at *M* indicating a strong charge superposition between the layers and from the point *G* to point *M* and from *M* to *K* one can verify the orbital character transition where the charge contribution alternate between the TL and the BL.

The two lowest conduction bands will be interpreted as the two-level system for the charge qubit and will be represented by $|0\rangle$ and $|1\rangle$ as depicted in Fig.(4.3). The orbital

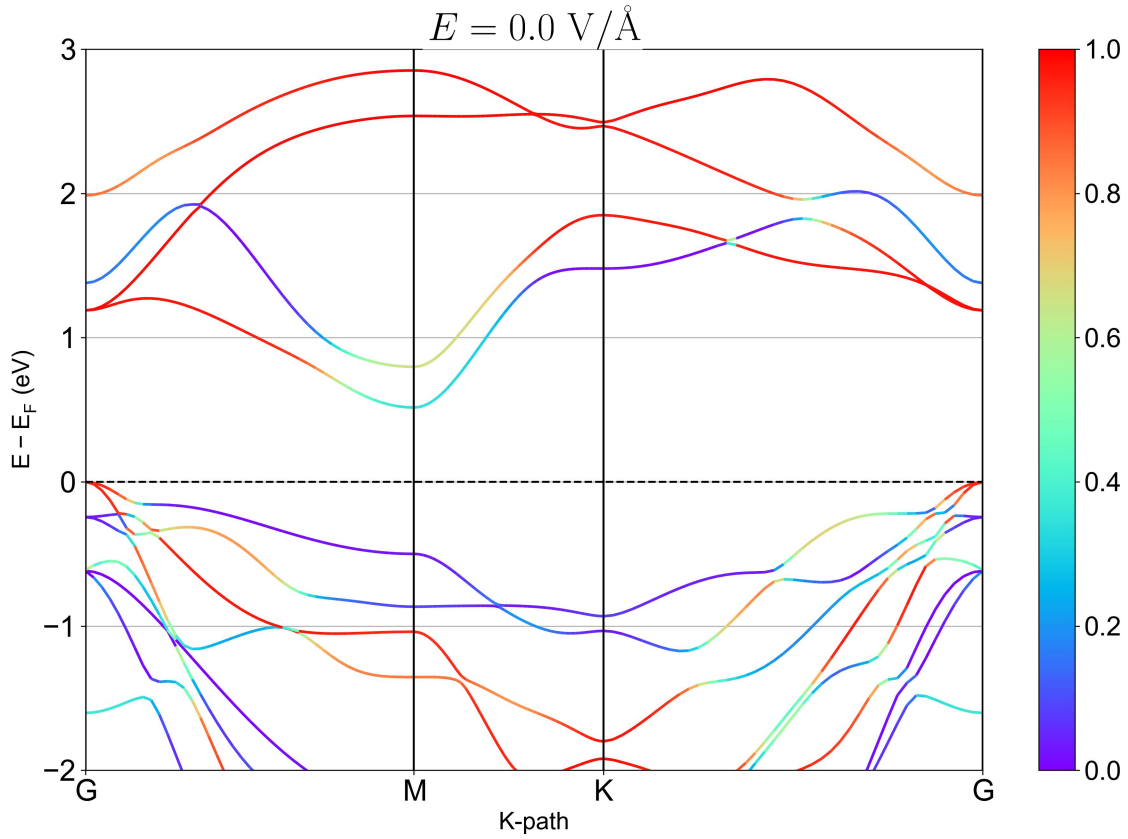


FIGURE 4.2 – $\text{ZrSe}_2/\text{SnSe}_2$ DFT band structure without electric field applied. A strong hybridization at the M point is present.

contribution of each layer at M point of the first (second) lowest conduction bands are 34% (65%) coming from the ZrSe_2 layer and 66% (35%) from the SnSe_2 in the case where there is no electric field applied which indicates that the $|0\rangle$ and $|1\rangle$ states have a nearly equal contribution of each layer. Since this contribution from the layers changes with the electric field applied, an electron occupying a superposition of these two states configures a charge qubit (vdW qubit) on the heterostructure due to hybridization.

Once the electric field is applied, the states $|0\rangle$ and $|1\rangle$, which before were a mixture of states of different layers, possess a strong character coming from one of them, depending on its applied direction. A generic quantum state of the vdW qubit can be written as a superposition

$$|\psi\rangle = c_A |A\rangle + c_B |B\rangle, \quad (4.2)$$

where the complex coefficients c_i are a function of the electric field respecting the orthonormality condition and $|A\rangle(|B\rangle)$ represents the BL (TL), respectively.

Applying an electric field in the stacking direction, it is clear that the control of the hybridization occurs. For negative fields, the $|0\rangle$ is mainly composed of states coming from

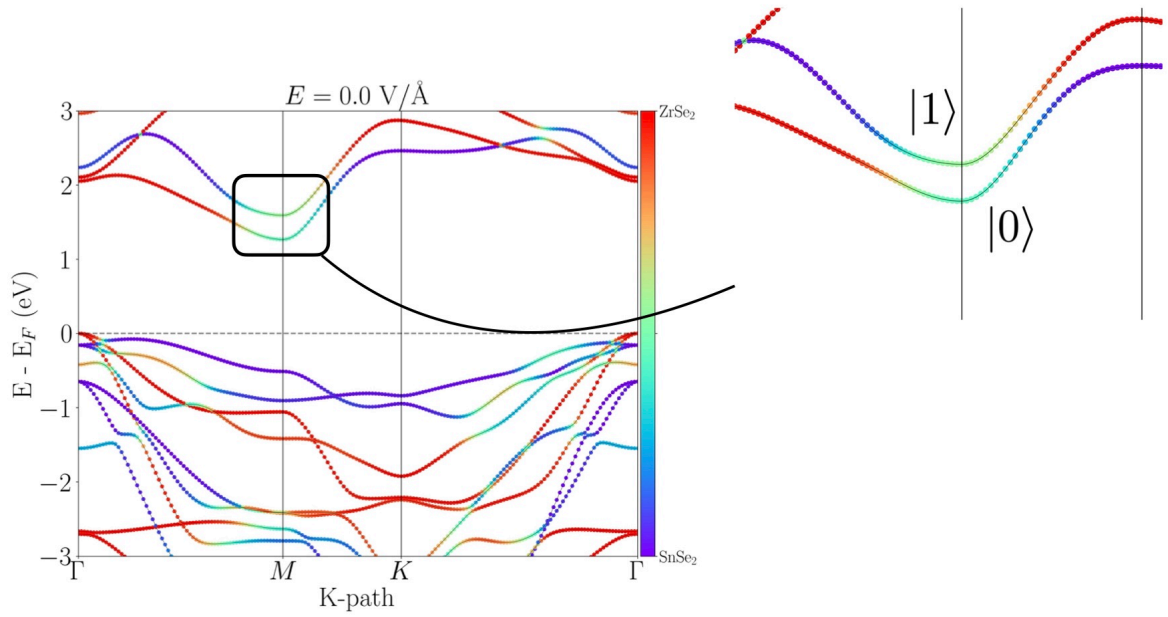


FIGURE 4.3 – The correspondence of the two lowest conduction bands as a two-level system for a charge qubit.

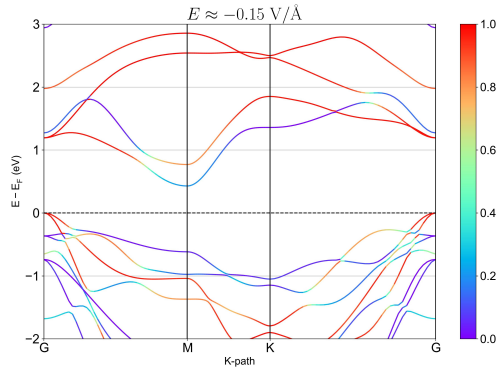
the SnSe₂ layer, as seen in Fig.(4.4a) from the coloring blue in the first lowest conduction band and the state $|1\rangle$ composed of states coming from the ZrSe₂ layer. The opposite occurs for positive fields.

As a first observation of this orbital change on the conduction bands, here we show in Fig.(4.5), for the state $|0\rangle$, how it changes with the intensity and direction in which the electric field is applied obtained by a DFT calculation.

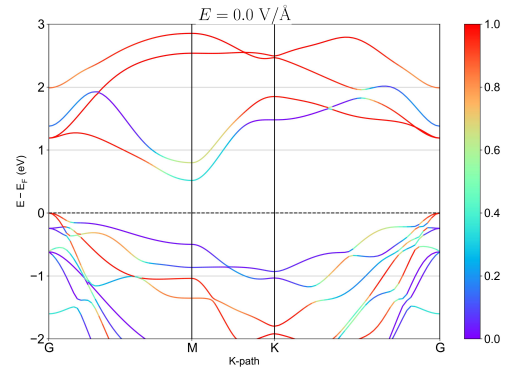
At a field of $0.125 \text{ V}/\text{\AA}$, the layers' contribution is equal for $|0\rangle$. For negative fields, the predominance is for state coming from the top layer, and for positive fields, the bottom layer. The change of the orbital character of state $|1\rangle$ is very similar due to the complementary of the levels and the normalization condition of the coefficients on Eq.(4.2). For this reason, it is not shown here.

To simplify the model and investigate whether the same hybridization control occurs on the two lowest conduction bands, we performed Wannierization to obtain an *ab initio* Tight-Binding Hamiltonian (TBH) from the Bloch wave functions. Based on an orbital character analysis, we considered the d_{xy} , d_{z^2} , and $d_{x^2-y^2}$ orbitals of Zirconium and p orbitals of Selenium, resulting in a TB model of 15 bands. The k-resolved elements' orbital contribution is shown in Fig.(4.6), which justifies their use as an initial guess for the Wannierization procedure.

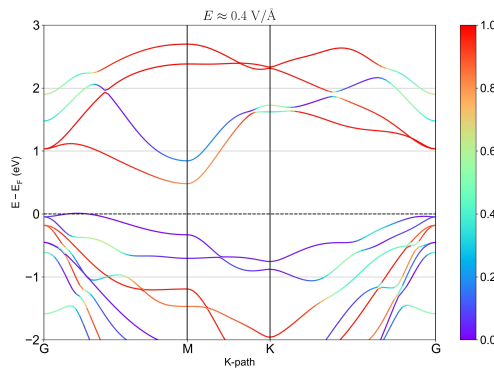
Given the initial projections for obtaining the TB model, the next step is to determine an energy window encompassing the bands around the Fermi energy, which their properties must be preserved. More details for the step-by-step of Wannierization are given in



(a) $\text{ZrSe}_2/\text{SnSe}_2$ with and electric field of $E \approx -0.15 \text{ V/\AA}$ on the stacking direction.



(b) $\text{ZrSe}_2/\text{SnSe}_2$ without electric field applied.



(c) $\text{ZrSe}_2/\text{SnSe}_2$ with and electric field of $E \approx 0.4 \text{ V/\AA}$ on the stacking direction

FIGURE 4.4 – $\text{ZrSe}_2/\text{SnSe}_2$ band structure subjected to different electric fields.

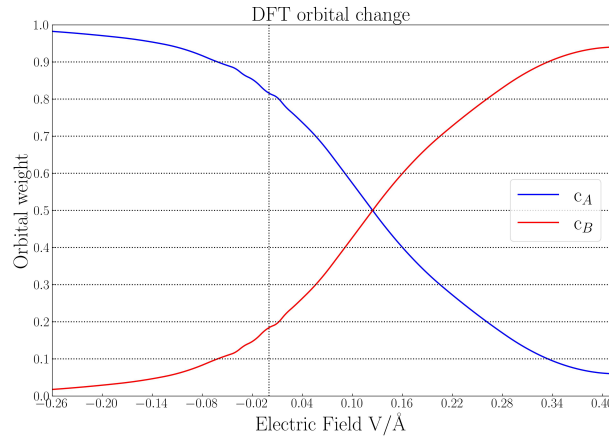
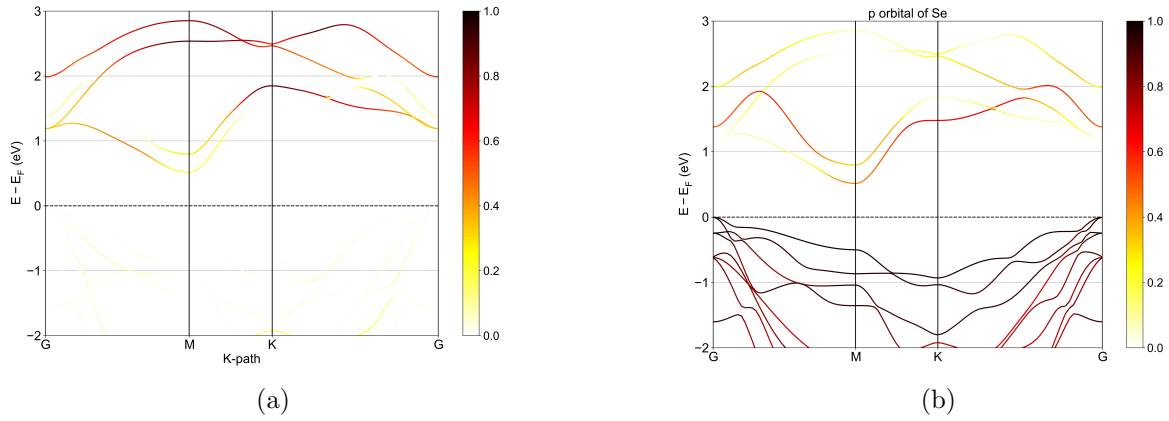
Appendix B. After minimizing the spread functional of the WFs, the basis of MLWF is obtained. Their final spreads measured by the functional Eq.(2.56) are given in Table 4.2.

TABLE 4.2 – Ω^2 of the WFs after the minimization procedure. The first line on the information about the spreads of p orbitals is for those connected with Zr, and the line below is for those bonded with Sn.

Element	Zirconium			Selenium		
orbital	dz^2	$d_{x^2-y^2}$	d_{xy}	p_z	p_x	p_y
$\Omega^2 (\text{\AA}^2)$	2.28	2.34	2.36	2.52/2.44	2.52/2.44	2.52/2.44
				3.67/3.74	3.67/3.74	3.67/3.74

As one may note from the spreads, the WFs are well localized around the atoms, resulting in MLWFs. The band structures obtained from the Wannierization are shown in Fig.(4.7), where it is possible to analyze the accuracy that the TB model gives. The result of the orbital control on the TB model is shown in Fig.(4.8). Here, the calculations were performed still without HSE06 correction.

From Fig.(4.7), one can verify that similar control of the hybridization occurs in this

FIGURE 4.5 – Orbital change for the state $|0\rangle$ obtained from a DFT calculation.FIGURE 4.6 – Orbital resolved band structure of $\text{ZrSe}_2/\text{SnSe}_2$ used to provide an initial guess to obtain the MLWFs. (a) Projected band structure showing the orbital contribution of the $d_{xy} + d_{z^2} + d_{x^2-y^2}$ orbitals of Zirconium. (b) Projected band structure showing the orbital contribution of the p orbital of Selenium.

simplified model. However, one may note two different features that differentiate the simplified model, where the electric field is considered approximately acting as a first-order perturbation on the onsite energies with hoppings kept fixed from the DFT calculation where the electric field is considered exactly: (i) To concentrate 90% of the charge in one of the layers on the DFT approach it is necessary an electric field of around 0.34 V/\AA where it is needed 0.09 V/\AA in the TB model, which is four times smaller. This implies that in the TB model, the control of the charge character is accomplished with shorter field pulses; (ii) the field where the charge is equally distributed between the layers is different in the two approaches - in the TB model, this is obtained at a field of 0.012 V/\AA while on the DFT is around 0.125 V/\AA .

However, since the quasi-particle effects are essential for the band alignments, a TB model was obtained considering such effects. In the same way, a Wannierization considering the same previous orbitals is performed, resulting in a model with 15 bands. The

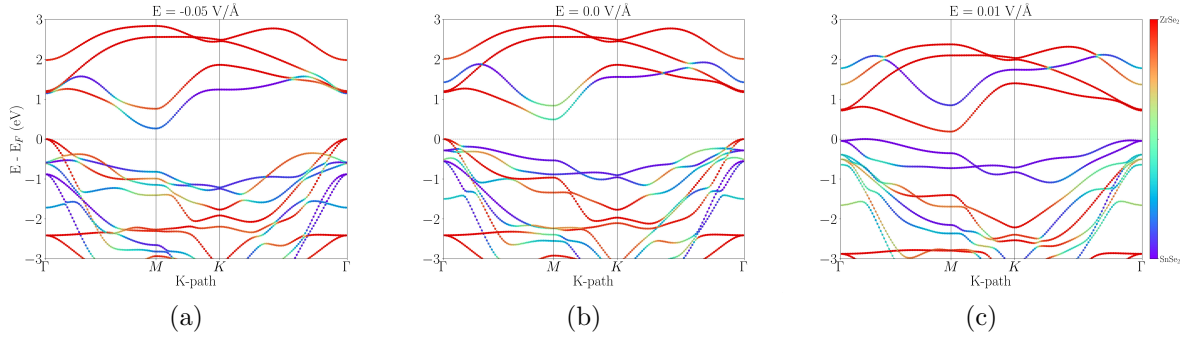


FIGURE 4.7 – TB band structures for the $\text{ZrSe}_2/\text{SnSe}_2$ heterobilayer when an electric field of (a) -0.05 V/\AA (b) 0.0 V/\AA and (c) $+0.1 \text{ V/\AA}$ is applied in the z direction. Palette color indicates the percentage of bands formed by orbitals from the SnSe_2 and ZrSe_2 layers. The top of the valence band is taken as reference.

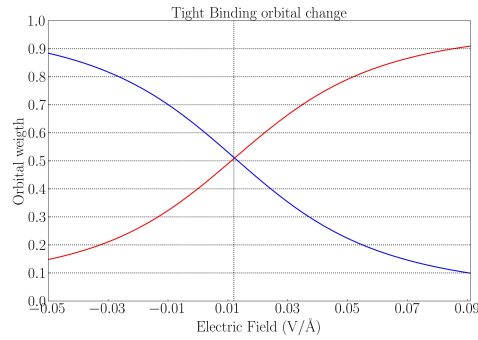


FIGURE 4.8 – Change of the orbital contribution to the state $|0\rangle$ from the TB model as a function of the electric field applied.

full Hamiltonian generated after the minimization procedure results in several hopping terms that accurately reproduce all the features of the whole DFT band structure. However, to obtain a small Hamiltonian that captures the central physics of bands of interest, it is considered hoppings with a module above a certain threshold, here represented by $|hop|$, and between orbitals separated by a certain distance, d_{hop} . Tests were performed to obtain these values to truncate the Hamiltonian. It was verified that some features are, in fact, sensitive to the changes in these parameters. For instance, considering hoppings $|hop| \geq 0.01 \text{ eV}$, the change or the orbital character of the first lowest conduction band and the band gap is shown in Table 4.3.

The change in the TB band structure varies with d_{hop} as shown in Fig.(4.9). As can be seen, for the case where $d_{hop} = 5.0 \text{ \AA}$, the agreement between TB and DFT bands is not so good, and the band gap differs from the one obtained by HSE06, which has the value of 1.24 eV . For the case where $d_{hop} = 10.0 \text{ \AA}$, there is a good agreement between the bands and the band gap; however, the orbital character does not correspond to the one obtained from the DFT calculation, which is 48% for ZrSe_2 and 52% for SnSe_2 for the lowest conduction band (KODA *et al.*, 2018).

TABLE 4.3 – Change on the orbital contribution and band gap with parameter d_{hop} . CBM1 (ZrSe₂/SnSe₂) is the orbital contribution of the respective layer to the first lowest conduction band.

d_{hop} (Å)	CBM 1 (ZrSe ₂)	CBM 1 (SnSe ₂)	E_g (eV)
5.0	47%	51%	1.32
5.5	30%	70%	1.29
6.0	67%	33%	1.22
6.5	64%	36%	1.17
7.0	52%	48%	1.14
7.5	52%	48%	1.15
10	37%	63%	1.22

Now the parameter d_{hop} will be constant and equal to 7 Å, and the parameter $|hop|$ will be changed. The modification in the orbital contribution and the band gap are shown in Table 4.4.

TABLE 4.4 – Change on the orbital contribution and band gap with parameter $|hop|$. CBM 1 (ZrSe₂/SnSe₂) is the orbital contribution of the respective layer to the first lowest conduction band.

$ hop $ (eV)	CBM 1 (ZrSe ₂)	CBM 1 (SnSe ₂)	E_g (eV)
0.01	52%	48%	1.14
0.012	55%	45%	1.11
0.014	57%	43%	1.13
0.016	58%	42%	1.13
0.018	55%	45%	1.14
0.02	52%	48%	1.15
0.03	66%	34%	1.15

Here it is possible to note that by increasing the cutoff on the hoppings, the orbital contribution tends to increase for the state coming from the ZrSe₂ whereas the band gap remains nearly constant.

From the previous analysis, the parameters to truncate the Hamiltonian preserving the band gap, agreement of TB and DFT band structures, and the orbital contribution of the layers can be obtained. For this system, it was considered $|hop| \geq 0.015$ eV, and $d_{hop} \leq 9.0$ Å, resulting in a TB model with first and second neighbors interactions only. The resulting band structures are shown in Fig.(4.10). The orbital characters of the truncated Hamiltonian are 45% (ZrSe₂) and 55% for (SnSe₂) in the lowest conduction band, in good agreement with DFT results (KODA *et al.*, 2018). The band gap was also 1.24 eV.

The control of the orbital character is shown in Fig.(4.11), where the change on hybridization occurs. For negative fields, $|0\rangle$ comprises states coming from SnSe₂, and $|1\rangle$ from ZrSe₂, and the opposite occurs for positive fields. One may also note the change of

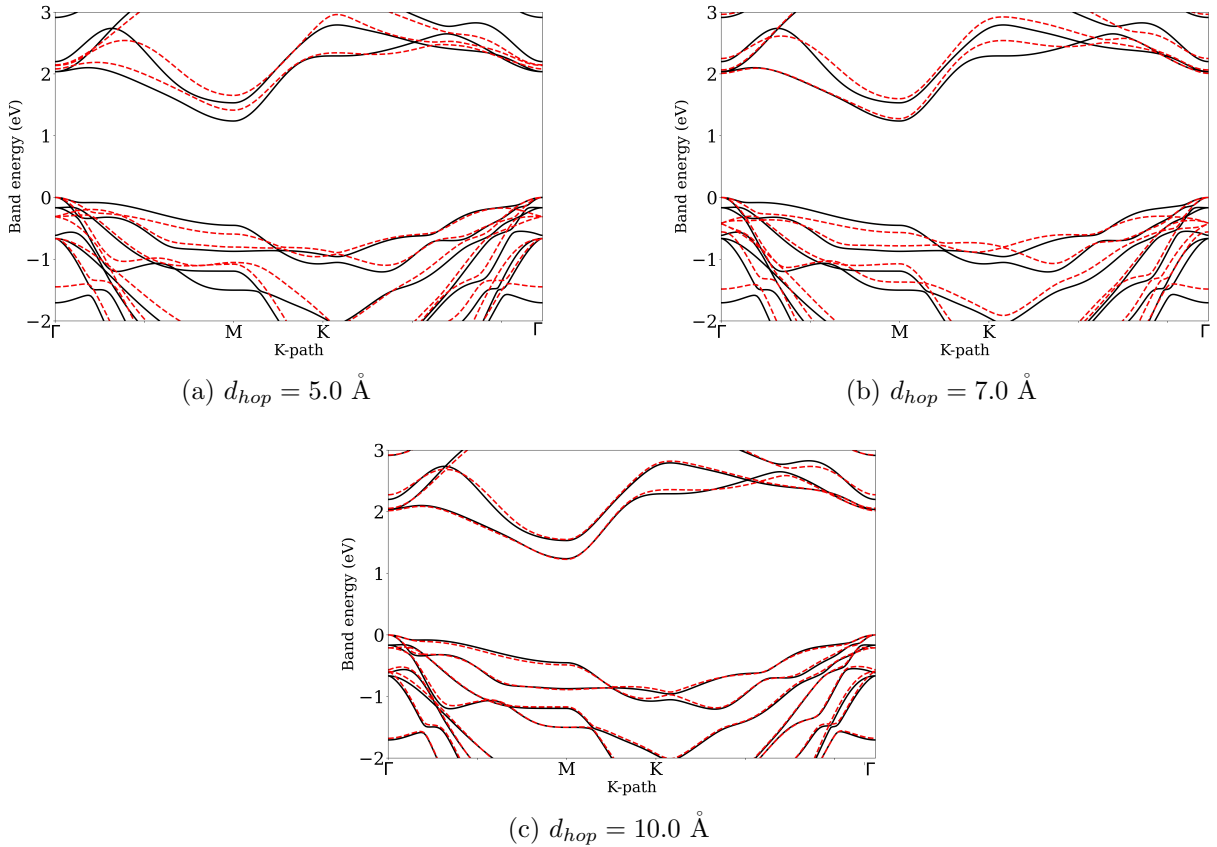


FIGURE 4.9 – ZrSe₂/SnSe₂ TB band structure in red and DFT band structure in black with the change of d_{hop} .

orbital contribution on the valence bands at Γ point. The hole states are concentrated at the ZrSe₂ layer from zero towards negative fields. For positive fields, the energy levels in the valence are shifted, making the hole states concentrated in the SnSe₂ layer. All these results are consistent with the previous work that analyzes these properties from *ab initio* calculations (LUCATTO *et al.*, 2019).

It's important to acknowledge the significance of considering quasi-particle effects. The TB model exhibits remarkable consistency with DFT band structures, band gap, and orbital contributions for the two lowest conduction bands under zero fields. However, the TB model achieves electronic state localization with a smaller electric field compared to DFT, possibly owing to certain imposed simplifications: (i) applying the electric field perturbatively to onsite energies while keeping hoppings fixed and (ii) selecting specific orbitals for constructing the TB model. Henceforth, only TB models preceded by a DFT calculation with quasi-particle corrections will be considered.

These findings align qualitatively with the previous work that analyzed these properties from *ab initio* calculation (LUCATTO *et al.*, 2019). However, due to approximations such as treating the electric field as a first-order perturbation to onsite energies while holding hoppings constant, and considering selected orbitals for model construction, there's a

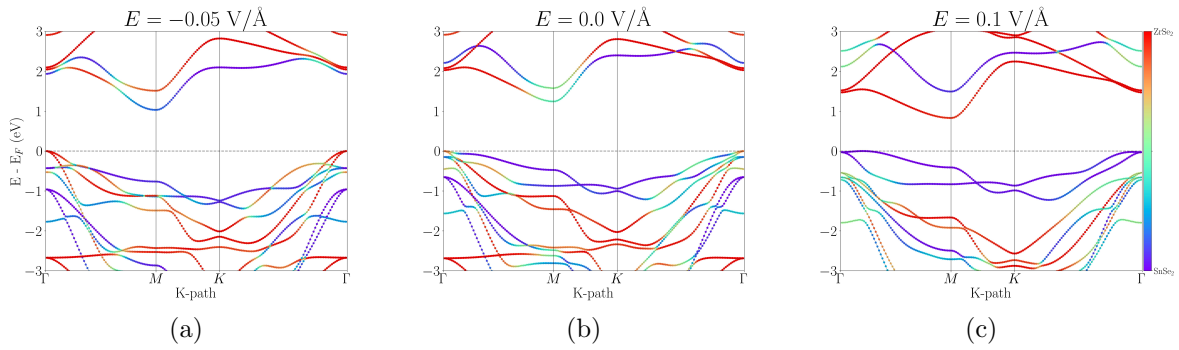


FIGURE 4.10 – TB band structures considering quasi particle effects for the $\text{ZrSe}_2/\text{SnSe}_2$ heterobilayer when an electric field of (a) -0.05 V/\AA (b) 0.0 V/\AA and (c) $+0.1 \text{ V/\AA}$ is applied in the z direction. Palette color indicates the percentage of bands formed by orbitals from the SnSe_2 and ZrSe_2 layers. The top of the valence band is taken as reference.

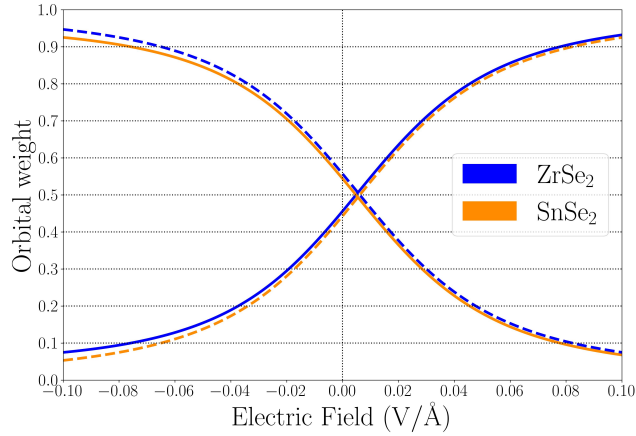


FIGURE 4.11 – Change of the orbital contribution in the function of the electric field applied. The solid lines represent the change on $|0\rangle$, and the dotted lines represent the change on $|1\rangle$. The colors are used to identify the layers: orange is for ZrSe_2 and blue for SnSe_2 .

disparity in the magnitude of the electric field. In the *ab initio* calculation, achieving 80% charge concentration in one layer requires approximately -0.3 V/\AA , whereas in the TB model, this is attained at -0.04 V/\AA , in the case of negative fields, indicating an order of magnitude difference. Moreover, despite similar orbital control curves in both approaches, the TB model achieves electronic state localization with a smaller electric field.

This discrepancy can be attributed to the fact that in our TB model we introduced an unscreened electric field represented by the term $eE_z^{ext}z$. This simplified representation overlooks local effects and polarization. To incorporate polarizability effects, we consider the static dielectric constant and define the resulting field as $E_{res} = E_z^{ext}/\epsilon_{z,hetero}$, where $\epsilon_{z,hetero}$ is the transverse dielectric permittivity of the heterostructure, accounting for any induced field present in the system. To compute $\epsilon_{z,hetero}$, we individually considered the dielectric constants of the layers constituting the heterostructure, following a similar reasoning to the quantum electrostatic heterostructure (QHE) model, that determines the

heterostructure's dielectric function by considering the electrostatic interactions among its components (THYGESEN, 2017). Here, we approximate the heterostructure's dielectric constant as the harmonic mean of these individual constants, in which the resultant dielectric constant is given by

$$\epsilon_{z,hetero} = \frac{\epsilon_1\epsilon_2(d_1 + d_2)}{\epsilon_1d_2 + \epsilon_2d_1}, \quad (4.3)$$

where $\epsilon_{1,2}$ is the 2D dielectric constant of the layers that composes the material and $d_{1,2}$ is their thickness. Since TMDs layers possess similar thickness, we can approximate $d_1 \approx d_2$, giving

$$\epsilon_{z,hetero} \approx \frac{2\epsilon_1\epsilon_2}{\epsilon_1 + \epsilon_2}. \quad (4.4)$$

For the individual components, the values for the static dielectric constants are 5.81 for ZrSe₂ and 16.95 for SnSe₂. Using Eq. (4.4), the dielectric constant for the heterostructure is determined to be 8.65. With this adjustment, the range of fields required to manipulate the orbital composition of the two lowest conduction bands is comparable with that obtained from the DFT calculation, as illustrated in Fig.(4.12). In this scenario, the electric field intensity required to concentrate the orbital contribution of 80% coming from one layer is -0.32 V/\AA now in agreement with the full DFT calculation.

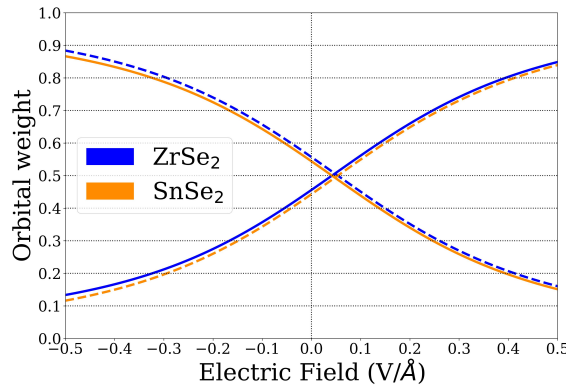


FIGURE 4.12 – The *ab initio* TBH results for the orbital contribution as a function of the electric field applied considering the effect of polarizability. The solid lines represent the change on $|0\rangle$, and the dotted lines represent the change on $|1\rangle$. Blue is for ZrSe₂ and orange for SnSe₂.

The band structure subjected to different fields considering now that it is smotted by the presence of the dielectric constant is shown in Fig.(4.13), perfectly agreeing with previous DFT results (LUCATTO *et al.*, 2019).

All the dielectric constants used in this work were taken from the Materials Project Database (JAIN *et al.*, 2013; ONG *et al.*, 2013) which were computed within Density Functional Perturbation Theory (DFPT) approach (PETOUSIS *et al.*, 2016; PETOUSIS *et al.*,

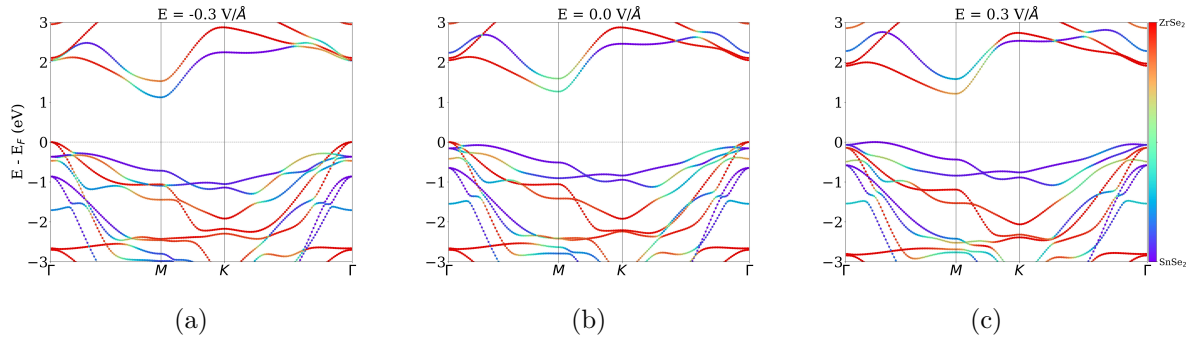


FIGURE 4.13 – Band structures for the $\text{ZrSe}_2/\text{SnSe}_2$ heterobilayer when an electric field of (a) $-0.3 \text{ V}/\text{\AA}$ (b) $0.0 \text{ V}/\text{\AA}$ and (c) $+0.3 \text{ V}/\text{\AA}$ is applied in the z direction. Palette color indicates the percentage of bands formed by orbitals from the SnSe_2 and ZrSe_2 layers. The top of the valence band is taken as reference.

2017).

4.3 $\text{HfS}_2/\text{SnS}_2$ heterostructure

After thoroughly exploring the methodology and noting its impressive accuracy when compared to DFT results, we proceeded to examine other combinations based on band offsets, as detailed in Appendix C, to ascertain whether this property exhibits a consistent trend across various systems.

The $\text{HfS}_2/\text{SnS}_2$ heterostructure was chosen for further investigation, consisting of two layers on 1T phase as depicted in Fig.(4.14), with six atoms in the unit cell. While there is a minor lattice mismatch between the layers, the HfS_2 layer has a lattice parameter of 3.65 \AA and the SnS_2 layer has a lattice parameter of 3.71 \AA , the mean value of the lattice parameters was calculated to obtain the unit cell, resulting in a value of 3.68 \AA , and each layer was subjected to relative stress of about 0.8%. After the relaxation of the atomic positions in the unit cell, the interlayer distance was found to be 2.99 \AA .

The heterostructure's components have already been assembled experimentally as reported in Refs. (SU *et al.*, 2015; FU *et al.*, 2017), and their potential applications have been explored. These experimental findings make the construction of such heterostructure viable. In addition, our *ab initio* calculations demonstrate that this stacking configuration is energetically favorable. From the previously computed energy levels, their band offsets are

$$\begin{aligned} \Delta E_v &= -0.318 \text{ eV} \\ \Delta E_c &= 0.263 \text{ eV.} \end{aligned} \tag{4.5}$$

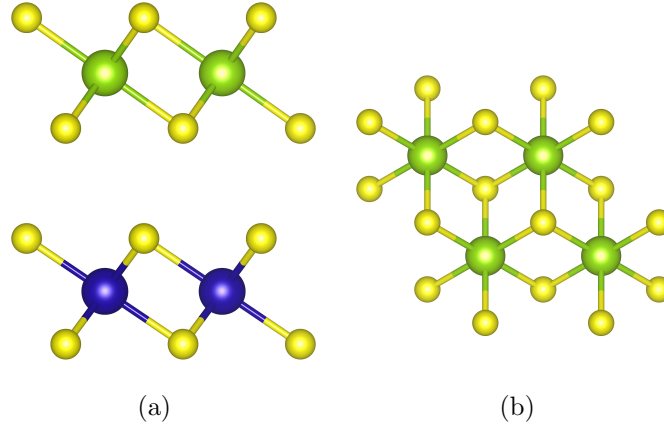


FIGURE 4.14 – (a) Side view of the heterostructure. (b) Top view of the heterostructure. Light green atoms represent Thin, blue Hafnium and yellow Sulfur.

The small values here favor a possible hybridization of states to give rise to a vdW qubit. Table 4.5 summarizes the energy levels for this system.

TABLE 4.5 – Summary of the energy levels (DFT) of freestanding monolayers and the heterojunction. All values are in eV.

HfS ₂		SnS ₂		HfS ₂ /SnS ₂	
I	A	I	A	VBM	CBM
7.081	4.890	7.399	5.152	-7.184	-5.143

From the fat band analysis of the present heterostructure, the d_{xy} , d_{z^2} and $d_{x^2-y^2}$ orbitals of Hafnium and p orbitals of Sulfur showed to contribute for the low energy bands. Consequently, these orbitals were used as an initial guess for the Wannierization procedure to obtain the MLWFs, resulting in a TB model of 15 bands. The final spreads of the orbitals are shown in Table 4.6.

TABLE 4.6 – Ω^2 of the WFs after the minimization procedure. The first line on the information about the spreads of p orbitals is for those connected with Hf, and the line below is for those bonded with Sn.

Element orbital	Hafnium				Selenium	
	dz^2	$d_{x^2-y^2}$	d_{xy}	p_z	p_x	p_y
Ω^2	3.34	3.34	3.34	2.11/2.00	2.14/2.14	2.14/2.14
				5.23/3.32	2.73/3.32	2.73/2.54

Following a similar procedure to obtain the parameters to truncate the sparse hamiltonian preserving main quantities of interest, the values considered where were $d_{hop} \leq 7\text{\AA}$ and $|hop| \geq 0.02$ eV, which resulted in a match of DFT and TB bands, as shown in Fig.(4.15) where it is included hoppings up to second neighbors interactions. The band gap is 2.0 eV, in good agreement with the DFT+HSE06 value of 2.04 eV, and the orbital contribution of the HfS₂ (SnS₂) for the lowest conduction band is 64% (36%) at M point, which in this case agrees exactly with previous DFT results (KODA *et al.*, 2018).

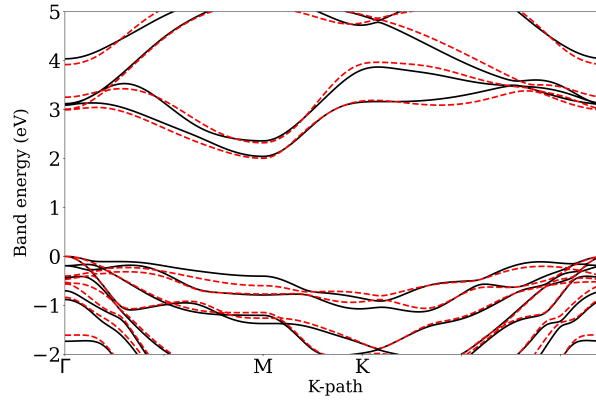


FIGURE 4.15 – $\text{HfS}_2/\text{SnS}_2$ TB band structure in red and DFT band structure in black for the values $d_{hop} \leq 7\text{\AA}$ and $|hop| \geq 0.02$ eV.

Proceeding with the approximation of inserting the electric field on the onsite energies, the magnitude of the electric field applied is similar to the previous case of the $\text{ZrSe}_2/\text{SnSe}_2$ system. The band structures are shown in Fig.(4.16).

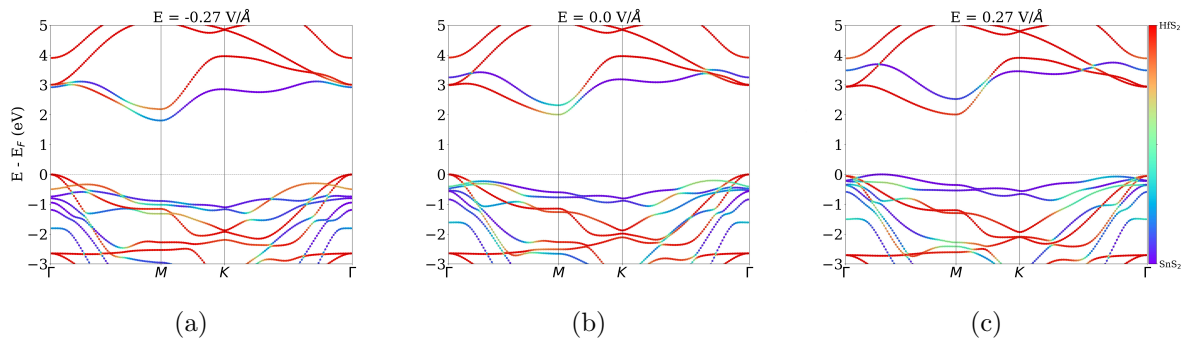


FIGURE 4.16 – Band structures for the $\text{HfS}_2/\text{SnS}_2$ heterobilayer when an electric field of (a) -0.27 V/Å (b) 0.0 V/Å and (c) $+0.27$ V/Å is applied in the z direction. Palette color indicates the percentage of bands formed by orbitals from the HfS_2 and SnS_2 layers. The top of the valence band is taken as reference.

Following the same notation as for the previous system, the orbital character change with the applied electric field is given in Fig.(4.17) where the polarizability effects were already taken into account. The dielectric constant of the heterostructure is 4.97.

In this system, the dominant contribution to the qubit state $|0\rangle$ arises from the SnS_2 layer, while $|1\rangle$ predominantly arises from states in the HfS_2 layer for negative electric fields. Applying an electric field of approximately -0.4 and $+0.3$ V/Å is sufficient to concentrate 90% of the charge in one layer for individual states. Additionally, the modulation of electronic properties is also observed in the valence bands. Moving from negative to positive fields, the hole states that were initially in HfS_2 go to the other layer, owing to changes in the alignment of the VBM.

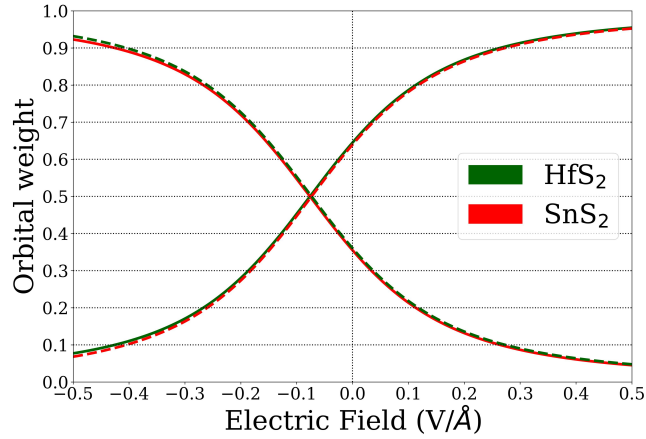


FIGURE 4.17 – The *ab initio* TBH results for the orbital contribution as a function of the electric field applied considering the effect of polarizability. The solid lines represent the change on $|0\rangle$, and the dotted lines represent the change on $|1\rangle$. Green is for HfS_2 and red for SnS_2 .

4.4 $\text{ZrS}_2/\text{SnS}_2$ heterostructure

Based on the previous discussion in Sections 4.2 and 4.3, the ability to control the orbital character is not unique to a particular vdW heterostructure but rather a general phenomenon. The alignment of energy levels in the individual layers prior to their combination in a heterostructure serves as a useful parameter for guiding the design of vdW qubits. This approach can be applied to various host materials, which makes vdW qubits attractive for electronic component applications due to the abundance of vdW materials available experimentally.

Similar to the first heterostructure discussed in this chapter, here only the chalcogen is replaced, Se to S, yielding on the $\text{ZrS}_2/\text{SnS}_2$ heterostructure, where both materials are also in their 1T phase, with six atoms in the unit cell. Fig.(4.18) shows the heterostructure, such as its stacking. An 1×1 unit cell is also feasible for this system due to the slight mismatch between the lattice parameters of ZrS_2 (3.69 Å) and SnS_2 (3.71 Å). By taking the mean value of these parameters, it is obtained a lattice parameter of 3.70 Å resulting in a relative stress of approximately 0.3% on both layers. Concerning the electronic properties, this heterostructure also exhibits a small offset in the conduction bands, appealing to be used as a host material for the vdW qubit

$$\begin{aligned}\Delta E_v &= -0.288 \text{ eV} \\ \Delta E_c &= 0.110 \text{ eV}.\end{aligned}\tag{4.6}$$

The energy levels involved in this system are summarized in Table 4.7. The band structure of $\text{ZrSe}_2/\text{SnSe}_2$ is similar to that of $\text{ZrS}_2/\text{SnS}_2$, which is expected since the chalcogen atoms in both systems belong to the same family on the periodic table. The interlayer distance

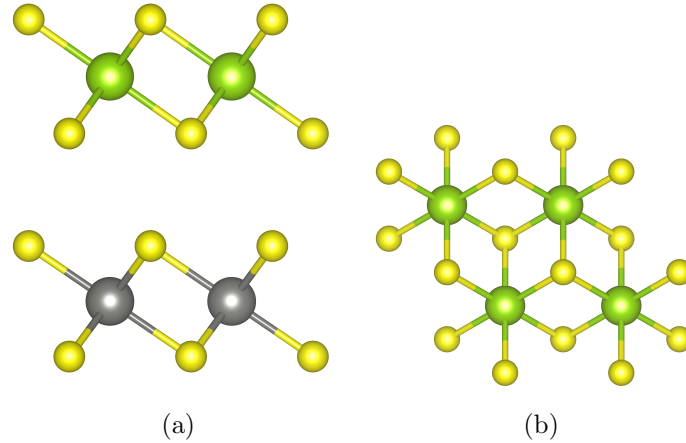


FIGURE 4.18 – (a) Side view of the heterostructure. (b) Top view of the heterostructure. Light green atoms represent Selenium, grey Zirconium, and yellow Sulfur.

TABLE 4.7 – Summary of the energy levels (DFT) of freestanding monolayers and the heterojunction.

ZrS ₂		SnS ₂		ZrS ₂ /SnS ₂	
I	A	I	A	VBM	CBM
7.110	5.043	7.399	5.152	-7.168	-5.259

obtained after full relaxation was 2.95 \AA , and the calculated band gap, considering quasi-particle effects, was 1.91 eV . The TB model derived from Wannierization used the same atomic orbitals as in the previous systems, given the similar chemistry of the compounds consisting, of 15 bands and a band gap of 1.89 eV , a value that closely matches the *ab initio* result of 1.91 eV .

Considering all possible hoppings, the full Hamiltonian reproduces all the features of the *ab initio* result. It gives an orbital contribution of 59% for ZrS₂ and 41% for SnS₂ in the lowest conduction band. In order to obtain a smaller Hamiltonian, with fewer hopping terms but that reproduces the DFT result with great accuracy, the truncation parameters considered for this system were $d_{hop} \leq 8.5 \text{ \AA}$ and $|hop| \geq 0.004 \text{ eV}$ where, besides first and second, 10 third-neighbor hoppings were included in order to the orbital character in the lowest conduction bands agree with DFT results. After the minimization procedure, the MLWF were obtained with their spreads given in Table 4.8 and the matching of DFT and TB band structures in Fig.(4.19), with the truncation parameters here considered. This smaller Hamiltonian has the same orbital character as the full one in the lowest conduction band.

The resulting band structure for this gated system is shown in Fig.(4.20). Similar to the case of the heterostructure ZrSe₂/SnSe₂, for negative fields the state $|0\rangle$ is mainly composed of state coming from the SnS₂ layer and $|1\rangle$ from ZrS₂ layer and the modulation of this contribution changes with the intensity and direction of the electric field. A similar change in the orbital composition is also observed at the top of the valence band. The

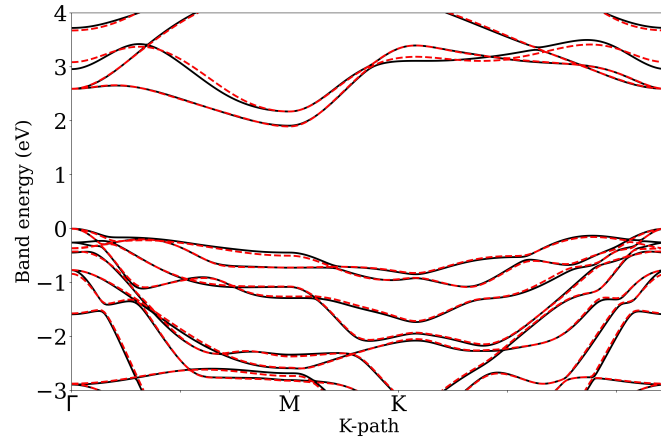


FIGURE 4.19 – $\text{ZrS}_2/\text{SnS}_2$ TB band structure in red and DFT band structure in black for the values $d_{hop} \leq 8.5\text{\AA}$ and $|hop| \geq 0.004\text{ eV}$.

TABLE 4.8 – Ω^2 of the WFs after the minimization procedure. The first line on the information about the spreads of p orbitals is for those connected with Zr, and the line below is for those bonded with Sn.

Element orbital	Zirconium				Selenium	
	dz2	$d_{x^2-y^2}$	d_{xy}	p_z	p_x	p_y
Ω^2	2.63	2.63	2.63	2.12/2.08	2.12/2.08	2.12/2.08
				2.80/3.58	5.15/2.37	2.80/3.58

dielectric constant for this heterostructure is 5.48. The orbital control, shown in Fig.(4.21), indicates that with a field around -0.24 V/\AA it is possible to concentrate 80% of the charge coming from one of the layers to each qubit state, a value that is in agreement with the two other systems investigated. Around 0.14 V/\AA is required for positive fields to localize the qubit state in one of the layers.

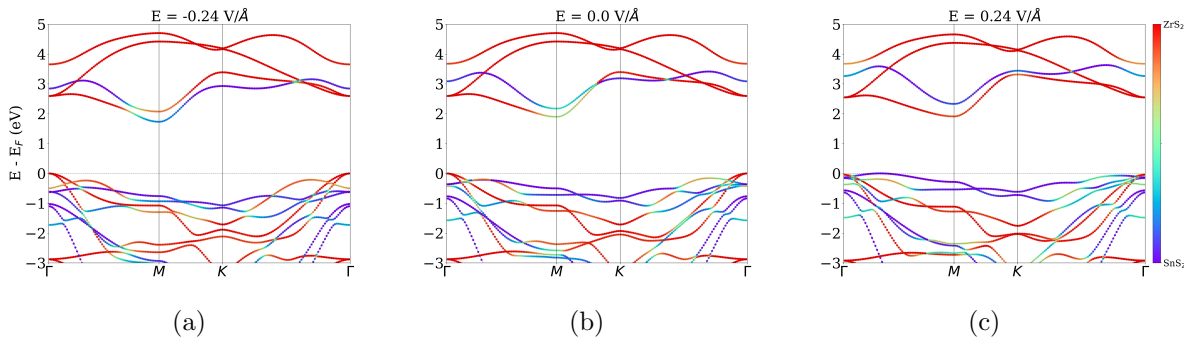


FIGURE 4.20 – Band structures for the $\text{ZrS}_2/\text{SnS}_2$ heterobilayer when an electric field of (a) -0.24 V/\AA (b) 0.0 V/\AA and (c) $+0.24\text{ V/\AA}$ is applied in the z direction. Palette color indicates the percentage of bands formed by orbitals from the ZrS_2 and SnS_2 layers. The top of the valence band is taken as reference.

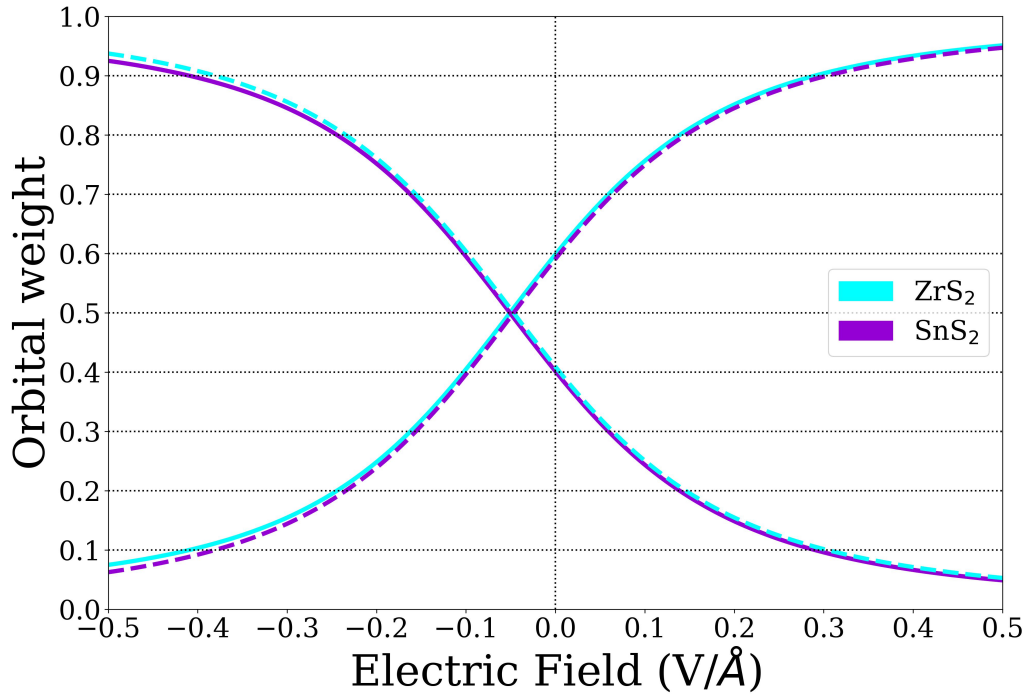


FIGURE 4.21 – The *ab initio* TBH results for the orbital contribution as a function of the electric field applied considering the effect of polarizability. The solid lines represent the change on $|0\rangle$, and the dotted lines represent the change on $|1\rangle$. Light-blue is for ZrS_2 and purple for SnS_2 .

4.5 $\text{ZrS}_2/\text{HfS}_2$ heterostructure

Up to this point, we have been discussing systems with a small band offset in the conduction bands. However, we will now examine a system that exhibits the superposition of states not in conduction, but rather in the valence bands. Specifically, we consider the $\text{ZrS}_2/\text{HfS}_2$ heterostructure, shown in Fig.(4.22), consisting of both materials in the 1T phase and six atoms in the unit cell. In this case, the lattice parameters of the individual layers are nearly commensurate, allowing for a 1×1 unit cell. At the commensurate lattice constant, each layer is subjected to a relative stress of only 0.5%, and the interlayer distance where the energy is minimized is 2.98 Å.

Table 4.9 summarizes the energy levels computed previously and shows that the offsets of the freestanding layers are small. Specifically, the valence band offset is only $\Delta E_v = 0.03$ eV, indicating that the energy levels of the individual layers are nearly aligned, suggesting a strong hybridization between these states. The CBM of the individual layers also exhibits a small offset of $\Delta E_c = -0.15$ eV.

To confirm this observation, we conducted a Wannierization analysis using the d_{xy} , d_{z^2} , and $d_{x^2-y^2}$ orbitals of Zirconium and Hafnium, as well as the p orbitals of Sulfur, which were identified through orbital composition analysis of the band structure. This

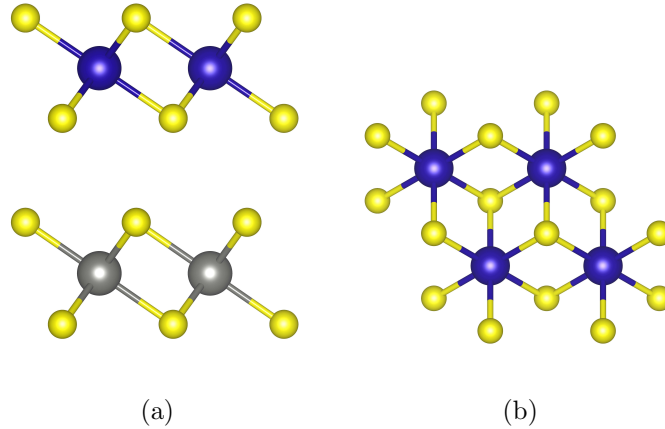


FIGURE 4.22 – (a) Side view of the heterostructure. (b) Top view of the heterostructure. Blue atoms represent Hafnium, grey Zirconium, and yellow Sulfur.

TABLE 4.9 – Summary of the energy levels (DFT) of freestanding monolayers and of the heterojunction.

ZrS ₂		HfS ₂		ZrS ₂ /HfS ₂	
I	A	I	A	VBM	CBM
7.110	5.043	7.081	4.889	-7.068	-5.160

resulted in a basis of 18 atomic orbitals that were minimized to produce the MLWFs. The final spreads of the MLWFs obtained from the minimization procedure are summarized in Table 4.10.

TABLE 4.10 – Ω^2 of the WFs after the minimization procedure. The first line on the information about the spreads of p orbitals is for those connected with Zr and Hf, and the line below is for those bonded with Se.

Element	Zirconium/Hafnium				Selenium	
orbital	d_{z^2} ,	$d_{x^2-y^2}$	d_{xy}	p_z	p_x	p_y
Ω^2	2.60/3.43	2.60/3.43	2.60/3.43	2.10/2.07	2.10/2.07	2.10/2.07
				2.01/ 2.14	2.14/2.14	2.14/2.14

The resulting TB band structure of the vdW heterostructure is depicted in Fig.(4.23). As expected, the alignment of energy levels of individual layers results in hybridization on the valence bands. The band gap obtained from the DFT+HSE06 calculation was 1.90 eV, while the TB model yielded a gap of 1.86 eV. To reduce the Hamiltonian, only hoppings with a modulo $|hop| \geq 0.02$ eV and between neighbors located at a distance below $d_{hop} \leq 8.0 \text{ \AA}$ were kept, considering only first and second neighbors.

One can observe in Fig.(4.23) that in this heterostructure, having the dielectric constant of 3.75, it is possible to confine holes in one of the layers at the Γ point by applying very small electric fields ($\pm 0.05 \text{ V/\AA}$). Specifically, a negative electric field leads to hole localization in the ZrS₂ layer, whereas a positive field leads to hole concentration in the HfS₂ layer.

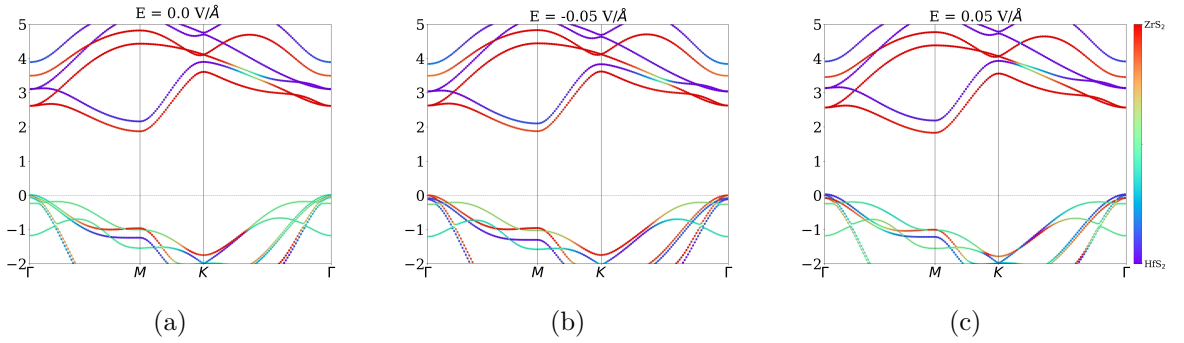


FIGURE 4.23 – Band structures for the $\text{ZrS}_2/\text{HfS}_2$ heterobilayer when an electric field of (a) 0.0 V/\AA (b) -0.05 V/\AA and (c) $+0.05 \text{ V/\AA}$ is applied in the z direction showing the change of hybridization at the Γ point. Palette color indicates the percentage of bands formed by orbitals from the ZrS_2 and HfS_2 layers. The top of the valence band is taken as reference.

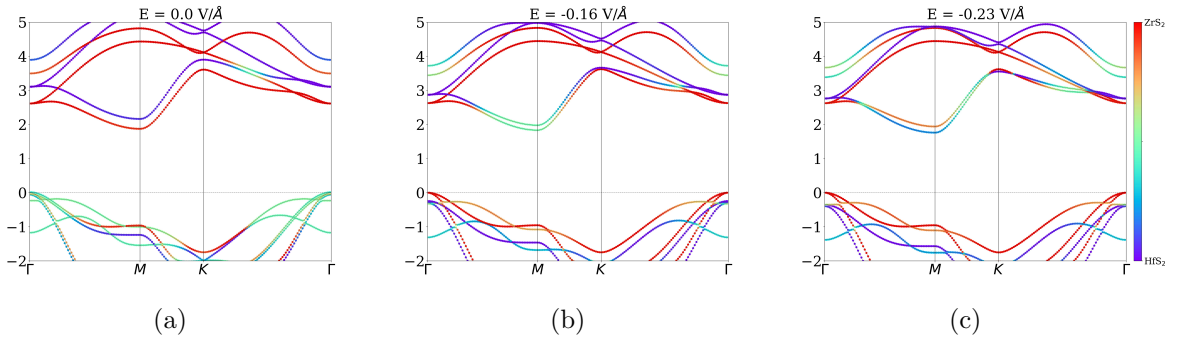


FIGURE 4.24 – Band structures for the $\text{ZrS}_2/\text{HfS}_2$ heterobilayer when an electric field of (a) 0.0 V/\AA (b) -0.16 V/\AA and (c) -0.23 V/\AA is applied in the z direction showing the change of hybridization now at the conduction bands at the M point. Palette color indicates the percentage of bands formed by orbitals from the ZrS_2 and HfS_2 layers. The top of the valence band is taken as reference.

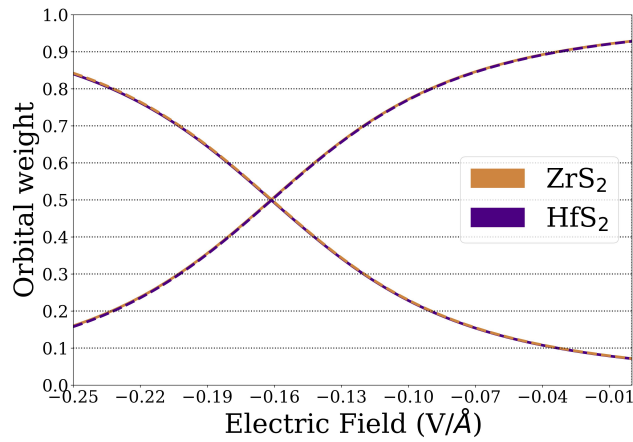
Due to the versatility of modeling electronic properties in vdW heterostructures, hybridization can also be made to occur in the conduction bands in this system. The hybridization “jumps” from the valence bands to the two lowest conduction bands for more intense and negative electric fields, resulting in a two-level system similar to the previous heterostructures. This system demonstrates the ability to manipulate the electronic structures of vdW heterostructures, allowing for control over the superposition of quantum states in either the valence or the conduction bands, which can affect transport properties. In this case, an electric field is used to first obtain the desired superposition of quantum states in the two lowest conduction bands, resulting in a charge distribution between the layers, or a two-level system of $|0\rangle$ and $|1\rangle$, followed by further control of the charge contribution of each layer for this qubit. Figure (4.24) clearly shows that as the electric field is turned on, the electron is localized in one of the layers, and the orbital character of these two bands changes.

At zero field, the state $|0\rangle$ ($|1\rangle$) is formed entirely from the ZrS_2 (HfS_2) layer and with

TABLE 4.11 – Summary of electric field required to concentrate 80% and 20% of the orbital contribution in the two lowest conduction bands.

Heterostructure	$E_{80/20}(V/\text{\AA})$	$E_{20/80}(V/\text{\AA})$
ZrSe ₂ /SnSe ₂	-0.32	+0.30
HfS ₂ /SnS ₂	-0.27	+0.11
ZrS ₂ /SnS ₂	-0.24	+0.14
ZrS ₂ /HfS ₂	-0.24	-0.09

the application of a negative electric field, this contribution changes. This change in the orbital character of the two lowest conduction bands is shown in Fig.(4.25)

FIGURE 4.25 – The same of Fig. 4.17, but now for ZrS₂/HfS₂.

From Fig.(4.25), it can also be noted that the equal distribution of states for the vdW qubit is in a situation where the heterostructure is subjected to a gate field, around -0.16 V/Å, which is justified by the offset that the conduction bands presents. Since at zero field, the equal contribution is on the valence, the energy levels on the conduction are aligned for negative fields, which explains the result.

The summary of the electric field required to concentrate 80% of the orbital contribution of the qubit's states is shown in Fig.(4.11). It can be seen that for each system, there is a range of fields required for such manipulation of the states.

The smaller range of electric field required for such manipulation can be more practical once the rotations in the Bloch sphere are achieved at a smaller field. Moreover, the ZrS₂/HfS₂ system has the advantage of a field in a fixed polarization, changing only its intensity.

5 Transition Metal Dichalcogenides Nanoribbons

5.1 Motivation

In Chapter 3, we explored the structural and electronic properties of layered materials, particularly focusing on TMDs. Within this discussion, we outlined the criteria utilized for constructing the vdW heterostructures based on the previously investigated TMDs to obtain the hybridized states desired for the charge qubit. Moving forward, in Chapter 4 we focus on manipulating electronic states with minimal computational effort, using the *ab initio* derived TB model obtained via the Wannierization procedure. However, our investigation thus far has primarily centered on the exploration of the electronic properties of layered materials and vdW heterostructures, focusing on their infinite spectrum, namely, their band structure across symmetry points throughout the BZ. As the final goal of this thesis, we aim to verify if the presence of these hybridized states on the vdW heterostructures results in the transfer of information between the layered materials that compose the heterostructure. To achieve this, we seek to verify whether a plane wave, for instance, propagates from one material to another due to the hybridization present in the heterostructure's band structure. This paves the way for further exploration into the development of quantum gates based on vdW heterostructures.

The split of the wave between the constituent materials forming the vdW heterostructure can be quantified through the current measured on contacts attached to each material. This current, in turn, can be correlated with the conductance using the formula $G = dI/dV$.

Simulating such systems and computing relevant quantities at the *ab initio* level often necessitates substantial computational resources or may even be impractical. Here, once again, our derived TB model proves its worth. To investigate mesoscopic systems, we deviate from the approach of working with infinite 2D materials; instead, we confine these systems further by segmenting them into nanoribbons (NRs). Sticking to the derived TB models, we preserve the low computational cost of simulations, rendering them more

manageable. Nonetheless, directly examining the impact of confinement on vdW heterostructures and computing their transport properties poses a difficult task. Therefore, our initial focus is on the investigation of the individual layers comprising these structures and evaluating the impact of confinement within such systems.

In this chapter, our attention shifts to investigating the effect of confinement on the TMDs nanoribbons and their transport properties. To avoid the computational expense associated with DFT calculations, we continue to use our *ab initio* derived TB models. The influence of this additional confinement and the investigation of NRs were first explored on carbon-based systems (CHICO *et al.*, 1998; MCCANN; FAL'KO, 2004). For instance, in the case of armchair (AR) graphene NRs, a distinctive pattern emerges: if the NR's length is expressed in lattice units as $3M+1$, it exhibits a metallic band structure; otherwise, it demonstrates insulating behavior (BREY; FERTIG, 2006). Successful experimental synthesis of such NRs has been achieved, facilitating the exploration of their theoretically predicted emergent properties (LI *et al.*, 2008; CAI *et al.*, 2010). Graphene NRs can be obtained experimentally through various methods, including lithography, bottom-up synthesis (which allows for the creation of very narrow ribbons), and unzipping carbon nanotubes, among others (YAGMURCUKARDES *et al.*, 2016).

Nevertheless, our focus will be in investigating NRs based on TMDs. As a preliminary step in our investigation, we begin by analyzing the properties of NRs constructed from monolayers of TMDs, referred to here as TMDNRs, before delving into the simulation of transport properties of the NRs based on vdW heterostructures themselves. Our objective is to gain a comprehensive understanding of the effects of confinement on TMDNRs, such as the presence of edge states. Subsequently, we broaden our examination to encompass the NRs derived from the 2D vdW heterostructures. Characterized by their hexagonal symmetry in either the 1T or 2H phase, the specific cut of the layered material results in zig-zag (ZZ) or armchair (AR) edges.

In Chapter 3, we extended our investigation for 10-layered TMDs across phases 1T and 2H, despite one of these phases not necessarily being the most thermodynamically stable for a specific compound, resulting in 20 systems. In this chapter, we focus on investigating NRs based on TMDs in their most stable phase, excluding those with the metal being Hf, since NRs based on this metal are unstable by usual experimental assembling (CANTON-VITORIA *et al.*, 2023). Specifically, we concentrate on TMDNRs MoS_2 , MoSe_2 , WS_2 , and WSe_2 , all of which exhibit the 2H phase as their most thermodynamically stable state. Then, we investigate TMDNRs ZrS_2 , ZrSe_2 , SnS_2 , SnSe_2 , all characterized by the 1T phase as their most stable state.

As previously outlined, our numerical simulations to investigate transport properties will be conducted using the KWANT software (GROTH *et al.*, 2014). These simulations entail a semi-infinite region (the leads), which generates subbands or transport channels

directing electrons into the finite region, called the scattering region. This workflow naturally guides our investigation towards the properties of NRs, as the finite scattering is subjected to additional confinement, not present in the previously studied 2D materials, into lower dimensions, resulting in NRs for 1D systems or quantum dots, which are regarded as zero-dimensional (0D). Additionally, the semi-infinite leads connected to the scattering region exhibit periodicity in one direction, while the other direction is confined and typically has the extension of the scattering region to which it is attached.

5.2 NR Terminations

Once we obtain the *ab initio*-derived TB model for freestanding monolayers, the subsequent step involves transforming these 2D materials into NRs by cutting the layered material along specific directions. Constructing such ribbons necessitates careful consideration of boundary conditions and the orientation for translational symmetry. Engineering the edges of NRs has proven to be a rich way for exploring intriguing physical phenomena, including the emergence of spin polarization in graphene NRs with chiral edges (BREDE *et al.*, 2023), and the manifestation of topological bound states in the Haldane model with ZZ edges (TRAVERSO *et al.*, 2024), among others.

In Fig.(5.1), we present the diverse edge configurations investigated for both allotropes in our study. Maintaining the translational symmetry of the lattice vectors \vec{a}_1 and \vec{a}_2 , as illustrated in Fig.(5.1a), we depict 2H-ZZ-NR characterized by metal-chalcogen (MC) chemical termination along the edges. In this structure, where chalcogens are aligned vertically, various edge patterns could emerge from different combinations of metal and chalcogen terminations. Specifically, in MC termination we obtain the usual ZZ pattern, while metal-metal (MM) and chalcogen-chalcogen (CC) terminations yield both ZZ and flat (asymmetric) edges. However, these flat edges, associated with compounds having lower coordination numbers, are not considered in our analysis due to their high tendency to form bonds with the neighboring atoms. In this configuration, the leads are attached along the \vec{a}_1 direction, while the width of the NR is measured along \vec{a}_2 . The 2H-AR-NR of the 2H allotrope is illustrated in Fig.(5.1c), with the semi-infinite lead attached along the direction of $\vec{a}_1 + 2\vec{a}_2$, as the lattice vectors are oriented at 120° to each other. The semi-infinite leads, displayed in Fig.(5.1c) in fading red, possess the AR edges.

Now regarding types of terminations for the NRs for those materials having the 1T-phase as being the most stable. The ZZ-edged ribbons are shown in Fig.(5.1b), also showcasing three distinctive terminations: MC, MM and CC in the orange, red, and light-blue rectangles, respectively. Since in this case, the chalcogens are not on the same vertical, independent of the chemical termination, the edges will be ZZ. Fig.(5.1d) shows

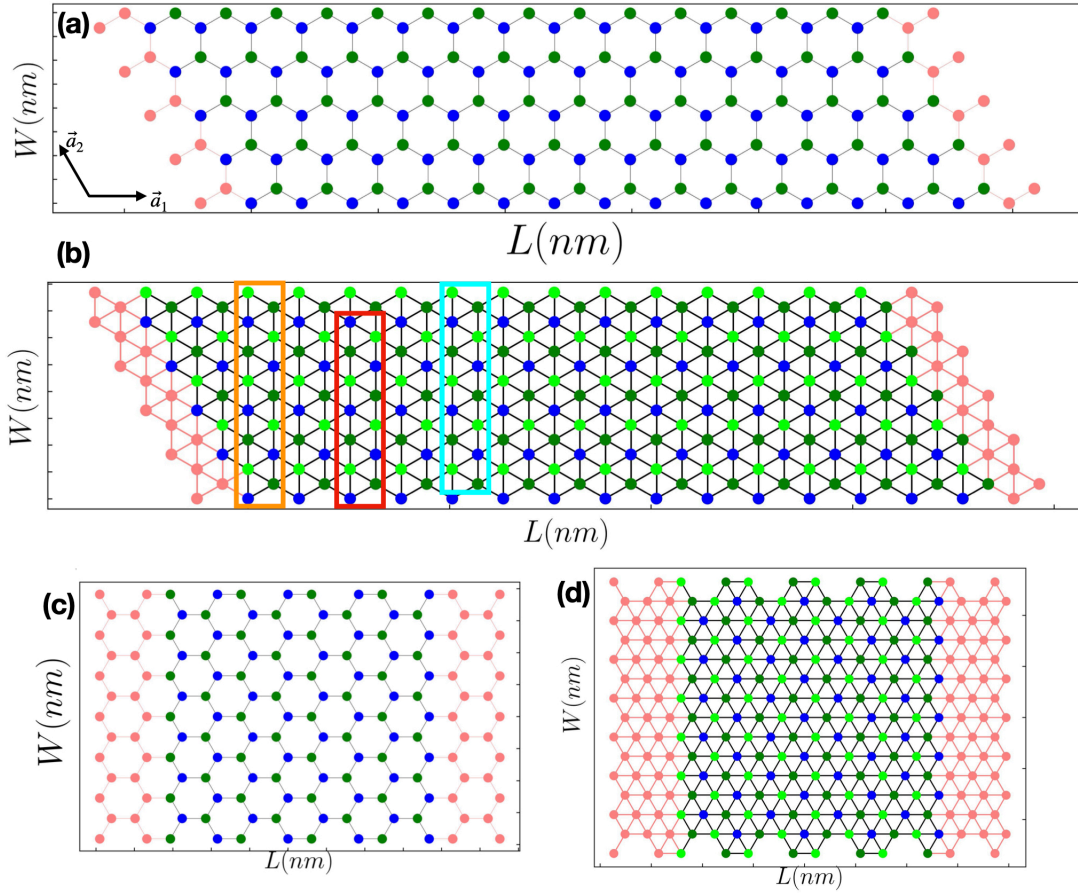


FIGURE 5.1 – Top view of NRs based on the allotropes 2H and 1T. (a) and (c) Top view of NRs based on the 2H allotrope, showcasing ZZ and AR edge configurations. (b) ZZ edge termination of NRs based on the 1T allotrope. Orange, red, and light-blue rectangles denote different chemical terminations: MC, MM, and CC, respectively. (d) AR-NR of the 1T allotrope. Blue atoms represent the metal, and dark and light green are the chalcogens.

the NR with AR edges. Both for the AR and ZZ edge NRs, the notation for L , which is the length of the NR along \vec{a}_1 and W which is the width of the NR along \vec{a}_2 is the same adopted for the 2H allotropes. The same for the leads as shown in Figs.(5.1a,c).

Our focus now shifts to understanding the impact of these various terminations on the dispersion of the semi-infinite leads and how these changes influence the conductance of the investigated TMDNRs. As discussed previously, the NRs with ZZ edges the leads are attached along \vec{a}_1 direction, and for the AR direction, the leads are attached along the $\vec{a}_1 + 2\vec{a}_2$ direction, since for the 2D materials the angle between the lattice vectors are 120° . In the direction where we do not have leads attached, we apply open boundary conditions. Further, we investigate the two terminal conductance throughout these different edge terminations and scattering regions.

5.3 Lead's band structure

5.3.1 NRs on the 2H phase

To examine the impact of various terminations on lead dispersion, we calculate the energy eigenstates of the leads relative to momentum variations along the translational symmetry direction. Beginning with the 2H-MoS₂-NR featuring AR edges, a system extensively studied in prior works (HU *et al.*, 2014; ROSTAMI *et al.*, 2016), our initial objective is to validate our methodology and underscore the efficacy of the *ab initio* Tight-Binding Hamiltonians. For an NR with $W = 50 \text{ nm}$ we have the lead dispersion shown in Fig.(5.2), where the typical semiconducting behavior is observed. The typical edge states are verified for the subbands labeled with 1 and 2 (ROSTAMI *et al.*, 2016; RIDOLFI *et al.*, 2017; ZHANG *et al.*, 2015). Plotting the wavefunction (depicted by pink circles at the edges), one can confirm that these indeed represent edge states stemming from the metal—specifically molybdenum (Mo). Regarding the state labeled as 1, it's apparent that both metals on either side of the lead contribute to the edge state, whereas only one metal on both sides contributes to state 2. While there are four subbands in total for states 1 and 2 combined, each state exhibits double degeneracy.

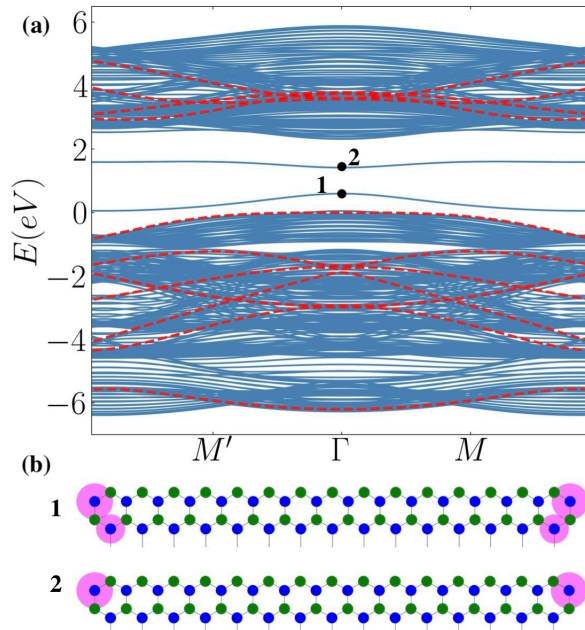


FIGURE 5.2 – (a) Band dispersion for the 2H-MoS₂-AR-NR in solid blue lines with the translational symmetry along the vector $\vec{a}_1 + 2\vec{a}_2$. In dotted red lines is the band structure for the 2D-MoS₂ 11 band TB model plotted along the path $M'-\Gamma-M$. (b) The plot of the wavefunctions of the edges states for each state is labeled on the dispersions in (a).

In the case of NR featuring ZZ edges, a common termination composed of both metal and chalcogen, as frequently explored (YANG *et al.*, 2012; ZHANG *et al.*, 2013), we examine the dispersion of the leads, illustrated in Fig.(5.3). Notably, the dispersion obtained from

our TB parameters for these NRs deviates from the expected metallic behavior (ROSTAMI *et al.*, 2016; GIBERTINI; MARZARI, 2015; RIDOLFI *et al.*, 2017). This discrepancy has been previously addressed in Ref.(GIBERTINI; MARZARI, 2015), wherein it was discussed that metallic states arise due to polar discontinuities along the NR edges. This phenomenon manifests particularly in NRs featuring metals such as Mo or W, characterized by nonzero bulk polarization (GÜLLER *et al.*, 2015; GIBERTINI *et al.*, 2014), inducing charge polarization that results in energy gap shrink. However, the dispersion depicted in Fig.(5.3) is consistent with that presented in Ref.(GIBERTINI; MARZARI, 2015), where the electrostatic effects of charge reconstruction were not considered within the model. While polarization charges and their accompanying electric fields are not essential for explaining the existence of edge states in TMDNRs, they play a crucial role in inducing metallicity (GIBERTINI; MARZARI, 2015).

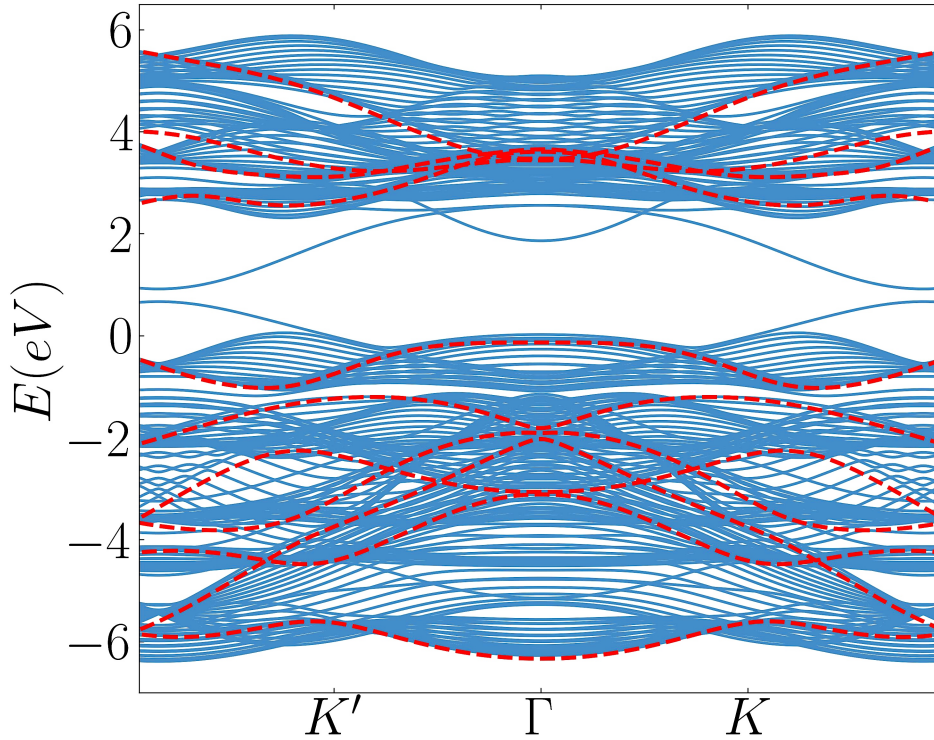


FIGURE 5.3 – Band dispersion for the 2H-MoS₂-ZZ-NR with edges ended with metal and chalcogen, for a width of 50 nm in solid blue lines with the translational symmetry along the vector \vec{a}_1 . In dotted red lines is the band structure for the 2D-MoS₂ 11 band TB model plotted along the path K'- Γ -K.

To address the limitation of the TB model, which neglects electrostatic effects, we can introduce a gate field along the NR to simulate the electric field generated by charge accumulation at the edges. For this NR, a uniform field of magnitude 0.01 V/Å across the lead, induces metallic behavior. Fig.(5.4) illustrates the subbands of the ZZ-NR with MC edges under the influence of a uniform field along the \vec{a}_2 direction, where the expected metallic behavior is observed.

To deepen our understanding of the emergence of states within the 2D gap, we inves-

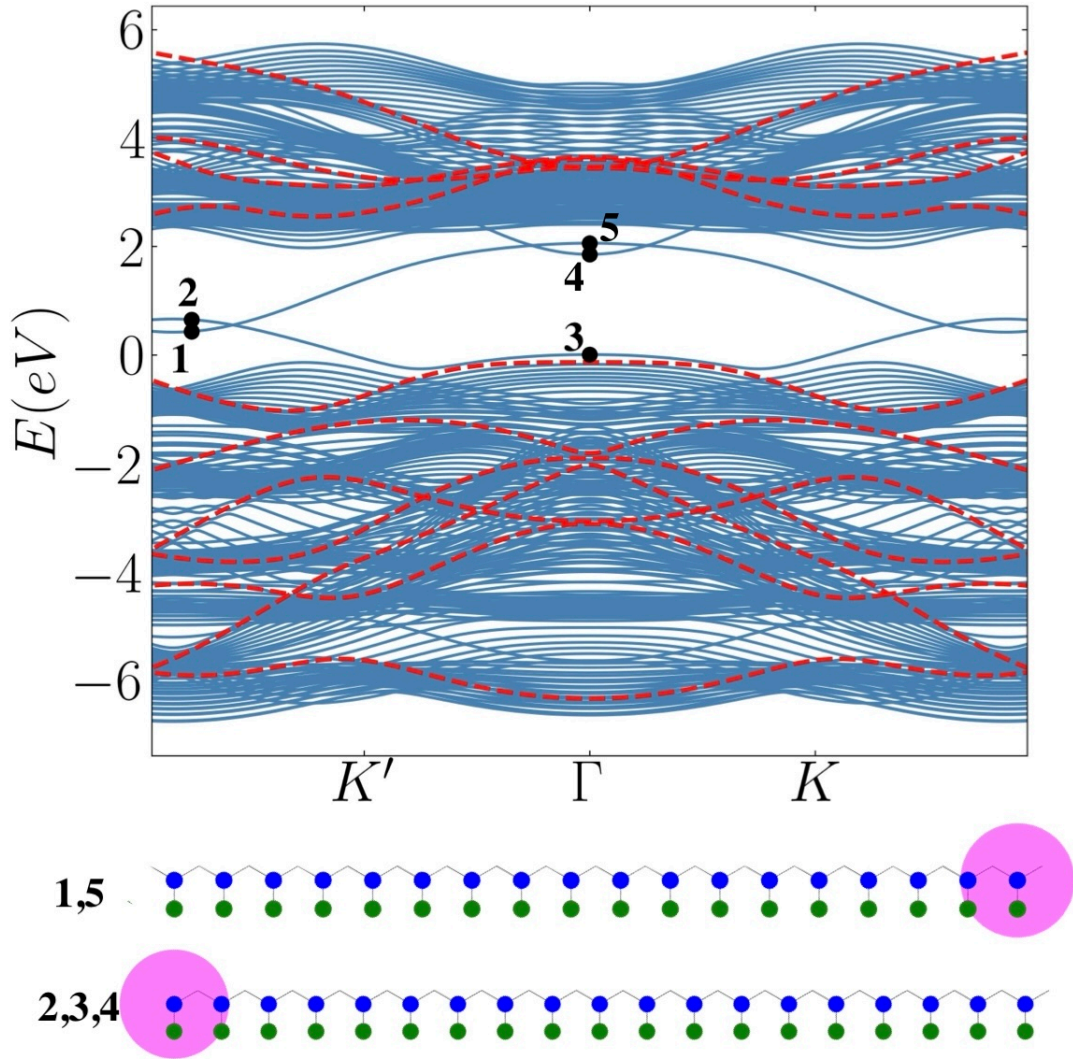


FIGURE 5.4 – Band dispersion for the 2H-MoS₂-ZZ-NR with edge terminations of (a) MC in solid blue lines subjected to an electric field of 0.01 V/Å in dotted red lines is the band structure for the 2D-MoS₂ 11 band TB model plotted along the path K' - Γ - K . (b) The plot of the wavefunctions of the edges states for each state labeled on the dispersions in (a).

tigate the localization of wave functions for the states labeled in Fig.(5.4). Our objective is to confirm whether these states concentrate on the edges and to verify the atom responsible for their emergence. Upon examining states labeled 1 and 2, we observe that edge states arise from Mo atoms positioned on different sides of the NR. Similarly, state 3 originates from Mo atoms located at the bottom of the NR, mirroring the behavior of state 2. This suggests that states 2 and 3 belong to the same subband, exhibiting a crossing with the band associated with state 1. State 5's wave function is situated at the top of the lead, resembling the behavior of state 1, indicating their belonging to the same subband. This implies a crossing of the subbands associated with states 1 and 4 as well. In summary, the edge states observed on the ZZ-MoS₂-NR are attributed to the presence of metal at the edge, with only the location of the edge state varying between sides.

Additionally, our consideration of various chemical terminations for the NRs based on the 1T allotrope highlights the significant edge dependence observed in the quantum transport properties of TMDNRs (SILVA *et al.*, 2016). This edge sensitivity is not unique to TMDNRs; it also plays a crucial role in twisted bilayer graphene systems. For instance, the type of edge termination has been shown to influence the breakdown mechanism of moire flat bands and their relationship with electronic localization. In these systems, electronic structures exhibit strong sensitivity to the edge configuration (ANDRADE *et al.*, 2023).

Still in the context of TMDs predominantly exhibiting the 2H phase as the most stable, examination of NRs with AR edges reveals similarities in the spectrum of MoSe₂, WS₂, and WSe₂ to that of MoS₂, as depicted in Fig.(5.5), albeit with subtle distinctions. Notably, in the MoSe₂-AR-NR spectrum, a slight split in the edge states is evident around Γ , as illustrated in the inset of Fig.(5.5a), even in the absence of SOC, a characteristic absent in MoS₂-AR-NRs. Conversely, an intriguing observation is made in WSe₂-AR-NRs: unlike previous cases where the VBM of the 2D material and the NR align, here, the VBM is lowered in energy. This shift is also observed in the lowest edge states, suggesting their possible association with hole states.

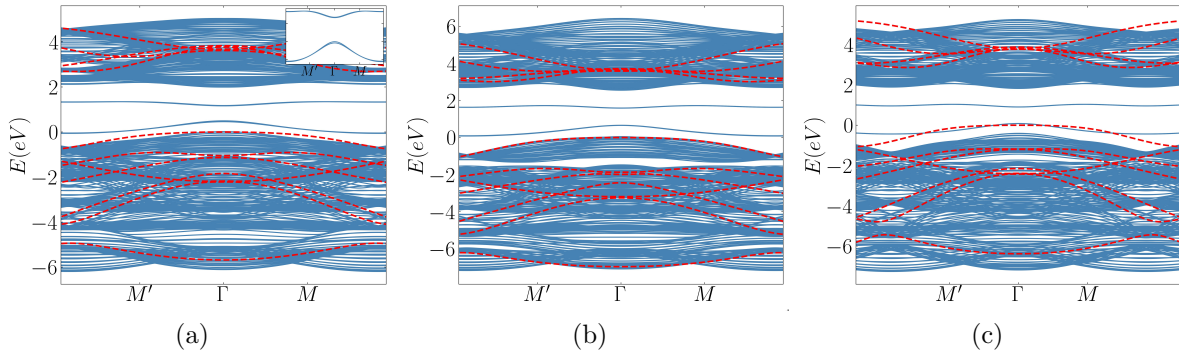


FIGURE 5.5 – Dispersions of AR (a) MoSe₂, (b) WS₂, and (c) WSe₂ NRs in solid blue lines. In dotted red lines is the band structure of the 2D material correspondent for each nanoribbon along the path $M'-\Gamma-M$.

It was already obtained experimentally NRs with controllable width up to 8000 nm and lengths up to 50 microns by O₂ etching (MoS₂, WS₂, MoSe₂, WSe₂) where application on devices, and be templates to synthesize new lateral or vertical heterostructures. The NRs showed chemical stability at high temperatures (CANTON-VITORIA *et al.*, 2023).

5.3.2 NRs on the 1T phase

Now, our attention shifts to materials characterized by the 1T phase as the stable allotrope. As discussed earlier, along the typical AR and ZZ terminations—where the chemical termination on ZZ edges is MC—we introduce additional chemical terminations

on the edges, namely Metal-Metal (MM) and Chalcogen-Chalcogen (CC), as depicted in Fig.(5.1b). These terminations arise since the chalcogens are not aligned vertically. The first TMDNR being investigated featuring the 1T phase as the most stable is ZrSe_2 .

It can be seen from Fig.(5.6) that across different terminations, certain subbands may either appear or remain absent. For instance, in Fig. (5.6a), for the MC termination, four dispersions seem detached from the bulk states, suggesting their potential association with edge states. Upon plotting the wave function, we observe that state 1 primarily arises from chalcogens located at the edges, while states 2 to 6 predominantly originate from the metal. Now considering the NR with edges composed of metal on the edges, state 1 disappears and states 2 to 6 remain, corroborating that they are in fact due to the metal as can be inferred from the plot of the wavefunction, as shown in Fig.(5.6b). Finally, when we have only chalcogens on the edges, the states 2 to 6 disappear, remaining only state 1, which shows, by its wave function, that it is only due to the chalcogen, as depicted in Fig.(5.6c).

For the ZrSe_2 -AR-NR, we have the following dispersion shown in Fig.(5.7). From the plot of the wave function for the states circled, the confinement of the wave function on the edges is not observed. On the contrary, the nodal behavior of the wavefunction, which is a characteristic of bulk states, is verified.

Continuing our investigation, we present the dispersion of the 1T- ZrS_2 -NR with ZZ edges with the different chemical terminations, as depicted in Fig.(5.8). Notably, the dispersions closely resemble those of the ZrSe_2 NR, featuring four distinct edge states, where state 1 originates from the chalcogens on the edges, while states 2 to 4 predominantly arise from the metals. This observation is justified by the similarity in chemistry between these two compounds, with the only variation being in the chalcogens. Furthermore, we observe a shift in the spectrum of subbands below zero towards negative energies. In addition, similarly to the ZrSe_2 NR, alterations in edge compositions lead to the appearance or disappearance of subbands, influenced upon the termination. In our investigation of this particular NR, we opt not to explore the AR edges. This is due to the similarity observed with ZrSe_2 , where no discernible edge states are observed. This similarity in behavior suggests that the electronic properties and edge phenomena in this NR, akin to ZrSe_2 , may not be significantly influenced by the AR termination.

In the case of SnSe_2 NRs, we observe the emergence of three edge states for the MC termination, as depicted in Fig.(5.9a). Specifically, the two low-energy subbands near zero energy localize on the chalcogens positioned on opposite sides of the NR, while state 3 originates from the metal at the edge. Conversely, for NRs featuring metallic edges, illustrated in Fig.(5.9b), only two double-degenerate edge states are evident. Notably, state 1 in Fig.(5.9b) is a combination of states 1 and 2 in Fig.(5.9a), indicating that these two edge states degenerate under MM termination. Additionally, state 2 in Fig.(5.9b) is

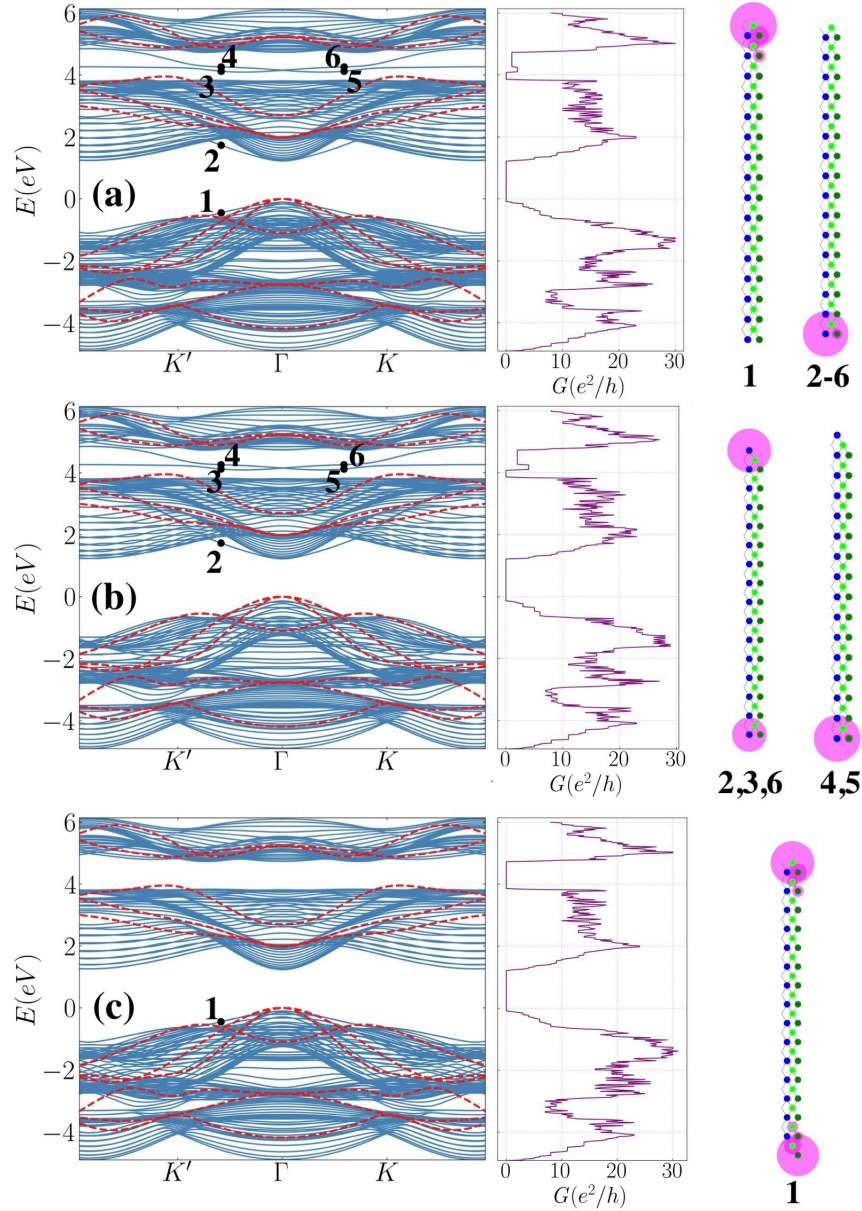


FIGURE 5.6 – Band dispersion for the 1T-ZrSe₂-NR with ZZ with edge terminations of (a) MC (b) MM and (c) CC in solid blue lines. In dotted red lines is the band structure for the 2D-ZrSe₂ 11 band TB model plotted along the path K' - Γ - K . At the bottom of each dispersion is shown the lead and in pink circles where the wave function is localized. The numbers label the subbands and are associated with the wave functions.

also doubly degenerate and arises from the metal on opposite sides of the NR. Lastly, for the CC termination, only one edge state is present, originating from the chalcogen on the edges, while the edge states due to the metal disappear in this configuration, as one may expect.

The dispersion for the AR-NR configuration is depicted in Fig.(5.10). In this arrangement, only two edge states are discernible, and each of them exhibits double degeneracy. The associated wave function for each edge is illustrated at the bottom of Fig.(5.10). Notably, for the edge state labeled as 1, it becomes evident that the innermost chalcogens

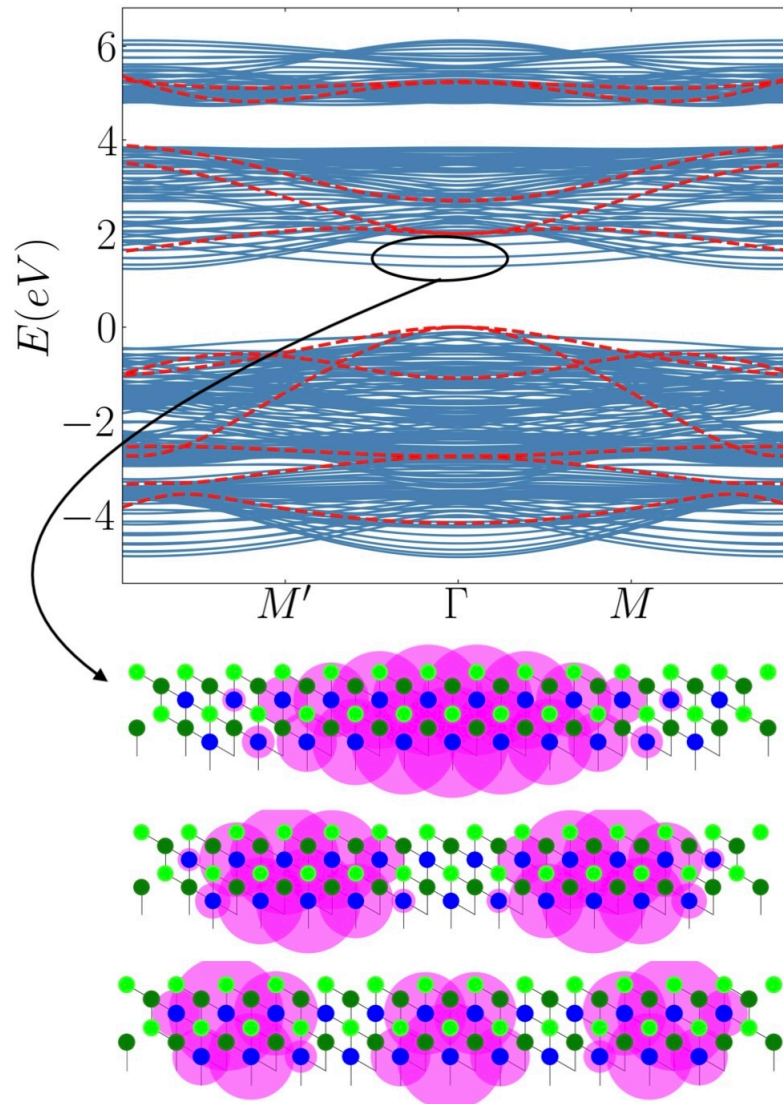


FIGURE 5.7 – Band dispersion for the 1T-ZrSe₂-NR with AR edges in solid blue lines. In dotted red lines is the band structure for the 2D-ZrSe₂ 11 band TB model plotted along the path M'- Γ -K. The plot of the wavefunctions of the states circled is shown at the bottom of the panel.

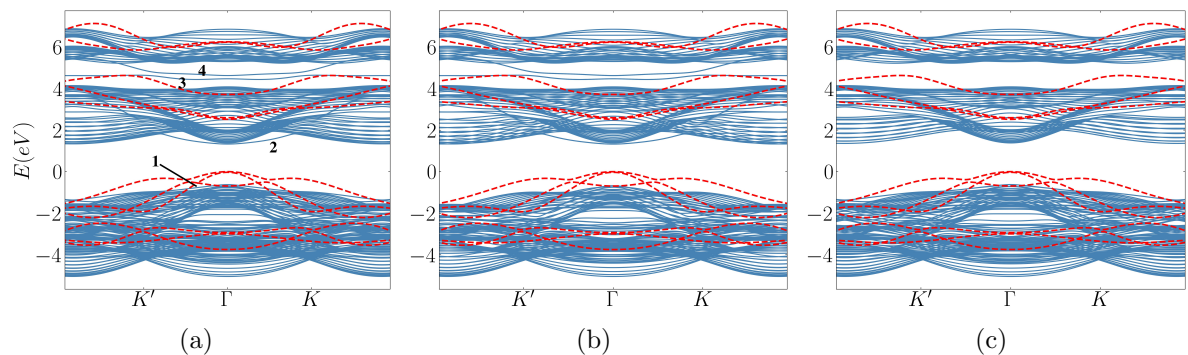


FIGURE 5.8 – Band dispersion for the ZrS₂ NR with edge terminations of (a) MC (b) MM (c) CC in solid blue lines. In dotted red lines is the band structure for the 2D-ZrS₂ 11 band TB model plotted along the path K'- Γ -K.

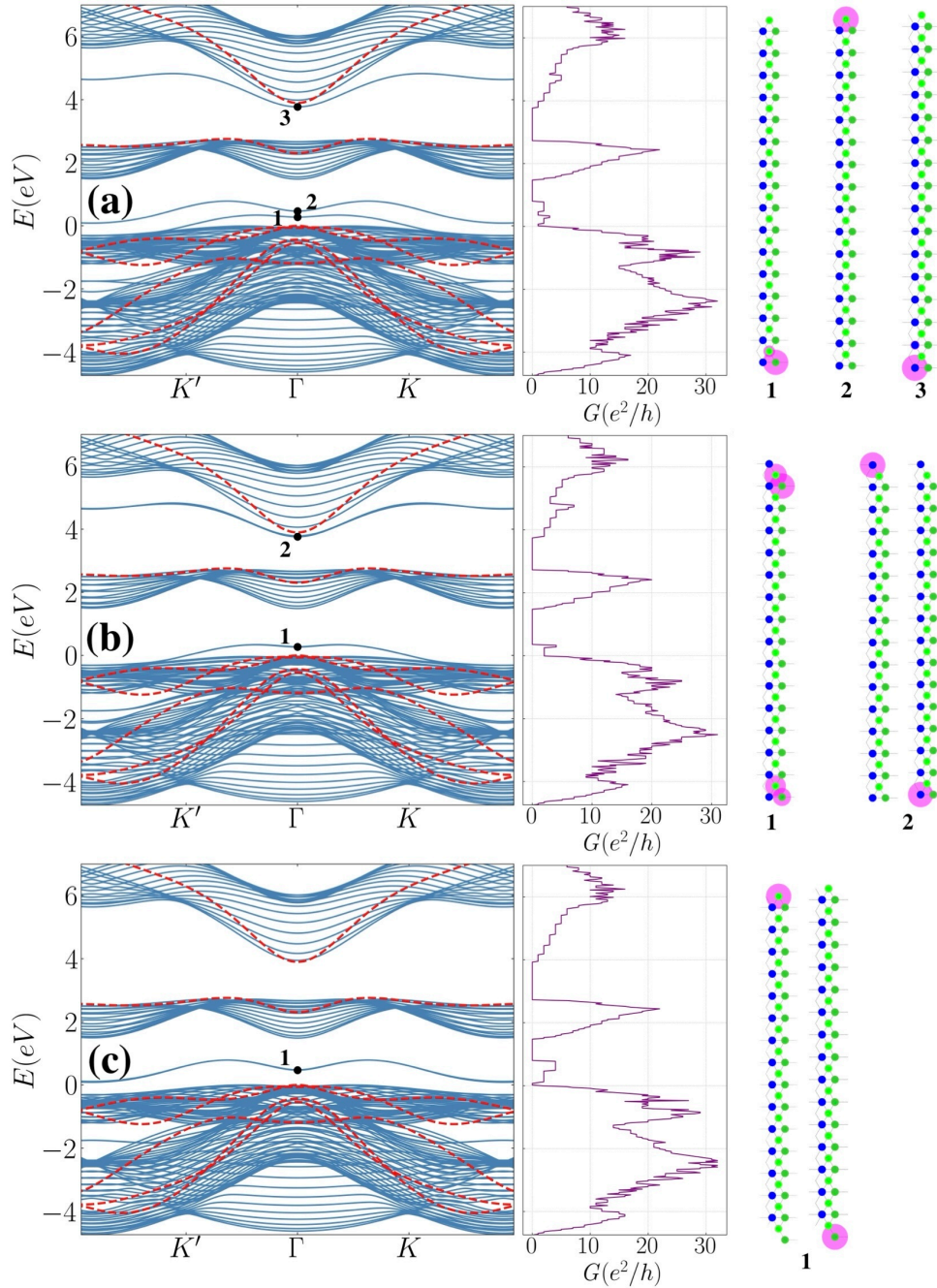


FIGURE 5.9 – Band dispersion for the 1T-SnSe₂-NR with edge terminations of (a) MC (b) MM and (c) CC in solid blue lines. In dotted red lines is the band structure for the 2D-SnSe₂ 11 band TB model plotted along the path K' - Γ - K . At the bottom of each dispersion, the plot of the wavefunctions of the edges states for each state labeled.

along the edges govern the subband, while for state 2, it is the outer chalcogens that are responsible for the edge state. It's noteworthy that in the AR structure, the high-energy edge states present in the ZZ-NR configuration are absent.

In our final investigation, we examine the dispersion of the 1T-SnS₂-NR with ZZ edges under various chemical terminations. As depicted in Fig.(5.11a), for the MC termination, three distinct edge states emerge. Analysis of the wave function plot reveals that each

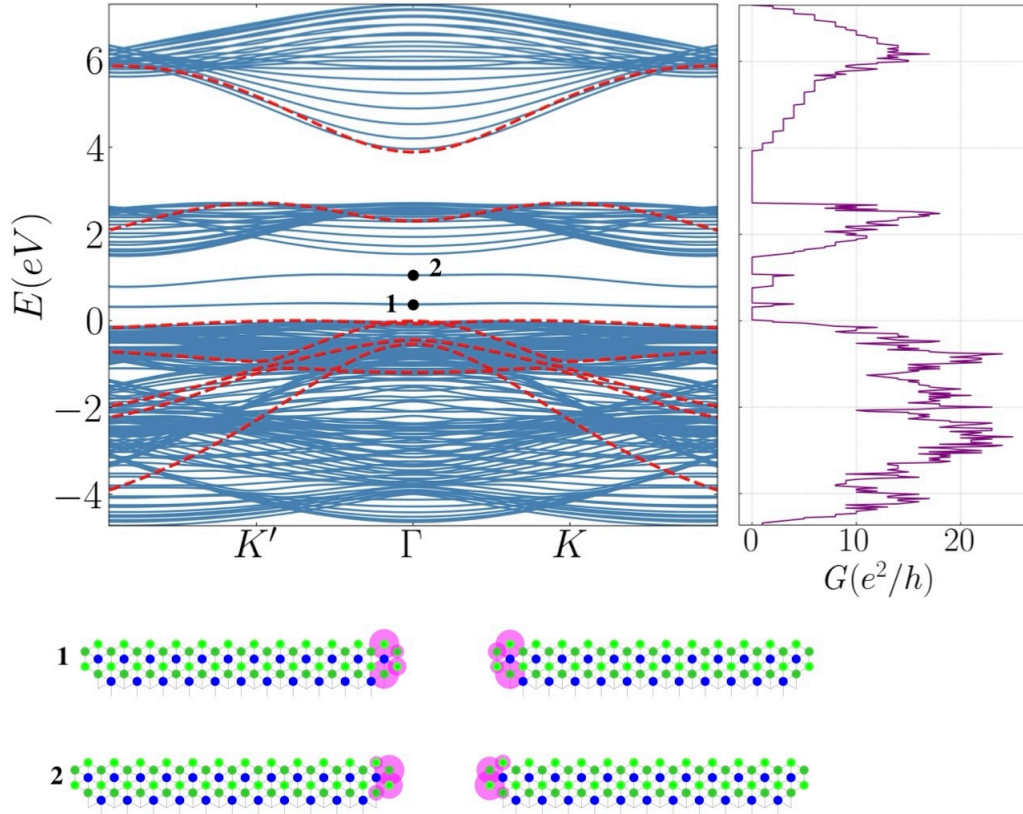


FIGURE 5.10 – Band dispersion for the 1T-SnSe₂-NR with AR edge in solid blue lines. In dotted red lines is the band structure for the 2D-SnSe₂ 11 band TB model plotted along the path $K'-\Gamma-K$. At the bottom of each dispersion, the plot of the wavefunctions of the edges states for each state is labeled.

edge state corresponds to a different compound: state 1 is associated with the dark-green chalcogen positioned beneath the metal, while state 2 arises from the light-green chalcogen, and state 3 originates from the metal. Upon transitioning to MM edges, an additional metallic edge state (state 4) emerges due to the presence of metal on both sides. Meanwhile, the edge states associated with the chalcogens persist, albeit with multiple crossings not observed in the MC termination. Finally, under CC termination, the metallic edge states vanish, leaving only the states associated with the chalcogens, as illustrated in Fig.(5.11c). These states appear nearly degenerate and detached from the subbands associated with the bulk.

For the SnS₂-NR featuring AR edges, the obtained edge states are illustrated in Fig.(5.12). Notably, the chalcogen atoms play a crucial role in all the observed edge states, with their positions influencing the electronic behavior significantly. Interestingly, there's a notable degeneracy observed among the pairs of edge states, suggesting a strong correlation or similarity in their electronic properties.

In this chapter, we explored the effect of confinement and edge terminations NRs based on TMDs across both allotrope phases, 2H and 1T. We observed a reduced band gap and the emergence of edge states due to confinement in all systems under investigation, except

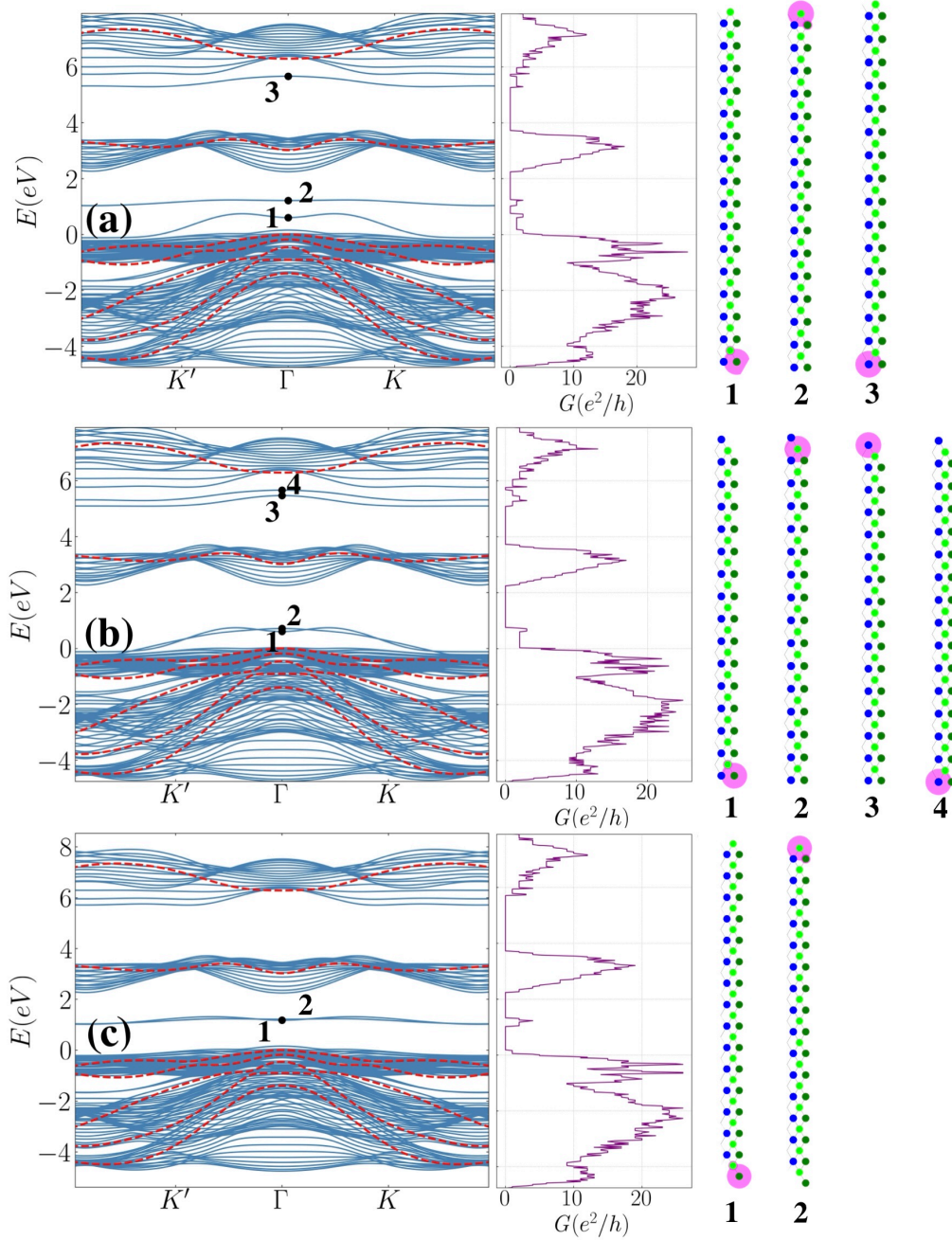


FIGURE 5.11 – Band dispersion for the 1T-SnS₂-NR with edge terminations of (a) MC (b) MM and (c) CC in solid blue lines. In dotted red lines is the band structure for the 2D-SnS₂ 11 band TB model plotted along the path K'- Γ -K. At the bottom of each dispersion, the plot of the wavefunctions of the edge states for each state is labeled.

for the AR termination of ZrSe₂ and ZrS₂, where no edge states were evident. Furthermore, our utilization of the *ab initio* derived TB model obtained from the wannierization procedure proved its value, showcasing its efficacy in exploring confinement effects that are computationally intensive or even infeasible via direct *ab initio* calculations.

In the case of NRs belonging to the 2H phase and featuring AR edges, namely MoS₂, MoSe₂, WS₂, and WSe₂, a consistent feature emerges: two doubly degenerated edge states are observed in each system. While this could underscore the generality of certain edge-

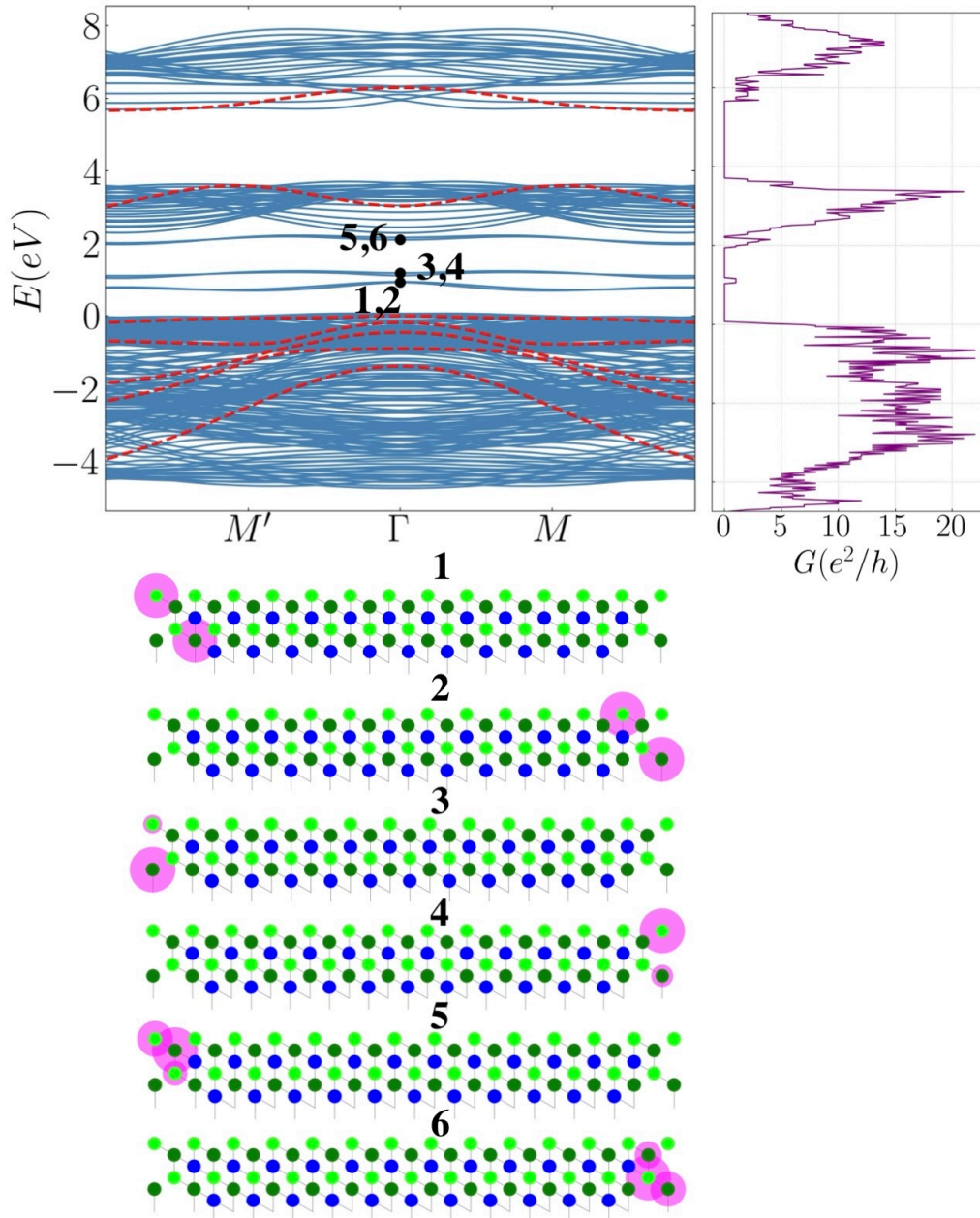


FIGURE 5.12 – Band dispersion for the 1T-SnS₂-NR with AR edge in solid blue lines. In dotted red lines is the band structure for the 2D-SnS₂ 11 band TB model plotted along the path K'- Γ -K. At the bottom of each dispersion, the plot of the wavefunctions of the edge states for each state is labeled.

related phenomena, subtle distinctions also manifest. For instance, in MoSe₂, a slightly broken degeneracy is noted in the subband at the Γ point. Similarly, WSe₂ exhibits a noteworthy shift in the position of the valence band relative to the bulk bands, suggesting distinct electronic properties compared to its counterparts. Importantly, across all these systems, the origin of the edge states can be attributed to the presence of metallic atoms along the edges. Furthermore, the observed semiconducting behavior underscores the fundamental electronic characteristics exhibited by these NRs.

In the case of ribbons featuring the 2H phase as the most stable allotrope, a uniform

electric field was applied along the translational symmetry vector \vec{a}_2 to simulate the effect of charge accumulation on the edges, driven by the nonzero bulk polarization inherent in these materials. This manipulation resulted in the manifestation of metallic behavior across all these ribbons.

Interestingly, the presence or absence of edge states varied depending on the chemical terminations employed with the ZZ edges. For instance, in the ZrSe₂ NR with MC terminations, the edge state of the valence band was primarily attributed to the chalcogen, while the edge state of the conduction band stemmed from the metal along the ribbon's edge. Conversely, when both edges were composed of metal, the valence edge state vanished, leaving only the conduction edge states. Similarly, for chalcogen termination, only the valence edge states persisted, as they were associated solely with the chalcogen. This chemical and confinement similarity extended to the ZrS₂ NR as well, where a comparable shift of the valence bands down in energy concerning the bulk bands was observed, reinforcing the consistency of these phenomena across similar materials.

In the case of the SnSe₂ NR, the edge states near the valence bands are predominantly due to the chalcogen, while those within the energy range of the conduction bands are attributed to the metal, specifically for ribbons with MC edges. Upon examination of ribbons with MM edges, an anticipated disappearance of one chalcogen-associated edge state occurs, along with the emergence of two doubly degenerated edge states related to the metal within the conduction band energy range. Conversely, for ribbons with CC edges, only the low-energy, doubly degenerated edge state persists. Additionally, in NRs featuring AR edges, two edge states positioned just above the valence bands, exhibit double degeneracy and showing wavefunctions primarily associated with the chalcogen at the edges.

Similar observations hold for the SnS₂-NR. Under the MC termination, the characteristics of the edge states, including their quantity and nature, closely resemble those of the SnSe₂-NR. However, for MM edges, degeneracies among the edge states are notably absent, with low-energy subbands remaining chalcogen-associated and high-energy subbands associated with the metal. As anticipated, CC edges exhibit solely low-energy edge states, displaying near degeneracy.

In summary, this throughout analysis of edge states that emerge due to confinement effects enables us to investigate how the propagation of plane waves on such NRs, with diverse scattering regions. We verified that the lattice (or chemical terminations) of the edges plays an important role once one desires to build devices based on TMDNRs, since depending on the edges, one can have conductance in certain regions of the bulk band gap or not.

Our comprehensive examination of edge states arising from confinement effects paves

the way for investigating the propagation of plane waves in these NRs, encompassing various scattering regions and disorder effects. Our findings underscore the important role of edge lattice configurations, or chemical terminations, in the development of TMDNR-based devices. Depending on the specific edge configurations, the presence or absence of conductance within certain regions of the bulk band gap can be observed, highlighting the significance of edge engineering in tailoring the electronic properties of these nanostructures.

6 van der Waals heterostructures nanoribbons

6.1 Introduction

In Chapter 5, we conducted a comprehensive investigation of NRs derived from monolayers of TMDs. Our investigation aimed to understand the influence of confinement on these systems, with a specific focus on the structural patterns and chemical compositions of their edges. Throughout that analysis, the emergence of edge states is intricately tied to both the confinement effect and the configurations of the edges. Thus, an examination of these factors is important for a comprehensive understanding of NR properties.

To advance our exploration of NRs, we now focus on NRs derived from vdW heterostructures, referred to here as vdWNRs. In this chapter, our objective is to investigate how the conductance of these highly hybridized structures is influenced by the length of the vdWNR and by an electric field along the stacking direction. Furthermore, we aim to elucidate how these structures can be useful as effective platforms for simulating the dynamics of vdW qubits.

We have explored the experimental assembly of vdW heterostructures, highlighting their significance, versatility, and immense potential for technological applications, including quantum technologies (CHOWDHURY *et al.*, 2020b). The formation of heterostructures aims to uncover novel properties and interactions between the constituent 2D materials, with possible implications for quantum technologies and other applications. Despite the challenges associated with the experimental fabrication of multilayer TMDNRs, substantial progress has been made by researchers in this field, advancing our understanding and capabilities in creating these complex structures.

The remarkable stability of TMDNRs, achievable through specific edge configurations, provides significant advantages for studying their properties under diverse experimental conditions (DAVELOU *et al.*, 2017). This stability facilitates research into potential applications, including the synthesis of multilayer TMDNRs via bottom-up methods. These multilayer nanoribbons have exhibited photoluminescence behavior comparable to mono-

layer ribbons under ambient conditions, stimulating further investigations into the interplay between exciton-polariton modes, photonic cavity modes, and decay channels in one-dimensional crystals (CHOWDHURY *et al.*, 2020a). Nanowires are proving to be valuable for optimizing the coupling between quantum dots since this coupling allows the hosting of Majorana bound states (BORDIN *et al.*, 2023). For example, Chen *et al.* successfully prepared MoO₃/MoS₂ nanowires, demonstrating the practical applications of these nanostructures (CHEN *et al.*, 2011).

In the field of quantum information science, the modulation of the Moiré potential landscape—from arrays of quantum dots to stripes of nanowires—can be achieved by applying uniaxial strain in a h-BN encapsulated WSe₂/MoSe₂ twisted hetero-bilayer (BAI *et al.*, 2020). Additionally, electrically driven single-photon emission has been demonstrated in vertically layered heterostructures composed of WSe₂ or WS₂ flakes, which are separated by h-BN layers to facilitate the tunneling of electrons and holes (PALACIOS-BERRAQUERO *et al.*, 2016; CLARK *et al.*, 2016).

6.2 ZrSe₂/SnSe₂ heterostructure nanoribbon

Based on recent findings highlighting the potential of these systems in quantum computation, we aim to investigate a vdWNR composed of 2D materials with highly hybridized states in their band structure. For this study, we have selected the ZrSe₂/SnSe₂ system as a representative example. The structural parameters discussed in section 3.2 and the band structure of this 2D material at different gate fields has already been shown in Fig.(4.13), where the changes in orbital contributions in the two lowest conduction bands due to the application of the field in the stacking direction were discussed. Additionally, the subbands of nanoribbons based on each individual material were examined in Chapter 5, along with a discussion on the emergence of edge states.

Figure 6.1 provides a schematic view of the vdWNR. Dark-blue atoms represent Zr, while purple, green, and orange atoms represent Se from the bottom and top layers, forming the scattering region. Red atoms indicate the leads attached to the layers composing the vdWNR. In this figure, leads A and B are connected to the bottom layer, and lead C is connected to the top layer. These leads are derived from the hoppings within the vdWNR, with intralayer hoppings excluded, reflecting the dispersion characteristics of ZrSe₂ and SnSe₂ nanoribbons. During the quantum transport simulations, the leads are fixed at a width of approximately 60 nm.

In the wannierization procedure, discussed in section 2.3, we consider a multi-orbital model. Zirconium is represented by a 3×3 matrix corresponding to the orbitals d_{z^2} , d_{xy} , and $d_{x^2-y^2}$. Similarly, Selenium is represented also by a 3×3 matrix corresponding to

the p orbitals. Each solid black line in the scattering region and the red lines in the leads represent hopping interactions, which can occur between different orbitals on the same atom or between orbitals on different atoms. Here, our objective is to determine if the

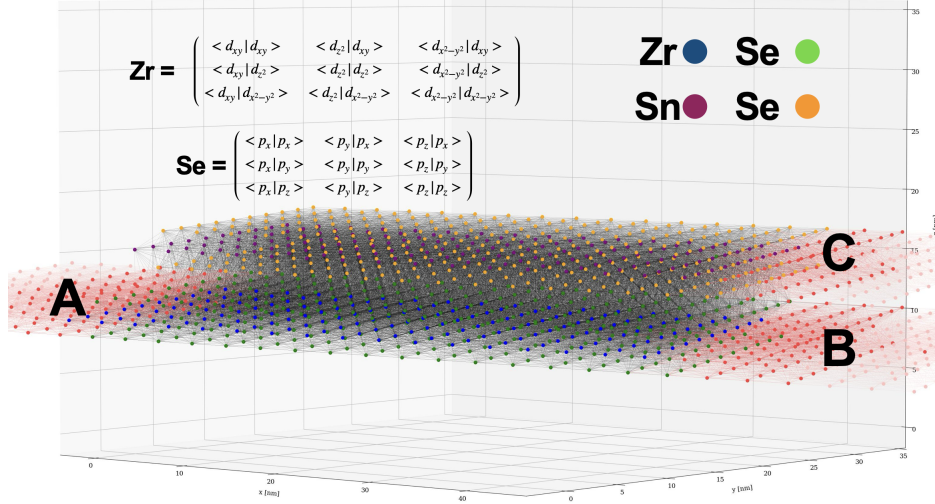


FIGURE 6.1 – vdWNR composed by a central scattering region with leads attached on the bottom layer (A and B) and the top layer (C).

hybridization observed in the 2D material persists in the NR based on the heterostructure. Specifically, we aim to assess how the conductance at lead C is influenced by the length (L) of the ribbon and the application of an electric field in the stacking direction when plane waves enter the scattering region solely through lead A.

6.3 Transport properties

Figure 6.2 presents the conductance results for a vdWNR with a length of approximately 115 nm, consisting in a system with 8745 atoms. Here, G_B and G_C represent the conductances measured at leads B and C, respectively. Notably, within the energy range (ΔE) between 1.4 and 2.8 eV, highlighted by the dark-grey rectangle, conductance is observed at lead C, despite electrons being injected solely at lead A. This phenomenon highlights the role of hybridized states in facilitating electron transmission between layers. Our next objective is to examine how the conductance G_C is modified when the vdWNR has different lengths L . To quantify this, we define the average conductance \bar{G} at lead C within the energy interval ΔE as follows:

$$\bar{G} = \frac{1}{N_E} \sum_{i=1}^{N_E} G_C(E_i), \quad (6.1)$$

where N_E represents the number of energy divisions within the interval where conductance is measured, and $G_C(E_i)$ is the conductance at a specific energy E_i within this interval.

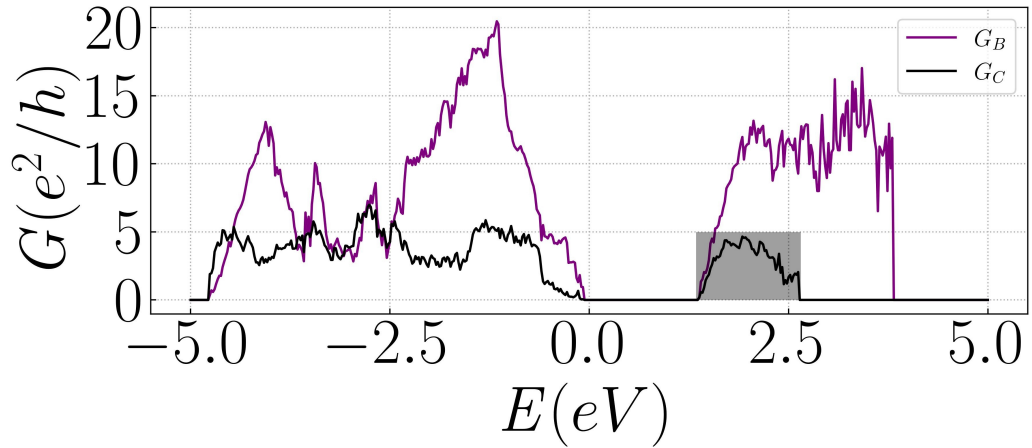


FIGURE 6.2 – Conductance on leads B (G_B) and C (G_C) for a vdWNR with a length of 115 nm.

From Fig.(6.3), we illustrate the impact of increasing the length of the vdWNR on the conductance \bar{G} . The length of the vdWNR is determined by the product of the dimension L and the lattice constant along the periodic direction \vec{a}_1 . Initially, the conductance rises as the length increases until it reaches $L = 15$ nm, resulting in a vdWNR length of approximately 57 nm. Subsequently, an oscillatory conductance behavior emerges, stabilizing around $L = 60$ nm, corresponding to a vdWNR length of about 230 nm (consisting in 4545 atoms), with the conductance plateauing at approximately $3.4 e^2/h$. A fitted curve of the data \bar{G} , following the form $G = G_0 e^{-L_0/L}$, is also presented.

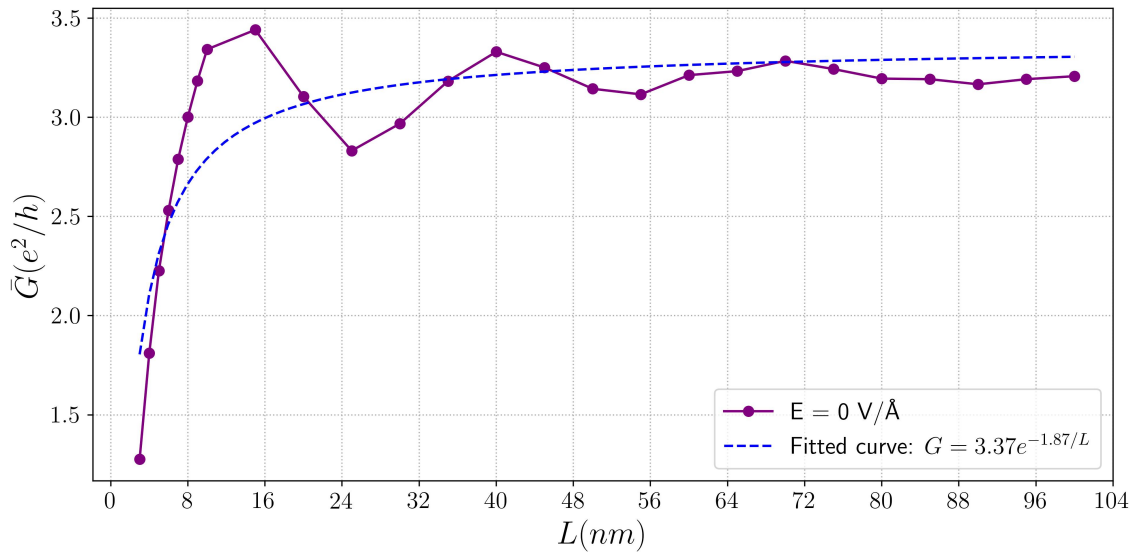


FIGURE 6.3 – Mean value of the conductance on lead C for a vdWNR with different lengths.

This oscillatory behavior mirrors the transmission coefficient of a potential barrier, where in our case, the length of the vdWNR acts as the thickness or quantity of barrier

(DAKHLAOUI *et al.*, 2021).

The conductance of a ribbon with 230 nm we observe the behavior of \bar{G} with different gate fields, as shown in Fig.6.4. As expected from the results of Chapter 4 regarding how the orbital composition of the band structure changed with the application of a gate field on the stacking direction. For negative electric fields, the conductance \bar{G} is

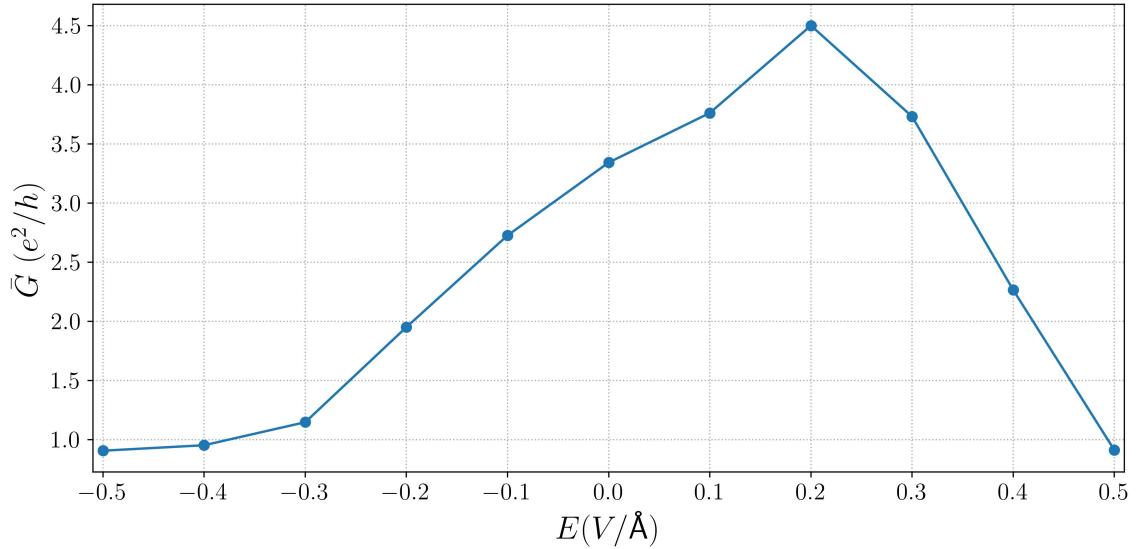


FIGURE 6.4 – Mean value of the conductance on lead C for a vdWNR with 230 nm subjected to different gate fields in the stacking direction.

suppressed, indicating that the wave function is mainly concentrated on the bottom layer. The conductance increases up to a field strength of 0.2 V/Å , beyond which it is again suppressed. This suppression occurs due to the shift in the band structure of the outer lead caused by the electric field, which reduces the number of available channels for the wave exiting the scattering region. At this field strength, the concentration of the wave function on the top layer is insufficient to counterbalance the shift in the band structure, resulting in a net decrease in conductance.

The dispersions of the outer lead are shown in Fig.(6.5), where one can observe that from the dispersions in the energy range where we are interested in observing the behavior of the conductance are indeed shifted in energy, resulting in a decreasing of available modes in which the wave function can propagate out of the scattering region. The utilization of these platforms as host materials for charge qubits has already demonstrated promising results in terms of coherence times and operational temperatures, reaching up to 120 K. This temperature range is considered high compared to other solid-state-based qubits (CAO *et al.*, 2022).

Our investigation of vdWNRs composed of 2D materials with highly hybridized states reveals their potential for quantum computation applications. Focusing on the $\text{ZrSe}_2/\text{SnSe}_2$ system, we examined the impact of confinement and electric fields on their transport

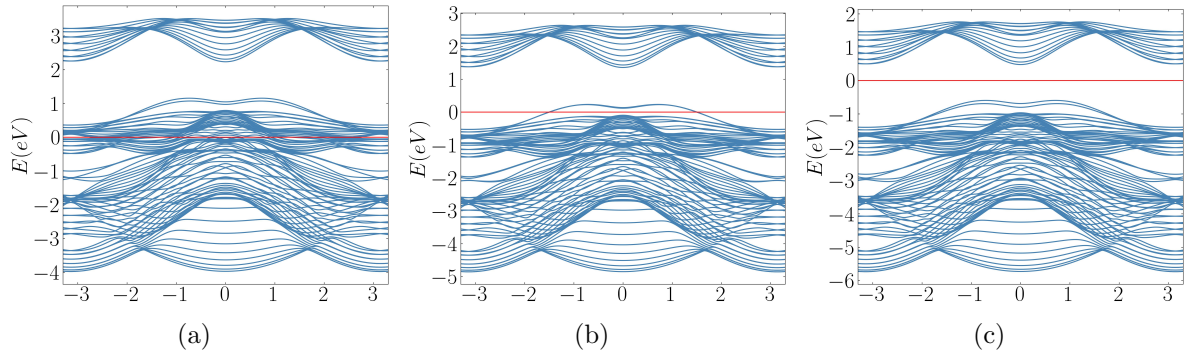


FIGURE 6.5 – Band dispersion for the lead C subjected to a field of (a) -0.5 V/\AA (b) 0 V/\AA (c) 0.5 V/\AA in solid blue lines.

properties. Our analysis demonstrated that even in nanoribbon form, hybridization observed in the 2D materials persisted, enabling electron transmission between layers. The conductance results for a vdWNR of approximately 115 nm in length showed significant conductance at lead C, despite electrons being injected only at lead A, as seen in Fig.(6.2). Further, we explored the effect of varying the length of the vdWNR on conductance. Figure 6.3 illustrated that conductance increased with length up to 57 nm, beyond which it exhibited oscillatory behavior, stabilizing around 230 nm. This behavior is consistent with the transmission coefficient of a potential barrier, where the length of the vdWNR acts as the barrier's thickness. Additionally, the application of gate fields along the stacking direction showed that conductance could be modulated. Figure 6.4 revealed that for negative electric fields, conductance decreased, indicating a wave function concentration on the bottom layer. Conductance increased up to a field strength of 0.2 V/\AA , beyond which it decreased again due to a shift in the band structure, as illustrated in Fig.(6.5). Our findings confirm the promising characteristics of these vdWNRs for charge qubit applications, paving the way for further exploration and development of vdW heterostructures in quantum computing technologies.

7 Conclusions

In this study, we harness the precision of DFT calculations to derive *ab initio* Tight-Binding Hamiltonians for vdW heterostructures composed of monolayers of transition metal dichalcogenides (TMDs). By applying Wannier transformation to the Bloch wave functions, we investigate the structural and electronic properties of 10 TMDCs monolayers in both of their possible allotropic phases (T and H), resulting in an analysis of 20 systems.

Our primary objective is to explore the potential combinations of material pairs to form heterostructures suitable platforms for vdW qubits. To achieve accurate energy levels critical for states' superposition from different materials, we utilized DFT calculations with the HSE06 exchange-correlation functional. Additionally, minor stress adjustments were applied to ensure the unit cells were commensurable for layers exhibiting good lattice matching.

The TB model obtained via Wannierization leverages a basis of Maximally Localized Wannier Functions derived from DFT calculations, without empirical parameters or fitting procedures. This simplified model, which includes first and second neighbor hoppings, is entirely determined by the overlap integrals of the projection orbitals and matrix elements from the full *ab initio* calculation, incorporating quasi-particle effects. To truncate the sparse Hamiltonian and retain only certain hoppings, two parameters are essential: d_{hop} , which controls the maximum distance between hopping orbitals, and $|hop|$, which sets the lower bound of the magnitude of hoppings. These parameters are critical for achieving high fidelity with *ab initio* results, as they impact the agreement of the DFT and TB band structures, the band gaps, and the orbital character, all of which are crucial for the composition of qubit states. Therefore, carefully selecting and analyzing these parameter values is vital, as they determine the presence or absence of hoppings between specific orbitals, directly influencing the accuracy of the model and effectiveness.

We compared the accuracy of our TB model, derived through the previously described methodology, with a pure DFT calculation of the ZrSe₂/SnSe₂ heterostructure reported earlier. Our findings revealed a slight offset in the energy levels of the conduction bands of the individual layers, which promotes the mixing of states from the different materials within the heterostructure. By applying the criterion of seeking material pairs with en-

ergy level offsets less than 0.6 eV relative to the vacuum level, we identified 222 potential candidates suitable for hosting a vdW qubit. Our TB model, obtained via the Wannierization procedure, accurately replicated the band gap and orbital character of the *ab initio* results, demonstrating its precision and reliability.

We investigated some heterostructures in addition to the ZrSe₂/SnSe₂ system, including HfS₂/SnS₂, ZrS₂/SnS₂, and ZrS₂/HfS₂. All these systems exhibited band structure hybridization due to the near alignment of the energy levels of the individual layers. As previously mentioned, the parameters $|hop|$ and d_{hop} play a crucial role in achieving agreement between DFT and TB results. However, we observed that the control of the orbital composition of the bands changed rapidly with an electric field, requiring a field strength an order of magnitude smaller than that needed for the DFT calculations. To enhance the TB model, we incorporated local effects and polarization by adjusting the onsite term to include a screened field that accounts for polarization effects. This was done by considering the dielectric constant of the heterostructure, leading to improved agreement between the DFT and TB models.

With these enhancements, we developed an accurate model based on DFT calculations with hybrid functionals. This model, utilizing inexpensive computational resources, reproduces the control of orbital character with the fidelity of full *ab initio* results. This versatility in modeling the electronic properties of vdW heterostructures is a promising feature for developing new qubit architectures.

In conclusion, to investigate the transport properties of nanoribbons based on van der Waals heterostructures derived from *ab initio* TB Hamiltonians, we first examined the electronic properties and confinement effects on nanoribbons composed of monolayer TMDs. As a benchmark for our TB Hamiltonians, we studied nanoribbons based on MoS₂ and validated our results against existing literature, particularly regarding the emergence of edge states for different edge configurations (zig-zag or armchair). Upon confirming the accuracy of our Hamiltonian, we extended our investigation to several other TMD nanoribbons (MoS₂, MoSe₂, WS₂, WSe₂, ZrSe₂, ZrS₂, SnSe₂, SnS₂) exploring the effects of edge patterns and chemical terminations to elucidate their impact on the nanoribbons.

Finally, we focused on a vdW nanoribbon based on the ZrSe₂/SnSe₂ heterostructure, known for its highly hybridized between the two layers to examine the impact of hybridization on the transport properties of the vdW nanoribbon. Specifically, whether the information could be transmitted from one layer to another. We found that the length of the nanoribbons plays a significant role in the conductance of a three-terminal system, where electrons injected into one layer are transmitted to the other layer even without an electric field. By applying an electric field, we observed that the conductance on the top layer could be tuned, highlighting the potential of these systems for use in solid-state platforms for quantum computing.

Bibliography

ALAM, M. H.; CHOWDHURY, S.; ROY, A.; BRAGA, M. H.; BANERJEE, S. K.; AKINWANDE, D. Direct growth of mos_2 on electrolytic substrate and realization of high-mobility transistors. **Phys. Rev. Materials**, v. 5, p. 054003, May 2021.

ALBERS, W.; VERBERKT, J. The snse-snse_2 eutectic; ap-n multilayer structure. **J Mater Sci**, v. 5, p. 24–28, 1970.

ANDRADE, E.; PANTALEÓN, P. A.; GUINEA, F.; NAUMIS, G. G. Flat bands and electronic localization in twisted bilayer graphene nanoribbons. **Phys. Rev. B**, American Physical Society, v. 108, p. 235418, Dec 2023 .<https://link.aps.org/doi/10.1103/PhysRevB.108.235418>.

ARETOULI, K. E.; TSOUTSOU, D.; TSIPAS, P.; MARQUEZ-VELASCO, J.; GIAMINI, S. A.; KELAIDIS, N.; PSYCHARIS, V.; DIMOULAS, A. Epitaxial 2d $\text{snse}_2/2\text{d wse}_2$ van der waals heterostructures. **ACS Applied Materials & Interfaces**, v. 8, n. 35, p. 23222–23229, PMID: 27537619, 2016. <https://doi.org/10.1021/acsami.6b02933>.

ARUTE, F.; ARYA, K.; BABBUSH, R. Quantum supremacy using a programmable superconducting processor. **Nature**, v. 574, p. 505–510, 2019. <https://doi.org/10.1038/s41586-019-1666-5>.

ASHCROFT, N. W.; MERMIN, N. D. **Solid State Physics**. [*S.l.*]: Holt-Saunders, 1976.

AUWÄRTER, W.; KREUTZ, T.; GREBER, T.; OSTERWALDER, J. Xpd and stm investigation of hexagonal boron nitride on $\text{ni}(111)$. **Surface Science**, v. 429, n. 1, p. 229–236, 1999. ISSN 0039-6028. <https://www.sciencedirect.com/science/article/pii/S0039602899003817>.

BAI, Y.; ZHOU, L.; WANG, J. Excitons in strain-induced one-dimensional moiré potentials at transition metal dichalcogenide heterojunctions. **Nat. Mater**, v. 19, p. 1068–1073, 2020. <https://doi.org/10.1038/s41563-020-0730-8>.

BARONE, V.; CASARIN, M.; FORRER, D.; PAVONE, M.; SAMBI, M.; VITTADINI, A. Role and effective treatment of dispersive forces in materials: Polyethylene and graphite crystals as test cases. **Journal of Computational Chemistry**, v. 30, n. 6, p. 934–939, 2009. <https://onlinelibrary.wiley.com/doi/abs/10.1002/jcc.21112>.

- BASKIN, Y.; MEYER, L. Lattice constants of graphite at low temperatures. **Phys. Rev.**, American Physical Society, v. 100, p. 544–544, Oct 1955.
<https://link.aps.org/doi/10.1103/PhysRev.100.544>.
- BASTOS, C. M. O.; BESSE, R.; SILVA, J. L. F. D.; SIPAHI, G. M. Ab initio investigation of structural stability and exfoliation energies in transition metal dichalcogenides based on ti-, v-, and mo-group elements. **Phys. Rev. Mater.**, American Physical Society, v. 3, p. 044002, Apr 2019.
<https://link.aps.org/doi/10.1103/PhysRevMaterials.3.044002>.
- BECKE, A. D. Density-functional exchange-energy approximation with correct asymptotic behavior. **Phys. Rev. A**, American Physical Society, v. 38, p. 3098–3100, Sep 1988. <https://link.aps.org/doi/10.1103/PhysRevA.38.3098>.
- BERLAND, K.; HYLDGAARD, P. Exchange functional that tests the robustness of the plasmon description of the van der waals density functional. **Phys. Rev. B**, American Physical Society, v. 89, p. 035412, Jan 2014.
<https://link.aps.org/doi/10.1103/PhysRevB.89.035412>.
- BERTRAND, Y.; SOLAL, F.; LEVY, F. Experimental band structure of 2h-snse2 by synchrotron radiation photoemission spectroscopy. **Journal of Physics C: Solid State Physics**, v. 17, n. 16, p. 2879, jun 1984.
<https://dx.doi.org/10.1088/0022-3719/17/16/007>.
- BHATTACHARYYA, S.; SINGH, A. K. Semiconductor-metal transition in semiconducting bilayer sheets of transition-metal dichalcogenides. **Phys. Rev. B**, American Physical Society, v. 86, p. 075454, Aug 2012.
<https://link.aps.org/doi/10.1103/PhysRevB.86.075454>.
- BISSETT, M. A.; WORRALL, S. D.; KINLOCH, I. A.; DRYFE, R. A. Comparison of two-dimensional transition metal dichalcogenides for electrochemical supercapacitors. **Electrochimica Acta**, v. 201, p. 30–37, 2016. ISSN 0013-4686.
<https://www.sciencedirect.com/science/article/pii/S0013468616307733>.
- BJÖRKMAN, T. Testing several recent van der waals density functionals for layered structures. **The Journal of Chemical Physics**, v. 141, n. 7, p. 074708, 2014. <https://doi.org/10.1063/1.4893329>.
- BLOCH, F. Über die quantenmechanik der elektronen in kristallgittern. **Zeitschrift für physik**, Springer, v. 52, n. 7, p. 555–600, 1929.
- BLOUNT, E. Formalisms of band theory. *In*: SEITZ, F.; TURNBULL, D. (Ed.). Academic Press, 1962, (Solid State Physics, v. 13). p. 305–373.
<https://www.sciencedirect.com/science/article/pii/S0081194708604592>.
- BOIX-CONSTANT, C.; MAÑAS-VALERO, S.; CÓRDOBA, R.; CORONADO, E. Van der waals heterostructures based on atomically-thin superconductors. **Advanced Electronic Materials**, v. 7, n. 7, p. 2000987, 2021.
<https://onlinelibrary.wiley.com/doi/abs/10.1002/aelm.202000987>.

- BORDIN, A.; WANG, G.; LIU, C.-X.; HAAF, S. L. D. ten; LOO, N. van; MAZUR, G. P.; XU, D.; DRIEL, D. van; ZATELLI, F.; GAZIBEGOVIĆ, S.; BADAWY, G.; BAKKERS, E. P. A. M.; WIMMER, M.; KOUWENHOVEN, L. P.; DVIR, T. Tunable crossed andreev reflection and elastic cotunneling in hybrid nanowires. **Phys. Rev. X**, American Physical Society, v. 13, p. 031031, Sep 2023. <https://link.aps.org/doi/10.1103/PhysRevX.13.031031>.
- BORN, M. Zur quantenmechanik der stoßvorgänge. **Z. Physik**, v. 37, p. 863–867, 1926. <https://doi.org/10.1007/BF01397477>.
- BORN, M.; OPPENHEIMER, R. Zur quantentheorie der molekeln. **Annalen der Physik**, v. 389, n. 20, p. 457–484, 1927. <https://onlinelibrary.wiley.com/doi/abs/10.1002/andp.19273892002>.
- BOUCHIAT, V.; VION, D.; JOYEZ, P.; ESTEVE, D.; DEVORET, M. H. Quantum coherence with a single cooper pair. **Physica Scripta**, v. 1998, n. T76, p. 165, jan 1998. <https://dx.doi.org/10.1238/Physica.Topical.076a00165>.
- BREDE, J.; MERINO-DÍEZ, N.; BERDONCES-LAYUNTA, A. Detecting the spin-polarization of edge states in graphene nanoribbons. **Nat Commun**, v. 14, p. 6677, 2023.
- BREY, L.; FERTIG, H. A. Electronic states of graphene nanoribbons studied with the dirac equation. **Phys. Rev. B**, American Physical Society, v. 73, p. 235411, Jun 2006. <https://link.aps.org/doi/10.1103/PhysRevB.73.235411>.
- BUTLER, S. Z.; HOLLEN, S. M.; CAO, L.; CUI, Y.; GUPTA, J. A.; GUTIÉRREZ, H. R.; HEINZ, T. F.; HONG, S. S.; HUANG, J.; ISMACH, A. F.; JOHNSTON-HALPERIN, E.; KUNO, M.; PLASHNITSA, V. V.; ROBINSON, R. D.; RUOFF, R. S.; SALAHUDDIN, S.; SHAN, J.; SHI, L.; SPENCER, M. G.; TERRONES, M.; WINDL, W.; GOLDBERGER, J. E. Progress, challenges, and opportunities in two-dimensional materials beyond graphene. **ACS Nano**, v. 7, n. 4, p. 2898–2926, PMID: 23464873, 2013. <https://doi.org/10.1021/nm400280c>.
- BUTTIKER, M. Symmetry of electrical conduction. **IBM Journal of Research and Development**, v. 32, n. 3, p. 317–334, 1988.
- CAI, J.; RUFFIEUX, P.; JAAFAR, R. Atomically precise bottom-up fabrication of graphene nanoribbons. **Nature**, v. 466, p. 470–473, 2010. <https://doi.org/10.1038/nature09211>.
- CANTON-VITORIA, R.; HOTTA, T.; XUE, M.; ZHANG, S.; KITAURA, R. Synthesis and characterization of transition metal dichalcogenide nanoribbons based on a controllable o₂ etching. **JACS Au**, v. 3, n. 3, p. 775–784, 2023. <https://doi.org/10.1021/jacsau.2c00536>.
- CAO, J.; GANDUS, G.; AGARWAL, T.; LUISIER, M.; LEE, Y. Dynamics of van der waals charge qubit in two-dimensional bilayer materials: Ab initio quantum transport and qubit measurement. **Phys. Rev. Res.**, American Physical Society, v. 4, p. 043073, Oct 2022. <https://link.aps.org/doi/10.1103/PhysRevResearch.4.043073>.

CARR, W. J.; MARADUDIN, A. A. Ground-state energy of a high-density electron gas. **Phys. Rev.**, American Physical Society, v. 133, p. A371–A374, Jan 1964. <https://link.aps.org/doi/10.1103/PhysRev.133.A371>.

CEPERLEY, D. M.; ALDER, B. J. Ground state of the electron gas by a stochastic method. **Phys. Rev. Lett.**, American Physical Society, v. 45, p. 566–569, Aug 1980. <https://link.aps.org/doi/10.1103/PhysRevLett.45.566>.

CHEN, X.; TIAN, F.; PERSSON, C. Interlayer interactions in graphites. **Sci Rep**, v. 3, p. 3046, 2013. <https://doi.org/10.1038/srep03046>.

CHEN, Z.; CUMMINS, D.; REINECKE, B. N.; CLARK, E.; SUNKARA, M. K.; JARAMILLO, T. F. Core-shell moo₃-mos₂ nanowires for hydrogen evolution: A functional design for electrocatalytic materials. **Nano Letters**, v. 11, n. 10, p. 4168–4175, PMID: 21894935, 2011. <https://doi.org/10.1021/nl2020476>.

CHICO, L.; SANCHO, M. P. L.; NOZ, M. C. M. Carbon-nanotube-based quantum dot. **Phys. Rev. Lett.**, American Physical Society, v. 81, p. 1278–1281, Aug 1998. <https://link.aps.org/doi/10.1103/PhysRevLett.81.1278>.

CHIESA, A.; ROCA, S.; CHICCO, S.; ORY, M. de; GÓMEZ-LEÓN, A.; GOMEZ, A.; ZUECO, D.; LUIS, F.; CARRETTA, S. Blueprint for a molecular-spin quantum processor. **Phys. Rev. Appl.**, American Physical Society, v. 19, p. 064060, Jun 2023. <https://link.aps.org/doi/10.1103/PhysRevApplied.19.064060>.

CHOWDHURY, T.; KIM, J.; SADLER, E. Substrate-directed synthesis of mos₂ nanocrystals with tunable dimensionality and optical properties. **Nat. Nanotechnol.**, v. 15, p. 29–34, 2020. <https://doi.org/10.1038/s41565-019-0571-2>.

CHOWDHURY, T.; SADLER, E. C.; KEMPA, T. J. Progress and prospects in transition-metal dichalcogenide research beyond 2d. **Chemical Reviews**, v. 120, n. 22, p. 12563–12591, PMID: 32960576, 2020. <https://doi.org/10.1021/acs.chemrev.0c00505>.

CHRISTIANSEN, P. A.; LEE, Y. S.; PITZER, K. S. Improved ab initio effective core potentials for molecular calculations. **The Journal of Chemical Physics**, v. 71, n. 11, p. 4445–4450, 12 1979. ISSN 0021-9606. <https://doi.org/10.1063/1.438197>.

CLARK, G.; SCHAIBLEY, J. R.; ROSS, J.; TANIGUCHI, T.; WATANABE, K.; HENDRICKSON, J. R.; MOU, S.; YAO, W.; XU, X. Single defect light-emitting diode in a van der waals heterostructure. **Nano Letters**, v. 16, n. 6, p. 3944–3948, PMID: 27213921, 2016. <https://doi.org/10.1021/acs.nanolett.6b01580>.

CLOIZEAUX, J. D. Energy bands and projection operators in a crystal: Analytic and asymptotic properties. **Phys. Rev.**, American Physical Society, v. 135, p. A685–A697, Aug 1964. <https://link.aps.org/doi/10.1103/PhysRev.135.A685>.

COOPER, V. R. Van der waals density functional: An appropriate exchange functional. **Phys. Rev. B**, American Physical Society, v. 81, p. 161104, Apr 2010. <https://link.aps.org/doi/10.1103/PhysRevB.81.161104>.

- DAKHLAOUI, H.; ALMANSOUR, S.; BELHADJ, W.; WONG, B. M. Modulating the conductance in graphene nanoribbons with multi-barriers under an applied voltage. **Results in Physics**, v. 27, p. 104505, 2021. ISSN 2211-3797.
<https://www.sciencedirect.com/science/article/pii/S221137972100615X>.
- DATTA, S. **Electronic Transport in Mesoscopic Systems**. [*S.l.*]: Cambridge University Press, 1995. (Cambridge Studies in Semiconductor Physics and Microelectronic Engineering).
- DAVELOU, D.; KOPIDAKIS, G.; KAXIRAS, E.; REMEDIAKIS, I. N. Nanoribbon edges of transition-metal dichalcogenides: Stability and electronic properties. **Phys. Rev. B**, American Physical Society, v. 96, p. 165436, Oct 2017.
<https://link.aps.org/doi/10.1103/PhysRevB.96.165436>.
- DEUTSCH, D. Dquantum theory, the church–turing principle and the universal quantum computer. *In*: **R. Soc. Lond.** [*S.l.*: *s.n.*], 1985. p. 40097–117.
- DION, M.; RYDBERG, H.; SCHRÖDER, E.; LANGRETH, D. C.; LUNDQVIST, B. I. Van der waals density functional for general geometries. **Phys. Rev. Lett.**, American Physical Society, v. 92, p. 246401, Jun 2004.
<https://link.aps.org/doi/10.1103/PhysRevLett.92.246401>.
- DION, M.; RYDBERG, H.; SCHRÖDER, E.; LANGRETH, D. C.; LUNDQVIST, B. I. Erratum: Van der waals density functional for general geometries [phys. rev. lett. 92, 246401 (2004)]. **Phys. Rev. Lett.**, American Physical Society, v. 95, p. 109902, Sep 2005.
<https://link.aps.org/doi/10.1103/PhysRevLett.95.109902>.
- DIVINCENZO, D. P. **Topics in Quantum Computers**. arXiv, 1996. <https://arxiv.org/abs/cond-mat/9612126>.
- DIVINCENZO, D. P.; IBM. The physical implementation of quantum computation. **Protein Science**, v. 48, p. 771–783, 2000.
- DOMARETSKIY, D.; PHILIPPI, M.; GIBERTINI, M. Quenching the bandgap of two-dimensional semiconductors with a perpendicular electric field. **Nat. Nanotechnol**, v. 17, p. 1078–1083, 2022.
- DRESSELHAUS, M.; JORIO, A.; SAITO, R. Characterizing graphene, graphite, and carbon nanotubes by raman spectroscopy. **Annual Review of Condensed Matter Physics**, v. 1, n. 1, p. 89–108, 2010.
<https://doi.org/10.1146/annurev-conmatphys-070909-103919>.
- EARNEST, N.; CHAKRAM, S.; LU, Y.; IRONS, N.; NAIK, R. K.; LEUNG, N.; OCOLA, L.; CZAPLEWSKI, D. A.; BAKER, B.; LAWRENCE, J.; KOCH, J.; SCHUSTER, D. I. Realization of a Λ system with metastable states of a capacitively shunted fluxonium. **Phys. Rev. Lett.**, American Physical Society, v. 120, p. 150504, Apr 2018. <https://link.aps.org/doi/10.1103/PhysRevLett.120.150504>.
- ENYASHIN, A. N.; YADGAROV, L.; HOUBEN, L.; POPOV, I.; WEIDENBACH, M.; TENNE, R.; BAR-SADAN, M.; SEIFERT, G. New route for stabilization of 1t-ws2 and mos2 phases. **The Journal of Physical Chemistry C**, v. 115, n. 50, p. 24586–24591, 2011.
<https://doi.org/10.1021/jp2076325>.

- FEI, Z.; PALOMAKI, T.; WU, S. Edge conduction in monolayer wte2. **Nature Phys**, v. 13, p. 677–682, 2017. <https://doi.org/10.1038/nphys4091>.
- FEIJÓ, T. O.; COPETTI, G.; GERLING, E. R. F.; HANKE, M.; LOPES, J. M. J.; RADTKE, C.; SOARES, G. V. The role of substrate on the growth of 2d heterostructures by cvd. **Applied Surface Science**, v. 539, p. 148226, 2021. ISSN 0169-4332. <https://www.sciencedirect.com/science/article/pii/S0169433220329834>.
- FEYNMAN, R. There's plenty of room at the bottom. **Reson**, v. 16, p. 890, 1959. <https://doi.org/10.1007/s12045-011-0109-x>.
- FEYNMAN, R. P. Forces in molecules. **Phys. Rev.**, American Physical Society, v. 56, p. 340–343, Aug 1939. <https://link.aps.org/doi/10.1103/PhysRev.56.340>.
- FLAMINI, F.; SPAGNOLO, N.; SCIARRINO, F. Photonic quantum information processing: a review. **Reports on Progress in Physics**, IOP Publishing, v. 82, n. 1, p. 016001, nov 2018. <https://dx.doi.org/10.1088/1361-6633/aad5b2>.
- FOCK, V. Näherungsmethode zur Lösung des quantenmechanischen Mehrkörperproblems. **Zeitschrift für Physik**, v. 61, n. 1-2, p. 126–148, jan. 1930.
- FRINDT, R. F. Single crystals of mos2 several molecular layers thick. **Journal of Applied Physics**, v. 37, n. 4, p. 1928–1929, 1966. <https://doi.org/10.1063/1.1708627>.
- FU, L.; WANG, F.; WU, B.; WU, N.; HUANG, W.; WANG, H.; JIN, C.; ZHUANG, L.; HE, J.; FU, L.; LIU, Y. Van der waals epitaxial growth of atomic layered hfs2 crystals for ultrasensitive near-infrared phototransistors. **Advanced Materials**, v. 29, n. 32, p. 1700439, 2017. <https://onlinelibrary.wiley.com/doi/abs/10.1002/adma.201700439>.
- GAN, X.; LEE, L. Y. S.; WONG, K.-y.; LO, T. W.; HO, K. H.; LEI, D. Y.; ZHAO, H. 2h/1t phase transition of multilayer mos2 by electrochemical incorporation of s vacancies. **ACS Applied Energy Materials**, v. 1, n. 9, p. 4754–4765, 2018. <https://doi.org/10.1021/acsaem.8b00875>.
- GAO, G.; JIAO, Y.; MA, F.; JIAO, Y.; WACLAWIK, E.; DU, A. Charge mediated semiconducting-to-metallic phase transition in molybdenum disulfide monolayer and hydrogen evolution reaction in new 1t phase. **The Journal of Physical Chemistry C**, v. 119, n. 23, p. 13124–13128, 2015. <https://doi.org/10.1021/acs.jpcc.5b04658>.
- GAO, J.; LI, B.; TAN, J.; CHOW, P.; LU, T.-M.; KORATKAR, N. Aging of transition metal dichalcogenide monolayers. **ACS Nano**, v. 10, n. 2, p. 2628–2635, pMID: 26808328, 2016. <https://doi.org/10.1021/acsnano.5b07677>.
- GAO, X.; VAIDYA, S.; LI, K. Nuclear spin polarization and control in hexagonal boron nitride. **Nat. Mater**, v. 21, p. 1024–1028, 2022. <https://doi.org/10.1038/s41563-022-01329-8>.
- GEIM, A.; GRIGORIEVA, I. Van der waals heterostructures. **Nature**, v. 499, p. 419–425, 2013. <https://doi.org/10.1038/nature12385>.

GEORGESCU, I.; NORI, F. Quantum technologies: an old new story. **Physics World**, v. 25, n. 05, p. 16, may 2012.

<https://dx.doi.org/10.1088/2058-7058/25/05/28>.

GIANNOZZI, P.; ANDREUSSI, O.; BRUMME, T.; BUNAU, O.; NARDELLI, M. B.; CALANDRA, M.; CAR, R.; CAVAZZONI, C.; CERESOLI, D.; COCOCCIONI, M.; COLONNA, N.; CARNIMEO, I.; CORSO, A. D.; GIRONCOLI, S. de; DELUGAS, P.; DISTASIO, R. A.; FERRETTI, A.; FLORIS, A.; FRATESI, G.; FUGALLO, G.; GEBAUER, R.; GERSTMANN, U.; GIUSTINO, F.; GORNI, T.; JIA, J.; KAWAMURA, M.; KO, H.-Y.; KOKALJ, A.; KüçüKBENLİ, E.; LAZZERI, M.; MARSILI, M.; MARZARI, N.; MAURI, F.; NGUYEN, N. L.; NGUYEN, H.-V.; ROZA, A. O. de-la; PAULATTO, L.; PONCÉ, S.; ROCCA, D.; SABATINI, R.; SANTRA, B.; SCHLIPF, M.; SEITSONEN, A. P.; SMOGUNOV, A.; TIMROV, I.; THONHAUSER, T.; UMARI, P.; VAST, N.; WU, X.; BARONI, S. Advanced capabilities for materials modelling with quantum espresso. **Journal of Physics: Condensed Matter**, IOP Publishing, v. 29, n. 46, p. 465901, oct 2017.

<https://dx.doi.org/10.1088/1361-648X/aa8f79>.

GIANNOZZI, P.; BARONI, S.; BONINI, N.; CALANDRA, M.; CAR, R.; CAVAZZONI, C.; CERESOLI, D.; CHIAROTTI, G. L.; COCOCCIONI, M.; DABO, I.; CORSO, A. D.; GIRONCOLI, S. de; FABRIS, S.; FRATESI, G.; GEBAUER, R.; GERSTMANN, U.; GOUGOUSSIS, C.; KOKALJ, A.; LAZZERI, M.; MARTIN-SAMOS, L.; MARZARI, N.; MAURI, F.; MAZZARELLO, R.; PAOLINI, S.; PASQUARELLO, A.; PAULATTO, L.; SBRACCIA, C.; SCANDOLO, S.; SCLAUZERO, G.; SEITSONEN, A. P.; SMOGUNOV, A.; UMARI, P.; WENTZCOVITCH, R. M. Quantum espresso: a modular and open-source software project for quantum simulations of materials. **Journal of Physics: Condensed Matter**, v. 21, n. 39, p. 395502, sep 2009.

<https://dx.doi.org/10.1088/0953-8984/21/39/395502>.

GIANNOZZI, P.; BASEGGIO, O.; BONFÀ, P.; BRUNATO, D.; CAR, R.; CARNIMEO, I.; CAVAZZONI, C.; GIRONCOLI, S. de; DELUGAS, P.; RUFFINO, F. F.; FERRETTI, A.; MARZARI, N.; TIMROV, I.; URRU, A.; BARONI, S. Quantum espresso toward the exascale. **The Journal of Chemical Physics**, v. 152, n. 15, p. 154105, 2020. <https://doi.org/10.1063/5.0005082>.

GIBERTINI, M.; MARZARI, N. Emergence of one-dimensional wires of free carriers in transition-metal-dichalcogenide nanostructures. **Nano Letters**, v. 15, n. 9, p. 6229–6238, PMID: 26291826, 2015. <https://doi.org/10.1021/acs.nanolett.5b02834>.

GIBERTINI, M.; PIZZI, G.; MARZARI, N. Engineering polar discontinuities in honeycomb lattices. **Nat Commun**, v. 5, p. 5157, 2014.

GLAZMAN, L. I.; JONSON, M. Global adiabatic regime in quantum ballistic transport. **Phys. Rev. B**, American Physical Society, v. 41, p. 10686–10699, May 1990. <https://link.aps.org/doi/10.1103/PhysRevB.41.10686>.

GRIMME, S. Semiempirical gga-type density functional constructed with a long-range dispersion correction. **Journal of Computational Chemistry**, v. 27, n. 15, p. 1787–1799, 2006. <https://onlinelibrary.wiley.com/doi/abs/10.1002/jcc.20495>.

- GROTH, C. W.; WIMMER, M.; AKHMEROV, A. R.; WAIN TAL, X. Kwant: a software package for quantum transport. **New Journal of Physics**, IOP Publishing, v. 16, n. 6, p. 063065, jun 2014. <https://dx.doi.org/10.1088/1367-2630/16/6/063065>.
- GROTZ, B.; HAUF, M.; DANKERL, M. Charge state manipulation of qubits in diamond. **Nat Commun**, v. 3, p. 729, 2012. <https://doi.org/10.1038/ncomms1729>.
- GRUMET, M.; LIU, P.; KALTAK, M.; s, J. c. v. Klime; KRESSE, G. Beyond the quasiparticle approximation: Fully self-consistent *gw* calculations. **Phys. Rev. B**, American Physical Society, v. 98, p. 155143, Oct 2018. <https://link.aps.org/doi/10.1103/PhysRevB.98.155143>.
- GÜLLER, F.; LLOIS, A. M.; GONIAKOWSKI, J.; NOGUERA, C. Prediction of structural and metal-to-semiconductor phase transitions in nanoscale mos₂, ws₂, and other transition metal dichalcogenide zigzag ribbons. **Phys. Rev. B**, American Physical Society, v. 91, p. 075407, Feb 2015. <https://link.aps.org/doi/10.1103/PhysRevB.91.075407>.
- HÄFFNER, H.; HÄNSEL, W.; ROOS, C. Scalable multiparticle entanglement of trapped ions. **Nature**, v. 438, p. 643–646, 2005.
- HAMADA, I. van der waals density functional made accurate. **Phys. Rev. B**, American Physical Society, v. 89, p. 121103, Mar 2014. <https://link.aps.org/doi/10.1103/PhysRevB.89.121103>.
- HAMANN, D. R. Optimized norm-conserving vanderbilt pseudopotentials. **Phys. Rev. B**, American Physical Society, v. 88, p. 085117, Aug 2013. <https://link.aps.org/doi/10.1103/PhysRevB.88.085117>.
- HAMANN, D. R. Erratum: Optimized norm-conserving vanderbilt pseudopotentials [phys. rev. b 88, 085117 (2013)]. **Phys. Rev. B**, American Physical Society, v. 95, p. 239906, Jun 2017. <https://link.aps.org/doi/10.1103/PhysRevB.95.239906>.
- HAMANN, D. R.; SCHLÜTER, M.; CHIANG, C. Norm-conserving pseudopotentials. **Phys. Rev. Lett.**, American Physical Society, v. 43, p. 1494–1497, Nov 1979. <https://link.aps.org/doi/10.1103/PhysRevLett.43.1494>.
- HARTREE, D. R. The wave mechanics of an atom with a non-coulomb central field. part i. theory and methods. **Mathematical Proceedings of the Cambridge Philosophical Society**, Cambridge University Press, v. 24, n. 1, p. 89–110, 1928.
- HEAD-MARSDEN, K.; FLICK, J.; CICCARINO, C. J.; NARANG, P. Quantum information and algorithms for correlated quantum matter. **Chemical Reviews**, v. 121, n. 5, p. 3061–3120, pMID: 33326218, 2021. <https://doi.org/10.1021/acs.chemrev.0c00620>.
- HEISENBERG, W. Die beobachtbaren größen in der theorie der elementarteilchen. **Z. Physik**, v. 120, p. 513–538, 1943. <https://doi.org/10.1007/BF01329800>.
- HEISING, J.; KANATZIDIS, M. G. Structure of restacked mos₂ and ws₂ elucidated by electron crystallography. **Journal of the American Chemical Society**, v. 121, n. 4, p. 638–643, 1999. <https://doi.org/10.1021/ja983043c>.

- HELVEG, S.; LAURITSEN, J. V.; LÆGSGAARD, E.; STENSGAARD, I.; NØRSKOV, J. K.; CLAUSEN, B. S.; TOPSØE, H.; BESENBACHER, F. Atomic-scale structure of single-layer mos_2 nanoclusters. **Phys. Rev. Lett.**, American Physical Society, v. 84, p. 951–954, Jan 2000. <https://link.aps.org/doi/10.1103/PhysRevLett.84.951>.
- HENDRICKX, N.; FRANKE, D.; SAMMAK, A. Fast two-qubit logic with holes in germanium. **Nature**, v. 577, p. 487–491, 2020. <https://doi.org/10.1038/s41586-019-1919-3>.
- HERMAN, F.; DYKE, J. P. V.; ORTENBURGER, I. B. Improved statistical exchange approximation for inhomogeneous many-electron systems. **Phys. Rev. Lett.**, American Physical Society, v. 22, p. 807–811, Apr 1969. <https://link.aps.org/doi/10.1103/PhysRevLett.22.807>.
- HEYD, J.; SCUSERIA, G. E. Efficient hybrid density functional calculations in solids: Assessment of the heyd–scuseria–ernzerhof screened coulomb hybrid functional. **The Journal of Chemical Physics**, v. 121, n. 3, p. 1187–1192, 2004. <https://doi.org/10.1063/1.1760074>.
- HEYD, J.; SCUSERIA, G. E.; ERNZERHOF, M. Hybrid functionals based on a screened coulomb potential. **The Journal of Chemical Physics**, v. 118, n. 18, p. 8207–8215, 2003. <https://doi.org/10.1063/1.1564060>.
- HEYD, J.; SCUSERIA, G. E.; ERNZERHOF, M. Erratum: “hybrid functionals based on a screened coulomb potential” [j. chem. phys. 118, 8207 (2003)]. **The Journal of Chemical Physics**, v. 124, n. 21, p. 219906, 2006. <https://doi.org/10.1063/1.2204597>.
- HIRATA, M.; GOTOU, T.; HORIUCHI, S.; FUJIWARA, M.; OHBA, M. Thin-film particles of graphite oxide 1:: High-yield synthesis and flexibility of the particles. **Carbon**, v. 42, n. 14, p. 2929–2937, 2004. ISSN 0008-6223. <https://www.sciencedirect.com/science/article/pii/S0008622304004440>.
- HOHENBERG, P.; KOHN, W. Inhomogeneous electron gas. **Phys. Rev.**, American Physical Society, v. 136, p. B864–B871, Nov 1964. <https://link.aps.org/doi/10.1103/PhysRev.136.B864>.
- HU, R.; LEI, W.; YUAN, H.; HAN, S.; LIU, H. High-throughput prediction of the band gaps of van der waals heterostructures via machine learning. **Nanomaterials**, v. 12, n. 13, 2022. ISSN 2079-4991. <https://www.mdpi.com/2079-4991/12/13/2301>.
- HU, T.; ZHOU, J.; DONG, J.; KAWAZOE, Y. Electronic and magnetic properties of armchair MoS_2 nanoribbons under both external strain and electric field, studied by first principles calculations. **Journal of Applied Physics**, v. 116, n. 6, p. 064301, 08 2014. ISSN 0021-8979. <https://doi.org/10.1063/1.4891997>.
- HUANG, Y.; SUTTER, E.; SADOWSKI, J. T.; COTLET, M.; MONTI, O. L.; RACKE, D. A.; NEUPANE, M. R.; WICKRAMARATNE, D.; LAKE, R. K.; PARKINSON, B. A.; SUTTER, P. Tin disulfide—an emerging layered metal dichalcogenide semiconductor: Materials properties and device characteristics. **ACS Nano**, v. 8, n. 10, p. 10743–10755, PMID: 25247490, 2014. <https://doi.org/10.1021/nn504481r>.

IHN, T. **Semiconductor Nanostructures: Quantum states and electronic transport**. [S.l.]: OUP Oxford, 2009.

JAIN, A.; ONG, S. P.; HAUTIER, G.; CHEN, W.; RICHARDS, W. D.; DACEK, S.; CHOLIA, S.; GUNTER, D.; SKINNER, D.; CEDER, G.; PERSSON, K. A. Commentary: The Materials Project: A materials genome approach to accelerating materials innovation. **APL Materials**, v. 1, n. 1, p. 011002, 07 2013. ISSN 2166-532X. <https://doi.org/10.1063/1.4812323>.

JOHANSSON, J.; NATION, P.; NORI, F. Qutip: An open-source python framework for the dynamics of open quantum systems. **Computer Physics Communications**, v. 183, n. 8, p. 1760–1772, 2012. ISSN 0010-4655. <https://www.sciencedirect.com/science/article/pii/S0010465512000835>.

JOHANSSON, J.; NATION, P.; NORI, F. Qutip 2: A python framework for the dynamics of open quantum systems. **Computer Physics Communications**, v. 184, n. 4, p. 1234–1240, 2013. ISSN 0010-4655. <https://www.sciencedirect.com/science/article/pii/S0010465512003955>.

KAN, M.; WANG, J. Y.; LI, X. W.; ZHANG, S. H.; LI, Y. W.; KAWAZOE, Y.; SUN, Q.; JENA, P. Structures and phase transition of a mos2 monolayer. **The Journal of Physical Chemistry C**, v. 118, n. 3, p. 1515–1522, 2014. <https://doi.org/10.1021/jp4076355>.

KANE, B. A silicon-based nuclear spin quantum computer. **Nature**, v. 393, p. 133–137, 1998. <https://doi.org/10.1038/30156>.

KIEMLE, J.; SIGGER, F.; LORKE, M.; MILLER, B.; WATANABE, K.; TANIGUCHI, T.; HOLLEITNER, A.; WURSTBAUER, U. Control of the orbital character of indirect excitons in mos₂/ws₂ heterobilayers. **Phys. Rev. B**, American Physical Society, v. 101, p. 121404, Mar 2020. <https://link.aps.org/doi/10.1103/PhysRevB.101.121404>.

KLIMEŠ, J.; BOWLER, D. R.; MICHAELIDES, A. Chemical accuracy for the van der waals density functional. **Journal of Physics: Condensed Matter**, v. 22, n. 2, p. 022201, dec 2009. <https://dx.doi.org/10.1088/0953-8984/22/2/022201>.

KLIMEŠ, J.; BOWLER, D. R.; MICHAELIDES, A. Van der waals density functionals applied to solids. **Phys. Rev. B**, American Physical Society, v. 83, p. 195131, May 2011. <https://link.aps.org/doi/10.1103/PhysRevB.83.195131>.

KOCH, W.; HOLTHAUSEN, M. A chemist's guide to density functional theory. *In*: _____. [S.l.: s.n.], 2001. v. 4.

KODA, D. S.; BECHSTEDT, F.; MARQUES, M.; TELES, L. K. Coincidence lattices of 2d crystals: Heterostructure predictions and applications. **The Journal of Physical Chemistry C**, v. 120, n. 20, p. 10895–10908, 2016. <https://doi.org/10.1021/acs.jpcc.6b01496>.

KODA, D. S.; BECHSTEDT, F.; MARQUES, M.; TELES, L. K. Trends on band alignments: Validity of anderson's rule in sns₂- and snse₂-based van der waals heterostructures. **Phys. Rev. B**, American Physical Society, v. 97, p. 165402, Apr 2018. <https://link.aps.org/doi/10.1103/PhysRevB.97.165402>.

KOHANOFF, J. **Electronic Structure Calculations for Solids and Molecules**. [*S.l.*: *s.n.*], 2006.

KOHN, W.; SHAM, L. J. Self-consistent equations including exchange and correlation effects. **Phys. Rev.**, American Physical Society, v. 140, p. A1133–A1138, Nov 1965. <https://link.aps.org/doi/10.1103/PhysRev.140.A1133>.

KOLMOGOROV, A. N.; CRESPI, V. H. Registry-dependent interlayer potential for graphitic systems. **Phys. Rev. B**, American Physical Society, v. 71, p. 235415, Jun 2005. <https://link.aps.org/doi/10.1103/PhysRevB.71.235415>.

KRANTZ, P.; KJAERGAARD, M.; YAN, F.; ORLANDO, T. P.; GUSTAVSSON, S.; OLIVER, W. D. A quantum engineer's guide to superconducting qubits. **Applied Physics Reviews**, v. 6, n. 2, p. 021318, 06 2019. ISSN 1931-9401. <https://doi.org/10.1063/1.5089550>.

KRAUSS, M.; STEVENS, W. J. Effective potentials in molecular quantum chemistry. **Annual Review of Physical Chemistry**, v. 35, n. 1, p. 357–385, 1984. <https://doi.org/10.1146/annurev.pc.35.100184.002041>.

KRESSE, G.; FURTHMÜLLER, J. Efficient iterative schemes for ab initio total-energy calculations using a plane-wave basis set. **Phys. Rev. B**, American Physical Society, v. 54, p. 11169–11186, Oct 1996. <https://link.aps.org/doi/10.1103/PhysRevB.54.11169>.

KRESSE, G.; JOUBERT, D. From ultrasoft pseudopotentials to the projector augmented-wave method. **Phys. Rev. B**, American Physical Society, v. 59, p. 1758–1775, Jan 1999. <https://link.aps.org/doi/10.1103/PhysRevB.59.1758>.

KRUKAU, A. V.; VYDROV, O. A.; IZMAYLOV, A. F.; SCUSERIA, G. E. Influence of the exchange screening parameter on the performance of screened hybrid functionals. **The Journal of Chemical Physics**, v. 125, n. 22, p. 224106, 2006. <https://doi.org/10.1063/1.2404663>.

LANDAU, L. D. Zur theorie der phasenumwandlungen ii. **Phys. Z. Sowjetunion**, v. 11, n. 545, p. 26–35, 1937.

LANDAUER, R. Spatial variation of currents and fields due to localized scatterers in metallic conduction. **IBM Journal of Research and Development**, v. 32, n. 3, p. 306–316, 1988.

LANGRETH, D. C.; LUNDQVIST, B. I.; CHAKAROVA-KäCK, S. D.; COOPER, V. R.; DION, M.; HYLDGAARD, P.; KELKKANEN, A.; KLEIS, J.; KONG, L.; LI, S.; MOSES, P. G.; MURRAY, E.; PUZDER, A.; RYDBERG, H.; SCHRÖDER, E.; THONHAUSER, T. A density functional for sparse matter. **Journal of Physics: Condensed Matter**, v. 21, n. 8, p. 084203, jan 2009. <https://dx.doi.org/10.1088/0953-8984/21/8/084203>.

LAUCHT, A.; KALRA, R.; SIMMONS, S. A dressed spin qubit in silicon. **Nature Nanotech**, v. 12, p. 61–66, 2017. <https://doi.org/10.1038/nnano.2016.178>.

LEE, C.; LEE, G.; ZANDE, A. Atomically thin p–n junctions with van der waals heterointerfaces. **Nature Nanotech**, v. 9, p. 676–681, 2014.

- LEE, C.; YANG, W.; PARR, R. G. Development of the colle-salvetti correlation-energy formula into a functional of the electron density. **Phys. Rev. B**, American Physical Society, v. 37, p. 785–789, Jan 1988.
<https://link.aps.org/doi/10.1103/PhysRevB.37.785>.
- LEE, K.; MURRAY, E. D.; KONG, L.; LUNDQVIST, B. I.; LANGRETH, D. C. Higher-accuracy van der waals density functional. **Phys. Rev. B**, American Physical Society, v. 82, p. 081101, Aug 2010.
<https://link.aps.org/doi/10.1103/PhysRevB.82.081101>.
- LEE, P. A.; FISHER, D. S. Anderson localization in two dimensions. **Phys. Rev. Lett.**, American Physical Society, v. 47, p. 882–885, Sep 1981.
<https://link.aps.org/doi/10.1103/PhysRevLett.47.882>.
- LESOVIK, G. B.; SADOVSKYY, I. A. Scattering matrix approach to the description of quantum electron transport. **Physics-Uspekhi**, Uspekhi Fizicheskikh Nauk (UFN) Journal, v. 54, n. 10, p. 1007–1059, out. 2011. ISSN 1468-4780.
<http://dx.doi.org/10.3367/UFNe.0181.201110b-1041>
<http://dx.doi.org/10.3367/UFNe.0181.201110b.1041>.
- LI, S.; CHEN, X.; ZHANG, Z.; LI, X.; DENG, W.; LIU, F.; LU, Y.; ZHANG, Y. Light-rewritable logic devices based on van der waals heterostructures. **Advanced Electronic Materials**, v. 8, n. 1, p. 2100708, 2022.
<https://onlinelibrary.wiley.com/doi/abs/10.1002/aelm.202100708>.
- LI, T.; TANG, Z.; HUANG, Z.; YU, J. Substrate effects on the thermal performance of in-plane graphene/hexagonal boron nitride heterostructures. **Carbon**, v. 130, p. 396–400, 2018. ISSN 0008-6223.
<https://www.sciencedirect.com/science/article/pii/S0008622318300174>.
- LI, X.; WANG, X.; ZHANG, L.; LEE, S.; DAI, H. Chemically derived, ultrasMOOTH graphene nanoribbon semiconductors. **Science**, v. 319, n. 5867, p. 1229–1232, 2008.
<https://www.science.org/doi/abs/10.1126/science.1150878>.
- LINDER, J.; SUDBØ, A. Dirac fermions and conductance oscillations in *s*- and *d*-wave superconductor-graphene junctions. **Phys. Rev. Lett.**, American Physical Society, v. 99, p. 147001, Oct 2007.
<https://link.aps.org/doi/10.1103/PhysRevLett.99.147001>.
- LONGO, R. C.; ADDOU, R.; KC, S.; NOH, J.-Y.; SMYTH, C. M.; BARRERA, D.; ZHANG, C.; HSU, J. W. P.; WALLACE, R. M.; CHO, K. Intrinsic air stability mechanisms of two-dimensional transition metal dichalcogenide surfaces: basal versus edge oxidation. **2D Materials**, IOP Publishing, v. 4, n. 2, p. 025050, mar 2017.
<https://dx.doi.org/10.1088/2053-1583/aa636c>.
- LOSS, D.; DIVINCENZO, D. P. Quantum computation with quantum dots. **Phys. Rev. A**, American Physical Society, v. 57, p. 120–126, Jan 1998.
<https://link.aps.org/doi/10.1103/PhysRevA.57.120>.
- LUCATTO, B.; KODA, D. S.; BECHSTEDT, F.; MARQUES, M.; TELES, L. K. Charge qubit in van der waals heterostructures. **Phys. Rev. B**, American Physical

Society, v. 100, p. 121406, Sep 2019.

<https://link.aps.org/doi/10.1103/PhysRevB.100.121406>.

LUCOVSKY, G.; WHITE, R. M.; BENDA, J. A.; REVELLI, J. F. Infrared-reflectance spectra of layered group-iv and group-vi transition-metal dichalcogenides. **Phys. Rev. B**, American Physical Society, v. 7, p. 3859–3870, Apr 1973.

MACDONALD, J. K. L. Successive approximations by the rayleigh-ritz variation method. **Phys. Rev.**, American Physical Society, v. 43, p. 830–833, May 1933. <https://link.aps.org/doi/10.1103/PhysRev.43.830>.

MACKINNON, A. The calculation of transport properties and density of states of disordered solids. **Z. Physik B - Condensed Matter**, v. 59, p. 385–390, 1985. <https://doi.org/10.1007/BF01328846>.

MAGGIO, E.; KRESSE, G. Correlation energy for the homogeneous electron gas: Exact bethe-salpeter solution and an approximate evaluation. **Phys. Rev. B**, American Physical Society, v. 93, p. 235113, Jun 2016.

<https://link.aps.org/doi/10.1103/PhysRevB.93.235113>.

MARTIN, R. M. **Electronic Structure: Basic Theory and Practical Methods**. 2. ed. [S.l.]: Cambridge University Press, 2020.

MARZARI, N.; MOSTOFI, A. A.; YATES, J. R.; SOUZA, I.; VANDERBILT, D. Maximally localized wannier functions: Theory and applications. **Rev. Mod. Phys.**, American Physical Society, v. 84, p. 1419–1475, Oct 2012.

<https://link.aps.org/doi/10.1103/RevModPhys.84.1419>.

MARZARI, N.; VANDERBILT, D. Maximally localized generalized wannier functions for composite energy bands. **Phys. Rev. B**, American Physical Society, v. 56, p. 12847–12865, Nov 1997.

<https://link.aps.org/doi/10.1103/PhysRevB.56.12847>.

MCCANN, E.; FAL'KO, V. I. Symmetry of boundary conditions of the dirac equation for electrons in carbon nanotubes. **Journal of Physics: Condensed Matter**, v. 16, n. 13, p. 2371, mar 2004. <https://dx.doi.org/10.1088/0953-8984/16/13/016>.

MCCANN, E.; KOSHINO, M. The electronic properties of bilayer graphene. **Reports on Progress in Physics**, IOP Publishing, v. 76, n. 5, p. 056503, apr 2013. <https://dx.doi.org/10.1088/0034-4885/76/5/056503>.

MIN, H.; SAHU, B.; BANERJEE, S. K.; MACDONALD, A. H. Ab initio theory of gate induced gaps in graphene bilayers. **Phys. Rev. B**, American Physical Society, v. 75, p. 155115, Apr 2007. <https://link.aps.org/doi/10.1103/PhysRevB.75.155115>.

MIRABELLI, G.; MCGEOUGH, C.; SCHMIDT, M.; MCCARTHY, E. K.; MONAGHAN, S.; POVEY, I. M.; MCCARTHY, M.; GITY, F.; NAGLE, R.; HUGHES, G.; CAFOLLA, A.; HURLEY, P. K.; DUFFY, R. Air sensitivity of mos2, mose2, mote2, hfs2, and hfse2. **Journal of Applied Physics**, v. 120, n. 12, p. 125102, 2016. <https://doi.org/10.1063/1.4963290>.

- MONKHORST, H. J.; PACK, J. D. Special points for brillouin-zone integrations. **Phys. Rev. B**, American Physical Society, v. 13, p. 5188–5192, Jun 1976. <https://link.aps.org/doi/10.1103/PhysRevB.13.5188>.
- MOORE, G. E. Cramming more components onto integrated circuits. **Proceedings of the IEEE**, Ieee, v. 86, p. 82–85, 1998.
- MOSTOFI, A. A.; YATES, J. R.; LEE, Y.-S.; SOUZA, I.; VANDERBILT, D.; MARZARI, N. wannier90: A tool for obtaining maximally-localised wannier functions. **Computer Physics Communications**, v. 178, n. 9, p. 685–699, 2008. ISSN 0010-4655. <https://www.sciencedirect.com/science/article/pii/S0010465507004936>.
- MOSTOFI, A. A.; YATES, J. R.; PIZZI, G.; LEE, Y.-S.; SOUZA, I.; VANDERBILT, D.; MARZARI, N. An updated version of wannier90: A tool for obtaining maximally-localised wannier functions. **Computer Physics Communications**, v. 185, n. 8, p. 2309–2310, 2014. ISSN 0010-4655. <https://www.sciencedirect.com/science/article/pii/S001046551400157X>.
- NAKAMURA, Y.; CHEN, C. D.; TSAI, J. S. Spectroscopy of energy-level splitting between two macroscopic quantum states of charge coherently superposed by josephson coupling. **Phys. Rev. Lett.**, American Physical Society, v. 79, p. 2328–2331, Sep 1997. <https://link.aps.org/doi/10.1103/PhysRevLett.79.2328>.
- NAKAMURA, Y.; PASHKIN, Y.; TSAI, J. Coherent control of macroscopic quantum states in a single-cooper-pair box. **Nature**, v. 398, p. 786–788, 1999.
- NAZAROV, Y. V.; BLANTER, Y. M. **Quantum transport: introduction to nanoscience**. [S.l.]: Cambridge university press, 2009.
- NOVOSELOV, K.; GEIM, A.; MOROZOV, S. Two-dimensional gas of massless dirac fermions in graphene. **Nature**, v. 438, p. 197–200, 2005. <https://doi.org/10.1038/nature04233>.
- NOVOSELOV, K. S.; GEIM, A. K.; MOROZOV, S. V.; JIANG, D.; ZHANG, Y.; DUBONOS, S. V.; GRIGORIEVA, I. V.; FIRSOV, A. A. Electric field effect in atomically thin carbon films. **Science**, v. 306, n. 5696, p. 666–669, 2004. <https://www.science.org/doi/abs/10.1126/science.1102896>.
- NOVOSELOV, K. S.; JIANG, D.; SCHEDIN, F.; BOOTH, T. J.; KHOTKEVICH, V. V.; MOROZOV, S. V.; GEIM, A. K. Two-dimensional atomic crystals. **Proceedings of the National Academy of Sciences**, v. 102, n. 30, p. 10451–10453, 2005. <https://www.pnas.org/doi/abs/10.1073/pnas.0502848102>.
- NOWACK, K. C.; SHAFIEI, M.; LAFOREST, M.; PRAWIROATMODJO, G. E. D. K.; SCHREIBER, L. R.; REICHL, C.; WEGSCHEIDER, W.; VANDERSYPEN, L. M. K. Single-shot correlations and two-qubit gate of solid-state spins. **Science**, v. 333, n. 6047, p. 1269–1272, 2011. <https://www.science.org/doi/abs/10.1126/science.1209524>.
- NULL null; ARUTE, F.; ARYA, K.; BABBUSH, R.; BACON, D.; BARDIN, J. C.; BARENDS, R.; BOIXO, S.; BROUGHTON, M.; BUCKLEY, B. B.; BUELL, D. A.; BURKETT, B.; BUSHNELL, N.; CHEN, Y.; CHEN, Z.; CHIARO, B.; COLLINS, R.;

COURTNEY, W.; DEMURA, S.; DUNSWORTH, A.; FARHI, E.; FOWLER, A.; FOXEN, B.; GIDNEY, C.; GIUSTINA, M.; GRAFF, R.; HABEGGER, S.; HARRIGAN, M. P.; HO, A.; HONG, S.; HUANG, T.; HUGGINS, W. J.; IOFFE, L.; ISAKOV, S. V.; JEFFREY, E.; JIANG, Z.; JONES, C.; KAFRI, D.; KECHEDZHI, K.; KELLY, J.; KIM, S.; KLIMOV, P. V.; KOROTKOV, A.; KOSTRITSA, F.; LANDHUIS, D.; LAPTEV, P.; LINDMARK, M.; LUCERO, E.; MARTIN, O.; MARTINIS, J. M.; MCCLEAN, J. R.; MCEWEN, M.; MEGRANT, A.; MI, X.; MOHSENI, M.; MRUCZKIEWICZ, W.; MUTUS, J.; NAAMAN, O.; NEELEY, M.; NEILL, C.; NEVEN, H.; NIU, M. Y.; O'BRIEN, T. E.; OSTBY, E.; PETUKHOV, A.; PUTTERMAN, H.; QUINTANA, C.; ROUSHAN, P.; RUBIN, N. C.; SANK, D.; SATZINGER, K. J.; SMELYANSKIY, V.; STRAIN, D.; SUNG, K. J.; SZALAY, M.; TAKESHITA, T. Y.; VAINSENER, A.; WHITE, T.; WIEBE, N.; YAO, Z. J.; YEH, P.; ZALCMAN, A. Hartree-fock on a superconducting qubit quantum computer.

Science, v. 369, n. 6507, p. 1084–1089, 2020.

<https://www.science.org/doi/abs/10.1126/science.abb9811>.

O'BRIEN, J.; FURUSAWA, A.; VUčković, J. Photonic quantum technologies. **Nature Photon**, v. 3, p. 687–695. <https://doi.org/10.1038/nphoton.2009.229>.

ONG, S. P.; RICHARDS, W. D.; JAIN, A.; HAUTIER, G.; KOCHER, M.; CHOLIA, S.; GUNTER, D.; CHEVRIER, V. L.; PERSSON, K. A.; CEDER, G. Python materials genomics (pymatgen): A robust, open-source python library for materials analysis.

Computational Materials Science, v. 68, p. 314–319, 2013. ISSN 0927-0256. <https://www.sciencedirect.com/science/article/pii/S0927025612006295>.

ORTIZ, G.; BALLONE, P. Correlation energy, structure factor, radial distribution function, and momentum distribution of the spin-polarized uniform electron gas. **Phys. Rev. B**, American Physical Society, v. 50, p. 1391–1405, Jul 1994. <https://link.aps.org/doi/10.1103/PhysRevB.50.1391>.

OSZ, B. P.; SALJE, E. Lattice parameters and spontaneous strain in ax₂ polytypes: Cdi₂, pbi₂ sns₂ and snse₂. **Journal of Applied Crystallography**, v. 22, n. 6, p. 622–623, 1989.

<https://onlinelibrary.wiley.com/doi/abs/10.1107/S0021889889006916>.

ÖZÇELİK, V. O.; AZADANI, J. G.; YANG, C.; KOESTER, S. J.; LOW, T. Band alignment of two-dimensional semiconductors for designing heterostructures with momentum space matching. **Phys. Rev. B**, American Physical Society, v. 94, p. 035125, Jul 2016. <https://link.aps.org/doi/10.1103/PhysRevB.94.035125>.

PALACIOS-BERRAQUERO, C.; BARBONE, M.; KARA, D. Atomically thin quantum light-emitting diodes. **Nat Commun**, v. 7, p. 12978, 2016.

<https://doi.org/10.1038/ncomms12978>.

PAN, F.; CHEN, K.; ZHANG, P. Solving the sampling problem of the sycamore quantum circuits. **Phys. Rev. Lett.**, American Physical Society, v. 129, p. 090502, Aug 2022. <https://link.aps.org/doi/10.1103/PhysRevLett.129.090502>.

PAULI, W. Über gasentartung und paramagnetismus. **Z. Physik**, v. 41, p. 81–102, 1927.

PEIERLS, R. Quelques propriétés typiques des corps solides. **Annales de l'institut Henri Poincaré**, INSTITUT HENRI POINCARÉ ET GAUTHIER-VILLARS, v. 5, n. 3, p. 177–222, 1935. <http://eudml.org/doc/78996><http://eudml.org/doc/78996>.

PERDEW, J. P. Density-functional approximation for the correlation energy of the inhomogeneous electron gas. **Phys. Rev. B**, American Physical Society, v. 33, p. 8822–8824, Jun 1986. <https://link.aps.org/doi/10.1103/PhysRevB.33.8822>.

PERDEW, J. P.; BURKE, K. Comparison shopping for a gradient-corrected density functional. **International Journal of Quantum Chemistry**, v. 57, n. 3, p. 309–319, 1996.

PERDEW, J. P.; BURKE, K.; ERNZERHOF, M. Generalized gradient approximation made simple. **Phys. Rev. Lett.**, American Physical Society, v. 77, p. 3865–3868, Oct 1996. <https://link.aps.org/doi/10.1103/PhysRevLett.77.3865>.

PERDEW, J. P.; BURKE, K.; ERNZERHOF, M. Generalized gradient approximation made simple [phys. rev. lett. 77, 3865 (1996)]. **Phys. Rev. Lett.**, American Physical Society, v. 78, p. 1396–1396, Feb 1997. <https://link.aps.org/doi/10.1103/PhysRevLett.78.1396>.

PERDEW, J. P.; BURKE, K.; ERNZERHOF, M. Perdew, burke, and ernzerhof reply:. **Phys. Rev. Lett.**, American Physical Society, v. 80, p. 891–891, Jan 1998. <https://link.aps.org/doi/10.1103/PhysRevLett.80.891>.

PERDEW, J. P.; ERNZERHOF, M.; BURKE, K. Rationale for mixing exact exchange with density functional approximations. **The Journal of Chemical Physics**, v. 105, n. 22, p. 9982–9985, 1996. <https://doi.org/10.1063/1.472933>.

PERDEW, J. P.; YUE, W. Accurate and simple density functional for the electronic exchange energy: Generalized gradient approximation. **Phys. Rev. B**, American Physical Society, v. 33, p. 8800–8802, Jun 1986. <https://link.aps.org/doi/10.1103/PhysRevB.33.8800>.

PETOUSIS, I.; CHEN, W.; HAUTIER, G.; GRAF, T.; SCHLADT, T. D.; PERSSON, K. A.; PRINZ, F. B. Benchmarking density functional perturbation theory to enable high-throughput screening of materials for dielectric constant and refractive index. **Phys. Rev. B**, American Physical Society, v. 93, p. 115151, Mar 2016. <https://link.aps.org/doi/10.1103/PhysRevB.93.115151>.

PETOUSIS, I.; MRDJENOVICH, D.; BALLOUZ, E. High-throughput screening of inorganic compounds for the discovery of novel dielectric and optical materials. **Sci Data**, v. 4, p. 160134, 2017. <https://doi.org/10.1038/sdata.2016.134>.

PHIL, N. D. I. on the constitution of atoms and molecules, the london. **Edinburgh, and Dublin Philosophical Magazine and Journal of Science**, v. 26, n. 151, p. 1–25 1913.

PHILLIPS, J. C.; KLEINMAN, L. New method for calculating wave functions in crystals and molecules. **Phys. Rev.**, American Physical Society, v. 116, p. 287–294, Oct 1959. <https://link.aps.org/doi/10.1103/PhysRev.116.287>.

- PIERUCCI, D.; HENCK, H.; AVILA, J.; BALAN, A.; NAYLOR, C. H.; PATRIARCHE, G.; DAPPE, Y. J.; SILLY, M. G.; SIROTTI, F.; JOHNSON, A. T. C.; ASENSIO, M. C.; OUEGHI, A. Band alignment and minigaps in monolayer mos₂-graphene van der waals heterostructures. **Nano Letters**, v. 16, n. 7, p. 4054–4061, pMID: 27281693, 2016. <https://doi.org/10.1021/acs.nanolett.6b00609>.
- PY, M. A.; HAERING, R. R. Structural destabilization induced by lithium intercalation in mos₂ and related compounds. **Canadian Journal of Physics**, v. 61, n. 1, p. 76–84, 1983. <https://doi.org/10.1139/p83-013>.
- QIAN, Z.; JIAO, L.; XIE, L. Phase engineering of two-dimensional transition metal dichalcogenides. **Chinese Journal of Chemistry**, v. 38, n. 7, p. 753–760, 2020. <https://onlinelibrary.wiley.com/doi/abs/10.1002/cjoc.202000064>.
- QU, Y.; PAN, H.; KWOK, C. Hydrogenation-controlled phase transition on two-dimensional transition metal dichalcogenides and their unique physical and catalytic properties. **Sci Rep**, v. 6, p. 34186, 2016. <https://doi.org/10.1038/srep34186>.
- RADISAVLJEVIC, B.; RADENOVIC, A.; BRIVIO, J. Single-layer mos₂ transistors. **Nature Nanotech**, v. 6, p. 147–150, 2011.
- RASMUSSEN, F. A.; THYGESEN, K. S. Computational 2d materials database: Electronic structure of transition-metal dichalcogenides and oxides. **The Journal of Physical Chemistry C**, v. 119, n. 23, p. 13169–13183, 2015. <https://doi.org/10.1021/acs.jpcc.5b02950>.
- RIDOLFI, E.; LIMA, L. R. F.; MUCCIOLO, E. R.; LEWENKOPF, C. H. Electronic transport in disordered mos₂ nanoribbons. **Phys. Rev. B**, American Physical Society, v. 95, p. 035430, Jan 2017. <https://link.aps.org/doi/10.1103/PhysRevB.95.035430>.
- RIEBE, M.; HäFFNER, H.; ROOS, C. Deterministic quantum teleportation with atoms. **Nature**, v. 429, p. 734–737, 2004.
- RIMMINGTON, H.; BALCHIN, A. Crystal data for layer compounds in the series hfsxse₂x. **J Mater Sci**, v. 9, p. 343–345, 1974. <https://doi.org/10.1007/BF00550964>.
- ROSTAMI, H.; ASGARI, R.; GUINEA, F. Edge modes in zigzag and armchair ribbons of monolayer mos₂. **Journal of Physics: Condensed Matter**, IOP Publishing, v. 28, n. 49, p. 495001, oct 2016. <https://dx.doi.org/10.1088/0953-8984/28/49/495001>.
- SADANA, S.; MACCONE, L.; SINHA, U. Testing quantum foundations with quantum computers. **Phys. Rev. Res.**, American Physical Society, v. 4, p. L022001, Apr 2022. <https://link.aps.org/doi/10.1103/PhysRevResearch.4.L022001>.
- SAHA, D.; MAHAPATRA, S. Atomistic modeling of the metallic-to-semiconducting phase boundaries in monolayer mos₂. **Applied Physics Letters**, v. 108, n. 25, p. 253106, 2016. <https://doi.org/10.1063/1.4954257>.

- SAHA, D.; VARGHESE, A.; LODHA, S. Atomistic modeling of van der waals heterostructures with group-6 and group-7 monolayer transition metal dichalcogenides for near infrared/short-wave infrared photodetection. **ACS Applied Nano Materials**, v. 3, n. 1, p. 820–829, 2020. <https://doi.org/10.1021/acsanm.9b02342>.
- SCAPPUCCI, G.; TAYLOR, P.; WILLIAMS, J. Crystalline materials for quantum computing: Semiconductor heterostructures and topological insulators exemplars. **MRS Bulletin**, v. 46, p. 596–606, 2021. <https://doi.org/10.1557/s43577-021-00147-8>.
- SCHLIEHE, C.; JUAREZ, B.; PELLETIER, M.; JANDER, S.; GRESHNYKH, D.; NAGEL, M.; MEYER, A.; FOERSTER, S.; KORNOWSKI, A.; KLINKE, C.; WELLER, H. Ultrathin pbs sheets by two-dimensional oriented attachment. **Science**, v. 303:329(5991):550-3, pMID: 20671184., 2010.
- SETTEN, M. van; GIANTOMASSI, M.; BOUSQUET, E.; VERSTRAETE, M.; HAMANN, D.; GONZE, X.; RIGNANESE, G.-M. The pseudodojo: Training and grading a 85 element optimized norm-conserving pseudopotential table. **Computer Physics Communications**, v. 226, p. 39–54, 2018. ISSN 0010-4655. <https://www.sciencedirect.com/science/article/pii/S0010465518300250>.
- SHADBOLT, P.; VERDE, M.; PERUZZO, A. Generating, manipulating and measuring entanglement and mixture with a reconfigurable photonic circuit. **Nature Photon**, v. 6, p. 45–49, 2012. <https://doi.org/10.1038/nphoton.2011.283>.
- SHI, Y.; ZHOU, W.; LU, A.-Y.; FANG, W.; LEE, Y.-H.; HSU, A. L.; KIM, S. M.; KIM, K. K.; YANG, H. Y.; LI, L.-J.; IDROBO, J.-C.; KONG, J. van der waals epitaxy of mos2 layers using graphene as growth templates. **Nano Letters**, v. 12, n. 6, p. 2784–2791, pMID: 22642717, 2012. <https://doi.org/10.1021/nl204562j>.
- SILVA, F. W. N.; COSTA, A. L. M. T.; LIU, L.; BARROS, E. B. Intense conductivity suppression by edge defects in zigzag mos2 and wse2 nanoribbons: a density functional based tight-binding study. **Nanotechnology**, IOP Publishing, v. 27, n. 44, p. 445202, sep 2016. <https://dx.doi.org/10.1088/0957-4484/27/44/445202>.
- SIMMONS, S.; BROWN, R.; RIEMANN, H. Entanglement in a solid-state spin ensemble. **Nature**, v. 470, p. 69–72, 2011. <https://doi.org/10.1038/nature09696>.
- SLATER, J. C.; KOSTER, G. F. Simplified lcao method for the periodic potential problem. **Phys. Rev.**, American Physical Society, v. 94, p. 1498–1524, Jun 1954. <https://link.aps.org/doi/10.1103/PhysRev.94.1498>.
- SOHIER, T.; CALANDRA, M.; MAURI, F. Density functional perturbation theory for gated two-dimensional heterostructures: Theoretical developments and application to flexural phonons in graphene. **Phys. Rev. B**, American Physical Society, v. 96, p. 075448, Aug 2017. <https://link.aps.org/doi/10.1103/PhysRevB.96.075448>.
- SOMMERFELD, A. Zur elektronentheorie der metalle auf grund der fermischen statistik. **Z. Physik**, v. 47, p. 1–32, 1928.

- SONG, L.; SONG, M.; LU, Z.; YU, G.; LIANG, Z.; HOU, W.; LIAO, Q.; SONG, Y. Recent advances of preparation and application of two-dimension van der waals heterostructure. **Coatings**, v. 12, n. 8, 2022. ISSN 2079-6412. <https://www.mdpi.com/2079-6412/12/8/1152>.
- SOUZA, I.; MARZARI, N.; VANDERBILT, D. Maximally localized wannier functions for entangled energy bands. **Phys. Rev. B**, American Physical Society, v. 65, p. 035109, Dec 2001. <https://link.aps.org/doi/10.1103/PhysRevB.65.035109>.
- SU, G.; HADJIEV, V. G.; LOYA, P. E.; ZHANG, J.; LEI, S.; MAHARJAN, S.; DONG, P.; AJAYAN, P. M.; LOU, J.; PENG, H. Chemical vapor deposition of thin crystals of layered semiconductor sns2 for fast photodetection application. **Nano Letters**, v. 15, n. 1, p. 506–513, pMID: 25494406, 2015. <https://doi.org/10.1021/nl503857r>.
- TAN, C.; LUO, Z.; CHATURVEDI, A.; CAI, Y.; DU, Y.; GONG, Y.; HUANG, Y.; LAI, Z.; ZHANG, X.; ZHENG, L.; QI, X.; GOH, M. H.; WANG, J.; HAN, S.; WU, X.-J.; GU, L.; KLOC, C.; ZHANG, H. Preparation of high-percentage 1t-phase transition metal dichalcogenide nanodots for electrochemical hydrogen evolution. **Advanced Materials**, v. 30, n. 9, p. 1705509, 2018. <https://onlinelibrary.wiley.com/doi/abs/10.1002/adma.201705509>.
- THONHAUSER, T.; COOPER, V. R.; LI, S.; PUZDER, A.; HYLDGAARD, P.; LANGRETH, D. C. Van der waals density functional: Self-consistent potential and the nature of the van der waals bond. **Phys. Rev. B**, American Physical Society, v. 76, p. 125112, Sep 2007. <https://link.aps.org/doi/10.1103/PhysRevB.76.125112>.
- THONHAUSER, T.; ZULUAGA, S.; ARTER, C. A.; BERLAND, K.; SCHRÖDER, E.; HYLDGAARD, P. Spin signature of nonlocal correlation binding in metal-organic frameworks. **Phys. Rev. Lett.**, American Physical Society, v. 115, p. 136402, Sep 2015. <https://link.aps.org/doi/10.1103/PhysRevLett.115.136402>.
- THOULESS, D. J.; KIRKPATRICK, S. Conductivity of the disordered linear chain. **Journal of Physics C: Solid State Physics**, v. 14, n. 3, p. 235, jan 1981. <https://dx.doi.org/10.1088/0022-3719/14/3/007>.
- THYGESEN, K. S. Calculating excitons, plasmons, and quasiparticles in 2d materials and van der waals heterostructures. **2D Materials**, IOP Publishing, v. 4, n. 2, p. 022004, jun 2017. <https://dx.doi.org/10.1088/2053-1583/aa6432>.
- TKATCHENKO, A.; SCHEFFLER, M. Accurate molecular van der waals interactions from ground-state electron density and free-atom reference data. **Phys. Rev. Lett.**, American Physical Society, v. 102, p. 073005, Feb 2009. <https://link.aps.org/doi/10.1103/PhysRevLett.102.073005>.
- TRAUZETTEL, B.; BULAEV, D.; LOSS, D. Spin qubits in graphene quantum dots. **Nature Phys**, v. 3, p. 192–196, 2007. <https://doi.org/10.1038/nphys544>.
- TRAVERSO, S.; SASSETTI, M.; ZIANI, N. T. Emerging topological bound states in haldane model zigzag nanoribbons. **npj Quantum Mater**, v. 9, 9, 2024.

TRIFONOVA, E.; YANCHEV, I.; STOYANOVA, V.; MANDALIDIS, S.; KAMBAS, K.; ANAGNOSTOPOULOS, A. Crystal growth and characterization of sns2. **Materials Research Bulletin**, v. 31, n. 8, p. 919–924, 1996. ISSN 0025-5408. <https://www.sciencedirect.com/science/article/pii/S0025540896000839>.

TSUKANOV, A. V. Measurement of a charge qubit using a single-electron transistor based on a triple quantum dot. **Phys. Rev. A**, American Physical Society, v. 100, p. 062305, Dec 2019. <https://link.aps.org/doi/10.1103/PhysRevA.100.062305>.

VELDHORST, M.; YANG, C.; HWANG, J. A two-qubit logic gate in silicon. **Nature**, v. 526, p. 410–414, 2015. <https://doi.org/10.1038/nature15263>.

WANG, J.; RODAN-LEGRAIN, D.; BRETHERAU, L. Coherent control of a hybrid superconducting circuit made with graphene-based van der waals heterostructures. **Nature Nanotech**, v. 14, p. 120–125, 2019. <https://doi.org/10.1038/s41565-018-0329-2>.

WANG, Y.; UM, M.; ZHANG, J. Single-qubit quantum memory exceeding ten-minute coherence time. **Nature Photon**, v. 11, p. 646–650, 2017. <https://doi.org/10.1038/s41566-017-0007-1>.

WANNIER, G. H. The structure of electronic excitation levels in insulating crystals. **Phys. Rev.**, American Physical Society, v. 52, p. 191–197, Aug 1937. <https://link.aps.org/doi/10.1103/PhysRev.52.191>.

WEES, B. J. van; HOUTEN, H. van; BEENAKKER, C. W. J.; WILLIAMSON, J. G.; KOUWENHOVEN, L. P.; MAREL, D. van der; FOXON, C. T. Quantized conductance of point contacts in a two-dimensional electron gas. **Phys. Rev. Lett.**, American Physical Society, v. 60, p. 848–850, Feb 1988. <https://link.aps.org/doi/10.1103/PhysRevLett.60.848>.

WEINTRUB, B.; HSIEH, Y.; KOVALCHUK, S. Generating intense electric fields in 2d materials by dual ionic gating. **Nat Commun**, v. 13, p. 6601, 2022. <https://doi.org/10.1038/s41467-022-34158-z>.

WENDIN, G. Quantum information processing with superconducting circuits: a review. **Reports on Progress in Physics**, IOP Publishing, v. 80, n. 10, p. 106001, sep 2017. <https://dx.doi.org/10.1088/1361-6633/aa7e1a>.

WHARAM, D. A.; THORNTON, T. J.; NEWBURY, R.; PEPPER, M.; AHMED, H.; FROST, J. E. F.; HASKO, D. G.; PEACOCK, D. C.; RITCHIE, D. A.; JONES, G. A. C. One-dimensional transport and the quantisation of the ballistic resistance. **Journal of Physics C: Solid State Physics**, v. 21, n. 8, p. L209, mar 1988. <https://dx.doi.org/10.1088/0022-3719/21/8/002>.

WHEELER, J. A. On the mathematical description of light nuclei by the method of resonating group structure. **Phys. Rev.**, American Physical Society, v. 52, p. 1107–1122, Dec 1937. <https://link.aps.org/doi/10.1103/PhysRev.52.1107>.

- WHITEHOUSE, C. R.; RIMMINGTON, H. P. B.; BALCHIN, A. A. Growth conditions and crystal structure parameters of layer compounds in the series $\text{zr}_x\text{se}_{2-x}$. **physica status solidi (a)**, v. 18, n. 2, p. 623–631, 1973.
<https://onlinelibrary.wiley.com/doi/abs/10.1002/pssa.2210180224>.
- WIGNER, E. On the interaction of electrons in metals. **Phys. Rev.**, American Physical Society, v. 46, p. 1002–1011, Dec 1934.
<https://link.aps.org/doi/10.1103/PhysRev.46.1002>.
- WIGNER, E. Effects of the electron interaction on the energy levels of electrons in metals. **Trans. Faraday Soc.**, The Royal Society of Chemistry, v. 34, p. 1002–1011, 1938.
- WILLHELM, D.; WILSON, N.; ARROYAVE, R.; QIAN, X.; CAGIN, T.; PACHTER, R.; QIAN, X. Predicting van der waals heterostructures by a combined machine learning and density functional theory approach. **ACS Applied Materials & Interfaces**, v. 14, n. 22, p. 25907–25919, pMID: 35622945, 2022.
<https://doi.org/10.1021/acsami.2c04403>.
- WU, N.; ZHAO, X.; MA, X.; XIN, Q.; LIU, X.; WANG, T.; WEI, S. Strain effect on the electronic properties of 1t-hfs2 monolayer. **Physica E: Low-dimensional Systems and Nanostructures**, v. 93, p. 1–5, 2017. ISSN 1386-9477.
<https://www.sciencedirect.com/science/article/pii/S1386947717303193>.
- WU, W.; WANG, L.; LI, Y. Piezoelectricity of single-atomic-layer mos2 for energy conversion and piezotronics. **Nature**, v. 514, p. 470–474, 2014.
<https://doi.org/10.1038/nature13792>.
- XIE, R.; HU, M.; LIU, D.; YU, Y.; LI, C.; HE, J.; LUO, J. Atomic observation of phase transition in layered sns2 driven by in situ heating and electron beam irradiation. **Applied Physics Letters**, v. 117, n. 16, p. 163103, 2020.
<https://doi.org/10.1063/5.0021180>.
- YAGMURCUKARDES, M.; PEETERS, F. M.; SENGER, R. T.; SAHIN, H. Nanoribbons: From fundamentals to state-of-the-art applications. **Applied Physics Reviews**, v. 3, n. 4, p. 041302, 11 2016. ISSN 1931-9401.
<https://doi.org/10.1063/1.4966963>.
- YANG, S.; LI, D.; ZHANG, T.; TAO, Z.; CHEN, J. First-principles study of zigzag mos2 nanoribbon as a promising cathode material for rechargeable mg batteries. **The Journal of Physical Chemistry C**, v. 116, n. 1, p. 1307–1312, 2012. <https://doi.org/10.1021/jp2097026>.
- YANG, T.; ZHENG, B.; WANG, Z. Van der waals epitaxial growth and optoelectronics of large-scale wse2/sns2 vertical bilayer p–n junctions. **Nat Commun**, v. 8, 2017.
<https://doi.org/10.1038/s41467-017-02093-z>.
- YIN, L.; CHENG, R.; WEN, Y.; LIU, C.; HE, J. Emerging 2d memory devices for in-memory computing. **Advanced Materials**, v. 33, n. 29, p. 2007081, 2021. <https://onlinelibrary.wiley.com/doi/abs/10.1002/adma.202007081>.
- YU, M.; LOURIE, O.; DYER, M.; MOLONI, K.; KELLY, T.; RUOFF, R. Strength and breaking mechanism of multiwalled carbon nanotubes under tensile load. **Science**, v. 28;287(5453):637-40, pMID: 10649994., 2000–01.

YUN, W. S.; HAN, S. W.; HONG, S. C.; KIM, I. G.; LEE, J. D. Thickness and strain effects on electronic structures of transition metal dichalcogenides: $2h-mX_2$ semiconductors ($m = \text{mo, w}; x = \text{s, se, te}$). **Phys. Rev. B**, American Physical Society, v. 85, p. 033305, Jan 2012.

<https://link.aps.org/doi/10.1103/PhysRevB.85.033305>.

ZHANG, H.; LI, X.-B.; LIU, L.-M. Tunable electronic and magnetic properties of WS₂ nanoribbons. **Journal of Applied Physics**, v. 114, n. 9, p. 093710, 09 2013. ISSN 0021-8979. <https://doi.org/10.1063/1.4820470>.

ZHANG, L.; WAN, L.; YU, Y.; WANG, B.; XU, F.; WEI, Y.; ZHAO, Y. Modulation of electronic structure of armchair mos₂ nanoribbon. **The Journal of Physical Chemistry C**, v. 119, n. 38, p. 22164–22171, 2015.

<https://doi.org/10.1021/acs.jpcc.5b04747>.

ZHANG, W. Mose₂/zrse₂ van der waals heterostructure tunneling field-effect transistor with substitutional doped source. *In: . Proceedings [...]. [S.l.: s.n.]*, 2019.

ZHANG, W.; MATSUDA, K.; MIYAUCHI, Y. Photostability of monolayer transition-metal dichalcogenides in ambient air and acidic/basic aqueous solutions. **ACS Omega**, v. 4, n. 6, p. 10322–10327, PMID: 31460125, 2019.

<https://doi.org/10.1021/acsomega.9b01067>.

ZHANG, Y.; SMALL, J. P.; AMORI, M. E. S.; KIM, P. Electric field modulation of galvanomagnetic properties of mesoscopic graphite. **Phys. Rev. Lett.**, American Physical Society, v. 94, p. 176803, May 2005.

<https://link.aps.org/doi/10.1103/PhysRevLett.94.176803>.

ZHANG, Y.; TAN, Y.; STORMER, H. Experimental observation of the quantum hall effect and berry's phase in graphene. **Nature**, v. 438, p. 201–204, 2005. <https://doi.org/10.1038/nature04235>.

ZHANG, Y.; YANG, W. Comment on “generalized gradient approximation made simple”. **Phys. Rev. Lett.**, American Physical Society, v. 80, p. 890–890, Jan 1998.

<https://link.aps.org/doi/10.1103/PhysRevLett.80.890>.

ZHAO, P.; KIRIYA, D.; AZCATL, A.; ZHANG, C.; TOSUN, M.; LIU, Y.-S.; HETTICK, M.; KANG, J. S.; MCDONNELL, S.; KC, S.; GUO, J.; CHO, K.; WALLACE, R. M.; JAVEY, A. Air stable p-doping of wse₂ by covalent functionalization. **ACS Nano**, v. 8, n. 10, p. 10808–10814, PMID: 25229426, 2014.

<https://doi.org/10.1021/nn5047844>.

ZHAO, X.; YANG, C.; WANG, T.; MA, X.; WEI, S.; XIA, C. 3d transition metal doping-induced electronic structures and magnetism in 1t-hfse₂ monolayers. **RSC Adv.**, The Royal Society of Chemistry, v. 7, p. 52747–52754, 2017.

ZHU, H.; WANG, Y.; XIAO, J. Observation of piezoelectricity in free-standing monolayer mos₂. **Nature Nanotech**, v. 10, p. 151–155, 2015.

<https://doi.org/10.1038/nnano.2014.309>.

ZHUANG, H. L.; HENNIG, R. G. Computational search for single-layer transition-metal dichalcogenide photocatalysts. **The Journal of Physical Chemistry C**, v. 117, n. 40, p. 20440–20445, 2013. <https://doi.org/10.1021/jp405808a>.

ZRIBI, J.; KHALIL, L.; ZHENG, B. Strong interlayer hybridization in the aligned sns2/wse2 hetero-bilayer structure. **npj 2D Mater Appl**, v. 3, p. 27, 2019.

Appendix A - Testing Functionals for Accurate van der Waals Interactions

A series of tests is performed to develop a solid methodology concerning the investigation of 2D materials and their stacking, resulting in the vdW heterostructures. Here, the best functional to accurately describe the vdW interactions will be chosen, electronic properties such as band structure, the density of states, and structural parameters to compare them with results consolidated on the literature, validating our methodology and going further to the investigation of other materials.

A test on the functionals implemented on QE was performed to give us solid ground to proceed with our investigation of a large class of materials: DFT-D (GRIMME, 2006; BARONE *et al.*, 2009), vdW-DF1 (DION *et al.*, 2004; THONHAUSER *et al.*, 2015), vdW-DF2 (LEE *et al.*, 2010), vdW-DF-C09 (DION *et al.*, 2004; THONHAUSER *et al.*, 2015; COOPER, 2010), vdW-DF2-C09 (LEE *et al.*, 2010; COOPER, 2010), revPBE (PERDEW *et al.*, 1996; ZHANG; YANG, 1998; PERDEW *et al.*, 1998), PW86 (PERDEW; YUE, 1986), optB88 (KLIMEŠ *et al.*, 2009; PERDEW, 1986), optB86 (KLIMEŠ *et al.*, 2011; PERDEW, 1986), vdW-DF-obk8 (KLIMEŠ *et al.*, 2009), vdW-DF-ob86 (KLIMEŠ *et al.*, 2011), vdW-DF2-B86R (LEE *et al.*, 2010; HAMADA, 2014), and vdW-DF-cx (BERLAND; HYLDGAARD, 2014). The structural parameters of graphite and graphene were calculated to perform a basic *benchmark*, considering the vdW interactions and comparing the results obtained with those in the literature. To ensure suitable parameters for the investigation, an optimization of the unit cell of graphite was performed in a mesh of the mesh of k-points 14x14x8, and the cut-off energy for the plane waves of 120 Ry was also investigated until convergence of 10^{-5} Ry/Bohr on the forces and 10^{-5} Ry on the energy, and a threshold for selfconsistency is 10^{-8} Ry. The convergence curves are shown in Fig.(A.1).

As the first test of vdW functionals, the lattice parameters in-plane (a) and out-of-plane (c) of graphite were computed as their band structures. The result for the parameters is given in figure A.2 and the table A.1 and the band structure on A.3.

For the in-plane lattice parameter, it is possible to see that all the functionals perform in good agreement with the experimental result, with the functional vdw-DF-obk8

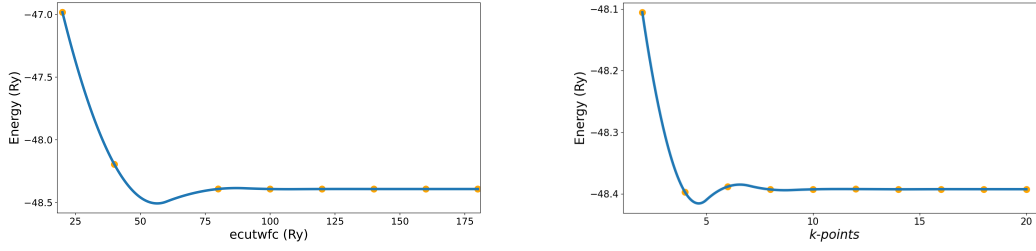


FIGURE A.1 – Graphite convergence: (a) Cutoff energy ($ecutwfc$) for the plane wave expansion; (b) k -points sampling on an $N \times N \times 8$ grid.

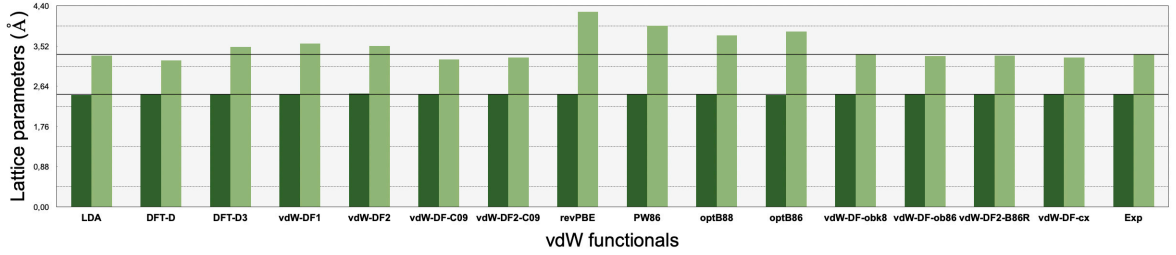


FIGURE A.2 – Results of several functionals for the structural parameters in-plane and out-of-plane compared with experimental results. Dark green represents the in-plane and light green out-of-plane graphite parameters.

TABLE A.1 – Parameters in-plane (a) and out-of-plane (c) compared with the experimental value.

Functionals	a (Å)	c (Å)
LDA	2.4490	3.314
LDA+DFT-D	2.4620	3.211
LDA+DFT-D3	2.4655	3.505
vdW-DF1	2.4680	3.577
vdW-DF2	2.4808	3.521
vdW-DF-C09	2.4543	3.223
vdW-DF2-C09	2.4556	3.268
revPBE	2.4580	4.269
PW86	2.4667	3.964
optB88	2.4545	3.755
optB86	2.4505	3.836
vdW-DF-obk8	2.4615	3.339
vdW-DF-ob86	2.4575	3.305
vdW-DF2-B86R	2.4583	3.314
vdW-DF-cx	2.455	3.274
Exp	2.46 ^[1]	3.336 ^[1]

Reference: [1](BASKIN; MEYER, 1955).

agreeing precisely equal the experimental value. For the out-of-plane lattice parameter c , the best results are given by $vdW-DF-obk8$ and $vdW-DF2-B86R$. Since $vdW-DF-obk8$ presents the best outcome for both parameters, it was chosen to use it for further calculations. The parameters found with this functional are in excellent agreement with previous theoretical and experimental results (CHEN *et al.*, 2013; BASKIN; MEYER, 1955). An ob-

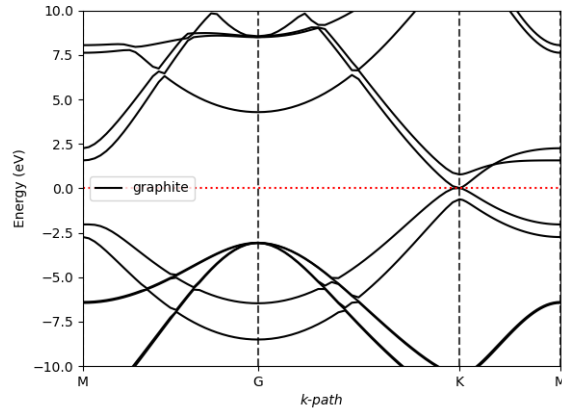


FIGURE A.3 – Band structure of graphite.

observation is done here to point out the result given by the LDA. Even in good agreement, the local approximation does not capture the vdW interactions, and it is impracticable to use it with the heterostructures. It also shown the band structure obtained for the graphite Fig.(A.3).

To ensure the result obtained from the vdW correction chosen, the same investigation was performed to graphene AA (interlayer distance obtained 3.56 \AA) and AB (interlayer distance obtained 3.35 \AA) also with excellent agreement with previous results (MIN *et al.*, 2007; KOLMOGOROV; CRESPI, 2005; MCCANN; KOSHINO, 2013). In addition, their dispersion relation throughout the Brillouin zone are in excellent agreement.

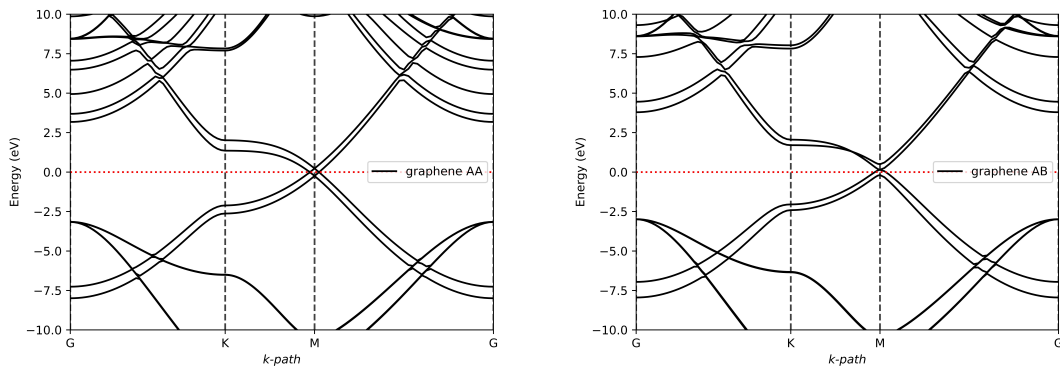


FIGURE A.4 – Graphene band structure: (a) Band structure of graphene AA stacking; (b) Band structure of graphene AB stacking.

This benchmark shows that the methodology for the *ab initio* calculations concerning the predictions of lattice parameters is adequated and can be used from now on.

Appendix B - Workflow of wannierization procedure

In Section (2.3), we explored the process of mapping Bloch eigenstates to the Wannier representation. This is accomplished through a unitary transformation that connects the two bases, as detailed in Eq.(2.53). To perform this transformation, we must carefully consider the degrees of freedom involved. One effective method is to project onto a set of predefined local orbitals, as demonstrated in Eq.(2.55). The resulting maximally localized Wannier functions (MLWFs) minimize the spread Ω of the localization functional, which measures the extent of orbital localization. This minimization is performed iteratively through a specialized algorithm implemented in the code (MARZARI; VANDERBILT, 1997).

Before obtaining an *ab initio* TB Hamiltonian, a DFT calculation is performed to obtain the Bloch wave functions. The next step involves selecting the relevant orbitals that describe the bands of interest in a specific energy window, which can be done using a fat band analysis. For instance, in the case of the $\text{ZrSe}_2/\text{SnSe}_2$ heterostructure, the orbitals d_{xy} , d_{z^2} , and $d_{x^2-y^2}$ of Zirconium and p orbitals of Sesium were chosen due to their main contribution to the bands around the Fermi energy, as shown in Fig.(B.1).

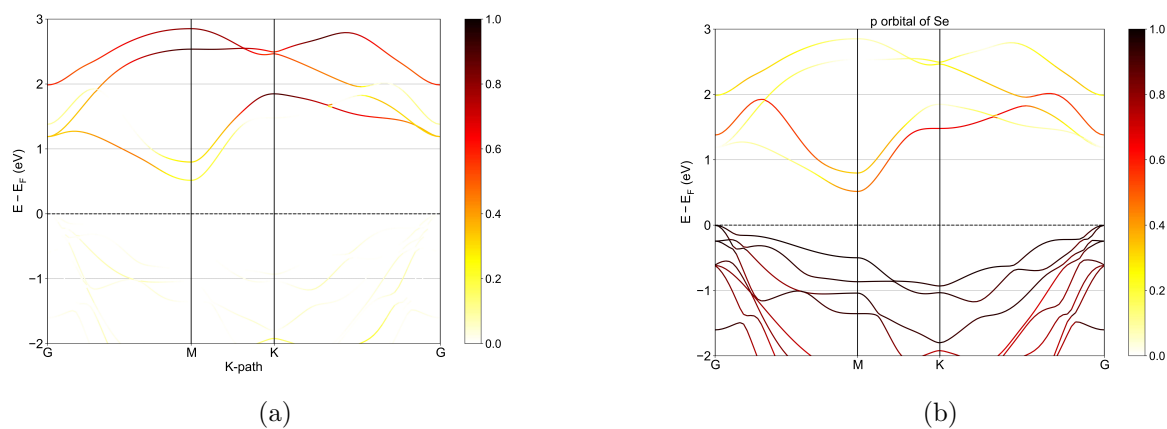


FIGURE B.1 – Fat bands of $\text{ZrSe}_2/\text{SnSe}_2$ used to provide an initial guess to obtain the MLWFs. (a) Projected band structure showing the orbital contribution of the $d_{xy} + d_{z^2} + d_{x^2-y^2}$ orbitals of Zirconium. (b) Projected band structure showing the orbital contribution of the p orbital of Selenium.

A schematic workflow of the procedure previously described is shown in Fig.(B.2). The initial projection is the g_n functions, given to the Wannier90 code, onto the Bloch states, and the matrices $M_{m,n}$ are the projections of the Bloch orbitals between band m and band n . The Wannier localization in R gives the Bloch smoothness in k .

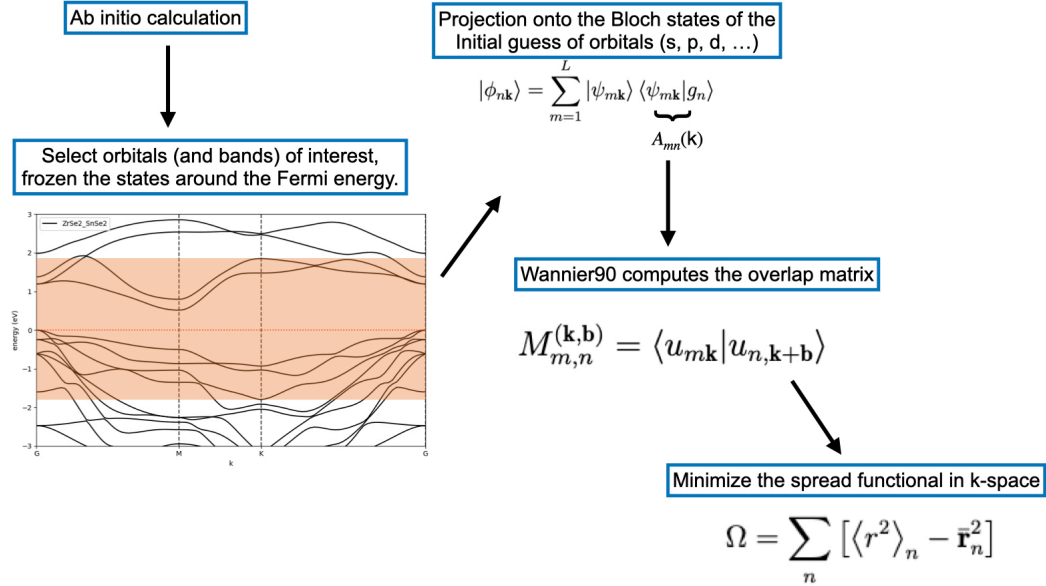


FIGURE B.2 – Workflow of typical Wannierization procedure.

For the heterostructure considered, it is obtained 15 MLWFs due to the initial projections that were given to the program. After the minimization procedure, their final spreads ranging from 2.4-3.8 Å confirm that the resulting WFs are well localized around the atoms. The final spread and the center of each WF can be seen in Fig.(B.3).

```

Final State
WF centre and spread  1 ( -0.000040, -0.001420,  8.988268 )  2.55031627
WF centre and spread  2 (  0.000001,  0.002388,  8.985649 )  2.60955751
WF centre and spread  3 (  0.000040, -0.000981,  8.983986 )  2.65294805
WF centre and spread  4 (  2.116208,  0.993130, 10.361358 )  2.48544242
WF centre and spread  5 (  1.720087,  0.993129, 10.361359 )  2.48544226
WF centre and spread  6 (  1.918149,  1.336124, 10.361270 )  2.48561703
WF centre and spread  7 ( -0.195139,  2.327513,  7.605988 )  2.40455949
WF centre and spread  8 (  0.195139,  2.327514,  7.605988 )  2.40456137
WF centre and spread  9 ( -0.000002,  1.989583,  7.606071 )  2.40473484
WF centre and spread 10 (  1.578327,  0.911247, 16.429730 )  3.72828480
WF centre and spread 11 (  2.257968,  0.911247, 16.429730 )  3.72828358
WF centre and spread 12 (  1.918148,  1.499834, 16.429730 )  3.72827680
WF centre and spread 13 (  0.352305,  2.418290, 13.943104 )  3.79539778
WF centre and spread 14 ( -0.352305,  2.418290, 13.943104 )  3.79540015
WF centre and spread 15 (  0.000000,  1.808080, 13.943104 )  3.79538471
Sum of centres and spreads ( 11.508886, 19.933967,171.978440 )  45.05420704

Spreads (Ang^2)      Omega I   =  43.173787051
=====              Omega D   =  0.008690287
                          Omega OD  =  1.871725496
Final Spread (Ang^2)  Omega Total =  45.054202834

```

FIGURE B.3 – Final spreads of the WFs and information about each term that composes the spread functional.

The values of Ω_I , Ω_D , and Ω_{OD} are presented, demonstrating the well-localized nature of the resulting Wannier functions in real space. This is due to the small value of the off-diagonal term of the spread functional. Details on each term are discussed in Section 2.3.

After the Wannierization procedure is complete, a truly *ab initio* tight-binding (TB) Hamiltonian is obtained, incorporating numerous hoppings that accurately replicate the band structure from the previous DFT calculation.

Appendix C - Electronic band offsets between monolayer materials

The table below shows the valence and conduction offsets (ΔE_v and ΔE_c) among freestanding monolayers. These offsets are important as they determine the orbital contribution of each layer to the states $|0\rangle$ and $|1\rangle$, as defined by the c coefficients in Eq. (4.2). To investigate this, the offsets were computed for various combinations of TMDs within the heterostructure.

The alignment of energy levels is determined by the electric field, which in turn affects the values of the band offsets. These offsets serve as a useful starting point for identifying materials suitable for hosting vdW qubits. With layers separated by a distance of 3-4 Å, and for fields with strength around 0.2 V/Å, the resulting offsets fall below 0.6 eV. Then, those materials that present such offsets are good candidates for hosting vdW qubits. The possible combinations are marked with green and the trivial combinations with red. It was found 222 possible combinations matching different layers on the conduction or the valence.

The alignment of energy levels is influenced by the electric field, which subsequently affects the band offsets. These offsets are critical for identifying materials suitable for hosting van der Waals qubits. When layers are separated by a distance of 3Å and subjected to electric fields around 0.2 V/Å, the resulting band offsets are below 0.6 eV. Materials exhibiting such offsets are considered promising candidates for hosting vdW qubits. In our analysis, we marked viable material combinations in green and trivial ones in red, identifying 222 possible combinations that match different layers in the conduction or valence bands.

	HfS2-T		HfS2-H		HfSe2-T		HfSe2-H		MoS2-T		MoS2-H		MoSe2-T		MoSe2-H		SnS2-T		SnS2-H		SnSe2-T		SnSe2-H		WS2-T		WS2-H		WSe2-T		WSe2-H		ZrS2-T		ZrS2-H		ZrSe2-T		ZrSe2-H			
	$ \Delta E_c $	$ \Delta E_v $	$ \Delta E_c $	$ \Delta E_v $	$ \Delta E_c $	$ \Delta E_v $	$ \Delta E_c $	$ \Delta E_v $	Metal	Metal	$ \Delta E_c $	$ \Delta E_v $	Metal	Metal	$ \Delta E_c $	$ \Delta E_v $	Metal	Metal	$ \Delta E_c $	$ \Delta E_v $	Metal	Metal	$ \Delta E_c $	$ \Delta E_v $	Metal	Metal	$ \Delta E_c $	$ \Delta E_v $	Metal	Metal	$ \Delta E_c $	$ \Delta E_v $	Metal	Metal	$ \Delta E_c $	$ \Delta E_v $	Metal	Metal	$ \Delta E_c $	$ \Delta E_v $	Metal	Metal
HfS2-T	0.0	0.0	0.59	0.81	0.71	0.05	0.11	0.56	Metal	Metal	0.63	0.79	Metal	Metal	1.19	0.89	0.32	0.26	0.12	0.69	0.36	0.43	0.80	0.81	Metal	Metal	0.88	1.18	Metal	Metal	1.45	1.28	0.03	0.15	0.50	0.87	0.69	0.20	0.05	0.63		
HfS2-H	0.59	0.81	0.0	0.0	1.30	0.85	0.48	0.25	Metal	Metal	1.22	1.59	Metal	Metal	1.78	1.70	0.27	0.54	0.71	0.12	0.95	0.38	1.38	0.005	Metal	Metal	1.47	1.98	Metal	Metal	2.03	2.09	0.56	0.65	0.09	0.07	1.28	0.61	0.54	0.17		
HfSe2-T	0.71	0.05	1.30	0.85	0.0	0.0	0.82	0.61	Metal	Metal	0.08	0.74	Metal	Metal	0.48	0.85	1.03	0.31	0.59	0.73	0.35	0.47	0.09	0.86	Metal	Metal	0.17	1.13	Metal	Metal	0.73	1.24	0.74	0.20	1.21	0.92	0.02	0.25	0.76	0.68		
HfSe2-H	0.11	0.56	0.48	0.25	0.82	0.61	0.0	0.0	Metal	Metal	0.74	1.35	Metal	Metal	1.30	1.45	0.21	0.30	0.23	0.12	0.47	0.13	0.91	0.25	Metal	Metal	0.99	1.74	Metal	Metal	1.56	1.85	0.08	0.41	0.39	0.31	0.80	0.36	0.06	0.07		
MoS2-T	Metal	Metal	Metal	Metal	Metal	Metal	Metal	Metal	0.0	0.0	Metal	Metal	Metal	Metal	Metal	Metal	Metal	Metal	Metal	Metal	Metal	Metal	Metal	Metal	Metal	Metal	Metal	Metal	Metal	Metal	Metal	Metal	Metal	Metal	Metal	Metal	Metal	Metal	Metal	Metal	Metal	Metal
MoS2-H	0.63	0.79	1.21	1.59	0.08	0.74	0.74	1.35	Metal	Metal	0.0	0.0	Metal	Metal	0.56	0.11	0.95	1.05	0.51	1.47	0.27	1.21	0.17	1.60	Metal	Metal	0.25	0.39	Metal	Metal	0.82	0.50	0.66	0.94	1.13	1.66	0.06	0.99	0.67	1.42		
MoSe2-T	Metal	Metal	Metal	Metal	Metal	Metal	Metal	Metal	Metal	Metal	Metal	Metal	Metal	Metal	Metal	Metal	Metal	Metal	Metal	Metal	Metal	Metal	Metal	Metal	Metal	Metal	Metal	Metal	Metal	Metal	Metal	Metal	Metal	Metal	Metal	Metal	Metal	Metal	Metal	Metal	Metal	Metal
MoSe2-H	1.19	0.89	1.78	1.70	0.48	0.85	1.30	1.45	Metal	Metal	0.56	0.11	Metal	Metal	0.0	0.0	1.51	1.15	1.07	1.58	0.83	1.32	0.39	1.70	Metal	Metal	0.31	0.28	Metal	Metal	0.25	0.39	1.22	1.04	1.68	1.77	0.50	1.09	1.23	1.53		
SnS2-T	0.32	0.26	0.27	0.55	1.03	0.31	0.21	0.30	Metal	Metal	0.95	1.05	Metal	Metal	1.51	1.15	0.0	0.0	0.44	0.42	0.68	0.16	1.12	0.55	Metal	Metal	1.20	1.44	Metal	Metal	1.77	1.55	0.29	0.11	0.18	0.61	1.01	0.06	0.27	0.37		
SnS2-H	0.12	0.68	0.71	0.12	0.59	0.73	0.23	0.12	Metal	Metal	0.51	1.47	Metal	Metal	1.07	1.58	0.44	0.42	0.0	0.0	0.24	0.26	0.67	0.13	Metal	Metal	0.76	1.86	Metal	Metal	1.32	1.97	0.15	0.53	0.62	0.19	0.57	0.48	0.17	0.05		
SnSe2-T	0.36	0.43	0.95	0.38	0.35	0.47	0.47	0.13	Metal	Metal	0.27	1.21	Metal	Metal	0.83	1.32	0.68	0.16	0.24	0.26	0.0	0.0	0.44	0.38	Metal	Metal	0.52	1.60	Metal	Metal	1.09	1.71	0.39	0.27	0.86	0.45	0.33	0.23	0.41	0.21		
SnSe2-H	0.80	0.81	1.38	0.005	0.09	0.86	0.91	0.25	Metal	Metal	0.17	1.60	Metal	Metal	0.39	1.70	1.12	0.55	0.67	0.13	0.44	0.38	0.0	0.0	Metal	Metal	0.08	1.99	Metal	Metal	0.65	2.10	0.83	0.66	1.29	0.06	0.11	0.61	0.84	0.18		
WS2-T	Metal	Metal	Metal	Metal	Metal	Metal	Metal	Metal	Metal	Metal	Metal	Metal	Metal	Metal	Metal	Metal	Metal	Metal	Metal	Metal	Metal	Metal	Metal	Metal	Metal	Metal	Metal	Metal	Metal	Metal	Metal	Metal	Metal	Metal	Metal	Metal	Metal	Metal	Metal	Metal	Metal	
WS2-H	0.88	1.18	1.47	1.98	0.17	1.13	0.99	1.74	Metal	Metal	0.25	0.39	Metal	Metal	0.31	0.28	1.20	1.44	0.76	1.86	0.52	1.60	0.08	1.99	Metal	Metal	0.0	0.0	Metal	Metal	0.57	0.11	0.91	1.33	1.39	2.05	0.19	1.38	0.92	1.81		
WSe2-T	2.24	0.51	2.83	1.31	1.53	0.46	2.35	1.07	Metal	Metal	1.61	0.28	Metal	Metal	1.05	0.38	2.56	0.77	2.12	1.19	1.88	0.93	1.45	1.32	Metal	Metal	1.36	0.67	0.0	0.0	0.80	0.78	2.27	0.66	2.74	1.38	1.55	0.71	2.28	1.14		
WSe2-H	1.44	1.28	2.03	2.09	0.74	1.24	1.56	1.85	Metal	Metal	0.82	0.50	Metal	Metal	0.26	0.39	1.77	1.55	1.32	1.97	1.07	1.71	0.65	2.10	Metal	Metal	0.57	0.11	Metal	Metal	0.0	0.0	1.48	1.44	1.96	2.16	0.76	1.49	1.49	1.92		
ZrS2-T	0.03	0.15	0.56	0.65	0.74	0.20	0.08	0.41	Metal	Metal	0.66	0.94	Metal	Metal	1.22	1.04	0.29	0.11	0.15	0.53	0.39	0.27	0.83	0.66	Metal	Metal	0.91	1.33	Metal	Metal	1.48	1.43	0.0	0.0	0.47	0.72	0.72	0.05	0.02	0.48		
ZrS2-H	0.50	0.88	0.09	0.07	1.21	0.92	0.39	0.31	Metal	Metal	1.13	1.66	Metal	Metal	1.69	1.78	0.18	0.61	0.62	0.19	0.86	0.45	1.30	0.06	Metal	Metal	1.38	2.05	Metal	Metal	1.95	2.16	0.47	0.72	0.0	0.0	1.19	0.67	0.45	0.24		
ZrSe2-T	0.69	0.20	1.28	0.61	0.02	0.25	0.80	0.36	Metal	Metal	0.06	0.99	Metal	Metal	0.50	1.09	1.01	0.06	0.57	0.48	0.33	0.23	0.11	0.61	Metal	Metal	0.19	1.38	Metal	Metal	0.76	1.49	0.72	0.05	1.19	0.67	0.0	0.0	0.73	0.43		
ZrSe2-H	0.05	0.63	0.54	0.17	0.75	0.68	0.06	0.07	Metal	Metal	0.68	1.42	Metal	Metal	1.23	1.53	0.27	0.37	0.17	0.05	0.41	0.21	0.84	0.18	Metal	Metal	0.92	1.81	Metal	Metal	1.49	1.92	0.01	0.48	0.45	0.24	0.73	0.43	0.0	0.0		

TABLE C.1 – Energy difference between conduction and valence edges. For those pairs of materials that presented offsets falling below 0.6 eV were marked in green, as promising candidates for hosting vdW qubits.

Annex A - Published works

- G. M. S. Brizolla, A. J. Chaves, L. K. Teles, I. Guilhon, and J. M. P. Junior, Electrically controlled charge qubit in van der waals heterostructures: From *ab initio* calculation to tight binding models. **Phys. Rev. B** **109**, 125416 (2024).
- Effects of Lattice Termination on Nanoribbons of Transition Metal Dichalcogenides. **To be submitted.**

Annex B - Participation in scientific congresses and conferences

- Gusthavo M. S Brizolla, et. al. Hybridized band structures on van der Waals heterostructures as a platform for charge qubits (Poster presentation). **20th workshop of semiconductor physics**, São José dos Campos-SP, BR, September, 2022.
- Gusthavo M. S Brizolla, et. al. Electrically controlled charge qubit in van der Waals heterostructure: from ab-initio calculations to Tight-Binding models (Poster presentation). **Autumn meeting (2023)**, Ouro Preto-MG, BR, May, 2023.
- Gusthavo M. S Brizolla, et. al. Investigation of electrically controlled charge qubit in van der Waals heterostructure: a Tight-Binding approach (Poster presentation - Awarded best poster of the conference). **Summer school: Simulation of van der Waals [hetero]structures**, Dresden, DE, August, 2023.
- Van Der Waals heterostructures as host platform for charge qubits (Talk). **University of Regensburg - Spintronics Research Group**. Gusthavo M.S. BRIZOLLA – Aeronautics Institute of Technology and Federal University of Ceará, Brazil, 2023.
- Electrically controlled charge qubit in van der Waals heterostructures: From ab initio calculations to the tight-binding model. **NOA seminar - Talk. Friedrich Schiller University Jena, Abbe Center of Photonics and Abbe School Photonics**. Gusthavo M.S. BRIZOLLA – Aeronautics Institute of Technology and Federal University of Ceará, Brazil, 2023.

FOLHA DE REGISTRO DO DOCUMENTO

^{1.} CLASSIFICAÇÃO/TIPO <p style="text-align: center;">TD</p>	^{2.} DATA <p style="text-align: center;">23 de julho de 2024</p>	^{3.} REGISTRO N° <p style="text-align: center;">DCTA/ITA/TD-025/2024</p>	^{4.} N° DE PÁGINAS <p style="text-align: center;">165</p>
^{5.} TÍTULO E SUBTÍTULO: <p>Tight-Binding modeling of van der Waals qubits</p>			
^{6.} AUTOR(ES): <p>Gusthavo Miranda Simões Brizolla</p>			
^{7.} INSTITUIÇÃO(ÕES)/ÓRGÃO(S) INTERNO(S)/DIVISÃO(ÕES): <p>Instituto Tecnológico de Aeronáutica - ITA</p>			
^{8.} PALAVRAS-CHAVE SUGERIDAS PELO AUTOR: <p>Materiais 2D, qubits, Teoria do Funcional da Densidade, Aproximação Tight-Binding</p>			
^{9.} PALAVRAS-CHAVE RESULTANTES DE INDEXAÇÃO: <p>1. Estruturas bidimensionais 2. Teoria de densidade funcional 3. Física</p>			
^{10.} APRESENTAÇÃO: (X) Nacional () Internacional <p>ITA, São José dos Campos. Curso de Doutorado. Programa de Pós-Graduação em Física. Área de Física Atômica e Molecular. Orientador: Prof. Dr. Ivan Guilhon Mitoso Rocha; co-orientador: Prof. Dr. João Milton Pereira Junior. Defesa em 10/07/2024. Publicada em 2024.</p>			
^{11.} RESUMO: <p>Quantum computing has the potential to revolutionize fields like drug development, disease prediction, materials design, machine learning, big data, and cybersecurity. The fundamental component of quantum information processes is the qubit, which leverages quantum superposition to represent both 0 and 1 simultaneously, unlike classical bits that can only represent one value at a time. Various approaches to qubit implementation have been proposed, including superconductors, nuclear and electronic spins, trapped ions, and photonic qubits. Recently, a new way of implementing the qubit for quantum computation through an innovative application of gated van der Waals (vdW) heterostructures as charge qubits has been proposed, here named vdW qubits. It explores the spatial superposition of electrons from the individual layers by studying the orbital composition of the bands as a function of the gate field. Given the extensive list of possible combinations of two-dimensional (2D) materials, the proposal provides a new perspective in the area. In this work, we investigate the structural and electronic properties of twenty 2D transition metal dichalcogenides (TMDs) using Density Functional Theory (DFT). We selected layers with well-aligned energy levels that resulted in hybridized states to form vdW qubits. To study these qubits with lower computational effort than DFT, we employed the Tight-Binding (TB) approach, using Maximally Localized Wannier Functions (MLWF) derived from DFT calculations. Our simplified model is consistent with DFT results, validated, and generalized to other systems with similar hybridized states. We identified new combinations of layered materials as promising candidates for implementing vdW qubits. To explore the transport properties of scattering regions influenced by hybridized states in 2D materials, we focused on nanoribbons (NRs) for our quantum transport calculations. These calculations allow us to analyze how plane waves split due to hybridized states, facilitating current transmission between layers within the heterostructure. The NRs simulated were based on previous TB models for the 2D materials with additional confinement, ensuring the <i>ab initio</i> character of our model while maintaining low computational cost. Initially, we explored the impact of confinement on NRs formed from TMD monolayers, assessing how chemical termination and edge configuration influence the appearance of edge states and transport properties. With a clear understanding of confinement effects, we proceeded to investigate transport in highly hybridized structures to observe wave packet splitting. These findings pave the way for implementing charge qubits.</p>			
^{12.} GRAU DE SIGILO: <p style="text-align: center;">(X) OSTENSIVO () RESERVADO () SECRETO</p>			